

ELECTRONIC AND THERMAL TRANSPORT IN COPPER-BASED CHALCOPYRITE  
SEMICONDUCTORS FOR THERMOELECTRIC APPLICATIONS

By

Winston D. Carr

A DISSERTATION

Submitted to  
Michigan State University  
in partial fulfillment of the requirements  
for the degree of

Physics — Doctor of Philosophy

2016

## ABSTRACT

### ELECTRONIC AND THERMAL TRANSPORT IN COPPER-BASED CHALCOPYRITE SEMICONDUCTORS FOR THERMOELECTRIC APPLICATIONS

By

Winston D. Carr

The thermoelectric effect was discovered in 1821 when Thomas Seebeck observed that a circuit made of two dissimilar metals, with junctions at two different temperatures, deflected a compass needle. However, in the ensuing nearly two-hundred years thermoelectric devices have failed to find use in any but niche applications. This slow progress, when compared to that of photo-voltaic devices which have greatly improved in roughly half the time, is due in large part to the contraindicated parameters which govern the efficiency of a thermoelectric material. Optimizing one parameter for thermoelectric performance often comes at the cost of hindering another, so multiple approaches must be used to improve the thermoelectric performance of a material. Therefore, material optimization requires a firm understanding of the underlying transport physics and materials science governing a material.

When evaluating the viability of a material for thermoelectric use the dimensionless figure of merit,  $ZT$ , is the standard metric. This dimensionless figure is a combination of the Seebeck coefficient and the electrical and thermal conductivities of the material, as well as the operating temperature, and is directly related to the efficiency of a thermoelectric generator. In the past 25 years the field of thermoelectricity has provided many materials with a  $ZT$  in excess of unity, and recently materials have been reported with values greater than two. However, element toxicity, low elemental abundance, and complex synthesis techniques have prevented many of these materials from reaching commercial viability.

This work presents a systematic study of the chalcopyrite family of semiconductors with

chemical structure I-III-VI<sub>2</sub> where the group I element is copper. This family contains many possibilities for non-toxic, earth abundant materials which can be simply, and in some cases rapidly, synthesized. A better understanding of the physics governing the transport mechanisms in these materials could lead to their adoption in future thermoelectric applications, helping improve the energy efficiency of devices of all sizes.

I would like to dedicate this work to my math teachers, Mrs. Brenda Charles and Mr. Terry Johnson, for starting and encouraging my passion for math and physics, to my parents, Bridget and Bob, for supporting me along the way, and especially to Ginger for helping me keep it all together. I could not have done this without you all.  
In the words of Mr. Johnson: “Perseverance, keep your nose to the grindstone”.

## ACKNOWLEDGMENTS

I would first like to thank my advisor, Dr. Donald T. Morelli, for giving me the opportunity to work in his research group, for allowing me to travel to conferences and present my work, for encouraging me to explore any ideas I had, and for putting up with endless questions on any topic.

I would also like to thank all of my group members who helped me throughout the years with synthesis, measurements, conversations, and thoughts: Dr. Vijay Ponnabalam, Dr. Steve Boona, Dr. Xu Lu, Dr. Gloria Lehr, Mr. Jared Williams, and Mr. Spencer Waldrop. I was also assisted by two talented undergrad researchers, Mr. Spencer Mathers, and Mr. Adam Marsh, for which I am thankful. Outside of our group, I would like to greatly thank Dr. Travis Thompson, Dr. Michael Bennett, and Mr. Christopher Willis all for hours of helpful discussion and insight. And, I have to thank my faithful writing companion, Daisy, for staying with me and offering moral support through all the hot days while I was writing this thesis. Her dedication was an inspiration to me.

I am grateful to my guidance committee members, Dr. Jeff Sakamoto, Dr. Phil Duxbury, Dr. Stuart Tessmer, and Dr. Tim Hogan. You were all very helpful any time I had questions, especially Dr. Duxbury who I pestered weekly during our statistical mechanics course.

I want to thank Dr. Si Hui as well as Dr. Ctirad Uher for providing laser flash measurements for me when the system at MSU was down.

Finally I would like acknowledge that this research was funded by the Department of Energy Office of Science through the Revolutionary Materials for Solid State Energy Conversion Energy Frontier Research Center, Award # DE-SC0001054.

# TABLE OF CONTENTS

<b>LIST OF TABLES</b> . . . . .	<b>viii</b>
<b>LIST OF FIGURES</b> . . . . .	<b>ix</b>
<b>Chapter 1 Introduction</b> . . . . .	<b>1</b>
1.1 The History and Importance of Thermoelectricity . . . . .	1
1.2 Motivation for Thermoelectric Power Generation . . . . .	7
<b>Chapter 2 The Physics of Thermoelectric Materials and Devices</b> . . . . .	<b>11</b>
2.1 Thermoelectric Device Efficiencies . . . . .	12
2.2 Electrical Conductivity . . . . .	16
2.3 The Seebeck Coefficient . . . . .	25
2.3.1 Band theory of transport . . . . .	30
2.4 Thermal Conductivity . . . . .	32
2.5 Motivation for Chalcopyrite Compounds . . . . .	39
<b>Chapter 3 Experimental Procedures</b> . . . . .	<b>43</b>
3.1 Materials Synthesis . . . . .	43
3.1.1 Furnace Heating Procedure . . . . .	44
3.1.2 Sintering Procedures . . . . .	45
3.2 Characterization Techniques . . . . .	46
3.2.1 X-ray Diffraction . . . . .	46
3.2.2 Differential Scanning Calorimetry . . . . .	47
3.2.3 Hall Measurements . . . . .	48
3.2.4 Low Temperature Transport Properties . . . . .	50
3.2.4.1 Electrical Resistivity . . . . .	51
3.2.4.2 Seebeck Coefficient and Thermal Conductivity . . . . .	51
3.2.5 High Temperature Transport Properties . . . . .	53
3.2.5.1 Electrical Resistivity and Seebeck Coefficient . . . . .	53
3.2.5.2 Thermal Conductivity and Thermal Diffusivity . . . . .	54
<b>Chapter 4 Tellurides</b> . . . . .	<b>55</b>
4.1 Family Overview . . . . .	55
4.2 CuAlTe <sub>2</sub> . . . . .	56
4.3 CuInTe <sub>2</sub> . . . . .	60
4.3.1 Electronic Doping . . . . .	60
4.4 CuGaTe <sub>2</sub> . . . . .	65
4.4.1 Transport Properties . . . . .	66
4.4.2 Electronic Doping . . . . .	69
4.4.2.1 N-type Dopants: Zinc, Germanium, Tin, and Iodine . . . . .	69

4.5	Solid Solutions . . . . .	75
4.5.1	$\text{CuIn}_{1-x}\text{Ga}_x\text{Te}_2$ . . . . .	75
4.5.2	$\text{Cu}(\text{In}_{1-x}\text{Ga}_x)_{0.99}\text{Zn}_{0.01}\text{Te}_2$ . . . . .	80
4.5.3	$\text{CuInTe}_2(1-x)\text{S}_{2x}$ . . . . .	84
4.6	Conclusions . . . . .	87
<b>Chapter 5 Selenides . . . . .</b>		<b>88</b>
5.1	Family Overview . . . . .	88
5.2	$\text{CuInSe}_2$ . . . . .	89
5.2.1	Electronic Doping . . . . .	90
5.3	$\text{CuGaSe}_2$ . . . . .	92
5.3.1	Electronic Doping . . . . .	93
5.4	Solid Solutions . . . . .	97
5.4.1	$\text{CuIn}_{0.99}\text{Zn}_{0.01}\text{Te}_2(1-x)\text{Se}_{2x}$ - Hotpressed . . . . .	97
5.4.2	$\text{CuInTe}_2(1-x)\text{Se}_{2x}$ - Spark Plasma Sintered . . . . .	103
5.4.3	$\text{CuIn}_{1-y}\text{Zn}_y\text{Te}_1\text{Se}_1$ . . . . .	107
5.4.4	$\text{CuGaTe}_2(1-x)\text{Se}_{2x}$ . . . . .	112
5.4.5	$\text{CuGa}_{1-y}\text{Zn}_y\text{TeSe}$ . . . . .	117
5.5	Conclusions . . . . .	120
<b>Chapter 6 Sulfides . . . . .</b>		<b>123</b>
6.1	Family Overview . . . . .	123
6.2	$\text{CuFeS}_2$ . . . . .	124
6.2.1	Electronic Doping . . . . .	128
6.2.2	$\text{CuFeS}_2$ Rapid SPS Synthesis . . . . .	132
6.3	$\text{CuInS}_2$ . . . . .	140
6.4	$\text{CuGaS}_2$ . . . . .	141
6.5	Solid Solutions . . . . .	142
6.5.1	$\text{CuFeS}_2(1-x)\text{Se}_{2x}$ . . . . .	142
6.5.2	$\text{CuFeS}_2(1-x)\text{Te}_{2x}$ . . . . .	149
6.5.3	$\text{CuFe}_{1-x}\text{Ga}_x\text{S}_2$ . . . . .	150
6.6	Conclusions . . . . .	151
<b>Chapter 7 Related Materials . . . . .</b>		<b>152</b>
7.1	Bornite: $\text{Cu}_5\text{FeS}_4$ . . . . .	152
7.2	Defect Chalcopyrite: $\text{Zn}_{0.5}\text{GaTe}_2$ and $\text{Zn}_{0.5}\text{InTe}_2$ . . . . .	158
7.2.1	Solid Solution: $\text{CuGaTe}_2$ - $\text{Zn}_{0.5}\text{GaTe}_2$ . . . . .	162
7.3	Copper Deficient $\text{CuGaTe}_2$ . . . . .	166
<b>Chapter 8 Conclusions and Future Work . . . . .</b>		<b>172</b>
<b>REFERENCES . . . . .</b>		<b>178</b>

## LIST OF TABLES

Table 6.1	Density of samples of CuFeS <sub>2</sub> synthesized by direct SPS reaction. The theoretical density of CuFeS <sub>2</sub> is 4.1823 g cm <sup>-3</sup> using the lattice parameters obtained from XRD. . . . .	134
-----------	---	-----

## LIST OF FIGURES

Figure 1.1	On the left, a temperature differential generates a voltage potential (the Seebeck effect) while on the right an applied voltage drives a current which will either liberate or generate heat at the junction (the Peltier effect). . . . .	2
Figure 1.2	Lawrence Livermore National Lab estimated 2013 energy use in the U.S. The left side represents the sources of energy, and the right side the end uses. . . . .	7
Figure 1.3	The E1 thermoelectric generator from Alphabet Energy. On the left is a large diesel generator, with the exhaust connected to the E1 TEG on the right.[1] . . . . .	9
Figure 2.1	Schematic of a thermoelectric unicouple. A generator is made from a group of these stacked electrically in series and thermally in parallel.	12
Figure 2.2	Efficiency of a thermoelectric generator as a function of $ZT$ and hot side temperature. The cold side is set at 300K. As $ZT$ tends to infinity the efficiency approaches the Carnot limit. . . . .	15
Figure 2.3	Carrier concentration ( $n$ ) in $\text{cm}^{-3}$ as a function of reduced Fermi energy ( $\eta \equiv \frac{E_f}{k_b T}$ ) calculated from equation (2.21). $\eta = 0$ refers the the conduction band edge. The effective mass ( $m^*$ ) is taken to be the free electron mass here. . . . .	18
Figure 2.4	Carrier concentration as a function of inverse temperature for a doped semiconductor, showing the freeze out region at low temperature, the saturation region, and the final high temperature region when intrinsic carriers dominate. . . . .	21
Figure 2.5	Electrical conductivity of $\text{CuInTe}_2$ and $\text{CuIn}_{0.99}\text{Zn}_{0.01}\text{Te}_2$ versus temperature. As shown, the doped sample has metallic behavior, with the electrical conductivity dropping with increasing temperature. At high enough temperatures, both samples become intrinsic. . . . .	24
Figure 2.6	Diagram of the Seebeck effect in an n-type material. The hot electrons flow from the left side and accumulate on the right side, inducing an electric field and a resultant potential difference. . . . .	25

Figure 2.7	Seebeck coefficient (S) in $\mu\text{V K}^{-1}$ as a function of reduced Fermi energy ( $\eta \equiv \frac{E_f}{k_b T}$ ) calculated from equations (2.43) and (2.44), assuming $\lambda = -1/2$ . . . . .	28
Figure 2.8	$S^2 n e^* 10^{-6}$ in $\mu\text{W V s cm}^{-3} \text{K}^{-2}$ as a function of reduced Fermi energy ( $\eta \equiv \frac{E_f}{k_b T}$ ) calculated from equation (2.45), using an effective mass of $1 m_e$ and a temperature of 800K. . . . .	29
Figure 2.9	Schematic diagramming Umklapp Scattering. Phonons $q_1$ and $q_2$ combine to form phonon $q_3$ which lies outside the 1st Brillouin zone and is subsequently folded back in to the 1st BZ. . . . .	38
Figure 2.10	Crystal structures of Si, ZnSe, $\text{Zn}_2\text{Se}_2$ , and $\text{CuGaSe}_2$ from left to right. At high temperatures the ordering in $\text{CuGaSe}_2$ breaks down, and the crystal can be reduced back to a cubic structure with Cu and Ga atoms occupying sites interchangeably, as will be shown in later chapters. . . . .	40
Figure 2.11	Electronic band structures of $\text{CuGaTe}_2$ (on the left) and of $\text{CuGaS}_2$ (on the right) showing the relatively flat valence bands, which indicate a high effective mass. [2, 3] . . . . .	41
Figure 3.1	Steps in material synthesis. From left to right, elements weighed out in ampoule, ampoule being sealed, and the resulting ingot after the furnace procedure. . . . .	44
Figure 3.2	Experimental setup for Hall measurements. The applied magnetic field is into the page. . . . .	48
Figure 3.3	Example of typical Hall data, showing the Hall resistance versus field relationship. The slope is equal to $1/ne t$ , where $t$ is the sample thickness, $e$ is the elementary charge, and $n$ is the carrier concentration. . . . .	49
Figure 3.4	Experimental setup for low temperature transport measurements. The measurement is performed under a liquid nitrogen flow, with the sample surrounded by vacuum. . . . .	50
Figure 4.1	X-ray diffraction pattern of $\text{CuAlTe}_2$ with PDF overlay. The y-scale is intensity, in arbitrary units. PDF # 01-075-0102 [4] . . . . .	56
Figure 4.2	Electrical resistivity of $\text{CuAlTe}_2$ as a function of temperature. . . . .	57
Figure 4.3	Seebeck coefficient of $\text{CuAlTe}_2$ as a function of temperature. . . . .	58

Figure 4.4	Thermal conductivity of CuAlTe <sub>2</sub> as a function of temperature. . . .	59
Figure 4.5	X-ray diffraction pattern of CuInTe <sub>2</sub> with PDF overlay. The y-scale is intensity, in arbitrary units. The pattern is PDF #01-082-0450. [5]	60
Figure 4.6	Electrical resistivity of the series CuIn <sub>1-y</sub> Zn <sub>y</sub> Te <sub>2</sub> as a function of temperature. Open symbols represent CuIn <sub>1-y</sub> Zn <sub>y</sub> Te <sub>2</sub> . Filled symbols are data from Liu <i>et al.</i> for CuInTe <sub>2</sub> annealed for 1, 72, and 168 hours. For comparison, our samples were annealed for 24 hours.[6] .	61
Figure 4.7	Seebeck coefficient of the series CuIn <sub>1-y</sub> Zn <sub>y</sub> Te <sub>2</sub> as a function of temperature. Open symbols represent CuIn <sub>1-y</sub> Zn <sub>y</sub> Te <sub>2</sub> . Filled symbols are data from Liu <i>et al.</i> for CuInTe <sub>2</sub> annealed for 1, 72, and 168 hours. For comparison, our samples were annealed for 24 hours.[6] .	62
Figure 4.8	Power factor of the series CuIn <sub>1-y</sub> Zn <sub>y</sub> Te <sub>2</sub> as a function of temperature. Open symbols represent CuIn <sub>1-y</sub> Zn <sub>y</sub> Te <sub>2</sub> . Filled symbols are data from Liu <i>et al.</i> for CuInTe <sub>2</sub> annealed for 1, 72, and 168 hours. For comparison, our samples were annealed for 24 hours.[6] . . . . .	63
Figure 4.9	Thermal conductivity of the series CuIn <sub>1-y</sub> Zn <sub>y</sub> Te <sub>2</sub> as a function of temperature. Open symbols represent CuIn <sub>1-y</sub> Zn <sub>y</sub> Te <sub>2</sub> . Filled symbols are data from Liu <i>et al.</i> for CuInTe <sub>2</sub> annealed for 1, 72, and 168 hours. For comparison, our samples were annealed for 24 hours.[6] .	64
Figure 4.10	$ZT$ of the series CuIn <sub>1-y</sub> Zn <sub>y</sub> Te <sub>2</sub> as a function of temperature. Open symbols represent CuIn <sub>1-y</sub> Zn <sub>y</sub> Te <sub>2</sub> . Filled symbols are data from Liu <i>et al.</i> for CuInTe <sub>2</sub> annealed for 1, 72, and 168 hours. For comparison, our samples were annealed for 24 hours.[6] . . . . .	64
Figure 4.11	XRD pattern of CuGaTe <sub>2</sub> , with a PDF overlay. The pattern is PDF # 01-079-2331. [7] . . . . .	65
Figure 4.12	Electrical resistivity of CuGaTe <sub>2</sub> as a function of temperature. Squares represent our data, while the diamonds are from Plirdpring <i>et al.</i> [8], and the triangles are from Li <i>et al.</i> [9]. . . . .	66
Figure 4.13	Seebeck coefficient of CuGaTe <sub>2</sub> as a function of temperature. Squares represent our data, while the diamonds are from Plirdpring <i>et al.</i> [8], and the triangles are from Li <i>et al.</i> [9] . . . . .	66
Figure 4.14	Power factor of CuGaTe <sub>2</sub> as a function of temperature. Squares represent our data, while the diamonds are from Plirdpring <i>et al.</i> [8], and the triangles are from Li <i>et al.</i> [9]. . . . .	67

Figure 4.15	Thermal conductivity of $\text{CuGaTe}_2$ as a function of temperature. Squares represent our data, while the diamonds are from Plirdpring <i>et al.</i> [8], and the triangles are from Li <i>et al.</i> [9]. . . . .	68
Figure 4.16	$ZT$ of $\text{CuGaTe}_2$ as a function of temperature. Squares represent our data, while the diamonds are from Plirdpring <i>et al.</i> [8], and the triangles are from Li <i>et al.</i> [9]. . . . .	68
Figure 4.17	Thermal conductivity of the series $\text{CuGaTe}_{2(1-x)}\text{I}_{2x}$ as a function of temperature. . . . .	70
Figure 4.18	Power factor of the series $\text{CuGaTe}_{2(1-x)}\text{I}_{2x}$ as a function of temperature. . . . .	71
Figure 4.19	$ZT$ of the series $\text{CuGaTe}_{2(1-x)}\text{I}_{2x}$ as a function of temperature. . . . .	71
Figure 4.20	Electrical resistivity of n-type doped samples of $\text{CuGaTe}_2$ as a function of temperature. . . . .	72
Figure 4.21	Seebeck coefficient of n-type doped samples of $\text{CuGaTe}_2$ as a function of temperature. . . . .	72
Figure 4.22	Power factor of n-type doped samples of $\text{CuGaTe}_2$ as a function of temperature. . . . .	73
Figure 4.23	Thermal conductivity of n-type doped samples of $\text{CuGaTe}_2$ as a function of temperature. . . . .	74
Figure 4.24	XRD patterns of the series $\text{CuIn}_{1-x}\text{Ga}_x\text{Te}_2$ . From bottom to top, samples are $x = [0, 0.25, 0.35, 0.5, 0.65, 0.75, 1]$ . The y-axis is shows intensity in arbitrary units. To top PDF is $\text{CuGaTe}_2$ (# 01-079-2331) and the bottom is $\text{CuInTe}_2$ (#01-082-0450).[5, 7] . . . . .	75
Figure 4.25	Calculated lattice parameters of the series $\text{CuIn}_{1-x}\text{Ga}_x\text{Te}_2$ as a function of gallium concentration ( $x$ ), using the 204 and 424 peaks. . . . .	76
Figure 4.26	Electrical resistivity of the series $\text{CuIn}_{1-x}\text{Ga}_x\text{Te}_2$ as a function of temperature. . . . .	77
Figure 4.27	Seebeck coefficient of the series $\text{CuIn}_{1-x}\text{Ga}_x\text{Te}_2$ as a function of temperature. . . . .	78
Figure 4.28	Power factor of the series $\text{CuIn}_{1-x}\text{Ga}_x\text{Te}_2$ as a function of temperature. . . . .	79

Figure 4.29	Thermal conductivity of the series $\text{CuIn}_{1-x}\text{Ga}_x\text{Te}_2$ as a function of temperature. . . . .	79
Figure 4.30	$ZT$ of the series $\text{CuIn}_{1-x}\text{Ga}_x\text{Te}_2$ as a function of temperature. . . . .	80
Figure 4.31	Electrical resistivity of the series $\text{Cu}(\text{In}_{1-x}\text{Ga}_x)_{0.99}\text{Zn}_{0.01}\text{Te}_2$ as a function of temperature. . . . .	81
Figure 4.32	Seebeck coefficient of the series $\text{Cu}(\text{In}_{1-x}\text{Ga}_x)_{0.99}\text{Zn}_{0.01}\text{Te}_2$ as a function of temperature. . . . .	81
Figure 4.33	Power factor of the series $\text{Cu}(\text{In}_{1-x}\text{Ga}_x)_{0.99}\text{Zn}_{0.01}\text{Te}_2$ as a function of temperature. . . . .	82
Figure 4.34	Thermal conductivity of the series $\text{Cu}(\text{In}_{1-x}\text{Ga}_x)_{0.99}\text{Zn}_{0.01}\text{Te}_2$ as a function of temperature. . . . .	83
Figure 4.35	$ZT$ of the series $\text{Cu}(\text{In}_{1-x}\text{Ga}_x)_{0.99}\text{Zn}_{0.01}\text{Te}_2$ as a function of temperature. . . . .	83
Figure 4.36	XRD pattern of $\text{CuInTe}_{2(1-x)}\text{S}_{2x}$ with PDF. The top pattern is $\text{CuInTe}_2$ , followed by $x = 0.005, 0.01, \text{ and } 0.015$ , at which point secondary peaks corresponding to $\text{CuInS}_2$ were observed. Patterns are PDF #01-082-0450 and #01-075-0106 for $\text{CuInTe}_2$ and $\text{CuInS}_2$ respectively.[5, 10] . . . . .	84
Figure 4.37	Electrical resistivity of the series $\text{CuInTe}_{2(1-x)}\text{S}_{2x}$ as a function of temperature. . . . .	85
Figure 4.38	Seebeck coefficient of the series $\text{CuInTe}_{2(1-x)}\text{S}_{2x}$ as a function of temperature. . . . .	85
Figure 4.39	Thermal conductivity of the series $\text{CuInTe}_{2(1-x)}\text{S}_{2x}$ as a function of temperature. . . . .	86
Figure 4.40	$ZT$ of the series $\text{CuInTe}_{2(1-x)}\text{S}_{2x}$ as a function of temperature. . . . .	86
Figure 5.1	XRD pattern of $\text{CuInSe}_2$ with PDF. The y-scale is intensity, in arbitrary units. The pattern is PDF #01-075-2916. [11] . . . . .	89
Figure 5.2	Electrical resistivity of the series $\text{CuIn}_{1-y}\text{Zn}_y\text{Se}_2$ versus temperature. The data for $\text{CuInSe}_2$ shows a large amount of fluctuation due to the large sample resistance and the difficulty in making good electrical contact to the sample. . . . .	90

Figure 5.3	Seebeck coefficient of the series $\text{CuIn}_{1-y}\text{Zn}_y\text{Se}_2$ as a function of temperature. . . . .	91
Figure 5.4	Power factor of the series $\text{CuIn}_{1-y}\text{Zn}_y\text{Se}_2$ as a function of temperature. . . . .	91
Figure 5.5	X-ray diffraction pattern for $\text{CuGaSe}_2$ with PDF overlay. The y-scale is intensity, in arbitrary units. The pattern is PDF #01-075-2916. [12]	92
Figure 5.6	Electrical resistivity of the series $\text{CuGa}_{1-x}\text{Zn}_x\text{Se}_2$ as a function of temperature. . . . .	94
Figure 5.7	Seebeck coefficient of the series $\text{CuGa}_{1-x}\text{Zn}_x\text{Se}_2$ as a function of temperature. . . . .	94
Figure 5.8	Power factor of the series $\text{CuGa}_{1-x}\text{Zn}_x\text{Se}_2$ as a function of temperature. . . . .	95
Figure 5.9	Thermal conductivity of the series $\text{CuGa}_{1-x}\text{Zn}_x\text{Se}_2$ as a function of temperature. . . . .	96
Figure 5.10	$ZT$ of the series $\text{CuGa}_{1-x}\text{Zn}_x\text{Se}_2$ as a function of temperature. . . . .	96
Figure 5.11	XRD patterns of the solid solution $\text{CuIn}_{0.99}\text{Zn}_{0.01}\text{Te}_{2(1-x)}\text{Se}_{2x}$ with PDFs. The top pattern is for $\text{CuIn}_{0.99}\text{Zn}_{0.01}\text{Te}_2$ , with each pattern showing substitutions in 25% increments. The y-scale is intensity, in arbitrary units. The patterns are PDF #01-082-0450 and #01-075-2916 for Te and Se respectively. [13, 11]	97
Figure 5.12	Lattice parameters of the solid solution $\text{CuIn}_{0.99}\text{Zn}_{0.01}\text{Te}_{2(1-x)}\text{Se}_{2x}$ with literature values shown in open symbols. The dashed lines are to guide the eyes.[4, 14, 13, 6, 15, 8]	98
Figure 5.13	Thermal conductivity and electrical resistivity of $\text{CuIn}_{0.99}\text{Zn}_{0.01}\text{Te}_{2(1-x)}\text{Se}_{2x}$ at 300K. Both show a strong dependence on selenium concentration.	99
Figure 5.14	Electrical resistivity of the series $\text{CuIn}_{0.99}\text{Zn}_{0.01}\text{Te}_{2(1-x)}\text{Se}_{2x}$ as a function of temperature, showing the strong dependence on selenium concentration. . . . .	100
Figure 5.15	Thermal conductivity of the series $\text{CuIn}_{0.99}\text{Zn}_{0.01}\text{Te}_{2(1-x)}\text{Se}_{2x}$ as a function of temperature, showing the strong dependence on selenium concentration . . . . .	101
Figure 5.16	Seebeck coefficient of the series $\text{CuIn}_{0.99}\text{Zn}_{0.01}\text{Te}_{2(1-x)}\text{Se}_{2x}$ as a function of temperature. . . . .	101

Figure 5.17	Power factor of the series $\text{CuIn}_{0.99}\text{Zn}_{0.01}\text{Te}_{2(1-x)}\text{Se}_{2x}$ as a function of temperature. . . . .	102
Figure 5.18	$ZT$ of the series $\text{CuIn}_{0.99}\text{Zn}_{0.01}\text{Te}_{2(1-x)}\text{Se}_{2x}$ as a function of temperature. . . . .	102
Figure 5.19	XRD patterns for the solid solution $\text{CuInTe}_{2(1-x)}\text{Se}_{2x}$ densified via SPS with PDFs. The bottom pattern is for $\text{CuInTe}_2$ , with each subsequent pattern showing substitutions in 25% increments. The y-scale is intensity, in arbitrary units. PDFs are #01-082-0450 and #01-075-2916 for Te and Se respectively. [13, 11] . . . . .	103
Figure 5.20	Seebeck coefficient of the series $\text{CuInTe}_{2(1-x)}\text{Se}_{2x}$ as a function of temperature. . . . .	104
Figure 5.21	Electrical resistivity of the series $\text{CuInTe}_{2(1-x)}\text{Se}_{2x}$ as a function of temperature. . . . .	105
Figure 5.22	Power factor of the series $\text{CuInTe}_{2(1-x)}\text{Se}_{2x}$ as a function of temperature. . . . .	105
Figure 5.23	Thermal conductivity of the series $\text{CuInTe}_{2(1-x)}\text{Se}_{2x}$ as a function of temperature. . . . .	106
Figure 5.24	$ZT$ of the series $\text{CuInTe}_{2(1-x)}\text{Se}_{2x}$ as a function of temperature. . .	106
Figure 5.25	Seebeck coefficient of the series $\text{CuIn}_{1-y}\text{Zn}_y\text{Te}_1\text{Se}_1$ as a function of temperature. . . . .	108
Figure 5.26	Electrical resistivity of the series $\text{CuIn}_{1-y}\text{Zn}_y\text{Te}_1\text{Se}_1$ as a function of temperature. . . . .	109
Figure 5.27	Power factor of the series $\text{CuIn}_{1-y}\text{Zn}_y\text{Te}_1\text{Se}_1$ as a function of temperature. . . . .	110
Figure 5.28	Thermal conductivity of the series $\text{CuIn}_{1-y}\text{Zn}_y\text{Te}_1\text{Se}_1$ as a function of temperature. . . . .	110
Figure 5.29	$ZT$ of the series $\text{CuIn}_{1-y}\text{Zn}_y\text{Te}_1\text{Se}_1$ as a function of temperature. .	111
Figure 5.30	XRD patterns of the series $\text{CuGaTe}_{2(1-x)}\text{Se}_{2x}$ with PDFs. The top pattern is for $\text{CuGaTe}_2$ , with each pattern showing selenium substitutions in 25% increments, with $\text{CuGaSe}_2$ shown at the bottom. The y-scale is intensity in arbitrary units. The PDFs are # 01-079-2331 and #01-075-2916 for Te and Se respectively. [7, 12] . . . . .	112

Figure 5.31	Lattice parameters of the series $\text{CuGaTe}_{2(1-x)}\text{Se}_{2x}$ . Open symbols represent literature data, while the filled symbols are data from the study here. [4, 14, 13, 15, 8, 16] . . . . .	113
Figure 5.32	Thermal conductivity and electrical resistivity of the series $\text{CuGaTe}_{2(1-x)}\text{Se}_{2x}$ at room temperature. Thermal conductivity shows the typical parabolic relationship, while the electrical resistivity shows an exponential dependence on selenium concentration. . . . .	114
Figure 5.33	Electrical resistivity of the series $\text{CuGaTe}_{2(1-x)}\text{Se}_{2x}$ as a function of temperature. . . . .	114
Figure 5.34	Seebeck coefficient of the series $\text{CuGaTe}_{2(1-x)}\text{Se}_{2x}$ as a function of temperature. . . . .	115
Figure 5.35	Power factor of the series $\text{CuGaTe}_{2(1-x)}\text{Se}_{2x}$ as a function of temperature. . . . .	115
Figure 5.36	Thermal conductivity of the series $\text{CuGaTe}_{2(1-x)}\text{Se}_{2x}$ as a function of temperature. . . . .	116
Figure 5.37	$ZT$ of the series $\text{CuGaTe}_{2(1-x)}\text{Se}_{2x}$ as a function of temperature. . .	117
Figure 5.38	Electrical resistivity of the series $\text{CuGa}_{1-y}\text{Zn}_y\text{TeSe}$ as a function of temperature. . . . .	118
Figure 5.39	Seebeck coefficient of the series $\text{CuGa}_{1-y}\text{Zn}_y\text{TeSe}$ as a function of temperature. . . . .	119
Figure 5.40	Power factor of the series $\text{CuGa}_{1-y}\text{Zn}_y\text{TeSe}$ as a function of temperature. . . . .	119
Figure 5.41	$ZT$ versus temperature for the series $\text{CuGa}_{1-y}\text{Zn}_y\text{TeSe}$ . . . . .	120
Figure 5.42	High temperature thermal conductivity of tellurium - selenium solid solutions as a function of selenium concentration. Compositions are $\text{CuGaTe}_{2(1-x)}\text{Se}_{2x}$ , $\text{CuInTe}_{2(1-x)}\text{Se}_{2x}$ (SPS) and $\text{CuIn}_{0.99}\text{Zn}_{0.01}\text{Te}_{2(1-x)}\text{Se}_{2x}$ (HP). Measurements were performed at 860K. . . . .	121
Figure 5.43	High temperature electrical resistivity of tellurium - selenium solid solutions as a function of selenium concentration. Compositions are $\text{CuGaTe}_{2(1-x)}\text{Se}_{2x}$ , $\text{CuInTe}_{2(1-x)}\text{Se}_{2x}$ (SPS) and $\text{CuIn}_{0.99}\text{Zn}_{0.01}\text{Te}_{2(1-x)}\text{Se}_{2x}$ (HP). Measurements were performed at 860K. . . . .	122

Figure 6.1	XRD pattern of $\text{CuFeS}_2$ . The pattern shown below is PDF# 01-083-0983.[17] . . . . .	124
Figure 6.2	Seebeck coefficient of $\text{CuFeS}_2$ as a function of temperature as compared to literature reports. Data is from Tsujii <i>et al.</i> and Li <i>et al.</i> . [18, 19, 20] . . . . .	125
Figure 6.3	Electrical resistivity of $\text{CuFeS}_2$ as a function of temperature as compared to literature reports. Data is from Tsujii <i>et al.</i> and Li <i>et al.</i> . [18, 19, 20] . . . . .	126
Figure 6.4	Power factor of $\text{CuFeS}_2$ as a function of temperature as compared to literature reports. Data is from Tsujii <i>et al.</i> and Li <i>et al.</i> . [18, 19, 20]	127
Figure 6.5	Thermal conductivity of $\text{CuFeS}_2$ as a function of temperature as compared to literature reports. Data is from Tsujii <i>et al.</i> and Li <i>et al.</i> . [18, 19, 20] . . . . .	127
Figure 6.6	$ZT$ of $\text{CuFeS}_2$ as a function of temperature as compared to literature reports. Data is from Tsujii <i>et al.</i> and Li <i>et al.</i> . [18, 19, 20] . . . . .	128
Figure 6.7	Electrical resistivity of the series $\text{Cu}_{1-y}\text{Zn}_y\text{FeS}_2$ as a function of temperature as compared to literature reports. Open symbols represent data obtained here, while the filled symbols represent data from Tsujii <i>et al.</i> and Li <i>et al.</i> . [18, 19, 20] . . . . .	129
Figure 6.8	Seebeck coefficient of the series $\text{Cu}_{1-y}\text{Zn}_y\text{FeS}_2$ as a function of temperature as compared to literature reports. Open symbols represent data obtained here, while the filled symbols represent data is from Tsujii <i>et al.</i> and Li <i>et al.</i> . [18, 19, 20] . . . . .	130
Figure 6.9	Power factor of the series $\text{Cu}_{1-y}\text{Zn}_y\text{FeS}_2$ as a function of temperature as compared to literature reports. Data is from Tsujii <i>et al.</i> and Li <i>et al.</i> . [18, 19, 20] . . . . .	130
Figure 6.10	Thermal conductivity of the series $\text{Cu}_{1-y}\text{Zn}_y\text{FeS}_2$ as a function of temperature as compared to literature reports. Data is from Tsujii <i>et al.</i> and Li <i>et al.</i> . [18, 19, 20] . . . . .	131
Figure 6.11	$ZT$ of the series $\text{Cu}_{1-y}\text{Zn}_y\text{FeS}_2$ as a function of temperature as compared to literature reports. Data is from Tsujii <i>et al.</i> and Li <i>et al.</i> . [18, 19, 20] . . . . .	132

Figure 6.12	The top pattern is for two powders mixed by hand, the middle pattern is the powder after 5 minutes of vibratory milling, and the bottom pattern is taken after the powder has been densified by the SPS. The patterns shown below are PDF# 01-083-0983, PDF# 01-079-2321, and PDF# 03-065-6841 for CuFeS <sub>2</sub> , CuS, and FeS respectively.[17, 21, 22] . . . . .	133
Figure 6.13	Electrical resistivity of several samples of CuFeS <sub>2</sub> as a function of temperature. Samples were synthesized by direct reaction during SPS. The squares represents CuFeS <sub>2</sub> made by traditional melting and hotpressing. . . . .	134
Figure 6.14	Seebeck coefficient of several samples of CuFeS <sub>2</sub> as a function of temperature. Samples were synthesized by direct reaction during SPS. The squares represents CuFeS <sub>2</sub> made by traditional melting and hotpressing. . . . .	135
Figure 6.15	Power factor of several samples of CuFeS <sub>2</sub> as a function of temperature. Samples were synthesized by direct reaction during SPS. The squares represents CuFeS <sub>2</sub> made by traditional melting and hotpressing.	136
Figure 6.16	Thermal conductivity of several samples of CuFeS <sub>2</sub> as a function of temperature. Samples were synthesized by direct reaction during SPS. The squares represents CuFeS <sub>2</sub> made by traditional melting and hotpressing. . . . .	137
Figure 6.17	$ZT$ of several samples of CuFeS <sub>2</sub> as a function of temperature. Samples were synthesized by direct reaction during SPS. The squares represents CuFeS <sub>2</sub> made by traditional melting and hotpressing. . .	138
Figure 6.18	Electrical resistivity of several samples of CuFeS <sub>2</sub> synthesized by direct reaction during SPS compared to literature values for CuFeS <sub>2-<math>\delta</math></sub> . The X symbol represents the data from samples made in this study, the other symbols are from Li <i>et al.</i> [23] . . . . .	139
Figure 6.19	Seebeck coefficient of several samples of CuFeS <sub>2</sub> synthesized by direct reaction during SPS compared to literature values for CuFeS <sub>2-<math>\delta</math></sub> . The X symbol represents the data from samples made in this study, the other symbols are from Li <i>et al.</i> [23] . . . . .	139
Figure 6.20	XRD pattern of CuInS <sub>2</sub> . The pattern shown below is PDF# 01-075-6866.[24] . . . . .	140
Figure 6.21	Electrical resistivity of CuInS <sub>2</sub> as a function of temperature . . . . .	141

Figure 6.22	Thermal conductivity of $\text{CuInS}_2$ as a function of temperature . . . .	141
Figure 6.23	Electrical resistivity of several samples of $\text{CuGaS}_2$ from work by Julien <i>et al.</i> The samples were simply described by their apparent colors.[25] . . . . .	142
Figure 6.24	XRD patterns of the series $\text{CuFeS}_{2(1-x)}\text{Se}_{2x}$ . The top pattern is pure $\text{CuFeS}_2$ , with each pattern beneath it increasing x by 0.05, the at the bottom being final pattern $\text{CuFeS}_{1.4}\text{Se}_{0.6}$ . Note the additional peaks in the bottom pattern, indicating the presence of a secondary phase. PDFs for patterns are #01-075-6866 and #01-081-1959 for $\text{CuFeS}_2$ and $\text{CuFeSe}_2$ respectively. [26, 27] . . . . .	143
Figure 6.25	Lattice parameters of the series $\text{CuFeS}_{2(1-x)}\text{Se}_{2x}$ as a function of x. Increasing selenium leads to a larger lattice, however at x = 0.3 the growth stops, as a solubility limit is reached. . . . .	144
Figure 6.26	Specific heat of the series $\text{CuFeS}_{2(1-x)}\text{Se}_{2x}$ as a function of temperature. The peaks indicate decomposition into a mixture of binary phases, followed by the sublimation of sulfur. . . . .	145
Figure 6.27	Temperature of the peak in the DSC curve for the series $\text{CuFeS}_{2(1-x)}\text{Se}_{2x}$ . The peaks indicate decomposition into a mixture of binary phases, followed by the sublimation of sulfur. . . . .	145
Figure 6.28	Electrical resistivity of the series $\text{CuFeS}_{2(1-x)}\text{Se}_{2x}$ as a function of temperature. . . . .	146
Figure 6.29	Seebeck coefficient of the series $\text{CuFeS}_{2(1-x)}\text{Se}_{2x}$ as a function of temperature. . . . .	147
Figure 6.30	Power factor of the series $\text{CuFeS}_{2(1-x)}\text{Se}_{2x}$ as a function of temperature.	148
Figure 6.31	Thermal conductivity of the series $\text{CuFeS}_{2(1-x)}\text{Se}_{2x}$ as a function of temperature. . . . .	148
Figure 6.32	$ZT$ of the series $\text{CuFeS}_{2(1-x)}\text{Se}_{2x}$ as a function of temperature. . . .	149
Figure 6.33	XRD Patterns of $\text{CuFeS}_{2(1-x)}\text{Te}_{2x}$ . The top pattern is for pure $\text{CuFeS}_2$ , followed by x = 0.05, 0.10, 0.2, and 0.3. The patterns below are from PDF #01-075-6866 and #01-070-3094 for $\text{CuFeS}_2$ and $\text{CuFeTe}_2$ respectively.[26, 28] . . . . .	150

Figure 7.1	XRD pattern of nominally pure bornite ( $\text{Cu}_5\text{FeS}_4$ ) and four doped compositions. The top pattern is pure $\text{Cu}_5\text{FeS}_4$ , followed by the 1% and 5% p-type doped samples, and finally the 1% and 5% n-type doped samples. The extra peaks observed in the 1% n-type sample are due to a secondary phase of FeS. The y-scale is intensity, in arbitrary units. Source: PDF #98-000-0123.[29] . . . . .	153
Figure 7.2	Electrical resistivity of samples of nominally pure bornite ( $\text{Cu}_5\text{FeS}_4$ ) and four doped compositions as a function of temperature. Literature data is shown with colored symbols for comparison.[30, 31] . . . . .	154
Figure 7.3	Seebeck coefficient of samples of nominally pure bornite ( $\text{Cu}_5\text{FeS}_4$ ) and four doped compositions as a function of temperature. Literature data is shown with colored symbols for comparison.[30, 31] . . . . .	154
Figure 7.4	Power factor of samples of nominally pure bornite ( $\text{Cu}_5\text{FeS}_4$ ) and four doped compositions as a function of temperature. Literature data is shown with colored symbols for comparison.[30, 31] . . . . .	156
Figure 7.5	Thermal conductivity of samples of nominally pure bornite ( $\text{Cu}_5\text{FeS}_4$ ) and four doped compositions as a function of temperature. Literature data is shown with colored symbols for comparison.[30, 31] . . . . .	157
Figure 7.6	$ZT$ of samples of nominally pure bornite ( $\text{Cu}_5\text{FeS}_4$ ) and four doped compositions as a function of temperature. Literature data is shown with colored symbols for comparison.[30, 31] . . . . .	158
Figure 7.7	XRD patterns of the defect chalcopyrite compounds: $\text{Zn}_{0.5}\text{GaTe}_2$ , $\text{Zn}_{0.475}\text{GaTe}_2$ , and $\text{Zn}_{0.5}\text{InTe}_2$ from top to bottom respectively. The y-scale is intensity, in arbitrary units. Source: PDF #01-089-4209 and #01-074-0218 for $\text{Zn}_{0.5}\text{GaTe}_2$ and $\text{Zn}_{0.5}\text{InTe}_2$ respectively. [4] .	159
Figure 7.8	Electrical resistivity of defect chalcopyrite compounds, with $\text{CuGaTe}_2$ as a reference, as a function of temperature. . . . .	160
Figure 7.9	Power factor of defect chalcopyrite compounds, with $\text{CuGaTe}_2$ as a reference, as a function of temperature. . . . .	160
Figure 7.10	Thermal conductivity of defect chalcopyrite compounds as a function of temperature. . . . .	161
Figure 7.11	$ZT$ of defect chalcopyrite compounds as a function of temperature. .	162

Figure 7.12	XRD patterns of the partial solid solution of $\text{CuGaTe}_2$ and $\text{Zn}_{0.5}\text{GaTe}_2$ . The top pattern is $\text{CuGaTe}_2$ , followed by $\text{Cu}_{0.995}\text{Zn}_{0.0025}\text{GaTe}_2$ , $\text{Cu}_{0.990}\text{Zn}_{0.0050}\text{GaTe}_2$ , $\text{Cu}_{0.900}\text{Zn}_{0.0500}\text{GaTe}_2$ , and at the bottom $\text{Cu}_{0.800}\text{Zn}_{0.1000}\text{GaTe}_2$ . The PDF overlay is for $\text{CuGaTe}_2$ . The y-scale is intensity, in arbitrary units. Source: PDF #01-079-2331. [7]	163
Figure 7.13	Electrical resistivity of the partial solid solution $\text{CuGaTe}_2 - \text{Zn}_{0.5}\text{GaTe}_2$ as a function of temperature. . . . .	163
Figure 7.14	Seebeck coefficient of the partial solid solution $\text{CuGaTe}_2 - \text{Zn}_{0.5}\text{GaTe}_2$ as a function of temperature. . . . .	164
Figure 7.15	Power factor of the partial solid solution $\text{CuGaTe}_2 - \text{Zn}_{0.5}\text{GaTe}_2$ as a function of temperature. . . . .	165
Figure 7.16	Thermal conductivity of the partial solid solution $\text{CuGaTe}_2 - \text{Zn}_{0.5}\text{GaTe}_2$ as a function of temperature. . . . .	165
Figure 7.17	$ZT$ of the partial solid solution $\text{CuGaTe}_2 - \text{Zn}_{0.5}\text{GaTe}_2$ as a function of temperature . . . . .	166
Figure 7.18	XRD pattern of copper deficient $\text{CuGaTe}_2$ . The top pattern is $\text{CuGaTe}_2$ , followed by the 5%, 10%, and 15% copper deficiency samples respectively. The y-scale is intensity, in arbitrary units. Source: PDF #01-079-2331. [7] . . . . .	167
Figure 7.19	Carrier concentration and mobility at 300K for the series $\text{Cu}_{1-x}\text{GaTe}_2$ as a function of vacancy concentration (x). . . . .	167
Figure 7.20	Electrical resistivity of the series $\text{Cu}_{1-x}\text{GaTe}_2$ as a function of temperature. . . . .	168
Figure 7.21	Seebeck coefficient of the series $\text{Cu}_{1-x}\text{GaTe}_2$ as a function of temperature. . . . .	169
Figure 7.22	Power factor of the series $\text{Cu}_{1-x}\text{GaTe}_2$ as a function of temperature.	169
Figure 7.23	Thermal conductivity of the series $\text{Cu}_{1-x}\text{GaTe}_2$ as a function of temperature. . . . .	170
Figure 7.24	$ZT$ of the series $\text{Cu}_{1-x}\text{GaTe}_2$ as a function of temperature. . . . .	171
Figure 8.1	Comparison of the electrical resistivity of the base compounds $\text{CuInTe}_2$ , $\text{CuGaTe}_2$ , $\text{CuInSe}_2$ , $\text{CuGaSe}_2$ , and $\text{CuFeS}_2$ . $\text{CuInS}_2$ is not shown here, but the values are on the order of $10^8 \text{ m}\Omega \text{ cm}$ . . . . .	173

Figure 8.2 Comparison of the thermal conductivity of the base chalcopyrite compounds. . . . . 175

# Chapter 1

## Introduction

### 1.1 The History and Importance of Thermoelectricity

The field of thermoelectricity began in 1821 when Thomas Johann Seebeck discovered that if he made a loop out of two different metals, and held one junction at a higher temperature than the other he could deflect a compass needle.[32] It was later determined that this was due to a thermally driven current flowing through the loop. This effect can be seen more easily by simply forming one junction between two materials, heating or cooling the junction, and measuring the resulting voltage across the two leads. The voltage generated by this effect is given as:

$$\Delta V = -(S_A - S_B)\Delta T \quad (1.1)$$

where  $\Delta V$  is the generated voltage difference along a materials,  $\Delta T$  is the temperature difference along the same material, and  $S_A$  and  $S_B$  are the Seebeck coefficients (also called the thermopowers) of the two materials. Since the junction is made of two materials, the result is a sum of the voltages of the two legs, however, by using a super conductor, which has a Seebeck coefficient of zero, one material can be measured independently. Alternatively,

one can use a material for which the Seebeck coefficient is very well known in one leg, and use that data to determine the value for the other material. The Seebeck coefficient has units of volts per Kelvin, in magnitude is typically in the range of 10s to 100s of  $\mu\text{V K}^{-1}$ , and can be both positive or negative. The sign convention is defined such that p-type materials have a positive Seebeck coefficient, and n-type materials have a negative coefficient. This effect is commonly used today in thermocouples to measure temperature.

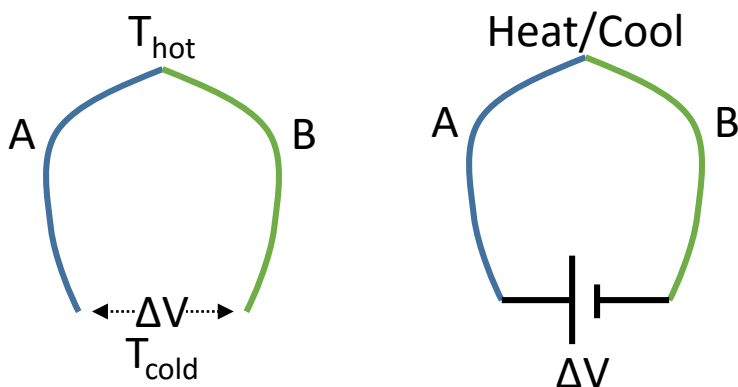


Figure 1.1: On the left, a temperature differential generates a voltage potential (the Seebeck effect) while on the right an applied voltage drives a current which will either liberate or generate heat at the junction (the Peltier effect).

Following Seebeck’s discovery, in 1834 Jean Charles Athanase Peltier discovered what is now called the Peltier effect.[33] He found that if one made a junction of two different metals and passed a current through it, the junction would either heat up or cool down depending on the direction of the current. The power of this heating or cooling can be expressed as:

$$\dot{Q} = (\Pi_A - \Pi_B)I \tag{1.2}$$

where  $\dot{Q}$  is the rate at which heat is being generated or removed,  $I$  is the current passing through the material, and  $\Pi_{A/B}$  is the Peltier coefficient of each material.

Finally, in 1851 Lord Kelvin (then William Thomson) predicted, and then observed, what is now called the Thomson effect.[34] His work showed that if one passed a current through a homogeneous material, which was also under a temperature gradient parallel the current flow, heat could be moved from one end to the other. This can be expressed mathematically as:

$$\dot{Q} = -K\mathbf{J} \cdot \nabla T \quad (1.3)$$

where  $\dot{Q}$  is again the heat flow,  $\mathbf{J}$  is the current density through the sample,  $\nabla T$  is the temperature gradient, and  $K$  is the Thomson coefficient. He also derived a relation between the Seebeck, Peltier, and Thomson coefficients:

$$K = \frac{d\Pi}{dT} - S \quad (1.4)$$

and

$$\Pi = TS \quad (1.5)$$

Equations (1.3) - (1.5) all describe interactions between electric charge and heat, and combined can be used to explain and understand thermoelectric materials. The Seebeck effect describes a method for measuring temperature, as we do with thermocouples today, or for generating power from a heat source as is done with thermoelectric generators. The Peltier effect describes a solid state method for heating or cooling devices, and the Thomson effect shows a connection between the two phenomena. While the three thermoelectric effects were discovered and described in the mid 1800s, progress in the field of thermoelectric coolers

and generators was quite slow, and large progress in the field was not made until the 1940s and 1950s.

In 1909 and 1911 a theory and formula for the maximum efficiency for power generation (which will be discussed in the following chapter), as well as maximum cooling power for refrigeration, was developed by Altenkirch, giving the first guide to optimizing thermoelectric materials.[35, 36] That work showed the importance of the dimensionless figure of merit,  $ZT$ , which determines the efficiency of a thermoelectric generator or refrigerator:

$$\eta = \frac{T_h - T_c}{T_h} \frac{\sqrt{1 + ZT} - 1}{\sqrt{1 + ZT} + T_c/T_h} \quad (1.6)$$

$$ZT = \frac{S^2 \sigma}{\kappa} T \quad (1.7)$$

Later work in the 1930s by Onsager would show a deeper connection between all three effects, earning him the Nobel Prize in chemistry in 1968 for the Onsager reciprocal relations.[37, 38, 39] In 1957 *Semiconductor Thermoelements and Thermoelectric Cooling* by A. F. Ioffe (translated to English by A. Gelbtuch) was published, adding greatly to the theoretical framework for thermoelectric devices. He was one of the first scientists to put forward the idea of using semiconductors, and not metals, to make efficient thermoelectric devices.

The work by Goldsmid, especially the initial reports on the properties of  $\text{Bi}_2\text{Te}_3$ , contributed heavily to the field and this compound remained one of the best low temperature thermoelectric materials for the next 50 years.[40, 41] Work by Telkes surveyed a variety of alloys at use at the time, as well as the performance of both traditional and solar based generators in the late 1940s and 50s.[42, 43, 44] Her work suggested some ideal parame-

ters of materials comprising a thermoelectric generator, with a desired thermal conductivity of  $1 \text{ W m}^{-1} \text{ K}^{-1}$  and an electrical resistivity of  $1 \text{ m}\Omega \text{ cm}$ . However, she stated that at the time, no such materials were available. The report by Goldsmid on  $\text{Bi}_2\text{Te}_3$  which showed a room temperature thermal conductivity of  $2.1 \text{ W m}^{-1} \text{ K}^{-1}$  and an electrical resistivity of  $2.5 \text{ m}\Omega \text{ cm}$  for  $\text{Bi}_2\text{Te}_3$  came out the same year.[40]

Also in the late 1950s, work on lowering thermal conductivity by alloying, or the formation of solid solutions, was shown to be a successful technique for improving thermoelectric performance. Work on silicon-germanium alloys,  $\text{PbTe-PbSe}$  solid solutions,  $\text{Bi}_2\text{Te}_3 - \text{Bi}_2\text{Se}_3$  solid solutions, and other compounds showed that alloying can drastically lower thermal conductivity, and in some cases leave the electronic properties relatively unchanged.[45, 46, 47, 48] For example, comparing pure germanium to an alloy of composition  $\text{Si}_{0.4}\text{Ge}_{0.6}$ , work at RCA labs showed the thermal conductivity could be reduced by a factor of three at room temperature, while the Seebeck coefficient remained nearly constant.[46]

From the 1950s up in to the 1990s, progress made in the field of thermoelectrics was slow.  $\text{PbTe}$  and  $\text{Bi}_2\text{Te}_3$  based materials remained the central focus, and while modest  $ZT$  improvements were being made,  $ZT$  values still remained at or below unity. However, in the 1990s a new class of cage-like materials began to be studied for thermoelectric uses. Skutterudites have chemical composition  $\text{TPn}_3$ , where T is a transition metal (Fe, Ru, Os, Co, Rh, Ir) and Pn is a pnictogen (P, As, Sb), e.g.  $\text{CoSb}_3$ . Early work in the 1980s and early 1990s focused on the superconducting properties of skutterudite compounds with composition  $\text{LaT}_4\text{P}_{12}$ . [49, 50] However, for thermoelectrics one of the important aspects of the skutterudite structure was the ability to fill the “cage” formed by the pnictogen atoms with rare earth elements, creating so called “filled” skutterudites with composition of the form  $\text{RT}_4\text{Pn}_{12}$  where R represents a rare earth. Clathrate compounds, with chemical

composition  $A_xB_yC_{46-y}$ , possess similar structures, with cage like voids that can be filled to manipulate the transport properties. [51]

In 1995, work by Morelli and Meisner showed that  $CeFe_4Sb_{12}$  showed promising thermoelectric properties, with metallic-like electrical resistivity on the order of a few  $m\Omega\text{ cm}$ , and a Seebeck coefficient that rose linearly in  $T$  to a room temperature value near  $70\ \mu\text{V K}^{-1}$ , quite large for a metallic material. However, more importantly their work showed that the thermal conductivity of the filled skutterudite was one to two orders of magnitude lower than that of the unfilled  $CoSb_3$  and  $IrSb_3$ . [52] Further reports on the high temperature properties in 1996 showed that the iron atoms could be partially replaced with cobalt to optimize the electrical properties, and a peak  $ZT$  of 1.4 at  $625^\circ\text{C}$  was reported. [53] The effect of these initial reports could be clearly seen at the 1996 International Conference on Thermoelectrics by the sheer number of skutterudite presentations.[54, 55, 56, 57, 58]

Also in the 1990s, studies on the effects of quantum confinement on thermoelectrics, focused on quantum well superlattices, as well as simpler confined structures such as a nanowires, showed promise. [59, 60, 61, 62] However, while the initial studies led to more computational studies, there was limited experimental success with the concept. Reports of  $ZT$  values in excess of 2.0 were published, but have not been reproduced, and remain highly disputed.[63]

## 1.2 Motivation for Thermoelectric Power Generation

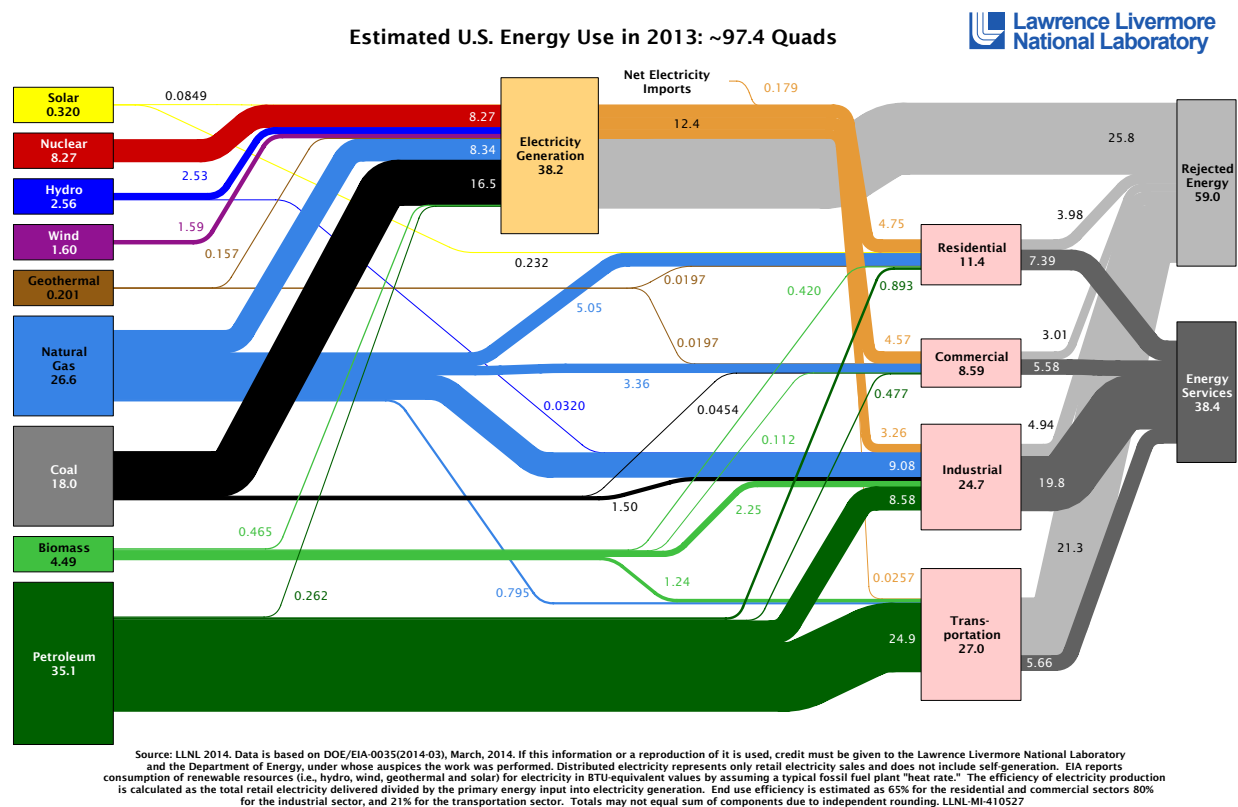


Figure 1.2: Lawrence Livermore National Lab estimated 2013 energy use in the U.S. The left side represents the sources of energy, and the right side the end uses.

As shown in Figure 1.2, the United States produces just shy of 100 Quads of energy per year, where one quad is equal to  $1 \times 10^{15}$  BTUs. Roughly 80% of that energy comes from nonrenewable fossil fuels, and while alternative energy is gaining, nonrenewable energy is likely to remain a crucial part of the energy market for some time. With an increasing global population, as well as increasing energy demands in developing countries, the need to increase energy efficiency is paramount. Further, from the Lawrence Livermore National Lab study, summarized in Figure 1.2, one can see that roughly 60% of the energy produced in the United States is lost as rejected energy, with the majority being lost in the form of waste heat rejected during electricity generation and in transportation.

The second law of thermodynamics informs us that entropy in a closed system will always increase or remain constant, and that a perfect engine is not possible, so losses will always be a part of our power generation technology. One option for improving efficiency then is to find a way to use the waste heat in a second stage of power generation. This has been heavily studied and applied in power generation plants in the form of Combined Cycle Gas Turbines (CCGT), where the exhaust gas from a turbine generator (burning coal or natural gas for example) is passed through a heat exchanger to boil water, which is then piped in to a steam turbine for the second stage of generation.[64, 65] While this technology works well for large power plants, it does not scale down to the level of an automobile or a home, and requires a threshold temperature of exhaust gas to work. Thermoelectric generators, on the other hand, can work with virtually any temperature gradient.

A thermoelectric generator is a scalable solid state energy conversion device, which can be optimized for different temperatures and sizes to convert heat directly into electricity. That scalability, as well as the low maintenance required due to no moving parts, has led to many niche applications. The first radioisotope thermoelectric generator (RTG) was used by NASA in 1961 in a US Navy satellite and produced 2.5W of power using plutonium-238 as the heat source.[66] RTGs have long stable lifetimes, the Voyager 1 and 2 probes have continued to run on RTGs for nearly 40 years with zero maintenance. The current Mars Rover (Curiosity) is powered by a RTG producing 125 W of power at its launch, with an expected power output of 100W after 14 years, still using Pu-238 as a heat source.[67]



Figure 1.3: The E1 thermoelectric generator from Alphabet Energy. On the left is a large diesel generator, with the exhaust connected to the E1 TEG on the right.[1]

Shown above in Figure 1.3 is the E1 thermoelectric generator produced by Alphabet Energy. Their generators are built in shipping containers for easy transportation. They are designed to be placed on the exhaust of large stationary diesel generators used in remote locations, such as mining operations, and use the exhaust gas to produce additional electricity.

Another niche application for TEGs is in industrial manufacturing. RGS Development BV, a Dutch company specializing in silicon tape casting technology, has developed thermoelectric generators aimed for deployment in steel casting lines. Their generators capture heat coming from the steel castings as they cool, and generate additional power for the factory.[68] This shows the unique applications possible for TEGs as compared to traditional steam turbines, where higher heat outputs would be required.

As Figure 1.2 shows, electricity generation has approximately 25 Quads of rejected energy in the United States. If 10% of that heat could be captured and converted to electricity, that would add back 2.5 Quads of energy, more than was generated by solar, wind, and

geothermal combined in 2013. Placing thermoelectric generators on power plants also avoids some of the issues of steady supply that are found with many renewable resources like solar. TEGs would produce power all hours of the day regardless of the weather, and could be placed at locations where connecting to the grid is easy.

For these applications to become a reality on a large scale, new materials with tailored thermoelectric properties and that can be produced inexpensively will be required. Physics plays the role of providing a fundamental understanding of the properties so that these new materials can be designed with the desired properties “built in” to their structure.

# Chapter 2

## The Physics of Thermoelectric

## Materials and Devices

Thermoelectric materials are subject to the laws of solid state physics, and their behavior can largely be understood in terms of three primary material properties governing their performance: the Seebeck coefficient ( $S$ ), the electrical conductivity ( $\sigma$ ), and the thermal conductivity ( $\kappa$ ). While the underlying theory is fairly developed, and computational power and techniques have advanced greatly over the last several decades, the complexity of many materials still makes theoretical predictions of properties difficult. In particular, the fact that thermoelectric devices are made from polycrystalline samples, where grain size and defects are hard to predict a-priori, along with the often large temperature gradients along the sample makes a full prediction of  $ZT$  highly difficult. This chapter will present the underlying transport theory, in an effort to give a better understanding of the important concepts and parameters involved in evaluating thermoelectric materials, as well as to help better understand the results presented in further chapters.

## 2.1 Thermoelectric Device Efficiencies

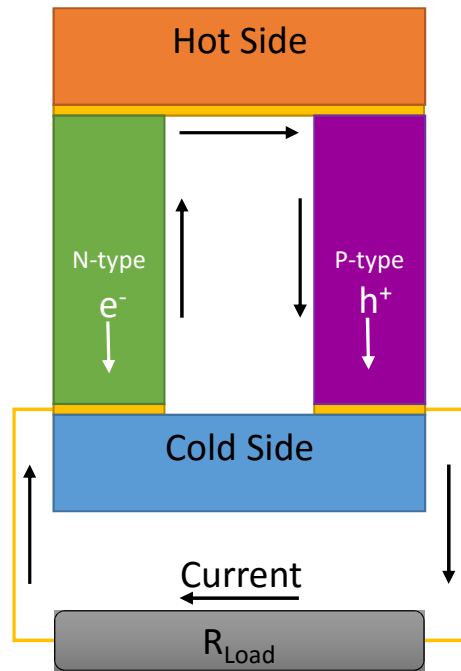


Figure 2.1: Schematic of a thermoelectric unicouple. A generator is made from a group of these stacked electrically in series and thermally in parallel.

As shown in Figure 2.1 a thermoelectric generator consists of two legs, one p- and one n-type, which are connected thermally in parallel and electrically in series. The higher temperature on the hot side causes charge carriers to flow down the legs towards the cold side, at which point they travel along electrical conductors to drive a load. If, instead of driving a load, power is supplied to the generator and current forced through the unicouple, the device would act as a Peltier cooler and charges would liberate heat from one side while carrying it to the other. While the basic unicouple shown in Figure 2.1 is adequate to generate power, the resulting voltage would be very low, typically on the order of 100s of microvolts. Connecting many unicouples in series, typically arranged in a grid, allows the device to be fit to the size of the heat source and to deliver the desired power.

The key concern with a thermoelectric generator is the efficiency. The efficiency is defined as the ratio of the output power supplied to the load to the power input at the hot side. The output power is simply:

$$P_{out} = I^2 R_L \quad (2.1)$$

where  $I$  is the current and  $R_L$  is the load resistance. The current can be found simply using Ohm's law and accounting for the resistance of both legs, as well as the load and using the Seebeck effect to calculate the voltage:

$$I = \frac{V}{R} = \frac{(S_p - S_n)\Delta T}{R_p + R_n + R_L} \quad (2.2)$$

where  $S_p$  and  $S_n$  are the Seebeck coefficients of the individual legs (n and p referring to the carrier types) and similarly,  $R_n$  and  $R_p$  are the resistances of the legs.

The input power is made up of three terms: the heat input from an outside source (a positive input), the heat carried away by conduction (negative because it is a loss), and the heat carried away by joule heating (another loss). Radiative losses will be neglected here.

$$P_{Seebeck} = (S_p - S_n)T_h I \quad (2.3)$$

$$P_{Conduction} = -(K_n + K_p)\Delta T \quad (2.4)$$

$$P_{Joule} = -\frac{1}{2}I^2(R_p + R_n) \quad (2.5)$$

Here,  $T_h$  is the hot side temperature,  $\Delta T$  is the temperature gradient,  $K$  is the thermal conductance of the leg (p or n) and  $R$  is again the resistance of the leg or the load itself (p,

n, or L). Combining all the terms gives the efficiency as:

$$\eta = \frac{I^2 R_L}{(S_p - S_n)T_h I - (K_n + K_p)\Delta T - \frac{1}{2}I^2(R_p + R_n)} \quad (2.6)$$

Next, defining new variables and simplifying:

$$S_{np} = (S_p - S_n) \quad (2.7)$$

$$K_{np} = (K_n + K_p) \quad (2.8)$$

$$r = \frac{R_L}{R_n + R_p} \quad (2.9)$$

$$\eta = \frac{\Delta T}{T_h} \frac{r}{1 + r - \frac{(R_p + R_n)K_{pn}}{S_{pn}^2} \frac{(1+r)^2}{T_h} - \frac{1}{2} \frac{\Delta T}{T_h}} \quad (2.10)$$

Then, defining the figure of merit,  $Z$ , as :

$$Z = \frac{S_{pn}^2}{K_{pn}R_{pn}} = \frac{S_{pn}^2}{\kappa\rho} \quad (2.11)$$

we can write the efficiency as a function of  $Z$ , temperature, and  $r$ :

$$\eta = \frac{\Delta T}{T_h} \frac{r}{1 + r - \frac{(1+r)^2}{T_h Z} - \frac{\Delta T}{2T_h}} \quad (2.12)$$

Finally, by optimizing equation (2.12) with respect to  $r$ , and simplifying further the efficiency is given as:

$$\eta = \frac{T_h - T_c}{T_h} \frac{\sqrt{1 + Z\bar{T}} - 1}{\sqrt{1 + Z\bar{T}} + T_c/T_h} \quad (2.13)$$

$$= \eta_{carnot} * \frac{\sqrt{1 + Z\bar{T}} - 1}{\sqrt{1 + Z\bar{T}} + T_c/T_h} \quad (2.14)$$

where  $T_c$ ,  $T_h$ , and  $T$  represent the cold side, hot side, and average temperature of the device.[69]  $Z$  has units of  $K^{-1}$ , so it is common to multiply by  $T$  to get the dimensionless figure of merit,  $ZT$ , which is typically expressed for each individual leg of the generator:

$$ZT = \frac{S^2\sigma}{\kappa}T \quad (2.15)$$

It is also common to isolate the numerator,  $S^2\sigma$ , which is called the power factor.

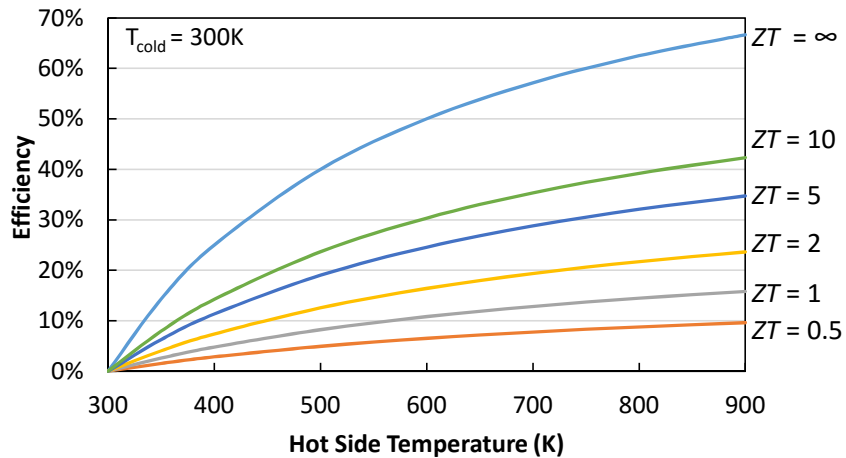


Figure 2.2: Efficiency of a thermoelectric generator as a function of  $ZT$  and hot side temperature. The cold side is set at 300K. As  $ZT$  tends to infinity the efficiency approaches the Carnot limit.

As shown in Figure 2.2, as  $ZT$  approaches infinity the efficiency simply tends towards the Carnot limit. Historically,  $ZT$  values greater than unity were difficult to achieve, giving a maximum efficiency of near 15%. Values of  $ZT$  have exceeded two in some recent cases,

opening up the possibility of efficiencies nearing 25%.

## 2.2 Electrical Conductivity

The electrical conductivity of a material is a product of the number of available charge carriers, the mobility of those charge carriers, and the charge they carry:

$$\sigma = ne\mu \tag{2.16}$$

where  $n$  is the carrier concentration, typically given in units of  $\text{cm}^{-3}$ ,  $e$  is the fundamental electric charge, and  $\mu$  is the mobility of the carriers, typically given in units of  $\text{cm}^2 \text{V}^{-1} \text{s}^{-1}$ .

The carrier concentration can be calculated using Fermi-Dirac statistics and the density of states for the material. Here, we will consider only electrons, however the equations for holes are very similar. With that information one can write that:

$$n = \int_0^\infty f_n(E)D(E)dE \tag{2.17}$$

where the Fermi-Dirac distribution and density of states for free electrons in three dimensions are: [70]

$$f_n(E) = \frac{1}{1 + e^{\frac{E-E_F}{k_bT}}} \tag{2.18}$$

$$D(E) = \frac{\sqrt{2}m^{*3/2}}{\hbar^3\pi^2}\sqrt{2E} \tag{2.19}$$

where  $m^*$  is the effective mass for the conduction band, and the energy is relative to the conduction band edge,  $E_c$ . Combining equations (2.17), (2.18), and (2.19) yields the following equations:

$$n = \frac{m^{*3/2}}{\hbar^3 \pi^2} \int_0^\infty \frac{\sqrt{2E}}{1 + e^{\frac{E-E_F}{k_b T}}} dE \quad (2.20)$$

$$n = N_c \frac{2}{\sqrt{\pi}} F_{1/2} \left( \frac{E_F}{k_b T} \right) = N_c \frac{2}{\sqrt{\pi}} F_{1/2}(\eta) \quad (2.21)$$

$$N_c = 2 \left( \frac{2\pi m^* k_b T}{h^2} \right)^{3/2} \quad (2.22)$$

where  $k_b$  is the Boltzmann constant,  $h$  is the Planck constant,  $N_c$  is the effective density of states at the band edge, and  $F_{1/2}(\eta)$  is the Fermi-Dirac integral, and  $\eta \equiv \frac{E_f}{k_b T}$ . The result for holes is similar. The effective mass will refer to either the conduction or valence band, depending on whether it pertains to holes or electrons. Shown in Figure 2.3 is the carrier concentration (in  $\text{cm}^{-3}$ ) as a function of the reduced Fermi energy,  $\eta$ , assuming an effective mass equal to the free electron mass.

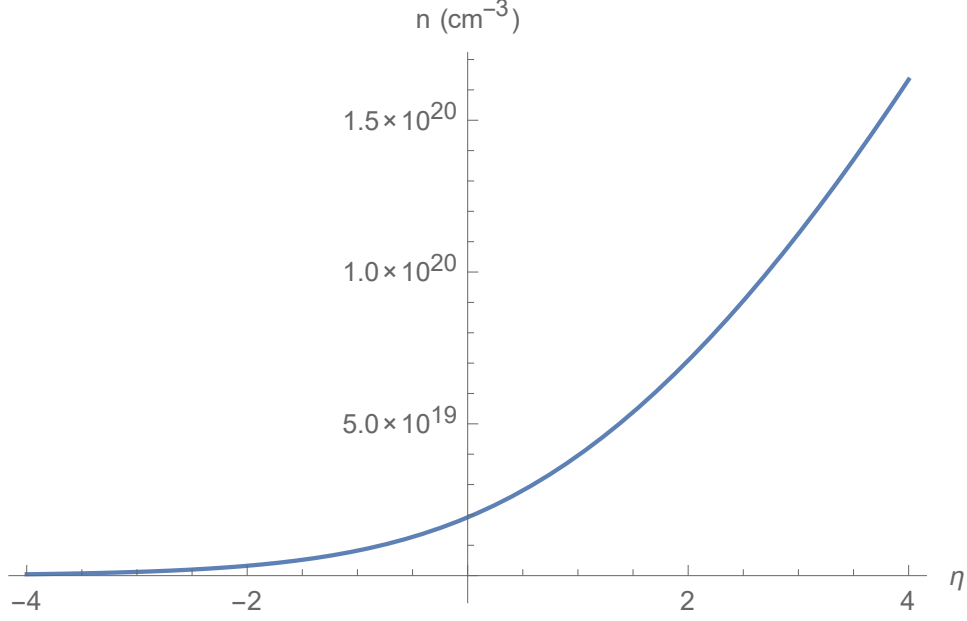


Figure 2.3: Carrier concentration ( $n$ ) in  $\text{cm}^{-3}$  as a function of reduced Fermi energy ( $\eta \equiv \frac{E_f}{k_b T}$ ) calculated from equation (2.21).  $\eta = 0$  refers to the conduction band edge. The effective mass ( $m^*$ ) is taken to be the free electron mass here.

At this point, further assumptions about the material must be made to elucidate information from the carrier concentration equation. If the assumption is made that the Fermi energy is several factors of  $k_b T$  into the gap from the band edge (that is the semiconductor is "non-degenerate"), then the Fermi distribution can be simplified, and the carrier concentration can be rewritten as:

$$n \approx \frac{m^{*3/2}}{\hbar^3 \pi^2} e^{\frac{-(E_c - E_f)}{k_b T}} \int_{E_c}^{\infty} e^{\frac{-(E - E_c)}{k_b T}} \sqrt{2E} dE \quad (2.23)$$

The law of mass action states that the product of the electron and hole carrier concentrations are fixed, and equal to the intrinsic concentration squared ( $np = n_i^2$ ). [70, 71, 72] Multiplying the equations for  $n$  and  $p$  and assuming that only energies within a few  $k_b T$  of the band edge contribute to the integral above (due to the exponential factor in the

integrand) one can get an expression for the intrinsic carrier concentration:

$$n_i(T) = \sqrt{N_c N_v} e^{-E_g/2k_b T} \quad (2.24)$$

$$n_i \propto m_v^{*3/2} T^{3/2} e^{-\frac{E_g}{2k_b T}} \quad (2.25)$$

And, for intrinsic semiconductors the Fermi energy can be expressed as:[70]

$$E_{f,int} = E_v + \frac{1}{2}E_g + \frac{3}{4}k_b T \ln \left( \frac{m_v}{m_c} \right) \quad (2.26)$$

Equation (2.24) shows that for an intrinsic semiconductor the carrier concentration is governed primarily by the band gap of the material and the temperature. This is because intrinsic semiconductors only have carriers if an electron is excited across the gap, moving into the conduction band and leaving behind a hole in the valence band.

Equation (2.26) shows that for an intrinsic semiconductor with  $m_v = m_c$  the Fermi level lies in the middle of the gap. If the masses are not equal the Fermi level is pulled towards the lighter band, however for most materials the ratio of masses will be near unity, and as such the Fermi level will only be a few  $k_b T$  from center. Even in cases with large mass differences the change is typically small, for example, InP has a band-gap of 1.35 eV, an effective valence band mass of 0.64  $m_0$  and conduction band mass of 0.077  $m_0$  at 300K. [72] Even with the large mass difference at 300K the Fermi energy has moved up towards the conduction band by only 41 meV.

One of the most useful features of semiconductors is the ability to dope them by intentionally substituting impurity atoms into the crystal structure. By replacing one atom in a

compound with another element which has a valence higher or lower the number of carriers can be adjusted, e.g. replacing silicon (four valence electrons) with phosphorus (five valence electrons) will add electrons to the system, while replacing silicon with boron (three valence electrons) will remove electrons (i.e add holes). Atoms which add electrons (n-type dopants) are known as donors (because they donate electrons) while atoms that remove electrons (p-type dopants) are called acceptors (because they will accept another electron). Because charge neutrality must be maintained in the crystal, for the case of n-type doping the number of electrons in the conduction band will now equal the number of holes in the valence band ( $n = p$  in an intrinsic semiconductor) *plus* the number of ionized donor atoms.

At low temperatures, the donor impurity atoms are not fully excited, and the material is said to be “frozen out”, with an electron carrier concentration given as:

$$n \approx \sqrt{\frac{N_D N_c}{2}} e^{-E_d/2k_b T} \quad \text{if} \quad N_D \gg \frac{1}{2} N_c e^{-E_d/k_b T} \gg N_A \quad (2.27)$$

where  $N_c$  is given by equation (2.22) and  $E_d$  is defined as  $E_c - E_D$ , the energy difference between the conduction band and the energy level of the donor atom. However, once all of the donor and acceptor atoms are excited, the carrier concentration in an n-type material is:[72]

$$n = \frac{1}{2} \left[ (N_D - N_A) + \sqrt{(N_D - N_A)^2 + 4n_i^2} \right] \quad (2.28)$$

$$\approx N_D \quad \text{if} \quad N_D \gg N_A \quad \text{and} \quad |N_D - N_A| \gg N_i \quad (2.29)$$

At high enough temperatures the thermal excitations cause intrinsic carriers to again become the dominant carrier. The temperature at which this transition occurs depends on the material and the doping level. Therefore in a doped semiconductor the carrier concentration initially increases with temperature as the dopant atoms become ionized and active, then a saturation will be reached once all of the dopants are activated and the carrier concentration becomes temperature independent, and finally at high enough temperatures the intrinsic carriers become excited across the gap and the carrier concentration again increases with temperature.

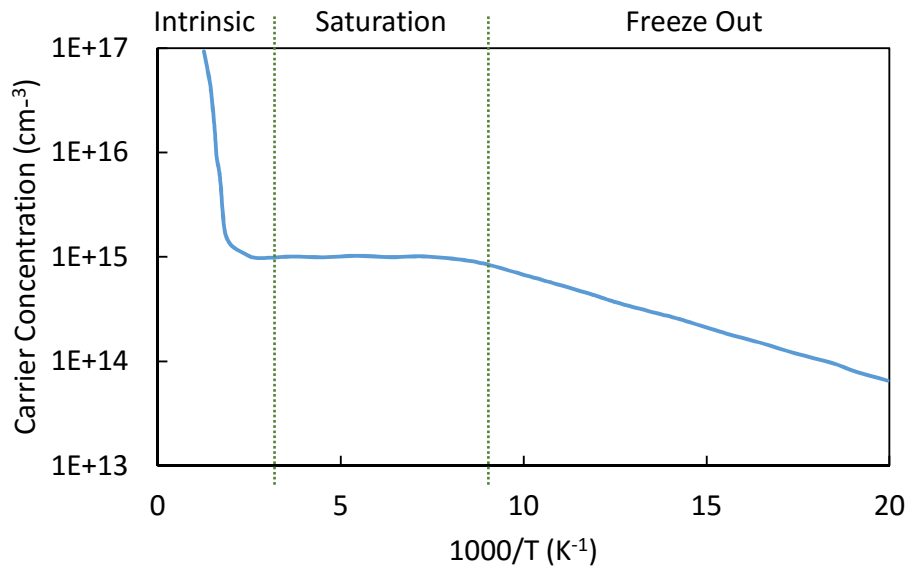


Figure 2.4: Carrier concentration as a function of inverse temperature for a doped semiconductor, showing the freeze out region at low temperature, the saturation region, and the final high temperature region when intrinsic carriers dominate.

It should be noted that for a “pure” intrinsic semiconductor the equations above yield a room temperature carrier concentration on the order of  $10^{10} \text{ cm}^{-3}$ .

While the previous equations describe the nature of the carrier concentration, the mobility is also needed to calculate the electrical conductivity, as shown in equation (2.16). The

mobility can be written in terms of the effective mass and the average scattering time of the carrier:

$$\mu = \frac{e\bar{\tau}}{m^*} \quad (2.30)$$

where  $m^*$  is again the effective mass, and  $\bar{\tau}$  is the average scattering time. Matthiessen's rule states that scattering rates (or the mobility) for different processes can be added:

$$\frac{1}{\tau} = \frac{1}{\tau_{impurities}} + \frac{1}{\tau_{lattice}} + \frac{1}{\tau_{defects}} + \dots \quad (2.31)$$

$$\frac{1}{\mu} = \frac{1}{\mu_{impurities}} + \frac{1}{\mu_{lattice}} + \frac{1}{\mu_{defects}} + \dots \quad (2.32)$$

For the work here, typically the two dominant scattering mechanisms were ionized impurity scattering (electrons or holes scattering from the ionized atoms used to dope the material) and lattice scattering (charge carriers being scattered by phonons).

If the mobility is due to ionized impurity scattering, then the more energy the charge carrier has (e.g. the faster the electron is moving) the less likely it is that it will be scattered by ionized atoms. And, as more impurities are added ( $N_I$ ) the scattering will be more prevalent and mobility will decrease. Calculations and experiments show that the mobility from ionized impurities is:[72, 73]

$$\mu_i \propto m^{*-1/2} N_I^{-1} T^{3/2} \quad (2.33)$$

Lattice scattering is due primarily to acoustic phonons interacting with and scattering charge carriers. As the temperature of the material increases there will be more and more

excited phonons, and as such the mobility would be expected to decrease. This is in fact what is seen experimentally, and the mobility, when governed by phonon scattering, can be expressed as:[74]

$$\mu_l \propto m^{*-5/2} T^{-3/2} \quad (2.34)$$

Equations (2.33) and (2.34) combined show that at some temperature the mobility will have a maximum after which it will decrease with increasing temperature, however it will decrease as a power law while the carrier concentration is constant (in the saturation region) or increasing exponentially (in the intrinsic region). This would indicate the electrical conductivity may have a hump in the saturation region as the mobility is rising, followed by a dip as mobility decreases while still in the saturation region, and will then increase exponentially as the intrinsic carrier concentration rises faster than the mobility falls. However, this depends on where the mobility peaks and where the saturation region is for a material.

At high temperatures, as a semiconductor enters the intrinsic region the carrier concentration will be large enough such that electron-electron scattering becomes another important scattering mechanism. Thus the mobility will decrease enough to balance the intrinsic carrier excitation and the electrical conductivity will decrease with temperature, showing metallic behavior.

For heavily doped, also called degenerate, semiconductors the electrical conductivity displays different trends. Typically, a semiconductor is defined as degenerate when the Fermi level is within 1-2  $k_b T$  of the band edge (for n-type, the Fermi level is just below the conduction band, for p-type just above the valence band). [72, 71] When this occurs, the electrical conductivity resembles that of a metal more than a semiconductor, as is shown

below in Figure 2.5. With the high carrier concentration electron-electron scattering is very important, and the electrical conductivity decreases with temperature.

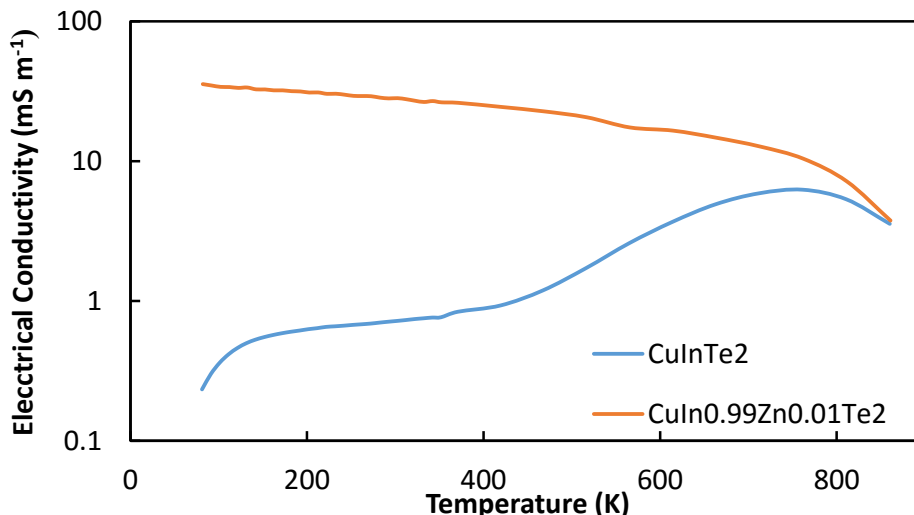


Figure 2.5: Electrical conductivity of  $\text{CuInTe}_2$  and  $\text{CuIn}_{0.99}\text{Zn}_{0.01}\text{Te}_2$  versus temperature. As shown, the doped sample has metallic behavior, with the electrical conductivity dropping with increasing temperature. At high enough temperatures, both samples become intrinsic.

Shown above in Figure 2.5 is the measured electrical conductivity for  $\text{CuInTe}_2$  and  $\text{CuIn}_{0.99}\text{Zn}_{0.01}\text{Te}_2$ . For the nominally undoped sample the conductivity initially rises, as carriers become excited, then flattens in a saturation region, and then again increases as intrinsic carriers become excited at high temperature. Then, near 750K the electrical conductivity peaks and begins to fall as the carrier concentration for both samples becomes intrinsic and carrier-phonon scattering increases and lowers the mobility. On the other hand, the sample which is doped with zinc shows a steady decline as a function of temperature until near 750K, where again, the sample enters the intrinsic region and carrier-phonon scattering begins to drastically lower the mobility. This also shows that even for heavily doped semiconductors with a large saturation region, eventually the intrinsic region will be reached, and the electrical conductivity will be comparable to that of an undoped sample.

## 2.3 The Seebeck Coefficient

The Seebeck coefficient (also called the thermopower) of a material is another key thermoelectric transport property. As stated in the introduction, the Seebeck coefficient can be written simply as the ratio of the voltage along a sample and the temperature gradient which produced it:

$$S = -\frac{\Delta V}{\Delta T} = -\frac{(V_{Hot} - V_{Cold})}{(T_{Hot} - T_{Cold})} \quad (2.35)$$

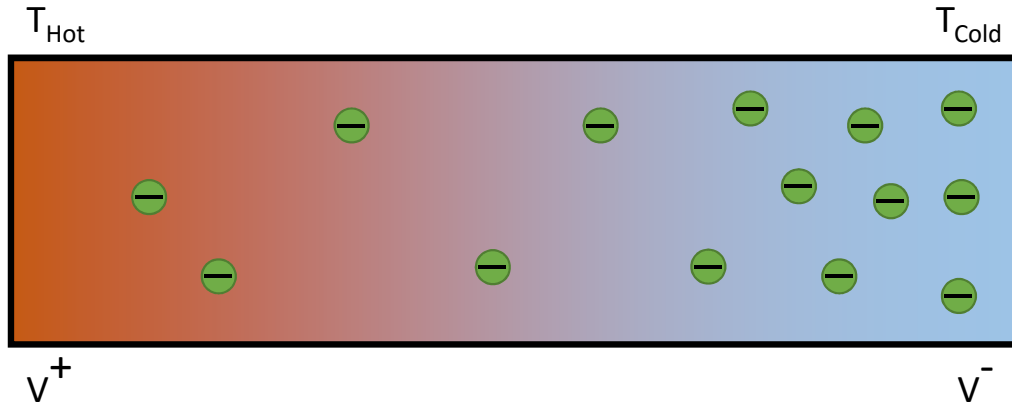


Figure 2.6: Diagram of the Seebeck effect in an n-type material. The hot electrons flow from the left side and accumulate on the right side, inducing an electric field and a resultant potential difference.

First, to understand the negative sign in equation (2.35), consider an electrically isolated bar with one end held at  $T_{Hot}$  while the other side is held at a lower temperature,  $T_{Cold}$ . The end which is hotter will have more energetic carriers, and those carriers will diffuse down to the cold end creating a charge imbalance across the bar. This build up of charge on the cold side will induce an electric field, and as a result the cold side will either have a lower potential than the hot side if the charge carriers are electrons, or will have a higher potential than the cold side if the carriers are holes. The net result is that equation (2.35) will yield

a negative Seebeck coefficient for an n-type material, and a positive Seebeck equation for a p-type material.

The Seebeck coefficient can be derived using Boltzmann transport theory and considering only small perturbations. Considering a parabolic band also simplifies the process, as the effective mass can be given a single value, rather than working with a tensor version. Using the Boltzmann transport equation, one can show that the electric current in a material with a temperature gradient is given by:[71]

$$J_e = \frac{e}{3\pi^2 m^*} \int_0^\infty k^3 \frac{\partial f_0}{\partial k} \tau(k) \left[ \frac{E - E_f}{T} \nabla T + \nabla(E_f - e\phi) \right] dk \quad (2.36)$$

where  $f_0$  is the equilibrium Fermi distribution,  $\tau$  is the relaxation time, and  $(E_f - e\phi)$  is the combined chemical and electrostatic potential energy. By assuming a parabolic band structure (e.g.  $E = \frac{\hbar^2 k^2}{2m^*}$ ) to change integration variables, and setting the current equal to zero (steady state open circuit conditions) equation (2.36) can be re-written as:

$$0 = \int_0^\infty E^{3/2} \frac{\partial f_0}{\partial E} \tau(E) \left[ \frac{E - E_f}{T} \nabla T + \nabla(E_f - e\phi) \right] dE \quad (2.37)$$

$$= \frac{\nabla T}{T} \int_0^\infty E^{5/2} \tau(E) \frac{\partial f_0}{\partial E} dE - E_f \frac{\nabla T}{T} \int_0^\infty E^{3/2} \tau(E) \frac{\partial f_0}{\partial E} dE \quad (2.38)$$

$$+ \nabla(E_f - e\phi) \int_0^\infty E^{3/2} \tau(E) \frac{\partial f_0}{\partial E} dE \quad (2.39)$$

Then, defining the Seebeck coefficient as the ratio of the electric field (from the potential) to the temperature gradient, and switching the integration variable to scaled energy ( $\epsilon =$

$E/k_bT, \eta = E_f/k_bT$ ):[71]

$$S = \frac{\nabla(\phi - \frac{E_f}{e})}{\nabla T} \quad (2.40)$$

$$= -\frac{k_b}{e} \left[ \frac{\int_0^\infty \epsilon^{5/2} \tau(\epsilon) \frac{\partial f_0}{\partial \epsilon} d\epsilon}{\int_0^\infty \epsilon^{3/2} \tau(\epsilon) \frac{\partial f_0}{\partial \epsilon} d\epsilon} - \eta \right] \quad (2.41)$$

By assuming a simple energy dependent relaxation time,  $\tau(E) \propto E^\lambda$ , equation (2.41) can be written in a form close to that of the Fermi-Dirac integrals found in the carrier concentration:

$$S = -\frac{k_b}{e} \left[ \frac{\int_0^\infty \epsilon^{5/2+\lambda} \frac{\partial f_0}{\partial \epsilon} d\epsilon}{\int_0^\infty \epsilon^{3/2+\lambda} \frac{\partial f_0}{\partial \epsilon} d\epsilon} - \eta \right] \quad (2.42)$$

And it can be shown that in fact this reduces to a relation involving the Fermi-Dirac integrals (see reference [71], appendix 5):

$$S = \pm \frac{k_b}{e} \left[ \frac{(\frac{5}{2} + \lambda) F_{3/2+\lambda}(\eta)}{(\frac{3}{2} + \lambda) F_{1/2+\lambda}(\eta)} - \eta \right] \quad (2.43)$$

where  $\lambda$  is  $3/2$  if ionized impurity scattering is the dominant mechanism, and  $-1/2$  when acoustic phonon scattering is the dominant mechanism. If the classical Boltzmann statistics were used, rather than Fermi-Dirac, the resulting equation would instead be simply linear in  $\eta$ :

$$S_{classical} = \frac{k_b}{e} ((5/2 + \lambda) - \eta) \quad (2.44)$$

Figure 2.7 shows equations (2.43) and (2.44) plotted as a function of the reduced Fermi energy, assuming  $\lambda = -1/2$ , showing that while the carrier concentration increases with  $\eta$  (Figure 2.3), the Seebeck coefficient decreases, one of the contraindicated parameters found in thermoelectrics.

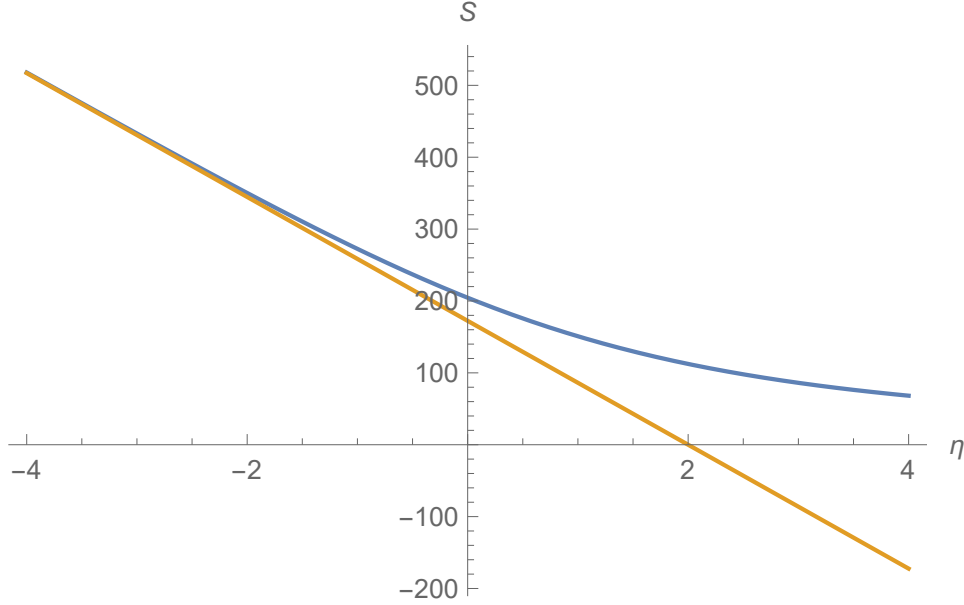


Figure 2.7: Seebeck coefficient ( $S$ ) in  $\mu\text{V K}^{-1}$  as a function of reduced Fermi energy ( $\eta \equiv \frac{E_f}{k_b T}$ ) calculated from equations (2.43) and (2.44), assuming  $\lambda = -1/2$ .

By combining equations (2.21) and (2.43) one can calculate a theoretical value for  $S^2 n$  as a function of the reduced Fermi energy. Again, assuming scattering is dominated by the lattice (typically true at high temperatures) so that  $\lambda = -1/2$ :

$$S^2 n = \frac{2}{\sqrt{\pi}} \frac{k_b^2}{e^2} N_c F_{1/2}(\eta) \left[ \frac{2F_1(\eta)}{F_0(\eta)} - \eta \right]^2 \quad (2.45)$$

$$= \frac{4}{\sqrt{\pi}} \frac{k_b^2}{e^2} \left( \frac{2\pi m k_b T}{h^2} \right)^{3/2} F_{1/2}(\eta) \left[ \frac{2F_1(\eta)}{F_0(\eta)} - \eta \right]^2 \quad (2.46)$$

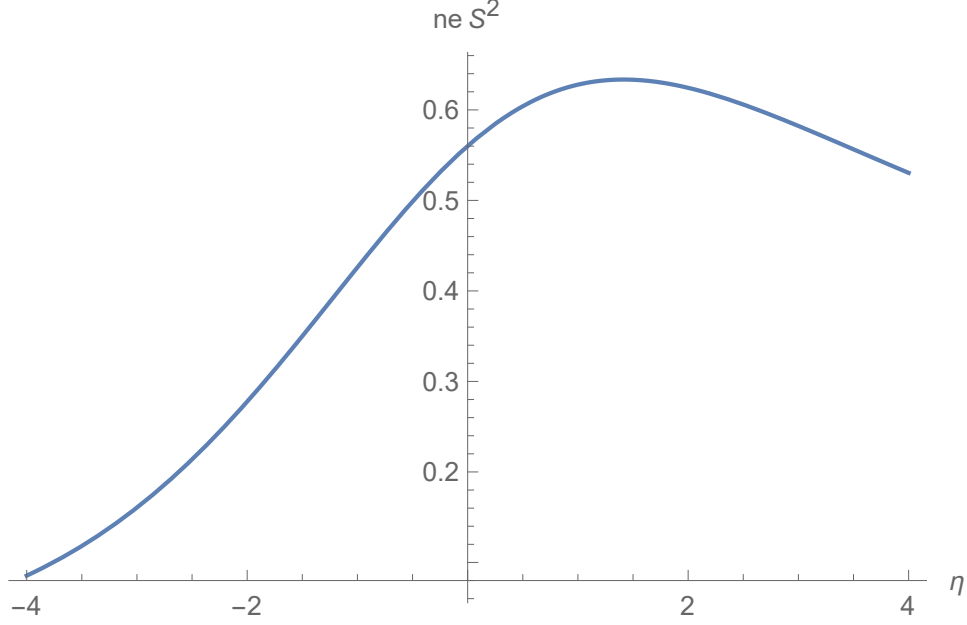


Figure 2.8:  $S^2 n e^* 10^{-6}$  in  $\mu\text{W V s cm}^{-3} \text{K}^{-2}$  as a function of reduced Fermi energy ( $\eta \equiv \frac{E_f}{k_b T}$ ) calculated from equation (2.45), using an effective mass of  $1 m_e$  and a temperature of 800K.

As Figure 2.8 shows, for the maximum value of  $S^2 n e$  the Fermi level should be slightly above (or below for p-type) the band edge with a value of  $\eta$  near unity. In the figure  $S^2 n$  has been multiplied by  $e$  as well, so that the plot really shows the power factor divided by the mobility. A larger effective mass will increase the product  $S^2 n$ , however, the mobility varies inversely as the mass, and increasing the effective mass will lower  $\mu$ . This is another example of a contraindicated parameters, where optimizing one property results in hindering another.

For a highly degenerate semiconductor, if one assumes a parabolic band it can also be shown that the Seebeck coefficient comes out as:[75]

$$S = \frac{8\pi^2 k_b^2}{3eh^2} m^* T \left( \frac{\pi}{3n} \right)^{2/3} \quad (2.47)$$

This relationship is often called the Pisarenko relationship, and just as was shown in Fig-

ure 2.8 it shows again that increasing the Fermi energy, and therefore the carrier concentration, is detrimental to the Seebeck coefficient. It also reveals that the effective mass plays a role, and a large effective mass increases  $S$ . However, again the electrical conductivity depends inversely on the effective mass showing the contraindicated parameters.

### 2.3.1 Band theory of transport

The previous theory on the Seebeck coefficient dealt primarily with the “free-electron” model of transport. However, modern semiconductor theory is based heavily on the band theory, which also offers helpful insight into the nature of electronic transport.

The basis of the band theory of electron levels is that due to the periodic potential found in crystals, the eigen-states for a single electron Hamiltonian can be expressed as: (Bloch’s Theorem)[70]

$$\psi_{n\mathbf{k}}(\mathbf{r}) = e^{i\mathbf{k}\cdot\mathbf{r}} u_{n\mathbf{k}}(\mathbf{r}) \quad (2.48)$$

where  $u_{n\mathbf{k}}(\mathbf{r})$  is periodic in the Bravais lattice vector  $\mathbf{R}$ . This in turn means that the eigen-states can be expressed as:

$$\psi_{n\mathbf{k}}(\mathbf{r}+\mathbf{R}) = e^{i\mathbf{k}\cdot\mathbf{R}} \psi_{n\mathbf{k}}(\mathbf{r}) \quad (2.49)$$

By restricting  $\mathbf{k}$  to the first Brillouin zone, allowed due to the periodicity in  $\mathbf{k}$ , one can express the solutions to the Hamiltonian in terms of a family of energies which depend on  $n$ , the band number, and  $\mathbf{k}$ , the wave vector, which yields the band-structure of the material. This in turn leads to an expression for the density of available energy levels:

$$D_n(E) = \int_{S_n(E)} \frac{dS}{4\pi^3} \frac{1}{|\nabla E_n(\mathbf{k})|} \quad (2.50)$$

where the integral is carried out over the surface of constant energy,  $S_n(\mathbf{k})$ . In equation (2.17) it was shown how the electrical resistivity depended directly on the density of states, along with the Fermi-distribution. However, equation (2.41) did not show any explicit dependence in the Seebeck coefficient on the density of states. The Mott equation expresses the Seebeck coefficient as:[76]

$$S = \frac{\pi^2}{3} \frac{k_b}{e} k_b T \left( \frac{d(\ln(\sigma(E)))}{dE} \right)_{E=E_f} \quad (2.51)$$

which, with  $\sigma = ne\mu$  and  $n \propto D(E)$ , shows the connection between S and the density of states, D(E). This dependence can also be seen in equation (2.47) in the effective mass term.

The effective mass ( $m^*$ ) is defined in band theory as:

$$\frac{1}{m^*} = \frac{1}{\hbar^2} \frac{\partial^2 E}{\partial \mathbf{k}^2} \quad (2.52)$$

$$m^* = \hbar^2 \frac{1}{\frac{\partial^2 E}{\partial \mathbf{k}^2}} \quad (2.53)$$

which means that for a large Seebeck coefficient, a material should possess a large effective mass, and therefor a second derivate, or in other words a flat band. A flat energy band would in turn mean a large derivative in the density of states. So from this analysis we find that for a large Seebeck coefficient, a large value for  $\frac{\partial D(E)}{\partial E}$  is desired. This is again an example of contraindicated parameters, as expressing  $\mu$  as  $e\tau/m^*$  in the equation for electrical conductivity shows that a small effective mass is desirable for increasing electrical conductivity.

There are two main possibilities for a large effective occur in a material. First, the electronic band structure could simply contain very flat bands, such as those found when f-shell electrons are involved. The second possibility is that of overlapping bands, which could be a combination of light or heavy bands, however when overlapping the density of states would be increased regardless. This case is found in PbTe, where at high temperatures it is suspected that a second “heavy hole” valence band moves up to align with the “light hole” valence band, giving an increase in the density of states, and a possible explanation for the large Seebeck coefficient ( $250 \mu\text{V K}^{-1}$ ) while also possessing a very low electrical resistivity ( $4 \text{ m}\Omega \text{ cm}$ ).[77]

Thus, band theory shows that sharply increasing density of states is desirable for a large Seebeck coefficient, and to maintain a low electrical resistivity it is more desirable to have a large amount of band overlap, or degeneracy, rather than simply one very flat band at the Fermi level. This desire for a high degeneracy can be achieved by finding crystal structures with high symmetry, however as will be shown in the following section, this high symmetry can be undesirable for achieving a low thermal conductivity.

## 2.4 Thermal Conductivity

The thermal conductivity is a material property which quantifies how well it transports heat. In semiconductors, there are two primary methods of transporting heat: via the charge carriers (electrons or holes), and via the movement of the actual atoms or lattice, in the form of quantized vibrations called phonons. Thus, the thermal conductivity can be split in to two parts,  $\kappa_e$  for the electronic component and  $\kappa_L$  for the lattice portion.

The electronic portion of the thermal conductivity is directly related to the electrical

conductivity through the Wiedemann-Franz law, which states that: [78]

$$\frac{\kappa_e}{\sigma} = LT \quad (2.54)$$

where  $L$  is the Lorenz number, which can vary, but will be taken in this work to be equal to the free electron value:

$$L_0 = \frac{\pi^2}{3} \left( \frac{k_b}{e} \right)^2 \quad (2.55)$$

$$L_0 = 2.44 \times 10^{-8} \text{ W } \Omega \text{ K}^{-2} \quad (2.56)$$

Again, from the equation for  $ZT$ , the electronic thermal conductivity and the electrical conductivity are contraindicated parameters, as increasing the electrical conductivity in an attempt to increase  $ZT$  will also increase thermal conductivity, thereby having no effect of possibly even lowering  $ZT$ . For the materials studied in this work, typically the electronic portion of the thermal conductivity is less than 10% of the total thermal conductivity at room temperature. The thermal conductivity shown in plots will always be the total (electronic and lattice) unless otherwise stated.

The lattice portion of the thermal conductivity depends on several properties of a material, and can be derived from the Boltzmann transport equation similarly to the Seebeck coefficient, but now applied to phonons. Starting with the equation for phonon heat flow through a material:

$$h = \sum N(k) \hbar \omega(k) v(k) \quad (2.57)$$

where  $N(k)$  is the number of phonons with momentum  $k$ ,  $\hbar \omega(k)$  is the energy of the

phonon, and  $v$  is the group velocity. The thermal conductivity is then the heat flow divided by the temperature gradient:

$$\kappa = -\frac{h}{\Delta T} = -\frac{1}{\Delta T} \sum N(k) \hbar \omega(k) v(k) \quad (2.58)$$

Using the relaxation time approximation,  $\left(\frac{\partial N}{\partial T}\right) = \frac{N^0 - N}{\tau}$ , and assuming the deviation in the phonon population from equilibrium is small such that  $\frac{\partial N}{\partial T} \approx \frac{\partial N^0}{\partial T}$  the Boltzmann transport equation yields: [79]

$$\kappa = \frac{1}{3} \int_0^{\omega_{max}} \hbar \omega v^2 \tau \frac{\partial N^0}{\partial T} f(\omega) d\omega \quad (2.59)$$

where  $f(\omega)$  is the phonon density of states and  $\tau$  is the relaxation time. The Debye model further assumes a linear dispersion curve ( $\omega(k) = vk$ ) and allows more simplification of equation (2.59). The lattice thermal conductivity can then be written (with  $x = \hbar\omega/k_bT$ ) as:[79]

$$\kappa = \frac{k_b}{2\pi^2 v} \left(\frac{k_b}{\hbar}\right)^3 T^3 \int_0^{\Theta_D/T} \tau(x) \frac{x^4 e^x}{(e^x - 1)^2} dx \quad (2.60)$$

$$= \frac{1}{3} v^2 \int_0^{\Theta_D/T} \tau(x) C(x) dx \quad (2.61)$$

$$= \frac{1}{3} v \int_0^{\Theta_D/T} l(x) C(x) dx \quad (2.62)$$

where  $\tau(x)$  is the relaxation time,  $l(x)$  is the mean free path ( $l = v\tau$ ),  $\Theta_D$  is the Debye

temperature of the material, and  $C(x)$  is the differential heat capacity:

$$C(x) = \frac{3k_b}{2\pi^2v^3} \left(\frac{k_b}{\hbar}\right)^3 T^3 \frac{x^4 e^x}{(e^x - 1)^2} \quad (2.63)$$

$$C = \int_0^{\Theta_D/T} C(x) dx = \frac{3k_b}{2\pi^2v^3} \left(\frac{k_b}{\hbar}\right)^3 T^3 \int_0^{\Theta_D/T} \frac{x^4 e^x}{(e^x - 1)^2} dx \quad (2.64)$$

Equation (2.62) is similar to the simple equation often given for thermal conductivity:  $\kappa = \frac{1}{3}c v l$ , but now in an integral form to account for changes in specific heat and mean free path with temperature and phonon frequency.[70] From here, the explanation of the thermal conductivity temperature dependence can be looked at from two pieces, first in terms of the specific heat, and second in terms of the relaxation time,  $\tau$ .

For the specific heat, at low temperatures  $\Theta_D/T$  is large and the upper limit on the integral in equation (2.64) can be taken to infinity to yield the typical result of a  $T^3$  dependence. At high temperatures,  $\Theta_D/T$  is small and the integrand can be Taylor expanded to yield the common result of a constant heat capacity at high temperatures, the Dulong-Petit law.

$$C \propto \left(\frac{T}{\Theta_D}\right)^3 \quad T \ll \Theta_D \quad (2.65)$$

$$C = \text{Constant} \quad T \gg \Theta_D \quad (2.66)$$

The relaxation time is more complicated than the specific heat, and depends not only on composition and crystal structure, but also on the sample size, shape, and purity. The main contributions to be considered here are: boundary scattering, impurity scattering, and Umklapp scattering.

Boundary scattering simply depends on the size of the sample itself, and typically is only important at low temperatures because at low temperature the majority of phonons are long wavelength phonons.[70, 79, 80] Reducing the grain size (by milling and sintering with various techniques for example) has a similar effect, and can be thought of as reducing the mean free path down from the crystallite size (at very low temperatures) to that of the average grain size.

Impurity scattering can come from several types of impurities. Predictions by Pomeranchuk, and later work by Slack studying Si, Ge, and KCl at low temperatures showed that isotopes, due to their different mass, played a very important role in scattering phonons, and limited the thermal conductivity.[81, 82] Work with neutron irradiation on diamonds showed that vacancies in the lattice could also play a very important role in reducing thermal conductivity and shifting the peak in  $\kappa$  towards higher temperatures.[83]

Related to that, mass mis-match scattering is caused when an atomic site is occupied by a different element with a differing mass. Early work by Rayleigh on sound wave scattering by an obstruction found the cross section for scattering was inversely proportional to the wavelength of sound to the fourth power.[84] Extending the theory to phonons in a lattice leads to the following scattering rate:

$$\frac{1}{\tau(\omega)} = \frac{c_p a^3 \omega^4}{4\pi v^3} \left( \frac{\Delta M}{M} \right)^2 \quad (2.67)$$

where  $c_p$  is the ratio of defects to lattice sites per volume and  $a^3$  is the volume per atom. Much later Klemens, using perturbation theory, got the same result, and showed that the thermal resistance due to a mass difference was: [85]

$$W_m = \frac{12\pi^2 TVB}{0.897hv^2} \left( \frac{\Delta M}{M} \right)^2 \quad (2.68)$$

where V is unit cell volume and B is a constant which he gives as 1/12. The key feature is that the thermal resistance is quadratic in the mass difference of the two elements.

Solid solution formation has been used heavily in thermoelectrics, most notably in Si-Ge and PbTe - PbSe, though it is a common practice now in the study of any thermoelectric material. Scattering can also occur due to dislocations and other crystal defects which will not be discussed here in detail, but details can be found in work by Slack.[86]

Finally, Umklapp scattering is a three (or more) phonon process by which two phonons with momentum  $\vec{q}_1$  and  $\vec{q}_2$  combine to form a resulting phonon with momentum  $\vec{q}_3$  whose vector is outside of the 1<sup>st</sup> Brillouin zone, as diagrammed in Figure 2.9. When this happens, by subtracting a lattice constant vector from the resulting vector to bring it back into the 1<sup>st</sup> Brillouin zone the resulting vector points away from the initial two.

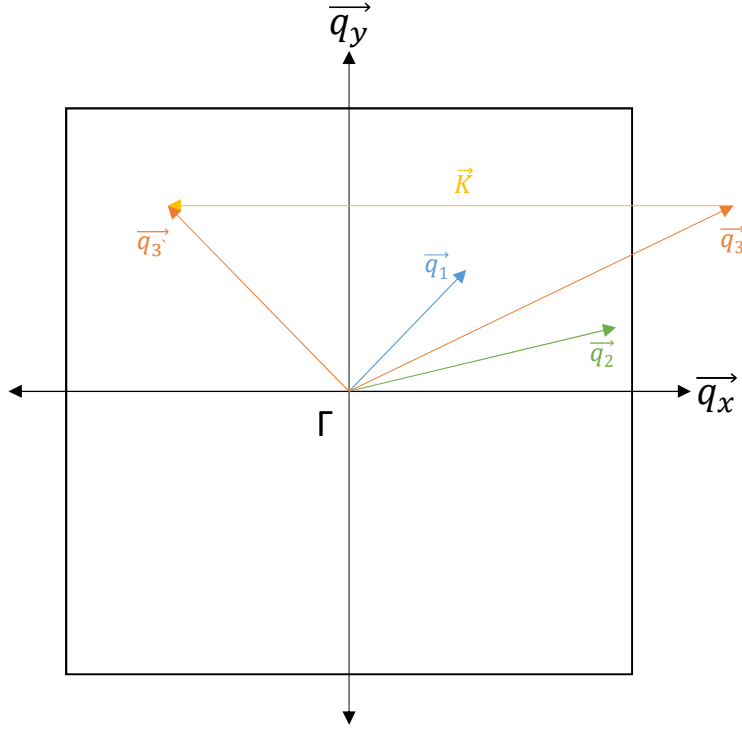


Figure 2.9: Schematic diagramming Umklapp Scattering. Phonons  $q_1$  and  $q_2$  combine to form phonon  $q_3$  which lies outside the 1st Brillouin zone and is subsequently folded back in to the 1st BZ.

For low temperatures Slack states that the scattering due to Umklapp gives a temperature dependence of:[86]

$$\kappa_U \propto T e^{\Theta_D/2T} \quad \text{for } 10T < \Theta_D \quad (2.69)$$

At high temperatures however, the temperature dependence is less clear. The phonon population begins to grow exponentially, and this causes an increase in phonon-phonon Umklapp scattering processes, which causes a strong decrease in the thermal conductivity. At high temperature the overall thermal conductivity is typically proportional to  $T^{-1}$ , due to a combination of all the scattering mechanisms. [86, 87, 79] An excellent overview of the various scattering methods is given by Glassbrenner and Slack in their study of silicon and germanium.[88]

A useful guide for the selection of a material based on the thermal conductivity comes from work by Slack, which gives the expression for the lattice thermal conductivity above the Debye temperature as:[89, 90, 91]

$$\kappa = A \frac{\bar{M}\Theta_d^3\delta}{\gamma^2 T n^{2/3}} \quad (2.70)$$

where A is a constant,  $\bar{M}$  is the average atomic mass,  $\delta^3$  is the volume per atom,  $\gamma$  is the Grüneisen parameter, and n is the number of atoms per unit cell. This gives a guide for selecting a material with low thermal conductivity. It shows that for low intrinsic thermal conductivity, a material should have a large Grüneisen parameter, many atoms per unit cell, and a low Debye temperature. While the equation appears to be linear in the average atomic mass, it should be noted that the Debye temperature varies inversely with the atomic mass, and therefore a heavier mass is actually desired for low thermal conductivity.

## 2.5 Motivation for Chalcopyrite Compounds

Combining equations (2.16), (2.47), and (2.70) can give some guidance to selecting a material with a potential high  $ZT$ . The three combined show:

$$ZT \propto \frac{m^{*2}\mu\gamma^2}{M\Theta_D^3\delta} \quad (2.71)$$

which means for a high  $ZT$  a material needs a small Debye temperature (and therefore a large average atomic mass) and a low volume per atom. It should also possess a large Grüneisen parameter, which is related to the anharmonicity of the lattice and to the thermal expansion. The more challenging combination comes in the electrical properties which

require a large effective mass but also a large mobility which are typically inversely related.

Work in this study was carried out on the copper based compounds of the I-III-VI<sub>2</sub> chalcopyrite family. The copper based compounds were studied in particular to avoid the issues of high cost involved in the other options (silver and gold). The chalcopyrite family of semiconductors come in two variants, II-IV-V<sub>2</sub> and I-III-VI<sub>2</sub>. These compounds can be thought of as a natural extension of the III-V and II-VI semiconductors, which are in turn can be thought of as derived from the classic elementary semiconductors, silicon and germanium.

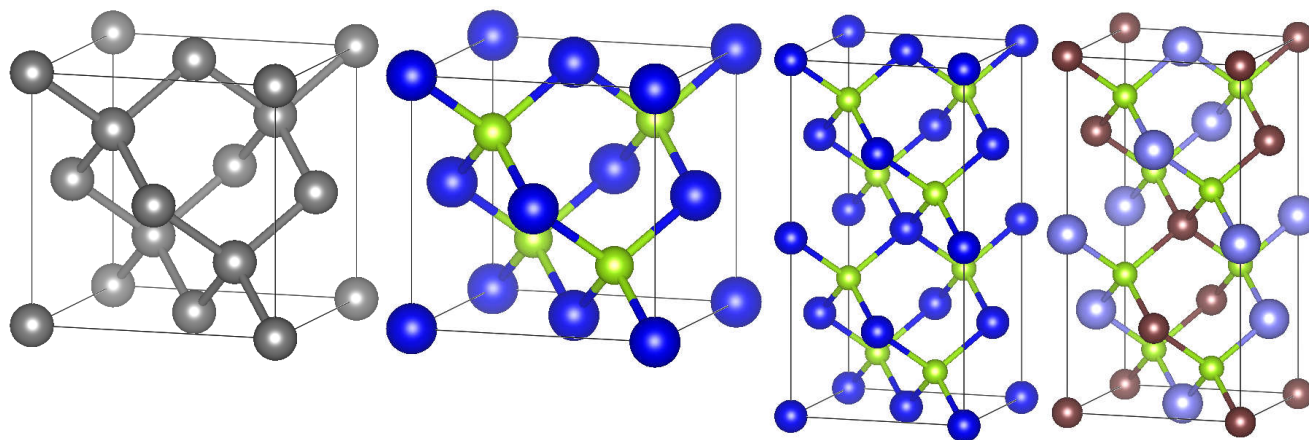


Figure 2.10: Crystal structures of Si, ZnSe, Zn<sub>2</sub>Se<sub>2</sub>, and CuGaSe<sub>2</sub> from left to right. At high temperatures the ordering in CuGaSe<sub>2</sub> breaks down, and the crystal can be reduced back to a cubic structure with Cu and Ga atoms occupying sites interchangeably, as will be shown in later chapters.

Starting from silicon (or germanium), which forms in the diamond structure, and replacing one half of the atomic sites with an element to the left on the periodic table, and one half with an element to right on the table leads to the family known as III-V semiconductors, for example GaAs. Moving another row left and right gives the II-VI compounds, such as ZnSe, as is shown in Figure 2.10. By doubling the unit cell of a II-VI (or III-V) unit cell to form, e.g. Zn<sub>2</sub>Se<sub>2</sub>, the same methodology can be performed on the cation, to give a ternary compound. For example, starting from II<sub>2</sub>-VI<sub>2</sub> and splitting the group II

element produces the I-III-VI<sub>2</sub> family. The same thought experiment can be done on III-V compounds to arrive at the II-IV-V<sub>2</sub> chalcopyrite compounds. Each time this doubling and replacing technique is used, an average of four valence electrons per atom is maintained, and in most cases the compound remains in a diamond-like form.[14] Recently this concept has been carried one step further from the I-III-VI<sub>2</sub> to study the kesterite structure, which has the form I<sub>2</sub>-II-IV-VI<sub>4</sub>, e.g. Cu<sub>2</sub>ZnSnS<sub>4</sub> (also known as CZTS).

This process leads to an interesting family of materials for multiple reasons. First, it gives several options for n- and p-type dopant atoms (I-III-VI<sub>2</sub> could be doped with a group II, IV, V, or VII material for instance). Second, the larger structure has twice as many atoms per unit cell as the cubic II-VI compounds, giving a lower thermal conductivity. Three differing atomic sites provides several options for solid solutions to lower thermal conductivity further. The reported band gaps range from 0.5 eV up to 3.49 eV for the family, offering a wide ability to tune the electronic properties and study the underlying physics.[92]

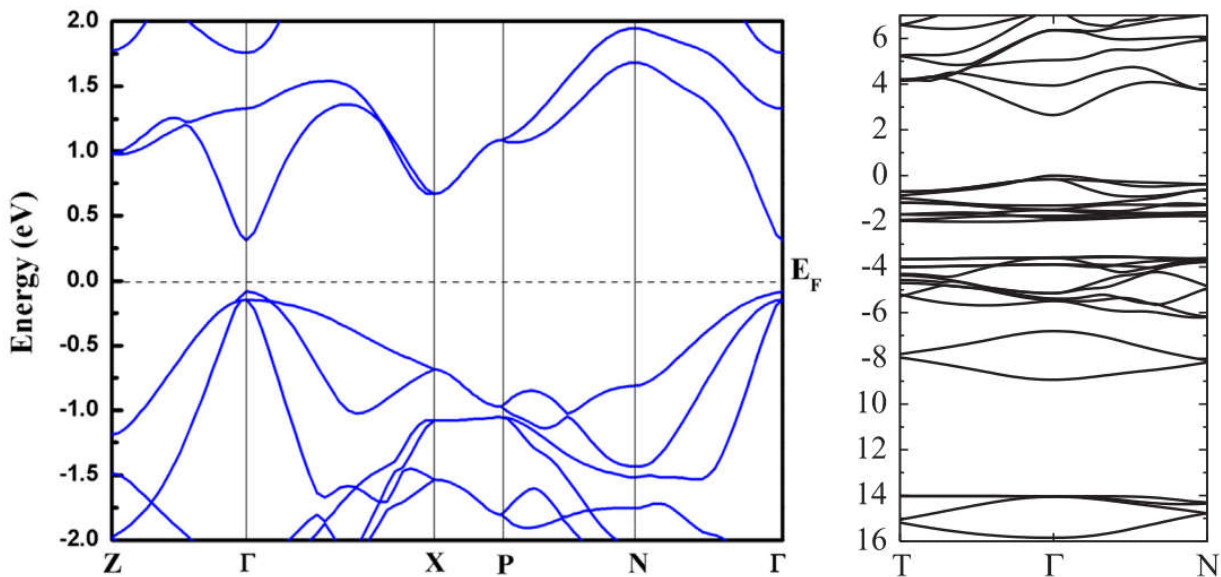


Figure 2.11: Electronic band structures of CuGaTe<sub>2</sub> (on the left) and of CuGaS<sub>2</sub> (on the right) showing the relatively flat valence bands, which indicate a high effective mass. [2, 3]

Shown in Figure 2.11, the band structures for  $\text{CuGaS}_2$  and  $\text{CuGaTe}_2$  (as well as many other chalcopyrite compounds) display relatively flat valence bands with several overlapping, or degenerate bands. The flat bands indicate a large effective mass, which is beneficial for the Seebeck coefficient, as is the overlapping bands near the valence edge. All of these factors lead to a complex and widely varied family of semiconductors, which show promise for use in thermoelectrics, solar cells, and many other semiconductor applications.

Interestingly, while chalcopyrite compounds have undergone significant development as photo-voltaic materials, with some products already on the market, there has been much less research and work done on their thermoelectric properties, and this provides the motivation for the present study.

# Chapter 3

## Experimental Procedures

### 3.1 Materials Synthesis

Sample synthesis began by weighing out stoichiometric amounts of each element and placing them into a quartz ampoule. The elements were purchased either from Alfa-Aesar or Sigma-Aldrich, depending on availability and purity. Typical elements were a minimum purity level of 99.99%. The ampoules were then placed into a sealing station and evacuated to a pressure less than  $1 \times 10^{-5}$  torr, and finally were sealed with an oxygen-methane torch.

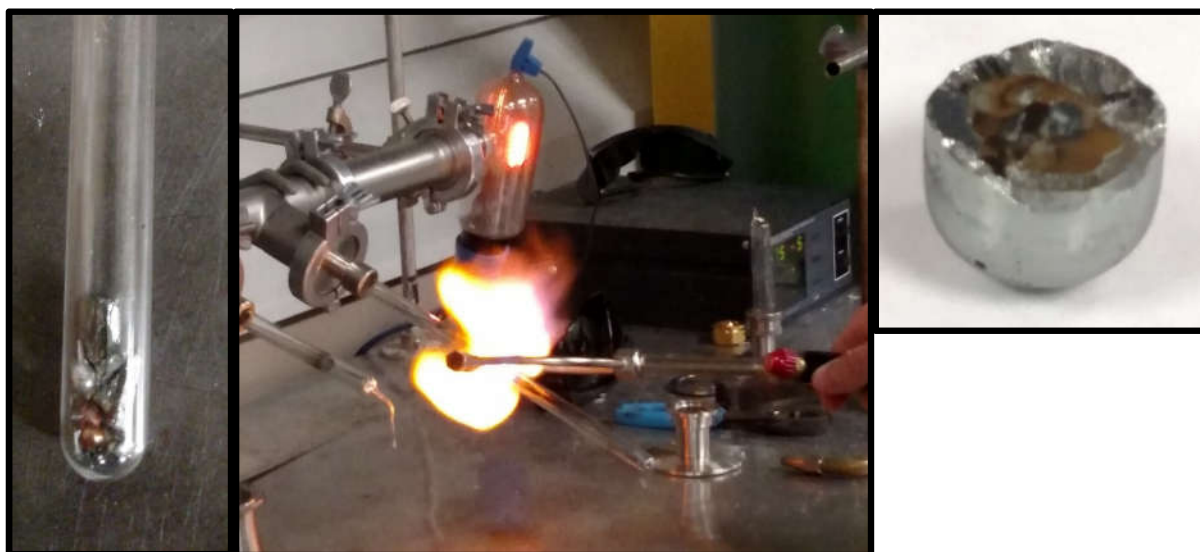


Figure 3.1: Steps in material synthesis. From left to right, elements weighed out in ampoule, ampoule being sealed, and the resulting ingot after the furnace procedure.

### 3.1.1 Furnace Heating Procedure

The tellurium based samples were heated at  $1.0^{\circ}\text{C min}^{-1}$  to an ultimate temperature of  $900^{\circ}\text{C}$ , at which point they were held for 24 hours to allow full mixing. After 24 hours the samples were water quenched, and placed back in to the furnace at  $600^{\circ}\text{C}$  to anneal for 24 hours. The selenide samples were made in the same manner, except the initial heating rate was lowered to  $0.4^{\circ}\text{C min}^{-1}$  to account for the volatility of selenium and concerns over the vapor pressure causing the ampoule to rupture. For the heating procedure either a Thermolyne F21100 tube furnace or a ThermoFisher BF51800 box furnace was used.

The sulfide samples were also heated at  $0.4^{\circ}\text{C min}^{-1}$  to  $900^{\circ}\text{C}$ , however after soaking for 24 hours they were cooled at  $1.0^{\circ}\text{C min}^{-1}$  to  $300^{\circ}\text{C}$  and annealed at that temperature for 24 hours before quenching. Quenching sulfide samples from high temperature often led to cracked ampoules so a change was made to slow cooling to  $300^{\circ}\text{C}$ . The annealing step was

required on all samples to incorporate any material deposited on the ampoule wall during quenching.

While in principle the thermoelectric characterization could be performed directly on the ingots, this was not done because many of the ingots obtained were porous and brittle. To overcome this issue, an additional powder processing and consolidation procedure was carried out in order to provide dense, crack free, small grain size samples suitable for cutting and measuring.

To carry out this step, the resulting ingot was then removed from the ampoule and ground using a mortar and pestle to obtain a fine powder. The purity of the powder was checked with x-ray diffraction. The powder was then placed into a stainless steel ball mill jar, sealed under an argon atmosphere and wrapped with Parafilm, and milled for sixty minutes in two thirty minute increments. A SPEX MixerMill 8000D or a MixerMill 8000M was used for the milling process. The powder was again checked with XRD, and then placed into a graphite die to be sintered. Sintering was performed either via hotpressing, or by spark plasma sintering.

### **3.1.2 Sintering Procedures**

Initial samples in the study were sintered by hotpressing. The sample powder was placed in a 10mm diameter graphite die, with stainless steel plungers placed in both ends and graphite foil spacers between the powder and plungers. The die was then placed into a uniaxial press and surrounded by a heater. The sample powder was heated to 475°C under 90MPa of pressure and held for 15 minutes before being allowed to cool. This procedure was performed entirely in an argon filled glovebox to prevent any oxidation. Final samples synthesized with the hotpress had densities greater than 90% theoretical density.

Later in the study samples were sintered using the newly acquired Dr. Sinter spark-plasma-sinter 211LX (SPS). In that process, the sample powder was again loaded into a 10mm diameter graphite die, with graphite foil spacers placed between the powder and graphite plungers. This was then placed into a uniaxial press, where it was placed under 40MPa of pressure, and heated at  $100\text{ }^{\circ}\text{C min}^{-1}$  to the desired temperature, held for 10 minutes, and then allowed to cool. The primary difference in the SPS versus the hotpress is that heating in the SPS was performed by passing a current through the die itself. The rams on the SPS were watercooled, and typically the sample would reach room temperature in under 15 minutes, much faster than the hotpress which had no active cooling. Final samples were sanded to remove the graphite foil and diced on a diamond saw. SPS samples typically had higher density than samples densified in the hot press, with values typically greater than 95% theoretical density.

## 3.2 Characterization Techniques

### 3.2.1 X-ray Diffraction

X-ray diffractometry (XRD) was performed on a Rigaku Miniflex-II using  $\text{Cu-K}\alpha$  radiation as a source with  $\lambda=1.54\text{\AA}$ . When calculating lattice parameters, to adjust for any offset caused by variance in the height of the powder on the XRD slide, the sample was scanned twice, once alone, and once with the addition of high purity silicon. Using the known silicon peaks one can shift the overall pattern to account for differences in the scanning plane of the sample. After this, peaks were fit using the Jade 9 software package, and compared to previously reported patterns in the PDF database. Using the fitted peaks, d-spacing values were then fit to extract the lattice parameters ( $a$  and  $c$ ) using the following equation, where

h, k, and l are the miller indices of crystallographic lattice plane:

$$\frac{1}{d_{hkl}^2} = \frac{h^2 + k^2}{a^2} + \frac{l^2}{c^2} \quad (3.1)$$

It should be noted that many patterns exhibit doublet peaks. For the chalcopyrite compounds studied in this work, many have an  $a:c$  ratio of very near 1:2, which leads to degeneracy in peaks. For example, the 106 and the 302 peaks have the exact same d-spacing when  $c = 2a$ , however if  $c = 1.98a$  the peaks will split and appear as a doublet. Shay and Wernick found a direct correlation between the deviance in the  $c:a$  ration and the value of the crystal field splitting correction to the band-gap. The cause of the deviance in  $c:a$  from 2:1 is likely due to changes in bond strengths.

### 3.2.2 Differential Scanning Calorimetry

Differential scanning calorimetry (DSC) was performed using Netzsch DSC 200 F3 Maia. A daily background measurement was performed before scanning a sapphire standard and finally the sample itself. Samples were approximately 50 mg in mass, and were polished to have a flat surface on the bottom. The samples were placed into aluminum crucibles with pierced lids (necessary for the release of vapors that occur during sublimation) for the measurement, which was carried out over a range of 50 to 600 °C. The ratio method was performed to calculate the specific heat of the samples, using the Netzsch Proteus Analysis software.

### 3.2.3 Hall Measurements

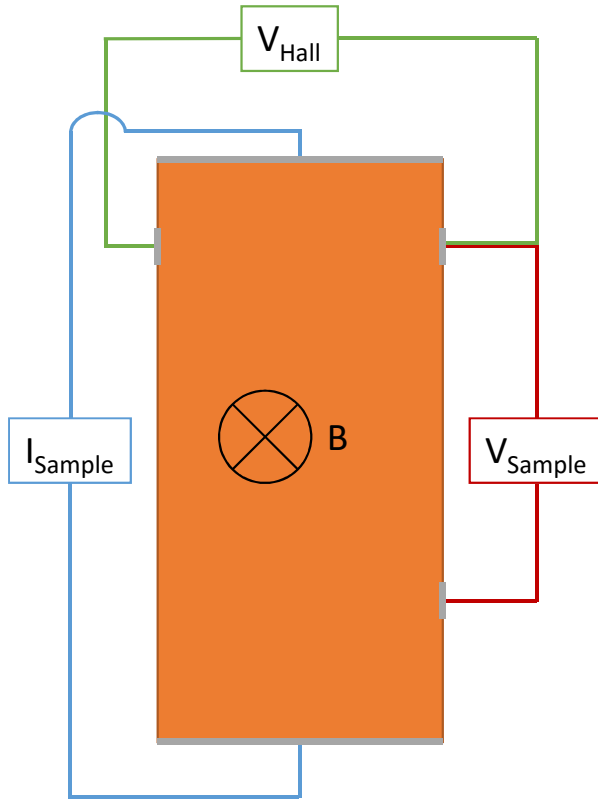


Figure 3.2: Experimental setup for Hall measurements. The applied magnetic field is into the page.

Hall measurements were performed at room temperature with a magnetic field ranging from  $-0.3$  to  $+0.3$  Tesla using a Power & Buckley model 3474 precision electromagnet, powered by a LakeShore model 668 electromagnet power supply. Typical sample dimensions were  $4\text{mm} \times 7\text{mm} \times 0.5\text{mm}$ . Sample current was supplied by a LakeShore 370 AC Resistance Bridge. Magnetic field measurements were made with a LakeShore 421 Gaussmeter.  $V_{Sample}$  was measured with a Keithley precision multimeter, and was used to calculate electrical resistivity, while  $V_{Hall}$  was used to calculate the carrier concentration according to the standard single carrier Hall model:

$$R_{Hall} = \frac{B}{net} \quad (3.2)$$

where  $B$  is the applied magnetic field,  $n$  is the carrier concentration,  $e$  is the elementary charge, and  $t$  is the thickness of the sample. Rather than a single point, a series of six points were made per temperature, and a line was fit to a plot of  $R_{Hall}$  versus  $B$ , where the slope is equal to  $1/net$ . The combined measurements yielded the mobility ( $\mu = \sigma/ne$ ).

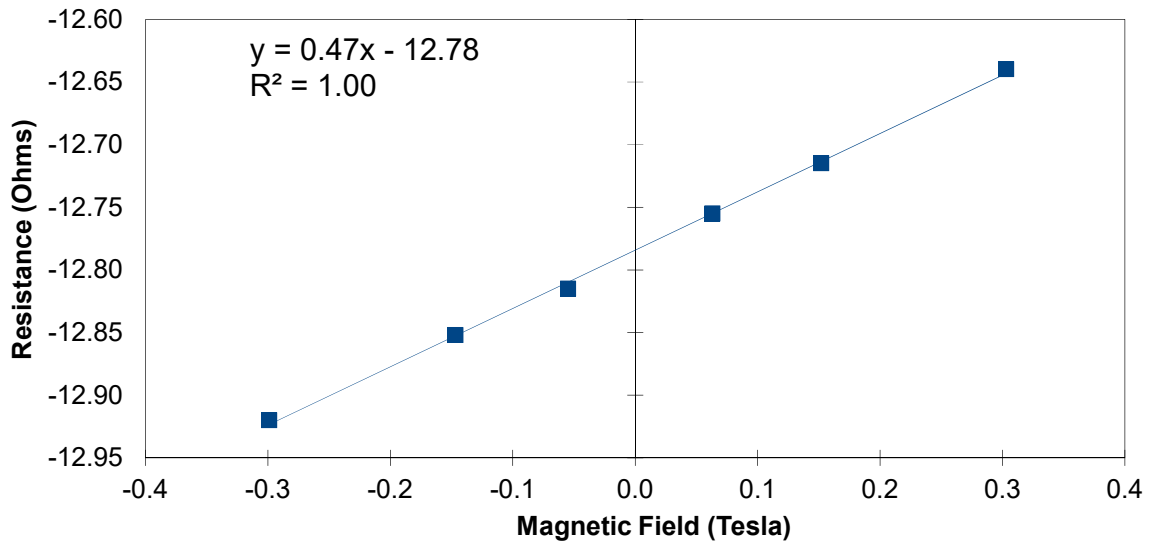


Figure 3.3: Example of typical Hall data, showing the Hall resistance versus field relationship. The slope is equal to  $1/net$ , where  $t$  is the sample thickness,  $e$  is the elementary charge, and  $n$  is the carrier concentration.

### 3.2.4 Low Temperature Transport Properties

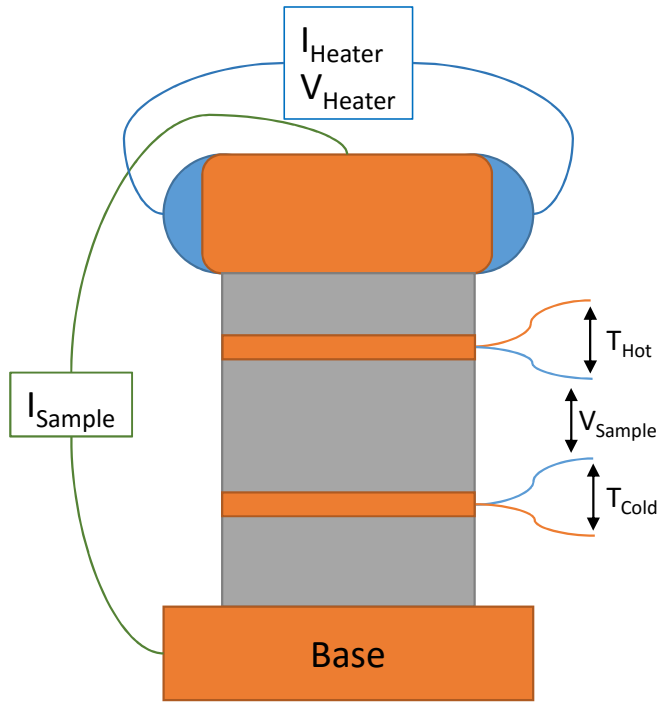


Figure 3.4: Experimental setup for low temperature transport measurements. The measurement is performed under a liquid nitrogen flow, with the sample surrounded by vacuum.

Low temperature properties were measured in a Janis cryostat under a flow of liquid nitrogen from 80K to 350K, in 10K increments. The cryostat chamber was evacuated using a Edwards T-Station 75 turbo pumping station to a pressure less than  $1 \times 10^{-5}$  torr. The temperature of the base was controlled by a LakeShore 311 temperature controller, while the thermocouples measured the temperature gradient along the sample. The sample and Seebeck voltages are measured by a Keithley 2000 multimeter, the heater voltage by a Keithley 2001, and the thermocouple measurements by Keithley 2182A nanovoltmeters. The heater and sample currents were supplied by Keithley 2400-LV sourcemeters.

The sample was diced into a rectangular prism, with typical dimensions of 3mm x 4mm x 8mm. Copper strips were attached across the sample, as shown in Figure 3.4, with Epo-Tek

H2OE silver epoxy. The sample was then attached to a copper base, and a resistor wrapped in copper attached to the top, again with silver epoxy, to ensure good electrical and thermal contact. The copper base was then attached to the cryostat, and wires were soldered on to the copper contacts. The thermocouples were made of copper and constantan, and the current leads were made of phosphor bronze wire.

### 3.2.4.1 Electrical Resistivity

Electrical resistivity was measured by passing a current through the sample and measuring the voltage drop, using the two copper wires of the thermocouples. The measurement was performed twice, with both a positive and a negative current. Using sample dimensions the electrical resistivity of the sample was calculated as follows:

$$\rho = \frac{V_{Sample}}{I_{Sample}} \left( \frac{wd}{p} \right) \quad (3.3)$$

where  $V_{Sample}$  and  $I_{Sample}$  represent the measured voltage and current, w, d, and p are the width, depth, and probe spacing of the sample. The measurement uncertainty is estimated based on equipment as 3%.

### 3.2.4.2 Seebeck Coefficient and Thermal Conductivity

After the electrical resistivity measurement was performed, current was supplied ( $I_{Heater}$ ) to the resistor on top of the sample to create a temperature gradient. The current to the heater was left on for ten minutes to ensure a steady state had been reached, and a current value was set to obtain a temperature difference of 1-1.5K. After that time had passed, the measurements were performed, with  $\Delta T$  being measured with the thermocouples and  $\Delta V$  measured from the copper leads of both thermocouples.

The Seebeck coefficient is defined as follows:

$$S = -\frac{\Delta V}{\Delta T} \quad (3.4)$$

The measurement includes the Seebeck coefficient of the copper leads, which are subtracted off to yield the Seebeck coefficient of the sample itself. The uncertainty in the Seebeck coefficient measurement is estimated at 5%. Simultaneously, the thermal conductivity measurement was performed. The current supplied to the heater ( $I_{Heater}$ ) and the voltage across the heater ( $V_{Heater}$ ) were measured at the same time as the temperature difference. The thermal conductivity was calculated from those values as well as from the dimensions as follows:

$$\kappa = \frac{I_{Heater} V_{Heater}}{\Delta T} \left( \frac{p}{wd} \right) = \frac{Power}{\Delta T} \left( \frac{p}{wd} \right) \quad (3.5)$$

where again p, w, and d are the sample dimensions. While the measurement was performed under a vacuum to prevent measurement uncertainty due to conduction and convection, radiation losses could not be prevented and must be corrected for manually. In our measurements, a radiation correction is applied as follows:

$$\kappa_{actual} = \left( \frac{wd}{p} \right) \left[ K_{measured} - K_{rad} \left( \frac{T}{300} \right)^3 \right] \quad (3.6)$$

where  $K_{measured}$  represents the measured thermal conductance, and  $K_{rad}$  is 0.0015  $W K^{-1}$ , a value obtained experimentally by calibration performed in our lab previously. The error in thermal conductivity measurement is estimated at 10% in the cryostat setup.

The thermal conductivity is composed of two components, the electronic and the lattice

portions, and through the use of the Wiedemann-Franz Law the electronic portion can be estimated as:

$$\kappa_{\text{electronic}} = L\sigma T \quad (3.7)$$

where  $L$  is the Lorenz number (taken in this work to be the free electron value,  $2.44 \times 10^{-8} \text{ W } \Omega \text{ K}^{-2}$ ),  $\sigma$  is the electrical conductivity, and  $T$  is the temperature. The lattice portion of the thermal conductivity was taken to be the measured value minus the electronic portion. In all of the samples reported in this work the thermal conductivity was composed primarily of the lattice component.

### 3.2.5 High Temperature Transport Properties

#### 3.2.5.1 Electrical Resistivity and Seebeck Coefficient

High temperature electrical resistivity and Seebeck coefficient measurements were performed on an Ulvac-Riko ZEM3 system. The same sample from the cryostat was sanded down to remove contacts and then mounted in the ZEM3 system. The sample was clamped between two electrodes and spring loaded thermocouples formed pressure contacts to the side of the sample. Measurements were performed exactly as they are at low temperature. Properties were measured from 300K up to 873K. An offset at 300K in measured properties will be seen in data when switching from the cryostat to the ZEM system for some samples. Calibration of the Seebeck coefficient and electrical resistivity measurement was performed using  $\text{Bi}_2\text{Te}_3$  standard from NIST. The uncertainty in electrical measurements at high temperature is estimated at 5%.

### 3.2.5.2 Thermal Conductivity and Thermal Diffusivity

At higher temperatures radiative losses make measuring thermal conductivity using the typical 4-probe technique, as was done at low temperature, impossible. Instead, the typical method involves measuring thermal diffusivity( $\alpha$ ) via laser flash method and then combining this with the specific heat and sample density. In our calculations room temperature density will be used in combination with the Dulong-Petit value for specific heat to calculate thermal conductivity by the following equation:

$$\kappa = \alpha\rho C_p \tag{3.8}$$

where  $\alpha$  is thermal diffusivity,  $\rho$  is the sample density, and  $C_p$  is the specific heat. Laser-flash measurements were performed in Dr. Tim Hogan's lab at Michigan State University on a Netzsch LFA 457 MicroFlash system, using a pyroceram standard for comparison. Sample density was measured using the Archimedes method in ethanol, and again, the Dulong-Petit value was used for specific heat capacity. The uncertainty in measurement is estimated at 10%.

# Chapter 4

## Tellurides

### 4.1 Family Overview

There are four tellurium containing members of the copper based chalcopyrite family:  $\text{CuAlTe}_2$ ,  $\text{CuGaTe}_2$ ,  $\text{CuInTe}_2$ , and  $\text{CuTlTe}_2$ .  $\text{CuAlTe}_2$  has been studied in thin films, and is reported as chalcopyrite structure with a band gap of 2.06 eV, however very few studies on the bulk compound have been done, likely due to the difficulty in synthesizing high purity samples.[93]  $\text{CuTlTe}_2$  was not studied here, due to the toxicity of thallium and its low melting point; however studies on the transport properties have been reported previously.[94]  $\text{CuFeTe}_2$  forms a layered structure with iron and copper atoms being interchangeable, rather than the chalcopyrite structure of the other compounds, and so was also not studied here.[95, 96]

$\text{CuInTe}_2$  has a reported band gap at 300°C of 0.97 eV to 1.07 eV, while  $\text{CuGaTe}_2$  has reported values of 1.2 eV to 1.23 eV.[97, 98, 99, 6, 92, 8] Both compounds have been previously reported as efficient thermoelectric materials, with a reported peak  $ZT$  of 1.4 for  $\text{CuGaTe}_2$  and 1.18 for  $\text{CuInTe}_2$ . [6, 8] In this chapter results will be shown for both compounds, as well as for solid solutions of the two.

## 4.2 $\text{CuAlTe}_2$

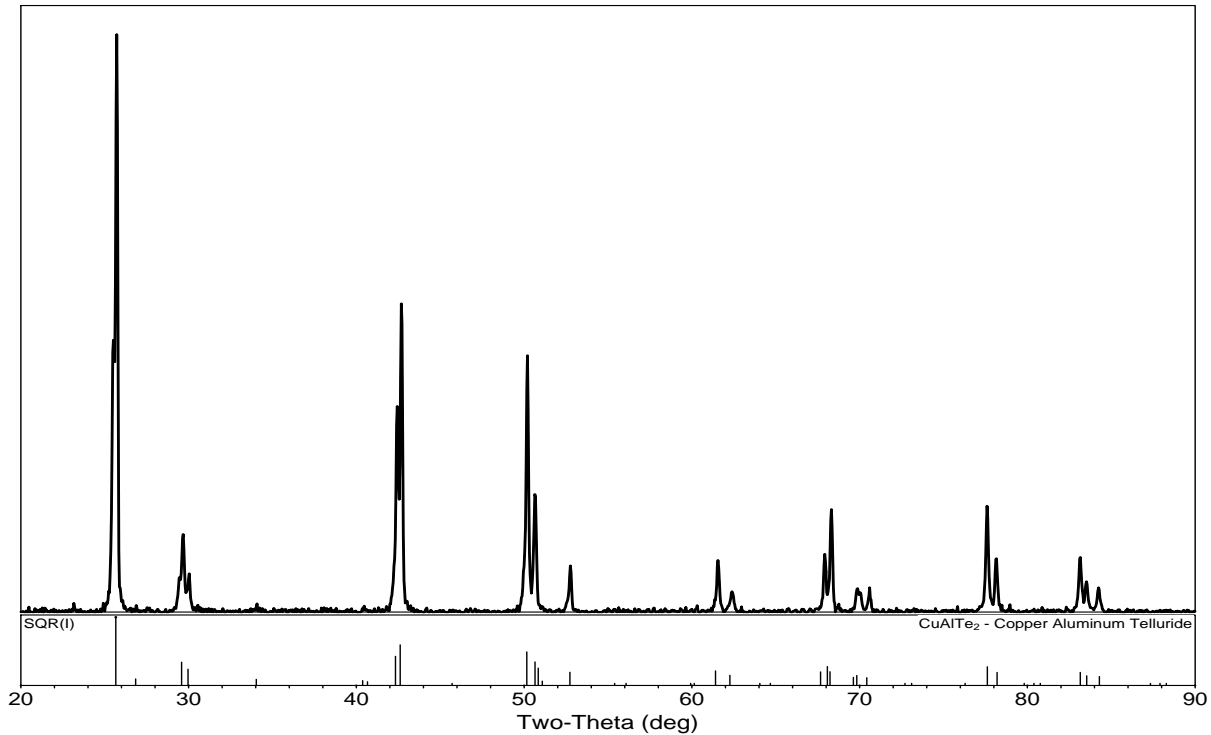


Figure 4.1: X-ray diffraction pattern of  $\text{CuAlTe}_2$  with PDF overlay. The y-scale is intensity, in arbitrary units. PDF # 01-075-0102 [4]

Literature data on  $\text{CuAlTe}_2$  primarily consists of thin film studies, typically synthesized by depositing alternating layers of copper, aluminum, and tellurium by vapor deposition followed by subsequent annealing. Bulk samples are difficult to make due to the affinity of aluminum for oxygen and volatility of tellurium. Two methods were used in this study in attempts to synthesize pure bulk samples. For the first attempt, copper (Alfa Aesar, 99.999%) and aluminum shot (Alfa Aesar, 99.9995%) were weighed out in a 1:2 molar ratio and reacted by arc melting to form  $\text{CuAl}_2$ . The arc melting was performed with a water cooled hearth under an argon atmosphere, and the material was melted several times for 10-15 seconds per melt until the ingot looked homogenous.

The resulting ingot was then ground using a mortar and pestle, checked with XRD, and then placed into a stainless steel ball mill jar. To that was added copper powder (Alfa Aesar, 10 $\mu$  99.999%) and tellurium chunks (Alfa Aesar 99.999%) to bring the molar ratio of Cu:Al:Te to 1:1:2. The jar was filled and sealed in an argon atmosphere, and ball milled for 60 minutes. The resulting powder was checked again with XRD, then was cold pressed and sealed in a quartz ampoule, which was subsequently evacuated and sealed. After that, the sample was placed in a box furnace and held at 450°C for 18 days until being quenched into water, and finally spark plasma sintered at 650°C for 10 minutes. The resulting sample was dense and x-ray diffraction showed primarily CuAlTe<sub>2</sub> with some secondary peaks observed.

After this, a second attempt was made using the same initial steps, but rather than annealing, the powder was placed directly into a graphite die and spark plasma sintered at 400 °C for 20 minutes. As shown in Figure 4.1 the sample again was primarily single phase, with some minor impurities.

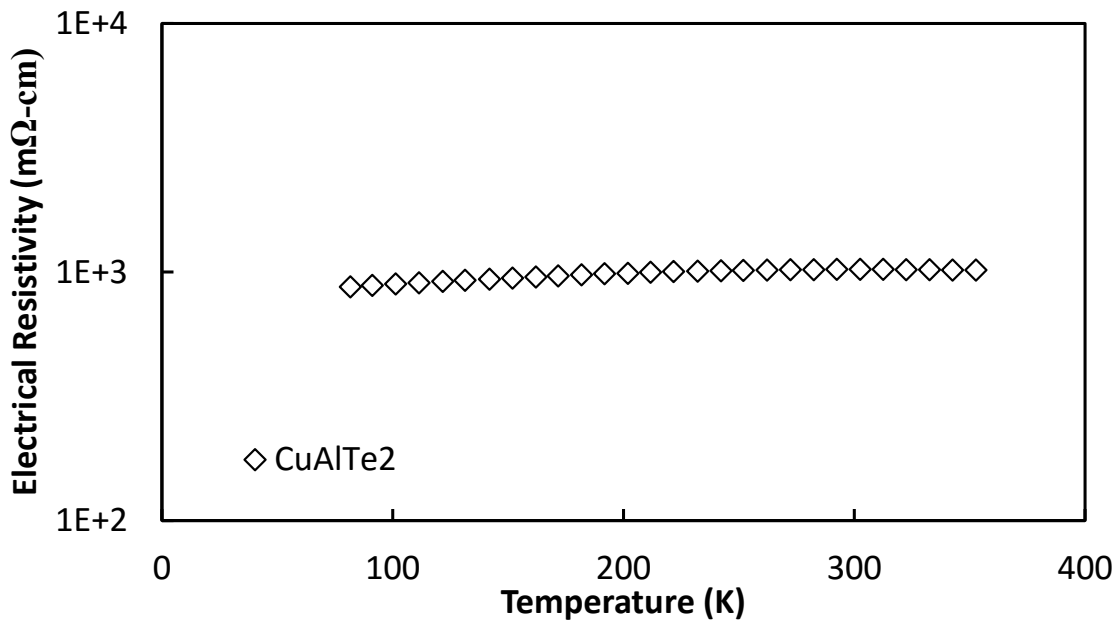


Figure 4.2: Electrical resistivity of CuAlTe<sub>2</sub> as a function of temperature.

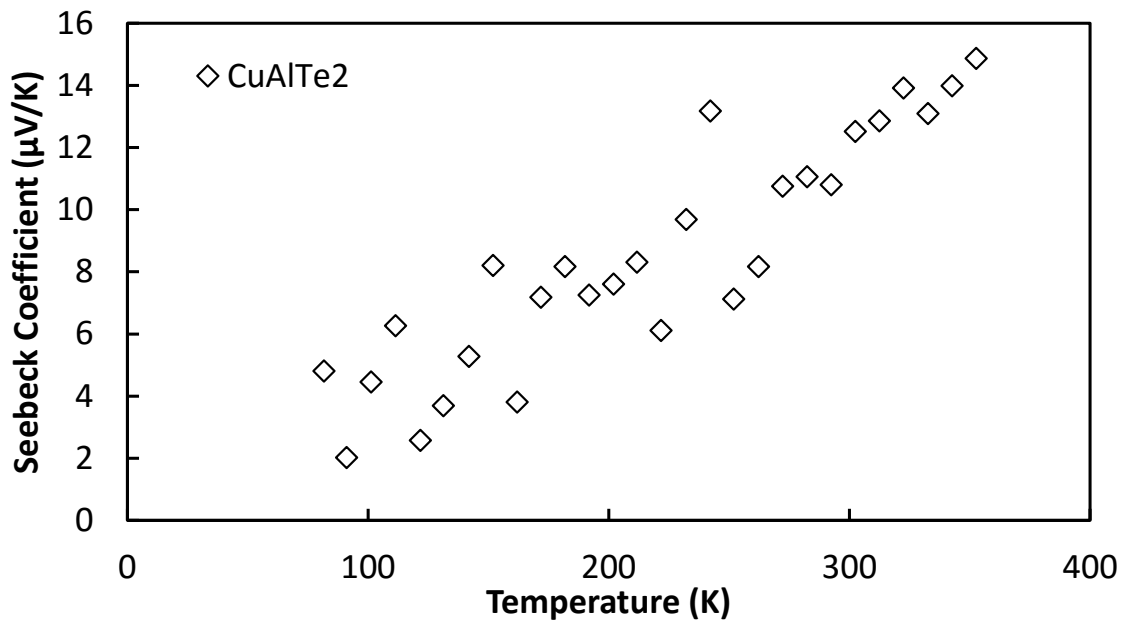


Figure 4.3: Seebeck coefficient of CuAlTe<sub>2</sub> as a function of temperature.

As shown in Figure 4.2 the electrical resistivity of CuAlTe<sub>2</sub> was found to be fairly high, and relatively temperature independent. Contrary to the high electrical resistivity, Figure 4.3 shows that the Seebeck coefficient was very low. Combined, the resulting power factor is minuscule, showing overall poor thermoelectric properties. The scattering in the data for the Seebeck coefficient is due to the small signal.

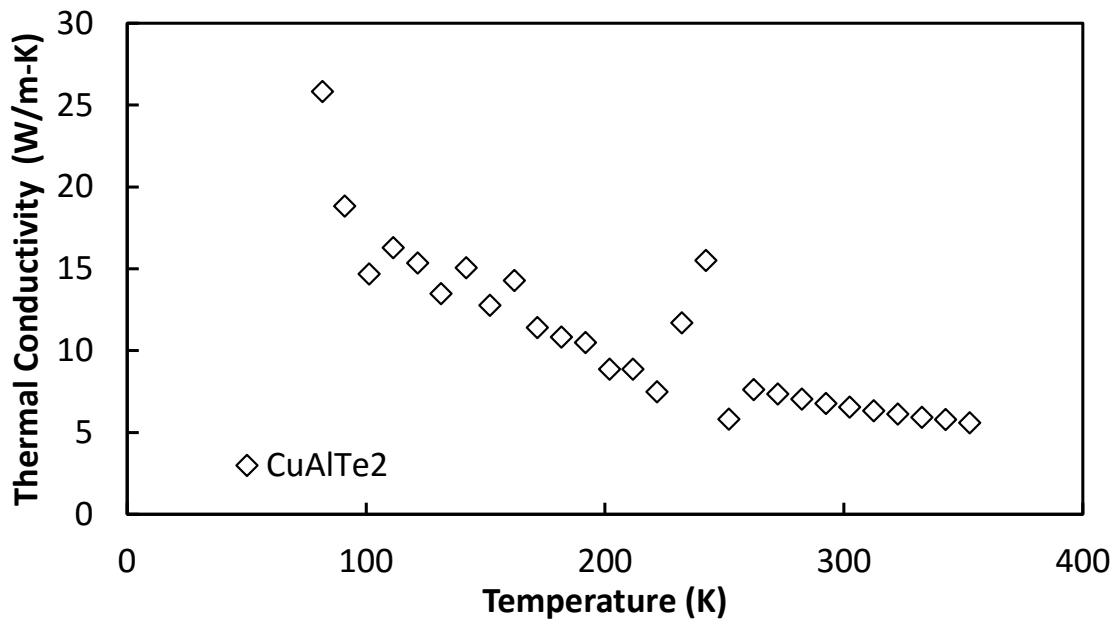


Figure 4.4: Thermal conductivity of CuAlTe<sub>2</sub> as a function of temperature.

The thermal conductivity was comparable to that of CuGaTe<sub>2</sub>, with values near 20 W m<sup>-1</sup> K<sup>-1</sup> at 80K, dropping to roughly 5.5 W m<sup>-1</sup> K<sup>-1</sup> at 350K. The jump in data in Figure 4.4 at 230K is due to a measurement issue and does not indicate an actual trend. It is suspected that the up-tick is due to moisture evaporating under vacuum as the sample heats up.

Overall the properties of CuAlTe<sub>2</sub> were found to be very ill suited for thermoelectrics.

## 4.3 CuInTe<sub>2</sub>

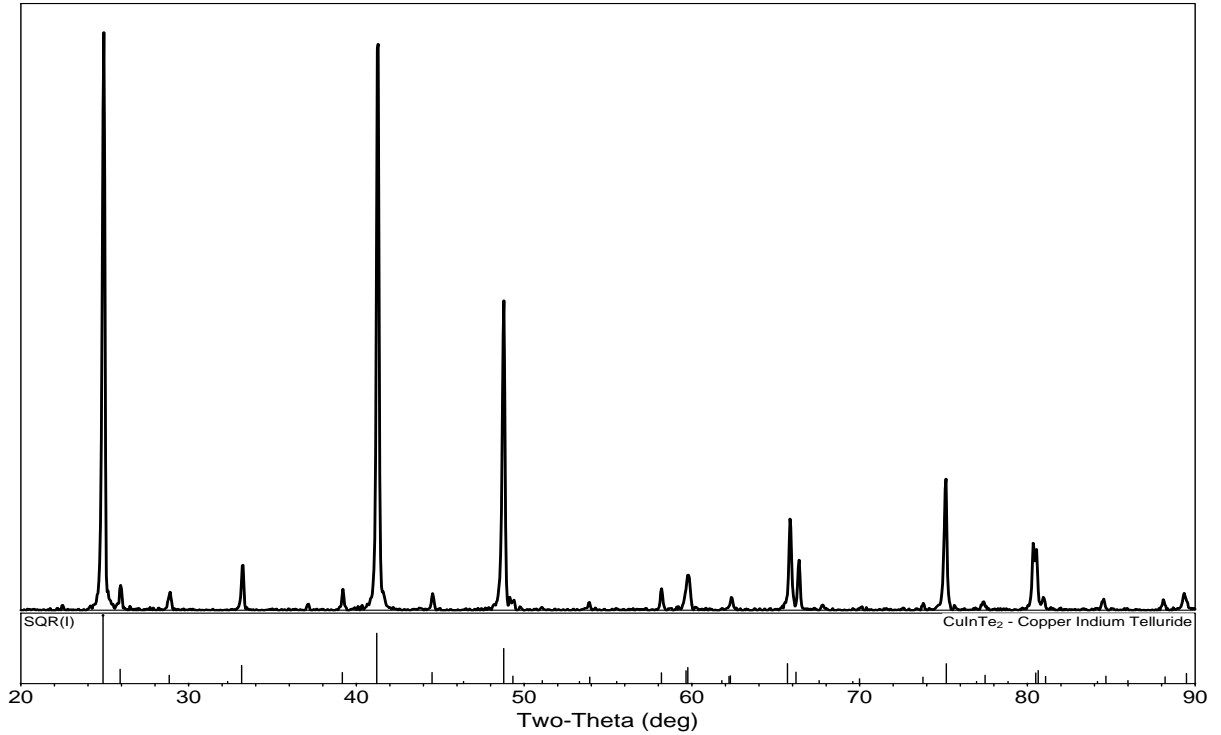


Figure 4.5: X-ray diffraction pattern of CuInTe<sub>2</sub> with PDF overlay. The y-scale is intensity, in arbitrary units. The pattern is PDF #01-082-0450. [5]

The reported lattice parameters range from 6.16Å to 6.1904Å for  $a$  and from 12.32Å to 12.3976Å for  $c$ . [6, 4, 14] The values calculated from the samples made in this study were 6.19Å and 12.33Å for  $a$  and  $c$  respectively. The XRD pattern shown in Figure 4.5 matches well to that of CuInTe<sub>2</sub>, indicating the sample was high purity.

### 4.3.1 Electronic Doping

Zinc was chosen as a p-type dopant, acting as an acceptor by replacing the nominally trivalent indium with di-valent zinc. Electronic measurements showed that zinc did in fact act as an acceptor, reducing the electrical resistivity by two orders of magnitude at low temper-

atures, as shown in Figure 4.6. Hall measurements showed an increase in room temperature carrier concentration from  $5.6 \times 10^{17} \text{cm}^{-3}$  to  $3.4 \times 10^{19} \text{cm}^{-3}$ , again indicating zinc was an effective p-type dopant. When comparing work by Liu *et al.* to this experiment, the  $y = 0.005$  sample agreed with the literature value at room temperature, however the literature data was independent of temperature above 600K, while all of the samples synthesized here showed a rise in resistivity above 700K.[6] The Seebeck coefficient showed the same results; at room temperature the data from Liu *et al.* for the 72- and 168-hour annealed samples matched closely to that of the 0.5% and 1% doped samples made here, but differed above 700K.

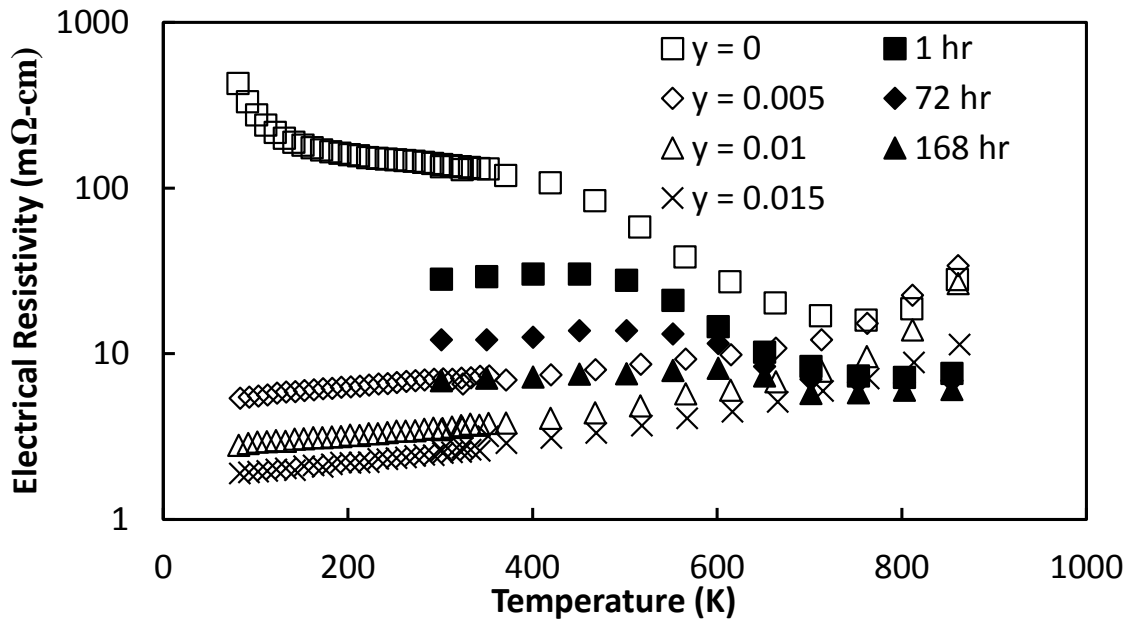


Figure 4.6: Electrical resistivity of the series  $\text{CuIn}_{1-y}\text{Zn}_y\text{Te}_2$  as a function of temperature. Open symbols represent  $\text{CuIn}_{1-y}\text{Zn}_y\text{Te}_2$ . Filled symbols are data from Liu *et al.* for  $\text{CuInTe}_2$  annealed for 1, 72, and 168 hours. For comparison, our samples were annealed for 24 hours.[6]

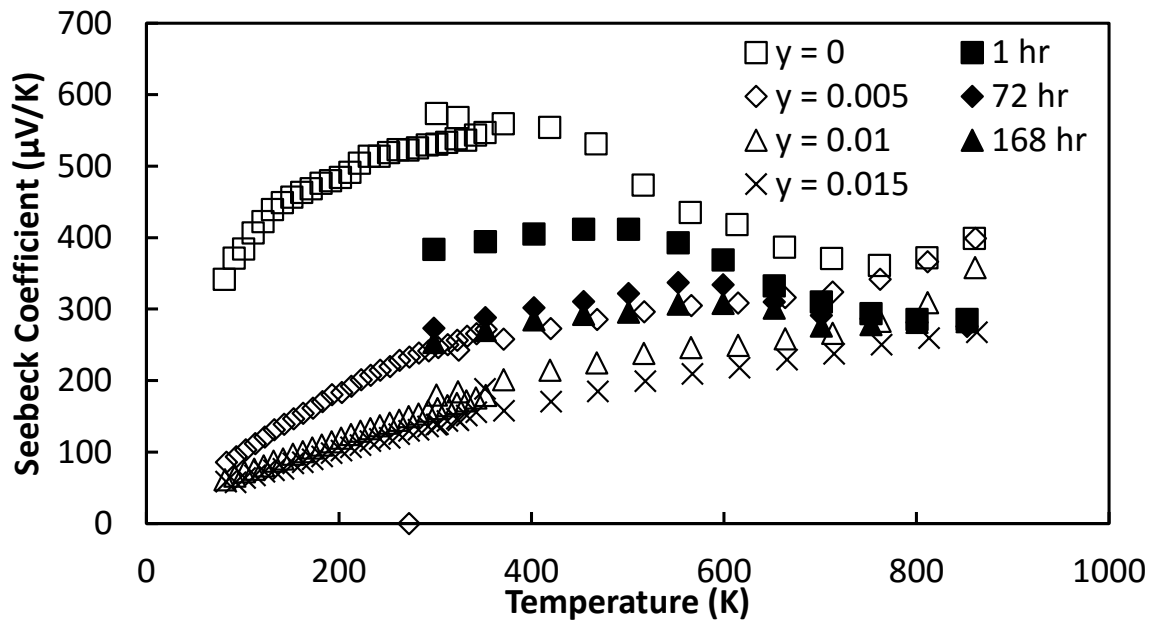


Figure 4.7: Seebeck coefficient of the series  $\text{CuIn}_{1-y}\text{Zn}_y\text{Te}_2$  as a function of temperature. Open symbols represent  $\text{CuIn}_{1-y}\text{Zn}_y\text{Te}_2$ . Filled symbols are data from Liu *et al.* for  $\text{CuInTe}_2$  annealed for 1, 72, and 168 hours. For comparison, our samples were annealed for 24 hours.[6]

In Figure 4.8 it was observed that doping greatly increased the power factor from 80K up to 700K, at which point the undoped sample matched that of the zinc doped samples as intrinsic carriers overrode extrinsic carriers. It was also observed in Figure 4.6 that the electrical resistivities converged at this point as well.

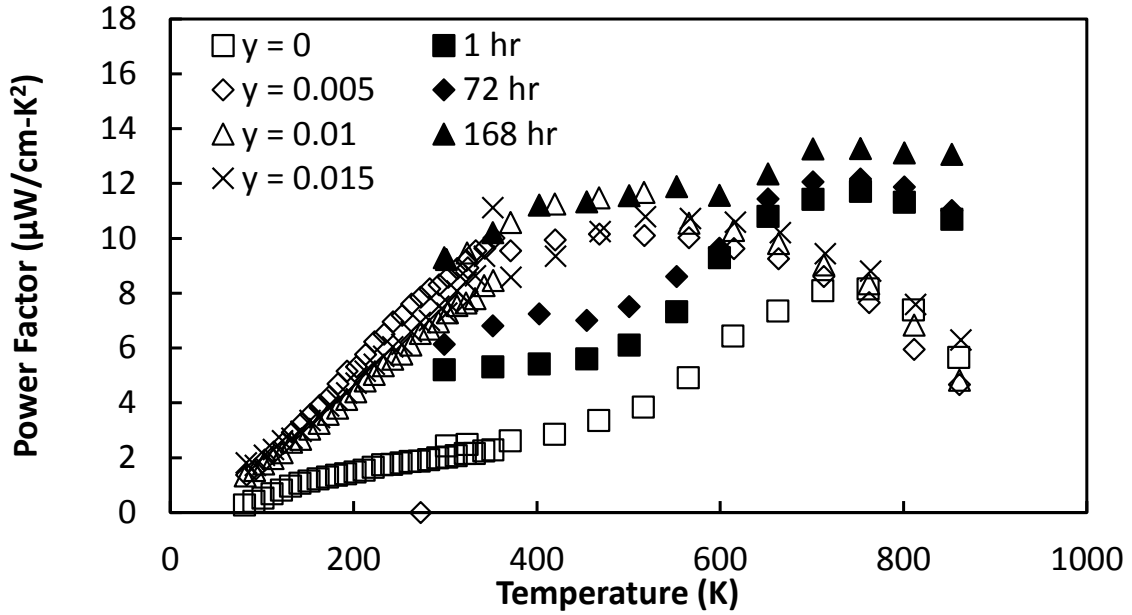


Figure 4.8: Power factor of the series  $\text{CuIn}_{1-y}\text{Zn}_y\text{Te}_2$  as a function of temperature. Open symbols represent  $\text{CuIn}_{1-y}\text{Zn}_y\text{Te}_2$ . Filled symbols are data from Liu *et al.* for  $\text{CuInTe}_2$  annealed for 1, 72, and 168 hours. For comparison, our samples were annealed for 24 hours.[6]

Comparing power factors in Figure 4.8 we find that our samples have a peak in power factor around 550K, while the literature data shows a power factor peaking around 700K and remaining constant above that temperature. From the power factor data it was shown that replacing 1% of the indium with zinc yielded the best electronic properties, however the reason for the difference in our data from that of the literature is unclear, but could be due to differences in sample density. The thermal conductivity for the samples were all similar, including the literature values as shown in Figure 4.9. The literature data showed a slightly higher peak  $ZT$ , as shown in Figure 4.10.

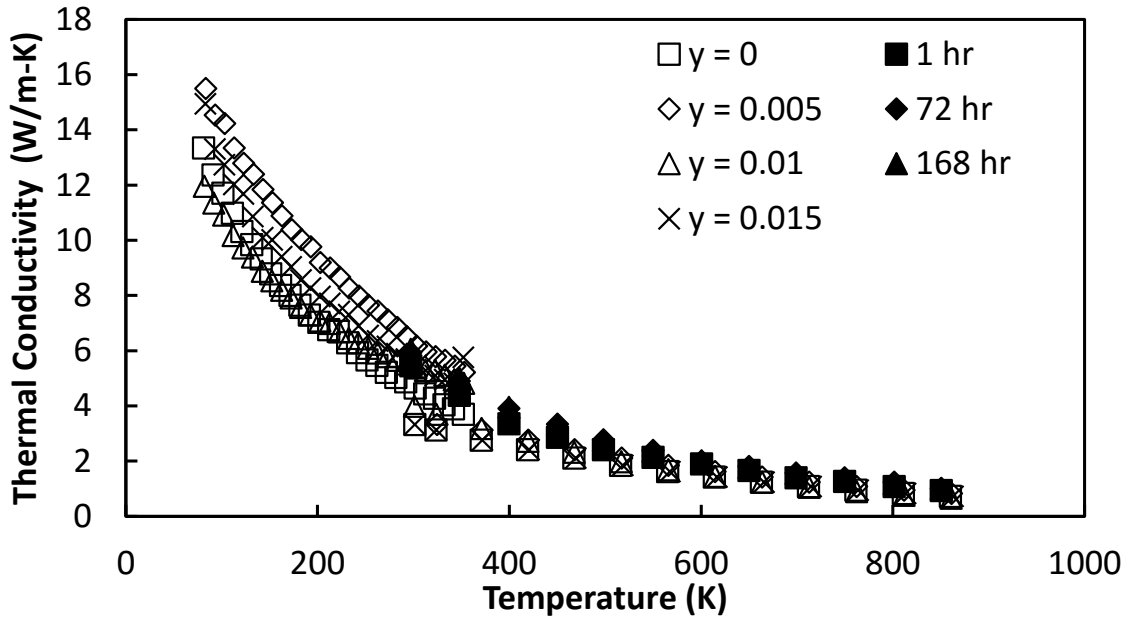


Figure 4.9: Thermal conductivity of the series  $\text{CuIn}_{1-y}\text{Zn}_y\text{Te}_2$  as a function of temperature. Open symbols represent  $\text{CuIn}_{1-y}\text{Zn}_y\text{Te}_2$ . Filled symbols are data from Liu *et al.* for  $\text{CuInTe}_2$  annealed for 1, 72, and 168 hours. For comparison, our samples were annealed for 24 hours.[6]

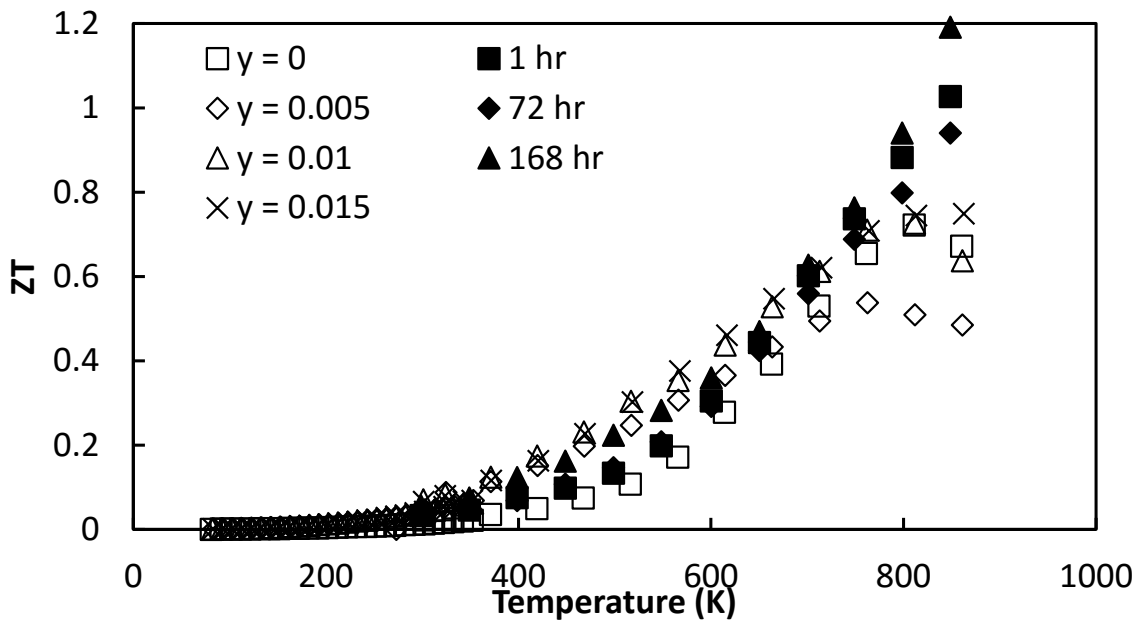


Figure 4.10:  $ZT$  of the series  $\text{CuIn}_{1-y}\text{Zn}_y\text{Te}_2$  as a function of temperature. Open symbols represent  $\text{CuIn}_{1-y}\text{Zn}_y\text{Te}_2$ . Filled symbols are data from Liu *et al.* for  $\text{CuInTe}_2$  annealed for 1, 72, and 168 hours. For comparison, our samples were annealed for 24 hours.[6]

## 4.4 CuGaTe<sub>2</sub>

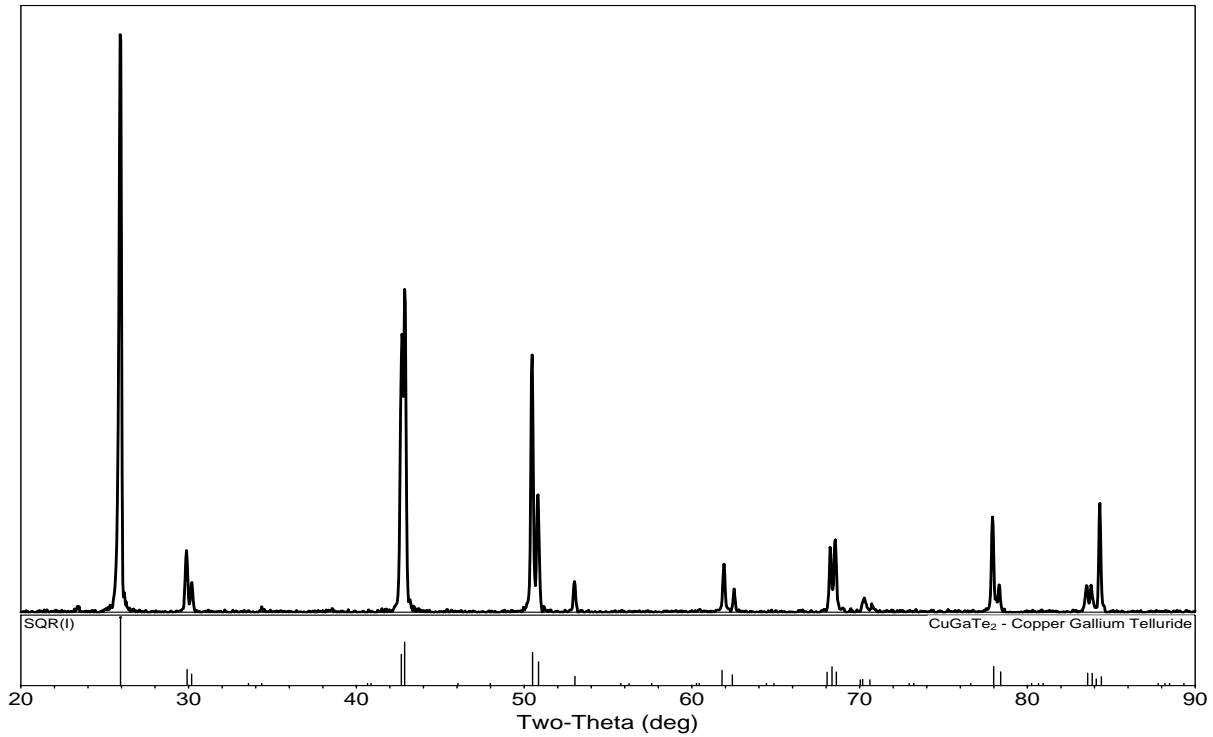


Figure 4.11: XRD pattern of CuGaTe<sub>2</sub>, with a PDF overlay. The pattern is PDF # 01-079-2331. [7]

The lattice parameters of CuGaTe<sub>2</sub> were slightly smaller than those of CuInTe<sub>2</sub>, as expected from the smaller ionic radius of gallium. Literature reports vary from 5.99 Å to 6.025 Å and 11.92 Å to 11.948 Å for *a* and *c* respectively.[8, 4, 14, 5, 15, 100] The values calculated from our XRD patterns are 6.02 Å and 11.85 Å, and our XRD pattern matches well with that of PDF# 01-079-2331.[7] CuGaTe<sub>2</sub> also has a larger band gap than CuInTe<sub>2</sub>, which is typical of diamond-like semiconductors when making an isoelectronic substitution with an element above it in the period table.[14]

### 4.4.1 Transport Properties

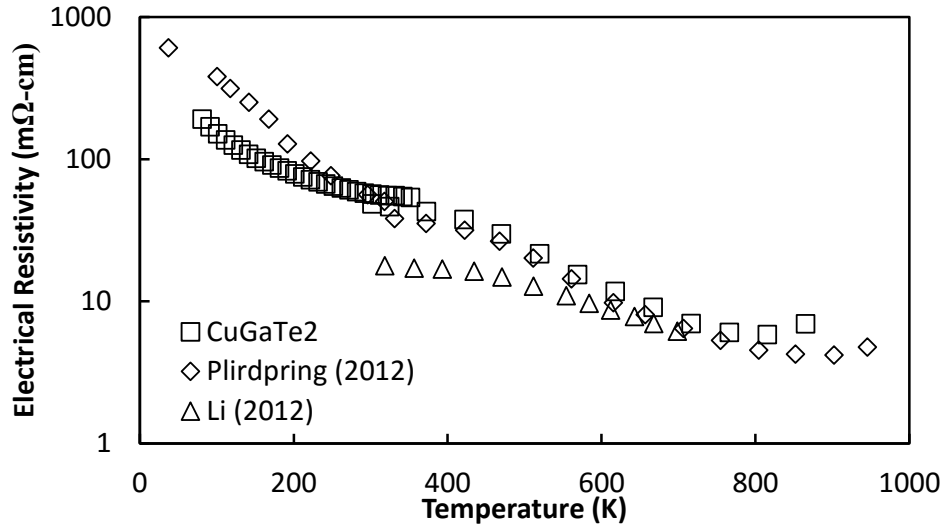


Figure 4.12: Electrical resistivity of  $\text{CuGaTe}_2$  as a function of temperature. Squares represent our data, while the diamonds are from Plirdpring *et al.* [8], and the triangles are from Li *et al.* [9].

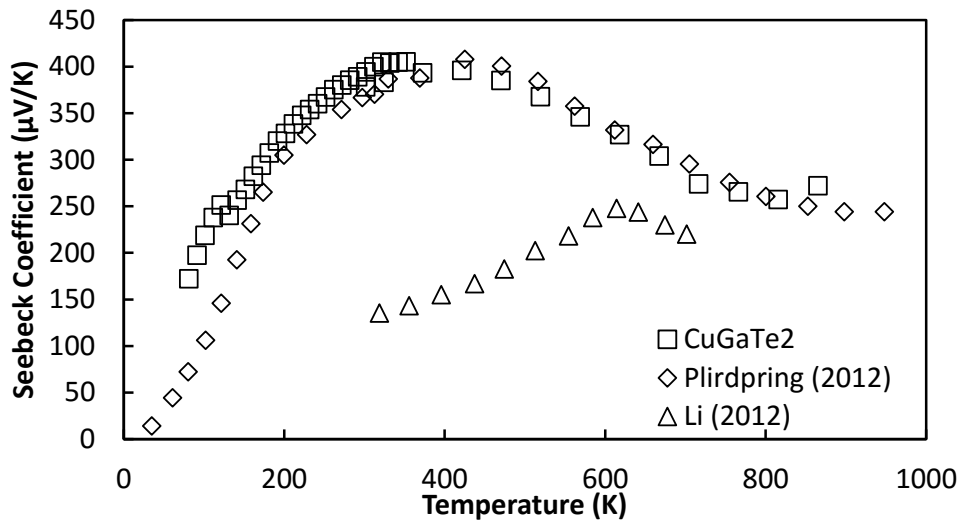


Figure 4.13: Seebeck coefficient of  $\text{CuGaTe}_2$  as a function of temperature. Squares represent our data, while the diamonds are from Plirdpring *et al.* [8], and the triangles are from Li *et al.* [9].

As shown in the Figure 4.12 and Figure 4.13, the samples synthesized here show close agreement with the literature data from Plirdpring *et al.* (2012), but the data from Li *et al.*

(2012) showed a lower resistance and a much lower Seebeck coefficient. That disagreement was likely due to differences in the amount of defects in the samples, as well as differences in density. For the sample synthesized here, the electrical resistivity decreased over the whole temperature range, typical of a semiconductor, while the Seebeck coefficient initially increases linearly in  $T$  until reaching a maximum of  $400 \mu\text{V K}^{-1}$  at 350 K, after which the Seebeck coefficient decreased, likely due to thermal excitation of minority carriers. The value is positive over the whole range indicating holes are the majority carriers in agreement with previous studies. [8, 101, 9]

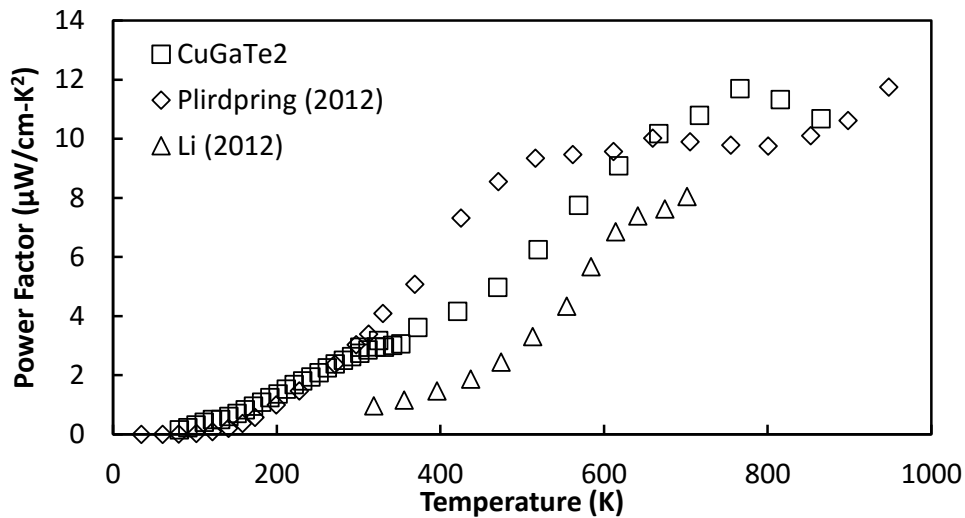


Figure 4.14: Power factor of  $\text{CuGaTe}_2$  as a function of temperature. Squares represent our data, while the diamonds are from Plirdpring *et al.* [8], and the triangles are from Li *et al.*[9].

The power factor of the sample increased up until 766K, above which the value dropped slightly, reaching a peak value of  $11.7 \mu\text{W cm}^{-1} \text{K}^{-2}$ , slightly higher than values present in the literature.

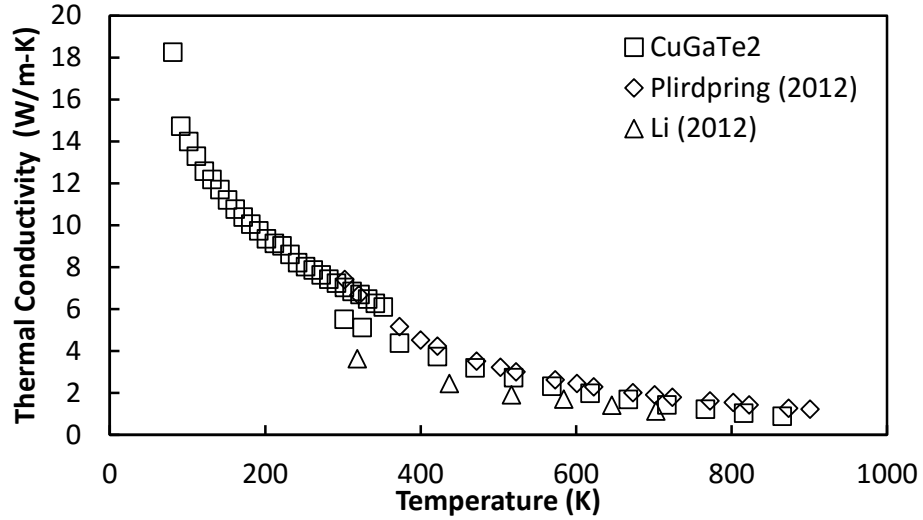


Figure 4.15: Thermal conductivity of CuGaTe<sub>2</sub> as a function of temperature. Squares represent our data, while the diamonds are from Plirdpring *et al.* [8], and the triangles are from Li *et al.*[9].

The thermal conductivity data for all of the samples showed a typical  $T^{-1}$  behavior, dropping from a value of  $6-8 \text{ W m}^{-1} \text{ K}^{-1}$  at 300K down to a value less than  $1 \text{ W m}^{-1} \text{ K}^{-1}$  at 870K. Previous studies agreed well with the values obtained in this study. The sample displayed a peak  $ZT$  of 1.04 at 870K, in line with values obtained by Plirdpring *et al.*[8]

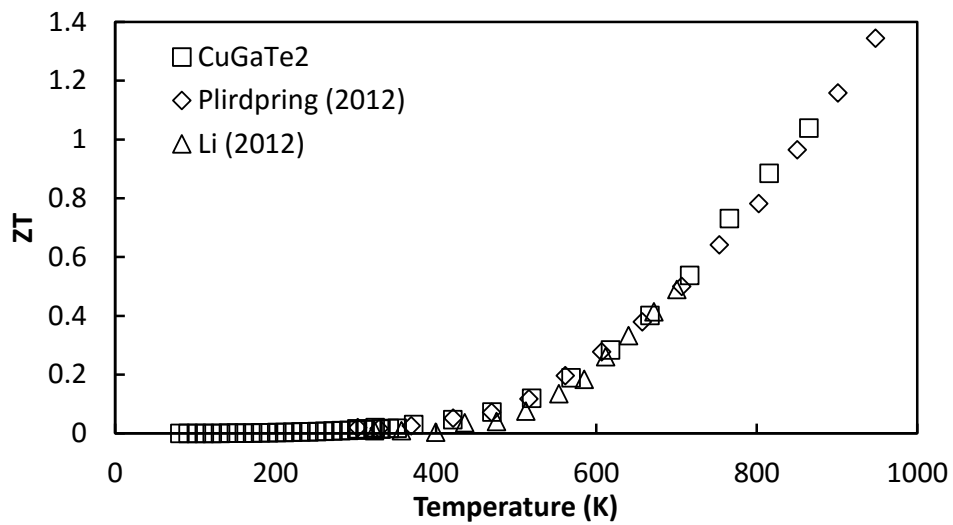


Figure 4.16:  $ZT$  of CuGaTe<sub>2</sub> as a function of temperature. Squares represent our data, while the diamonds are from Plirdpring *et al.* [8], and the triangles are from Li *et al.*[9].

## 4.4.2 Electronic Doping

Computational studies by Gudelli *et al.* in 2013 indicated that CuGaTe<sub>2</sub> could reach a  $ZT$  greater than 2.0 with a hole concentration of  $6 \times 10^{19} \text{ cm}^{-3}$ , however Hall measurements showed the synthesized sample to have a concentration of  $1.4 \times 10^{18} \text{ cm}^{-3}$  at room temperature. Substituting 1% zinc for gallium, as was done for CuInTe<sub>2</sub>, increased the room temperature carrier concentration up to  $6.2 \times 10^{19} \text{ cm}^{-3}$ , however the  $ZT$  for the undoped sample was 1.04, while the doped sample reached a peak  $ZT$  at 870K of 1.16, an increase, but still less than the predicted value.[102]

In 2014, calculations by Yang *et al.* using density functional theory showed that n-type CuGaTe<sub>2</sub> could be even more promising than the p-type compound, with a predicted  $ZT$  of 2.1 at 950K. [103] Several different elements were used in attempts to create an n-type sample of CuGaTe<sub>2</sub>, however none were successful. Their properties are reported in the following section.

### 4.4.2.1 N-type Dopants: Zinc, Germanium, Tin, and Iodine

A zinc atom substituting for copper should act as donor, with zinc being nominally divalent and copper monovalent, however samples with both 2% and 5% zinc substituted for copper still showed positive Seebeck coefficient values over all temperature ranges measured. No other divalent cations were attempted. On the gallium site, samples were made with 2% and 5% germanium and tin substitution, again none of which showed n-type character. Germanium was substituted up to 10%, at which point XRD showed multiple phases (a mixture of CuGaTe<sub>2</sub>, GaTe, Cu<sub>2</sub>GaTe<sub>2</sub> and raw gallium) indicating the solubility limit had been passed, but all samples up to then still exhibited positive Seebeck coefficient values. Finally on the tellurium site, samples were made with iodine substitution by using binary

CuI as a precursor.

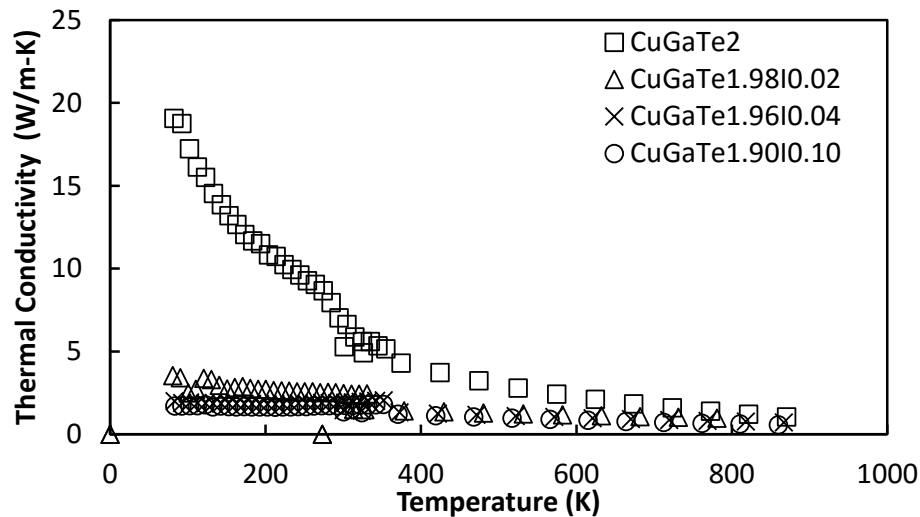


Figure 4.17: Thermal conductivity of the series  $\text{CuGaTe}_{2(1-x)}\text{I}_{2x}$  as a function of temperature.

The iodine containing samples showed a surprising drop in total thermal conductivity, as seen in Figure 4.17. Later work on placing vacancies in the lattice by copper deficiency showed similar results, indicating that the iodine may have sublimated out, leaving vacancies. They also showed a decrease in power factor with increasing iodine concentration. Samples showed poor high temperature stability, and often were deformed after high temperature measurements, likely due to iodine sublimating out, making the dopant poorly suited for thermoelectric use. Overall, the iodine doped samples showed similar  $ZT$  values to the undoped samples, but suffered from stability issue due to iodine sublimation.

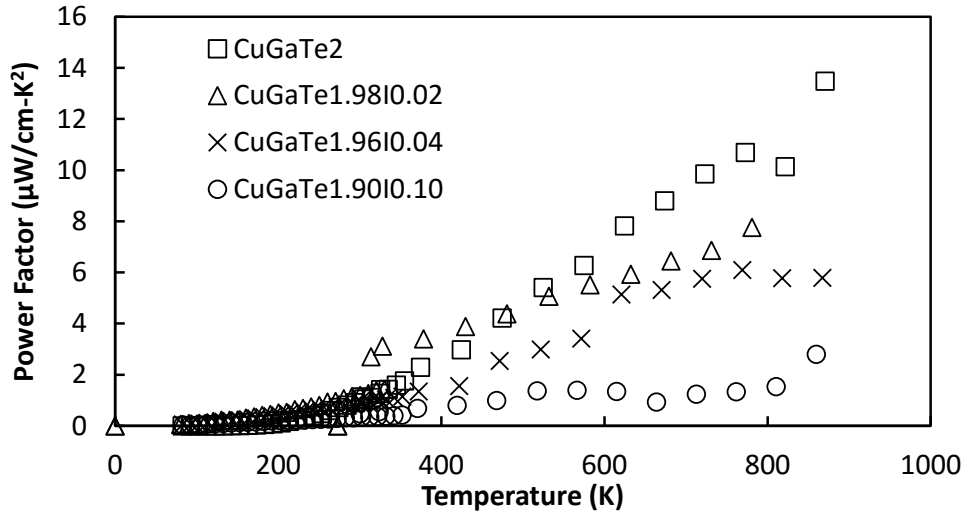


Figure 4.18: Power factor of the series  $\text{CuGaTe}_2(1-x)\text{I}_{2x}$  as a function of temperature.

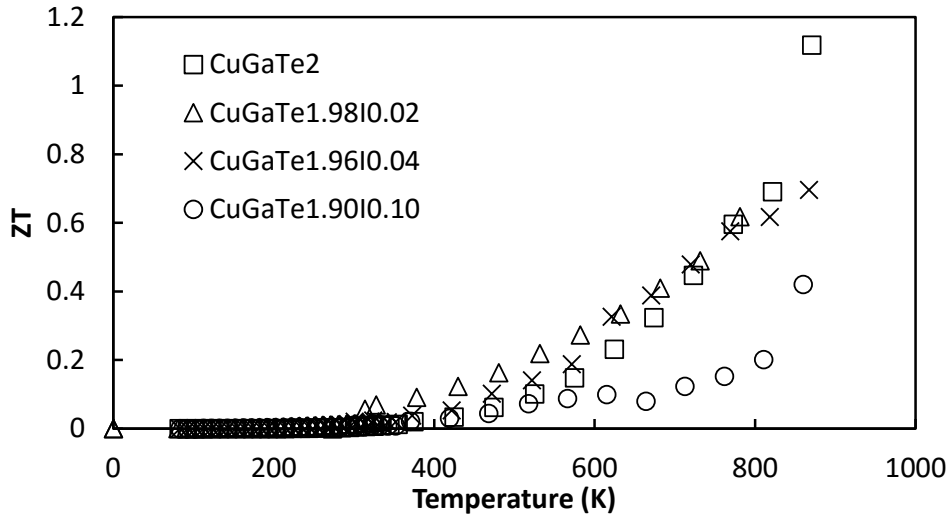


Figure 4.19:  $ZT$  of the series  $\text{CuGaTe}_2(1-x)\text{I}_{2x}$  as a function of temperature.

Figure 4.20 shows that 2% germanium substitution caused a slight increase in the room temperature electrical resistivity, and 5% showed an increase by a factor of ten, as would be expected when attempting to dope an already p-type semiconductor to be n-type. Substituting 2% germanium also caused a large drop in Seebeck coefficient, which could be indicative of minority carriers competing with the majority holes. The sample with 5% germanium

showed a higher Seebeck coefficient, albeit a value still half that of the pure  $\text{CuGaTe}_2$ .

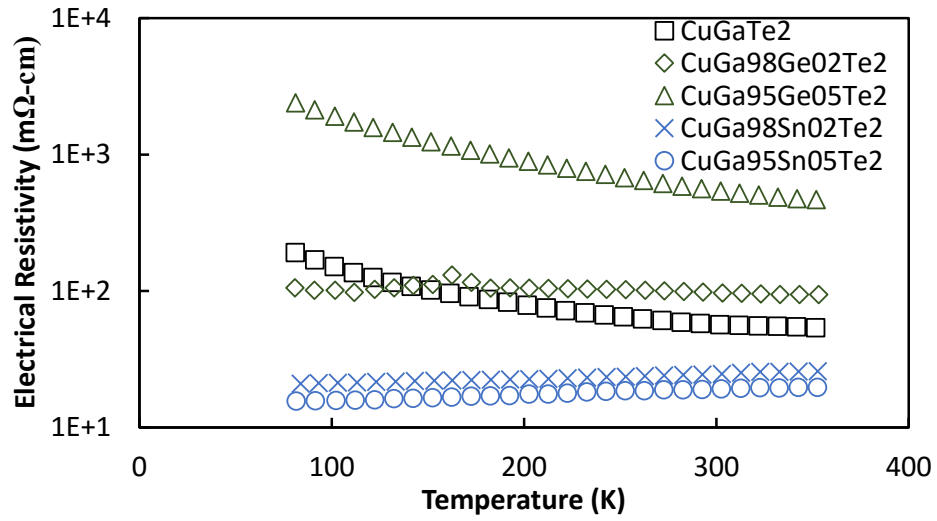


Figure 4.20: Electrical resistivity of n-type doped samples of  $\text{CuGaTe}_2$  as a function of temperature.

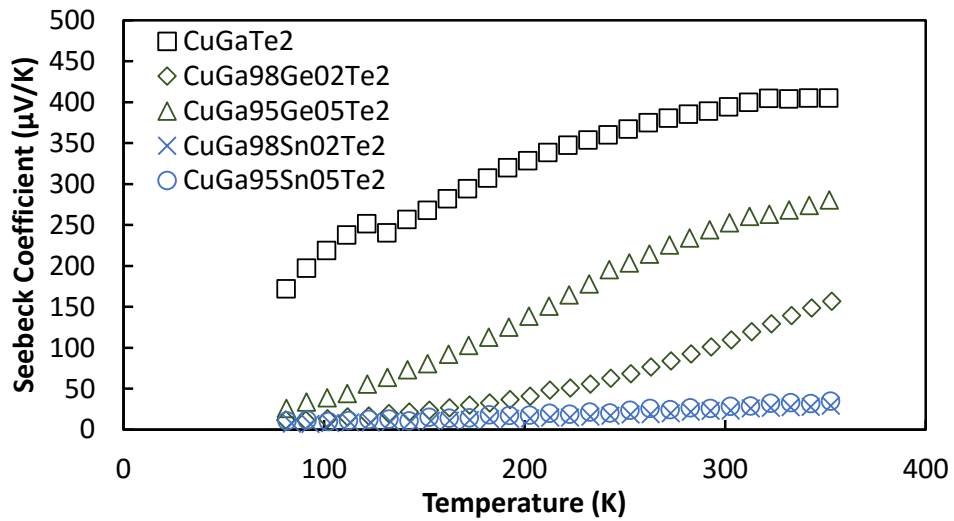


Figure 4.21: Seebeck coefficient of n-type doped samples of  $\text{CuGaTe}_2$  as a function of temperature.

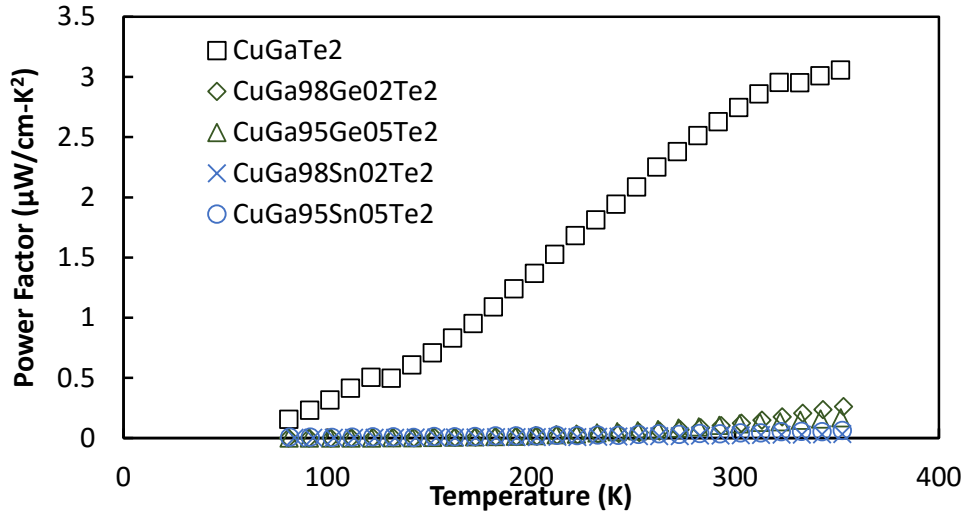


Figure 4.22: Power factor of n-type doped samples of  $\text{CuGaTe}_2$  as a function of temperature.

Tin substitution showed a different effect, with both 2% and 5% tin doped samples displaying an electrical resistivity that was a factor of two lower than the pure  $\text{CuGaTe}_2$ . The Seebeck coefficient agreed with this result, with a large drop as would be expected from a more metallic sample. These two factors indicated that the germanium is not acting as an n-type dopant, and rather appeared to be acting as a p-type dopant. The explanation for this is unclear, but it is likely that the germanium was either not residing on the gallium atomic site, or was causing other site anti-site defects offsetting the effect. Both tin and germanium were detrimental to the power factor of the sample, with room temperature power factors for all four samples a factor of roughly 20 less than the pure  $\text{CuGaTe}_2$ .

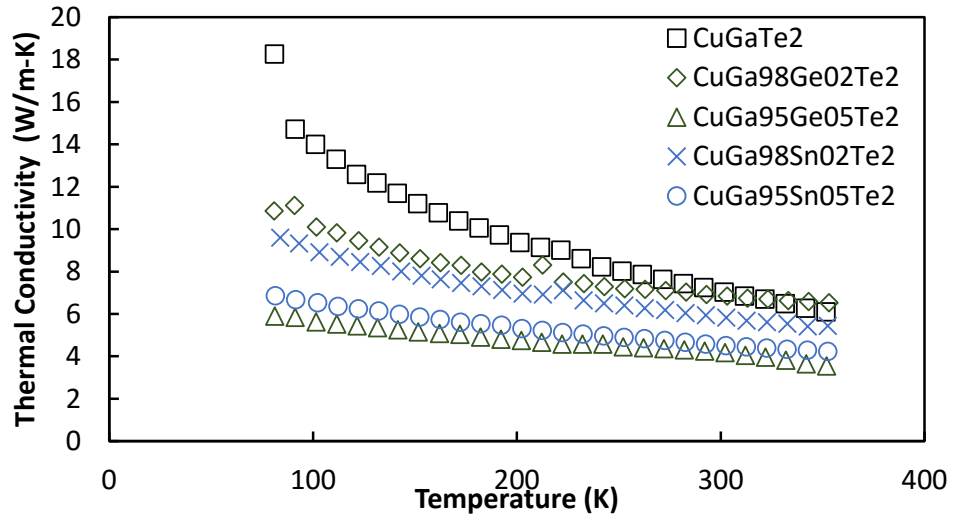


Figure 4.23: Thermal conductivity of n-type doped samples of  $\text{CuGaTe}_2$  as a function of temperature.

The thermal conductivity for both the tin and germanium doped sample showed a drop, as expected, with the 5% doped samples displaying a lower value than the 2%. Overall, the  $ZT$  was strongly reduced, as expected from the drastic drop in power factor.

## 4.5 Solid Solutions

### 4.5.1 $\text{CuIn}_{1-x}\text{Ga}_x\text{Te}_2$

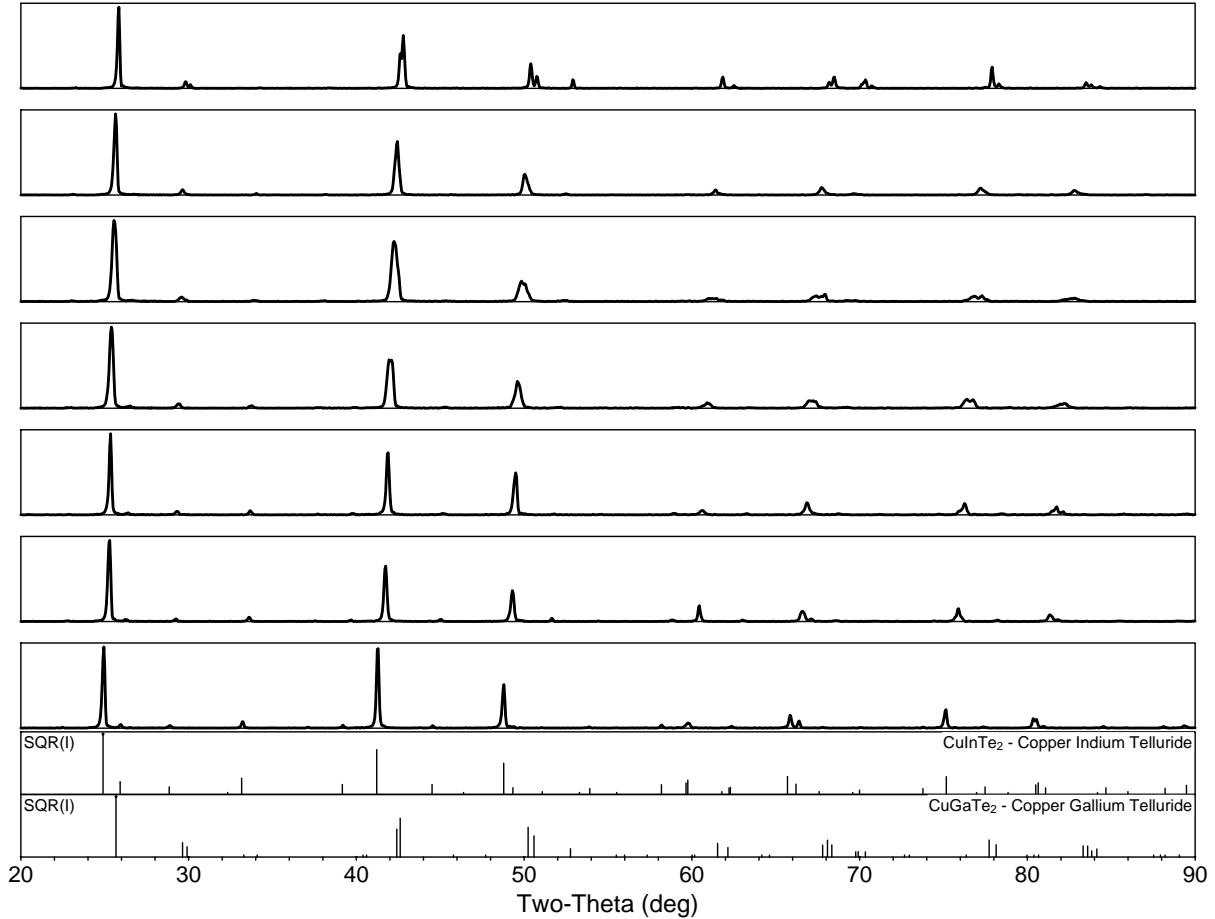


Figure 4.24: XRD patterns of the series  $\text{CuIn}_{1-x}\text{Ga}_x\text{Te}_2$ . From bottom to top, samples are  $x = [0, 0.25, 0.35, 0.5, 0.65, 0.75, 1]$ . The y-axis is shows intensity in arbitrary units. To top PDF is  $\text{CuGaTe}_2$  (# 01-079-2331) and the bottom is  $\text{CuInTe}_2$  (#01-082-0450).[5, 7]

With both  $\text{CuInTe}_2$  and  $\text{CuGaTe}_2$  displaying a  $ZT$  over unity, the next approach was to form a solid solution of the two compounds. It was hypothesized that given their close band gaps (1.07 eV vs 1.2 eV respectively) and because both indium and gallium nominally have the same valence, substituting one element for the other would have little effect on the electrical transport properties. However, the difference in mass of indium and gallium reduce the

thermal conductivity due to alloy scattering, as described in Chapter 2. Previous work by Li *et al.* had shown that samples with 36% and 64% indium substituted for gallium did display lower thermal conductivity than the end members, and they also reported a rise in electrical resistivity and a substantial increase in the Seebeck coefficient at room temperature.[9] To confirm and expand upon their results, a full solid solution of  $\text{CuIn}_{1-x}\text{Ga}_x\text{Te}_2$  was formed for values of  $x = [0, 0.25, 0.35, 0.5, 0.65, 0.75, 1]$ .

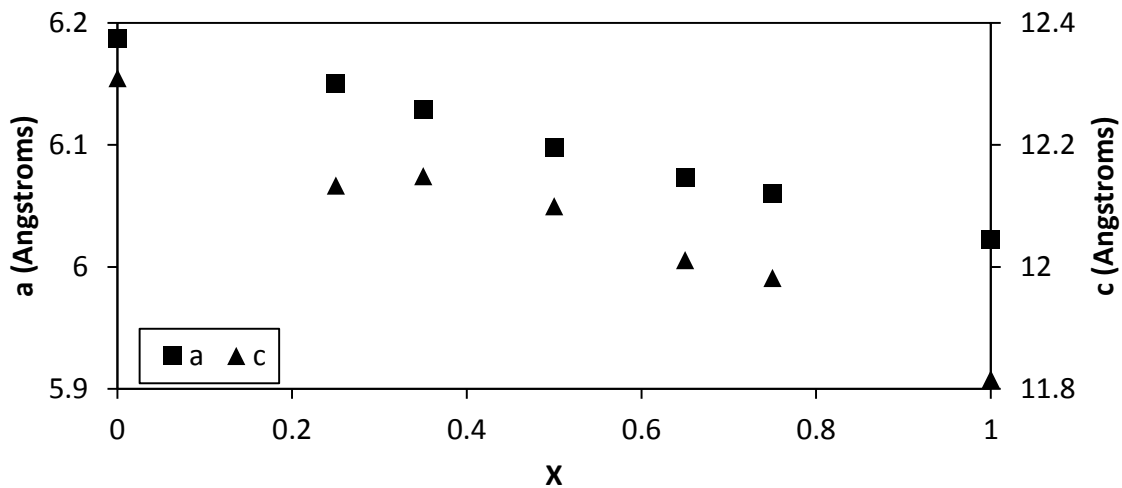


Figure 4.25: Calculated lattice parameters of the series  $\text{CuIn}_{1-x}\text{Ga}_x\text{Te}_2$  as a function of gallium concentration ( $x$ ), using the 204 and 424 peaks.

As seen in Figure 4.24, the XRD patterns exhibited a systematic shift in peaks towards higher  $2\theta$  with increasing gallium concentration, indicating a shrinking lattice parameter as was expected from the smaller size of gallium. This also agrees with the work done by Leon *et al.*[5] That work also showed that on top of a typical linear shift in both  $a$  and  $c$ , as gallium is replaced with indium the copper-tellurium bond length remains nearly fixed, while the bond between the group III atom and tellurium grows, leading to a distortion of

the lattice with increasing indium concentration, and subsequently a change in the ratio of the  $c$  to  $a$  lattice parameter.[5] The chalcopyrite compounds nominally have a ratio of  $c:a$  equal to 2.0, but defects and substitutions shift this slightly above or below, which leads to a splitting of peaks as observed in the XRD patterns in Figure 4.24. Show in Figure 4.25 are the values for the  $a$  and  $c$  lattice parameters in angstroms, showing the overall linear trend as a function of composition.

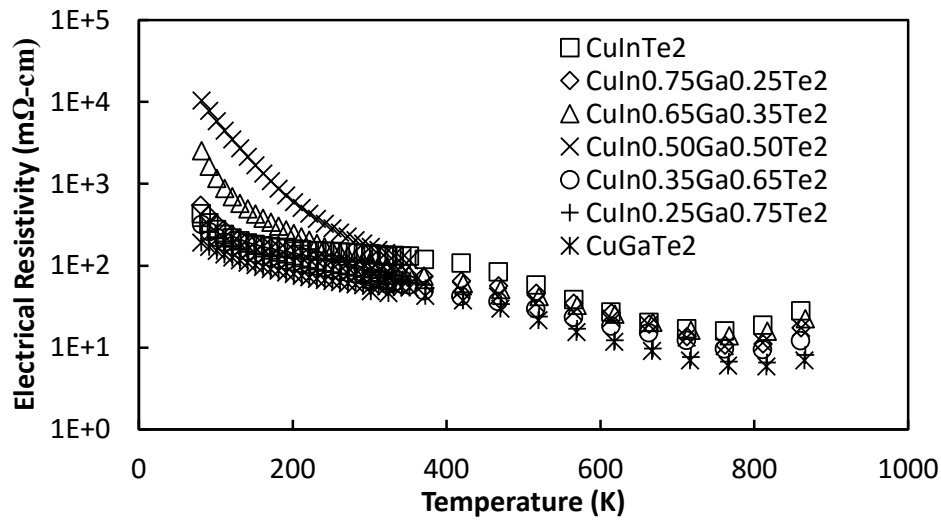


Figure 4.26: Electrical resistivity of the series  $\text{CuIn}_{1-x}\text{Ga}_x\text{Te}_2$  as a function of temperature.

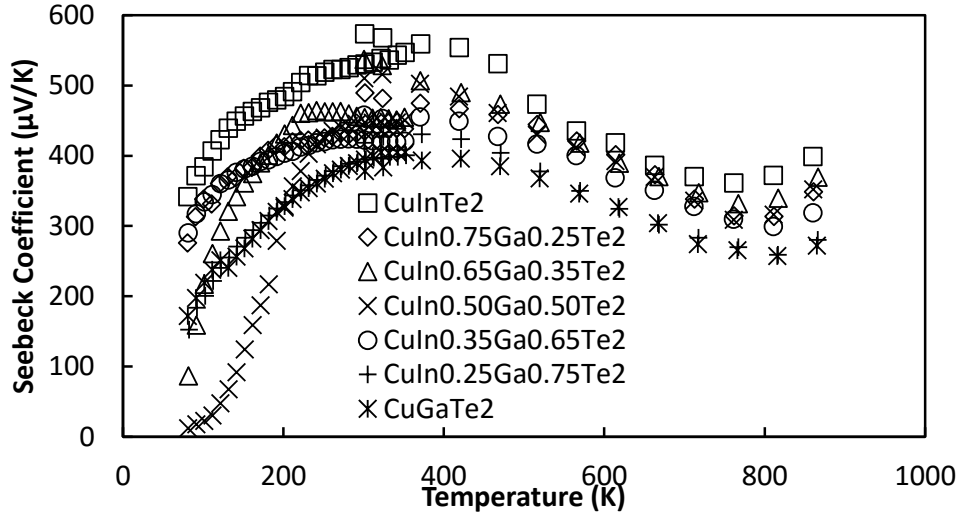


Figure 4.27: Seebeck coefficient of the series  $\text{CuIn}_{1-x}\text{Ga}_x\text{Te}_2$  as a function of temperature.

With the exception of  $\text{CuIn}_{0.5}\text{Ga}_{0.5}\text{Te}_2$ , which had the highest room temperature electrical resistivity, all of the other samples displayed a trend of decreasing electrical resistivity with increasing gallium concentration as shown in Figure 4.26. The samples also showed a decrease in Seebeck coefficient with increasing gallium concentration. As seen in Figure 4.28 this combination leads to a peak power factor in  $\text{CuGaTe}_2$  of nearly  $12 \mu\text{W cm}^{-1} \text{K}^{-2}$  at 766K, with values decreasing with increasing indium content down to  $\text{CuInTe}_2$ 's value of slightly over  $8 \mu\text{W cm}^{-1} \text{K}^{-2}$ .

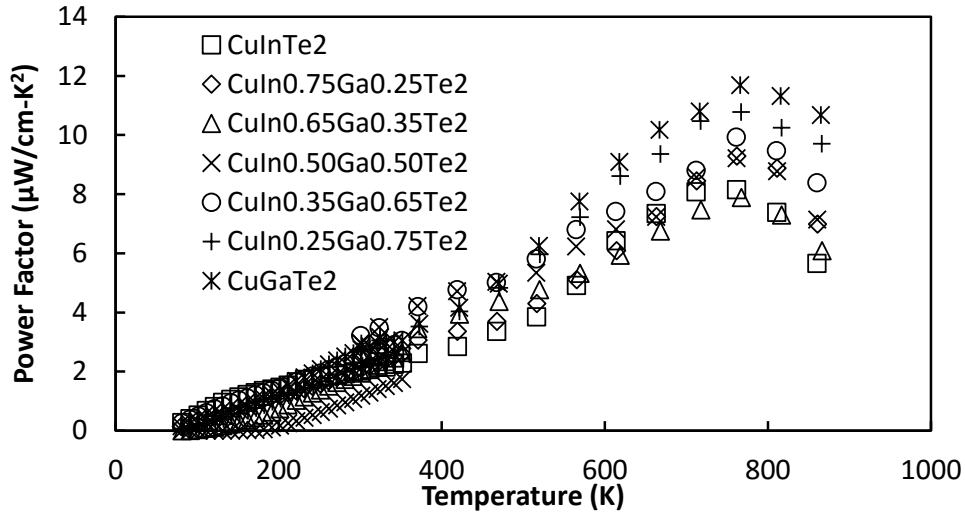


Figure 4.28: Power factor of the series  $\text{CuIn}_{1-x}\text{Ga}_x\text{Te}_2$  as a function of temperature.

The thermal conductivity measurements showed that the two end members of the compound have the highest values, as expected, with a roughly parabolic trend for the mixtures. The effect is more pronounced at lower temperatures, at 300K the thermal conductivity of  $\text{CuGaTe}_2$  is over twice that of  $\text{CuIn}_{0.5}\text{Ga}_{0.5}\text{Te}_2$ , while at high temperatures they are all less than  $1 \text{ W m}^{-1} \text{ K}^{-1}$ .

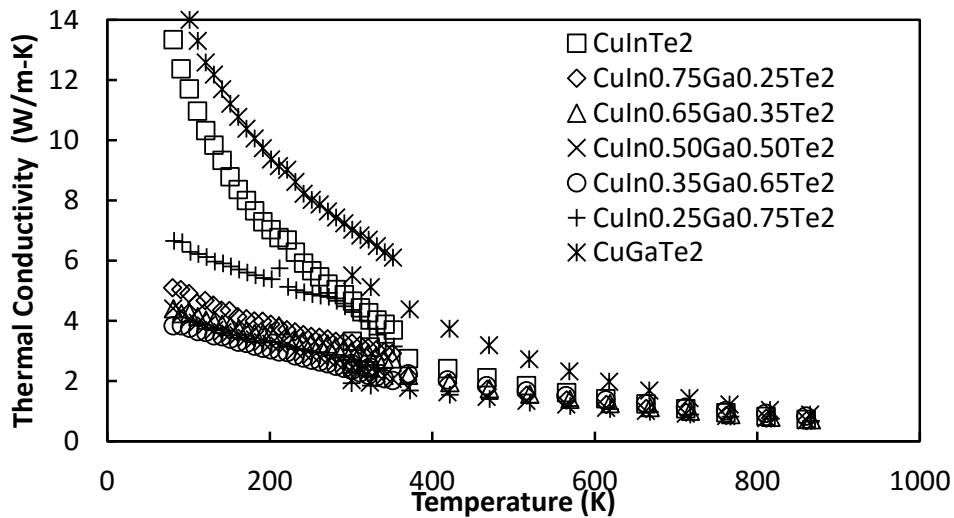


Figure 4.29: Thermal conductivity of the series  $\text{CuIn}_{1-x}\text{Ga}_x\text{Te}_2$  as a function of temperature.

Combining the power factor data and the thermal conductivity data to calculate  $ZT$ , Figure 4.30 shows that there is a general trend of increasing  $ZT$  with increasing gallium concentration, with the exception of  $\text{CuIn}_{0.25}\text{Ga}_{0.75}\text{Te}_2$  which is slightly higher than the pure gallium sample. Thus, a small amount of indium can lower the thermal conductivity enough to off set the reduction in the power factor, giving an increase in  $ZT$ .

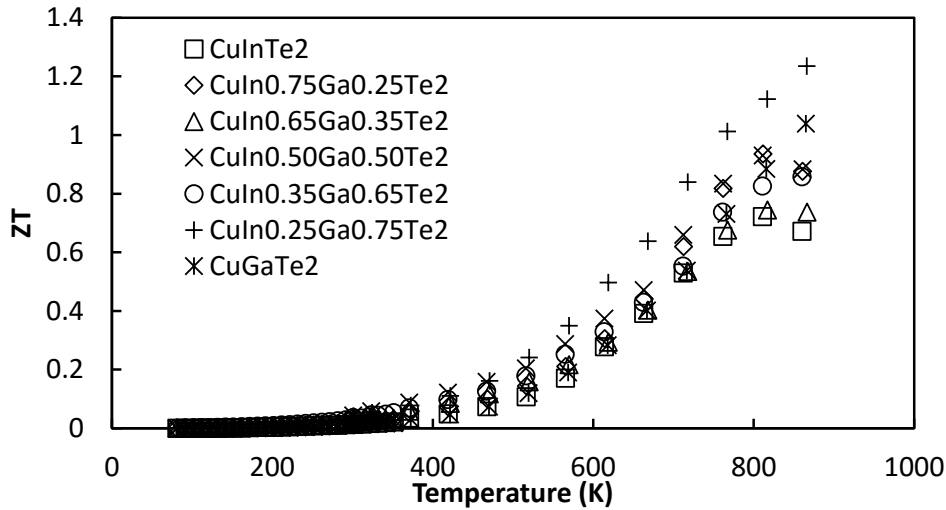


Figure 4.30:  $ZT$  of the series  $\text{CuIn}_{1-x}\text{Ga}_x\text{Te}_2$  as a function of temperature.

#### 4.5.2 $\text{Cu}(\text{In}_{1-x}\text{Ga}_x)_{0.99}\text{Zn}_{0.01}\text{Te}_2$

Following the previous work, and with the increased  $ZT$  of both  $\text{CuInTe}_2$  and  $\text{CuGaTe}_2$  by the substitution of 1% zinc, the previous solid solution was repeated, but with 1% of the group III atoms replaced by zinc. Unlike in the undoped series, where all of the samples showed a Seebeck coefficient peaking around 300K and then dropping off, the samples with zinc start at a value near  $50\mu\text{V K}^{-1}$  at 80K and rise linearly in temperature across the whole range, never turning over, as shown in Figure 4.31. The electrical resistivity of the zinc doped samples increased with temperature, while the undoped samples decreased in resistivity as the temperature increased.

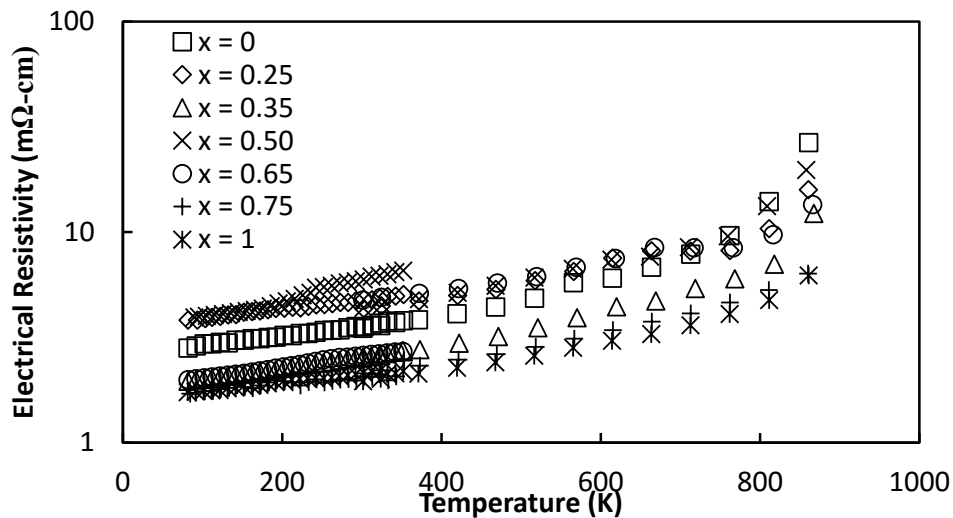


Figure 4.31: Electrical resistivity of the series  $\text{Cu}(\text{In}_{1-x}\text{Ga}_x)_{0.99}\text{Zn}_{0.01}\text{Te}_2$  as a function of temperature.

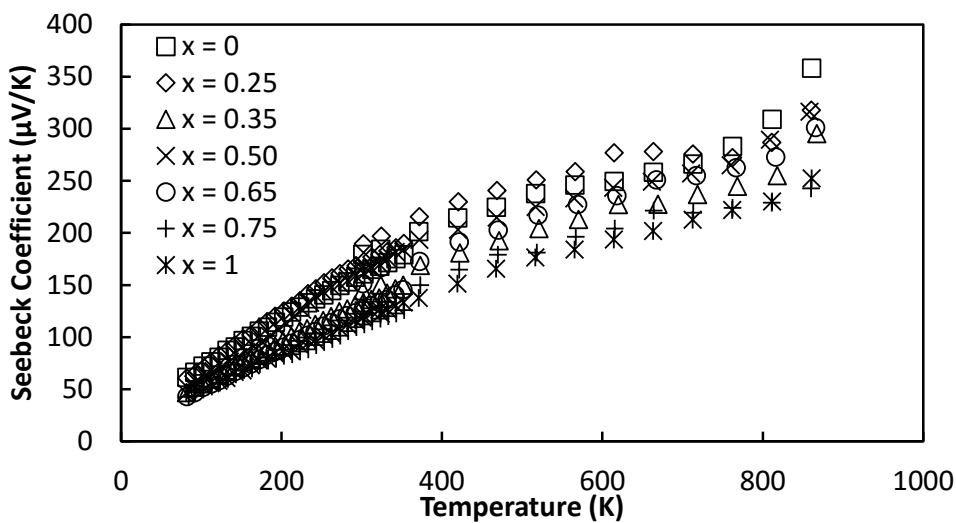


Figure 4.32: Seebeck coefficient of the series  $\text{Cu}(\text{In}_{1-x}\text{Ga}_x)_{0.99}\text{Zn}_{0.01}\text{Te}_2$  as a function of temperature.

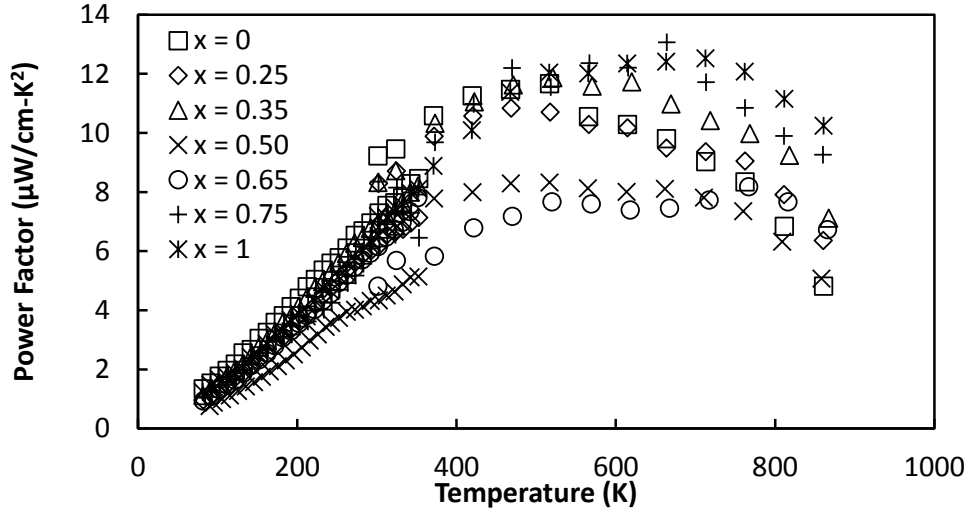


Figure 4.33: Power factor of the series  $\text{Cu}(\text{In}_{1-x}\text{Ga}_x)_{0.99}\text{Zn}_{0.01}\text{Te}_2$  as a function of temperature.

However, as we see in Figure 4.33, even with the decrease in Seebeck coefficient the zinc substitution leads to a broad peak in the power factor from 500-700K, rather than the sharp peak seen in Figure 4.28 for the undoped samples. The thermal conductivity shows the same trend as the undoped samples, and the values are nearly identical to the undoped as seen in Figure 4.34. This leads to  $ZT$  values that are above or equal to the undoped samples for each member in the series, as shown in refCuInTe2-CuGaTe2-ZN-ZT. As well as an increased peak  $ZT$ , the broad peaked power factor leads to an increased average  $ZT$ . And, again it was found that the sample with 25% indium and 75% gallium had the highest  $ZT$ .

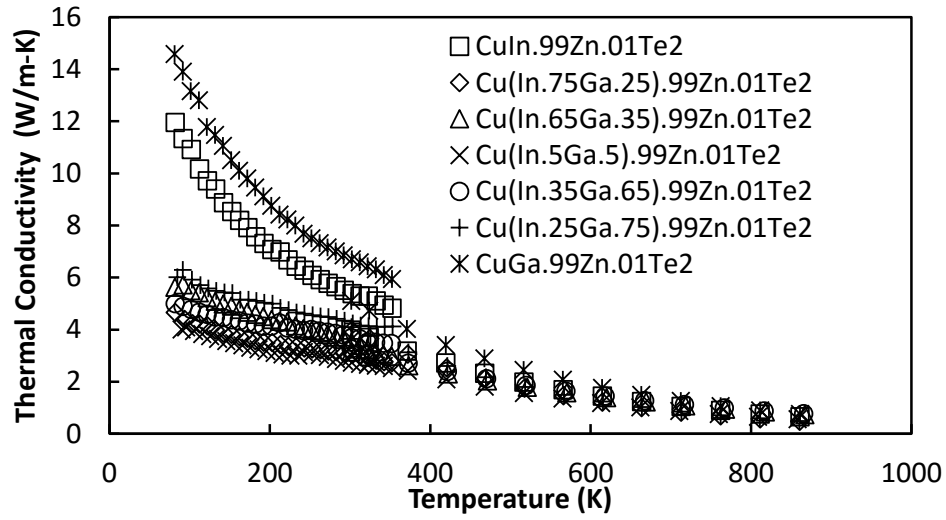


Figure 4.34: Thermal conductivity of the series  $\text{Cu}(\text{In}_{1-x}\text{Ga}_x)_{0.99}\text{Zn}_{0.01}\text{Te}_2$  as a function of temperature.

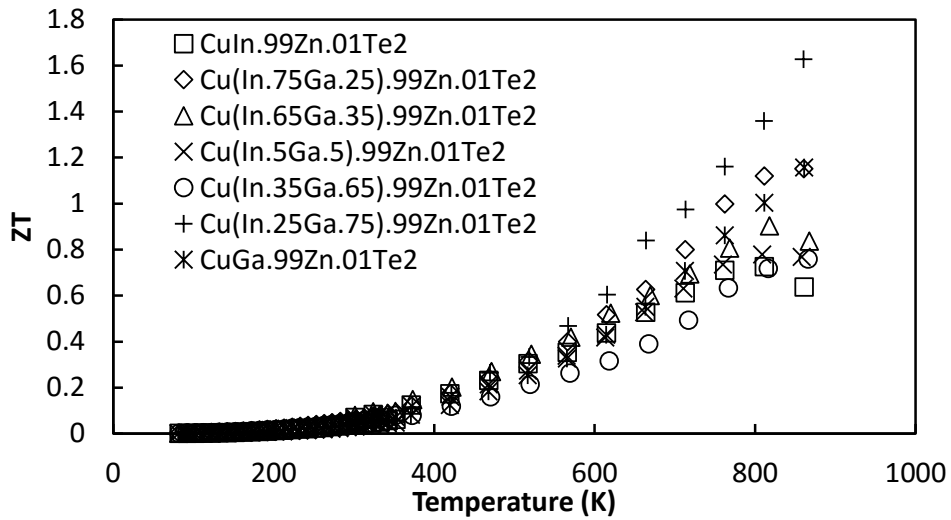


Figure 4.35:  $ZT$  of the series  $\text{Cu}(\text{In}_{1-x}\text{Ga}_x)_{0.99}\text{Zn}_{0.01}\text{Te}_2$  as a function of temperature.

### 4.5.3 $\text{CuInTe}_{2(1-x)}\text{S}_{2x}$

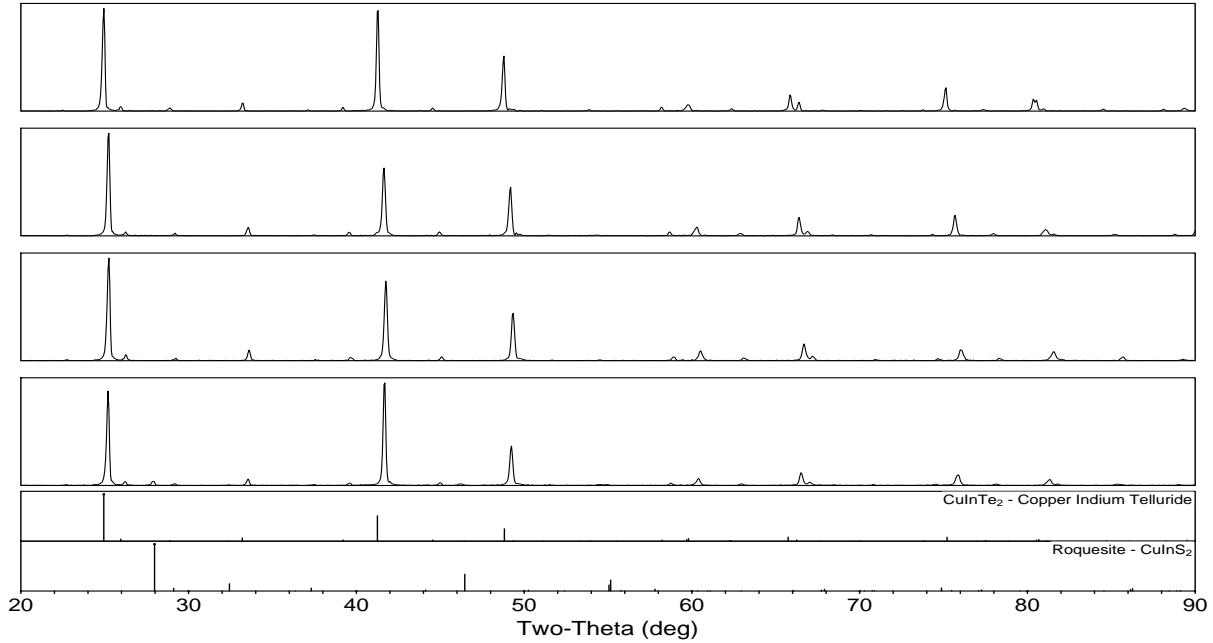


Figure 4.36: XRD pattern of  $\text{CuInTe}_{2(1-x)}\text{S}_{2x}$  with PDF. The top pattern is  $\text{CuInTe}_2$ , followed by  $x = 0.005$ ,  $0.01$ , and  $0.015$ , at which point secondary peaks corresponding to  $\text{CuInS}_2$  were observed. Patterns are PDF #01-082-0450 and #01-075-0106 for  $\text{CuInTe}_2$  and  $\text{CuInS}_2$  respectively.[5, 10]

A full solid solution of  $\text{CuInTe}_2$  and  $\text{CuInS}_2$  was unable to be formed due to the large difference in ionic radii of the elements, so smaller concentrations of sulfur were substituted to ascertain the solubility limit. At 15% sulfur substitution secondary peaks were observed in the XRD patterns, as shown in Figure 4.36, corresponding to  $\text{CuInS}_2$  indicating a solubility limit had been reached. Samples with 5% and 10% sulfur were synthesized and measured. The samples showed a slight decrease in lattice parameters as expected from the smaller atomic radius of sulfur.

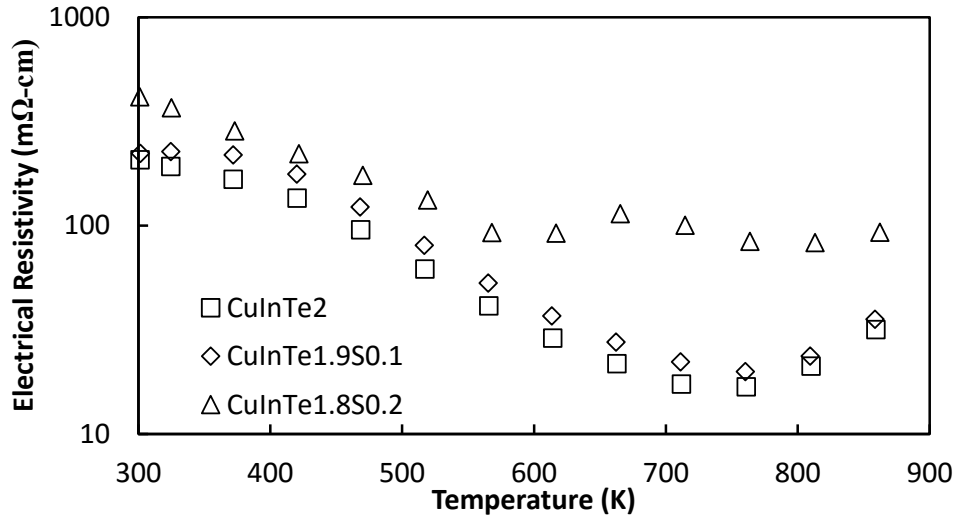


Figure 4.37: Electrical resistivity of the series  $\text{CuInTe}_{2(1-x)}\text{S}_{2x}$  as a function of temperature.

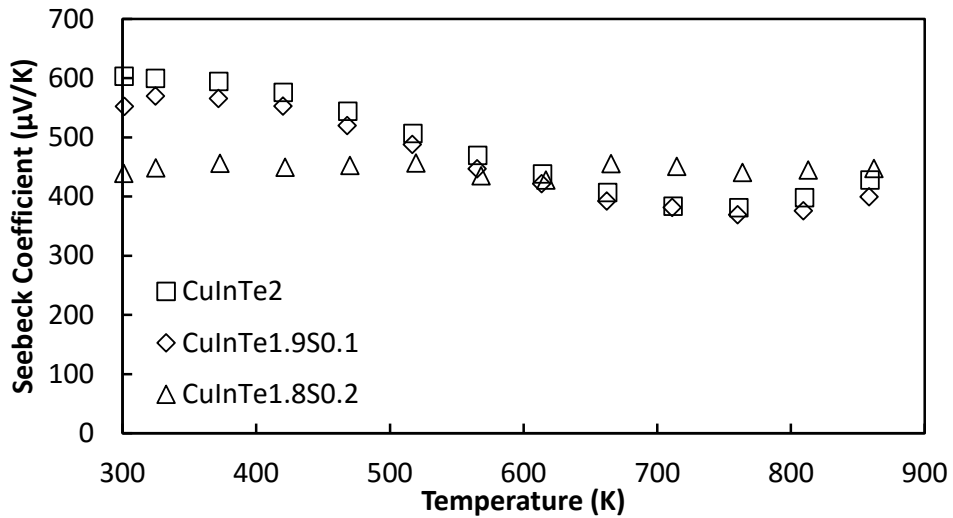


Figure 4.38: Seebeck coefficient of the series  $\text{CuInTe}_{2(1-x)}\text{S}_{2x}$  as a function of temperature.

The substitution of sulfur lead to an increase in electrical resistivity, but only a slight increase in the Seebeck coefficient at high temperature, leading to an overall decrease in power factor. The thermal conductivity decreased with sulfur content as expected, and the reduction was strong for a small even a 5% substitution, showing the strong effect of the large mass difference. However, as shown in Figure 4.40 even with the large decrease

in thermal conductivity the decrease in power factor was more detrimental.  $\text{CuInTe}_{1.9}\text{S}_{0.1}$  showed almost identical  $ZT$  values as the pure compound, while  $\text{CuInTe}_{1.8}\text{S}_{0.2}$  decreased by roughly a factor of 2 at high temperatures.

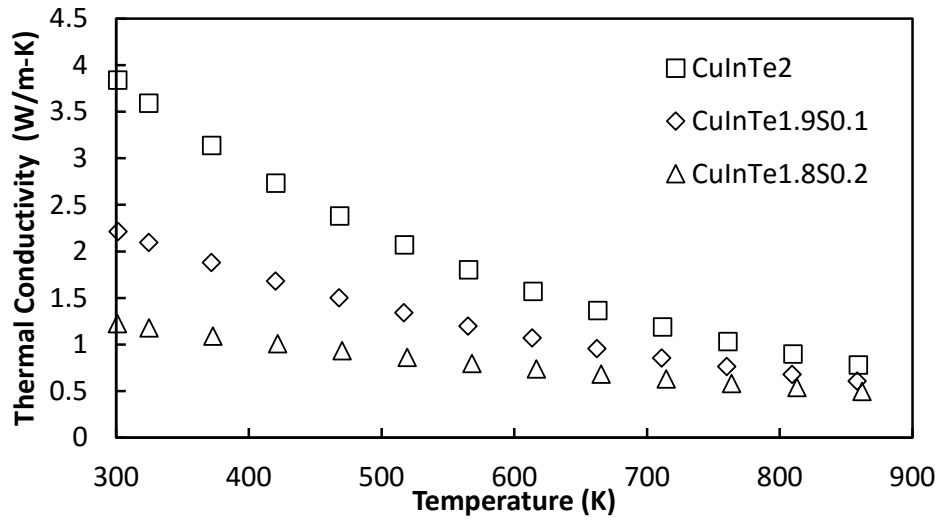


Figure 4.39: Thermal conductivity of the series  $\text{CuInTe}_{2(1-x)}\text{S}_{2x}$  as a function of temperature.

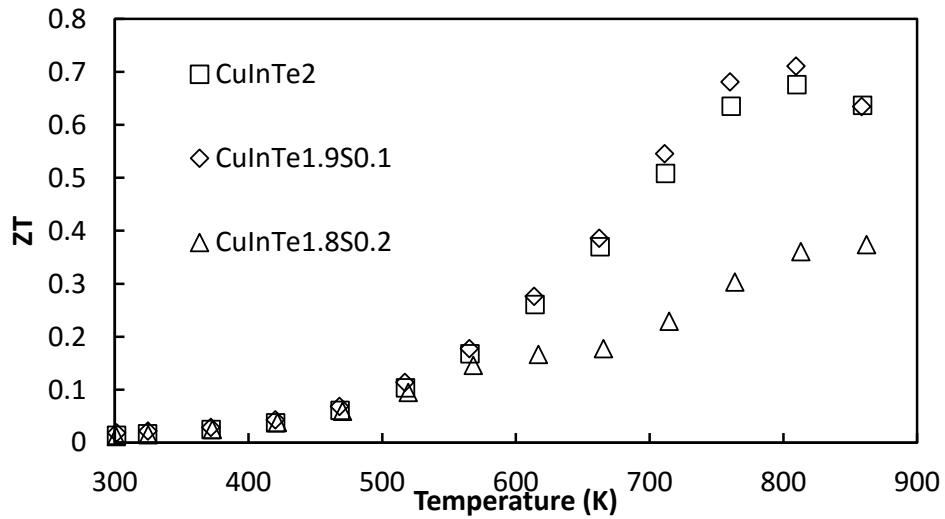


Figure 4.40:  $ZT$  of the series  $\text{CuInTe}_{2(1-x)}\text{S}_{2x}$  as a function of temperature.

## 4.6 Conclusions

In this chapter compounds of  $\text{CuGaTe}_2$ ,  $\text{CuInTe}_2$ ,  $\text{CuAlTe}_2$  and a full solid solution of the indium/gallium compounds were synthesized.  $\text{CuInTe}_2$  has both a higher electrical resistivity and Seebeck coefficient than  $\text{CuGaTe}_2$ , but a lower power factor. This trend is consistent across the solid solution, allowing for optimization by substitution. The thermal conductivity of  $\text{CuGaTe}_2$  is higher than that of  $\text{CuInTe}_2$ , and the solid solution followed the typical parabolic form of a mixture. All of the samples in the solid solution were found to have a thermal conductivity less than  $1 \text{ W m}^{-1} \text{ K}^{-1}$  above 700K due to the strong effect of Umklapp scattering at high temperatures. Finally, zinc was found to be an effective p-type dopant for both compounds, increasing the room temperature carrier concentrations from  $5.6 \times 10^{17} \text{ cm}^{-3}$  to  $3.4 \times 10^{19} \text{ cm}^{-3}$  for  $\text{CuInTe}_2$  and from  $1.4 \times 10^{18} \text{ cm}^{-3}$  to  $6.24 \times 10^{19} \text{ cm}^{-3}$  for  $\text{CuInTe}_2$  with a substitution of 1% zinc for the group III element. Several attempts were made to synthesize an n-type sample of  $\text{CuGaTe}_2$ , but none were successful.

With an optimized indium/gallium ratio as well as zinc doping,  $ZT$  values close to 1.6 were achieved, the highest reported for chalcopyrite compounds.

# Chapter 5

## Selenides

### 5.1 Family Overview

The selenide family of copper based chalcopyrite compounds contains  $\text{CuAlSe}_2$ ,  $\text{CuGaSe}_2$ , and  $\text{CuInSe}_2$ .  $\text{CuAlSe}_2$  was not studied here due to both the difficulty in synthesizing it and due to the large (2.71 eV) band gap.[104]  $\text{CuFeSe}_2$ , a naturally occurring mineral known as eskebornite, exists however it does not form in the chalcopyrite structure, and so was also not studied here.[105, 106]

Synthesis of these compounds was carried similar to the tellurium compounds, with the exception that the heating rate in the furnace was lowered from  $1.0^\circ\text{C min}^{-1}$  to  $0.4^\circ\text{C min}^{-1}$  to account for the volatility of selenium. All the samples in the family were again found to be p-type, but with noticeably higher electrical resistivity than the tellurium based samples.

## 5.2 CuInSe<sub>2</sub>

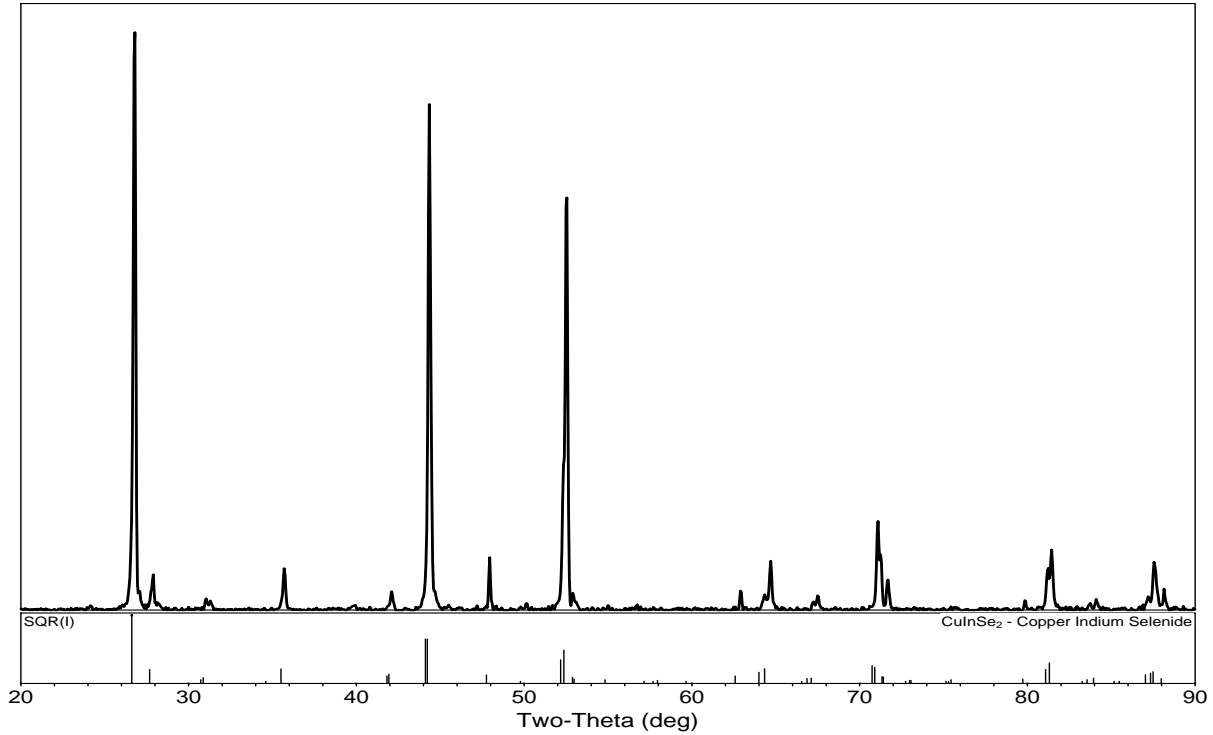


Figure 5.1: XRD pattern of CuInSe<sub>2</sub> with PDF. The y-scale is intensity, in arbitrary units. The pattern is PDF #01-075-2916. [11]

As Figure 5.1 shows, the sample synthesized was found to be single phase. The obtained lattice parameters showed good agreement with literature values, with values of  $a$  ranging from 5.77 Å to 5.78 Å,  $c$  from 11.54 Å to 11.63 Å, and the values obtained here of 5.79 Å and 11.51 Å for  $a$  and  $c$  respectively.[14, 4, 11]

CuInSe<sub>2</sub> has a reported band gap of 0.98 to 1.04eV [107, 108, 109], comparable to that of CuInTe<sub>2</sub>. Nevertheless, the samples were found to be highly resistive compared to the telluride counterpart. Undoped samples had a room temperature electrical resistivity of  $1 \times 10^4$  mΩ cm, versus  $1.4 \times 10^2$  mΩ cm for CuInTe<sub>2</sub>, and in fact could not be measured at higher temperatures in the ZEM3 due to their high resistance.

### 5.2.1 Electronic Doping

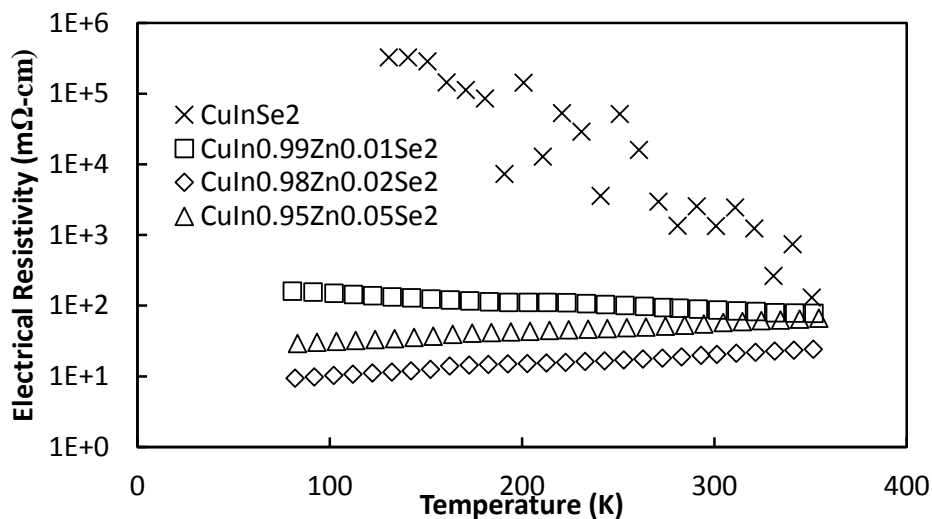


Figure 5.2: Electrical resistivity of the series  $\text{CuIn}_{1-y}\text{Zn}_y\text{Se}_2$  versus temperature. The data for  $\text{CuInSe}_2$  shows a large amount of fluctuation due to the large sample resistance and the difficulty in making good electrical contact to the sample.

As with  $\text{CuInTe}_2$ , initial doping to optimize electronic properties was carried out using zinc as a p-type dopant, in substitution for indium. Samples were made with 1%, 2%, and 5% zinc and did indeed exhibit a clear doping effect, with greatly decreased values of electrical resistivity, as shown in Figure 5.2.

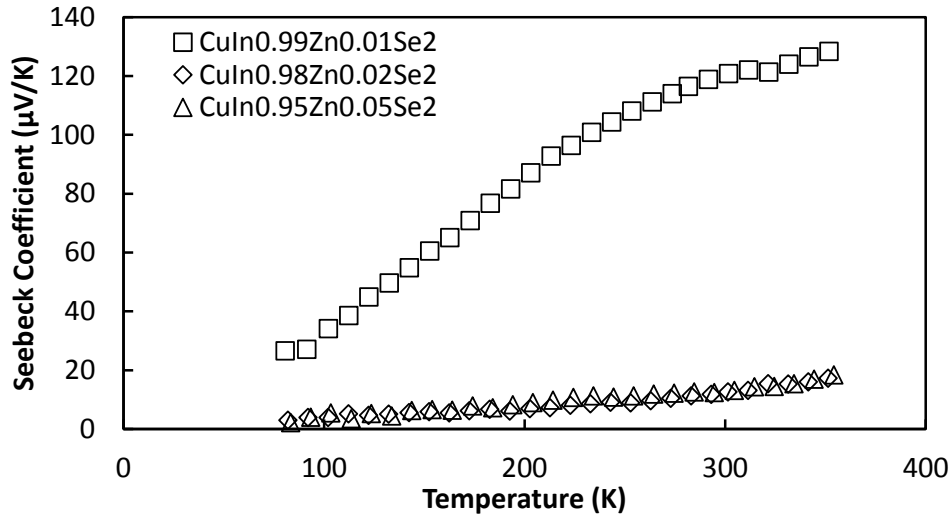


Figure 5.3: Seebeck coefficient of the series  $\text{CuIn}_{1-y}\text{Zn}_y\text{Se}_2$  as a function of temperature.

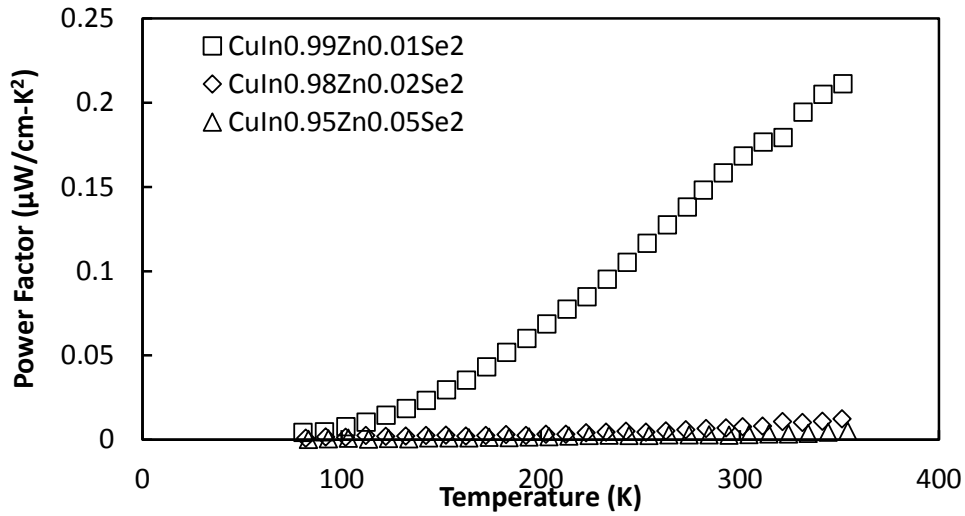


Figure 5.4: Power factor of the series  $\text{CuIn}_{1-y}\text{Zn}_y\text{Se}_2$  as a function of temperature.

While the samples with 2% and 5% zinc had lower electrical resistivity than the 1%, they also showed much lower Seebeck coefficient values and as a result a much lower power factor. The Seebeck coefficient data for undoped  $\text{CuInSe}_2$  is not shown; due to the large resistivity of the sample the Seebeck coefficient values were difficult to accurately measure on our equipment. The thermal conductivity was comparable to that of  $\text{CuInTe}_2$ , with room

temperature values of approximately  $3-4\text{W m}^{-1}\text{K}^{-1}$  for sample regardless of the doping level. Overall, the  $ZT$  for  $\text{CuInSe}_2$ , even for the best zinc doped sample, was less than 0.002 at 300K.

### 5.3 $\text{CuGaSe}_2$

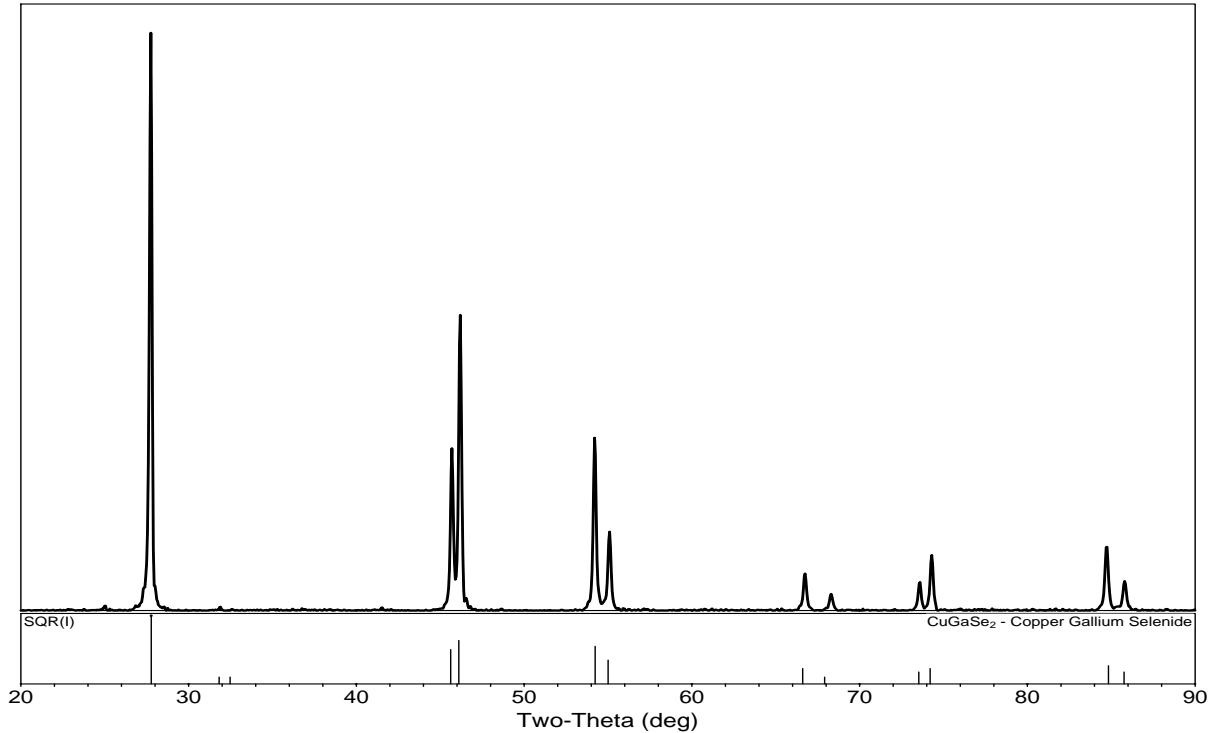


Figure 5.5: X-ray diffraction pattern for  $\text{CuGaSe}_2$  with PDF overlay. The y-scale is intensity, in arbitrary units. The pattern is PDF #01-075-2916. [12]

Unlike the case of  $\text{CuInTe}_2$  and  $\text{CuInSe}_2$ , the band gap of  $\text{CuGaSe}_2$  is larger than that of  $\text{CuGaTe}_2$ , as is the usual trend in diamond like semiconductors when replacing an element with another from a row above.[14] The reported band gap of  $\text{CuGaSe}_2$  ranges from to 1.6 eV to 1.7 eV, which is larger than typical for conventional thermoelectric materials. [109, 110, 111] Samples were synthesized despite that in order to better understand the

underlying physics of the chalcopyrite compounds.

As was the case for CuInSe<sub>2</sub>, CuGaSe<sub>2</sub> exhibited high electrical resistivity, not unexpected due to the large band gap, with electrical resistivity values starting at  $1 \times 10^4$  m $\Omega$  cm at 80K and dropping to  $2.5 \times 10^3$  m $\Omega$  cm at 300K. Previous studies on the hole mobility of CuGaSe<sub>2</sub> also showed the values to be quite low, in the range of 10-20 cm<sup>2</sup> V<sup>-1</sup> s<sup>-1</sup> at room temperature as compared to values near 100 for CuGaTe<sub>2</sub>.<sup>[112]</sup> The Seebeck coefficient was difficult to measure, and fluctuated from positive to negative, not reaching a value larger than 10  $\mu$ V K<sup>-1</sup> in magnitude until 300K. Together, this yielded a power factor that peaked at 820K with a value of 0.8  $\mu$ W cm<sup>-1</sup> K<sup>-2</sup>, more than an order of magnitude less than that of CuGaTe<sub>2</sub>.

### 5.3.1 Electronic Doping

Further samples were made using zinc as a dopant atom with the composition CuGa<sub>1-x</sub>Zn<sub>x</sub>Se<sub>2</sub> and  $x = 0.01, 0.02, 0.03,$  and  $0.05$ . As seen in Figure 5.6 the zinc doped samples displayed much lower electrical resistivity, with room temperature values in the range of 10s of m $\Omega$  cm, an order of magnitude less than the undoped CuGaSe<sub>2</sub>. As Figure 5.6 shows, at high temperature the samples all had similar values, on the order of 100s of m $\Omega$  cm.

The Seebeck coefficient for all of the doped samples was lower than than of the undoped sample, as shown in Figure 5.7. While the thermopower of the undoped composition was less than 50  $\mu$ V K<sup>-1</sup> until 320K, the value rose rapidly after this to level off at a value near 500  $\mu$ V K<sup>-1</sup> at 600K. However, the doped samples maintained low values over a much greater range, with 1% and 2% Zn samples showing nearly identical values until 750K.

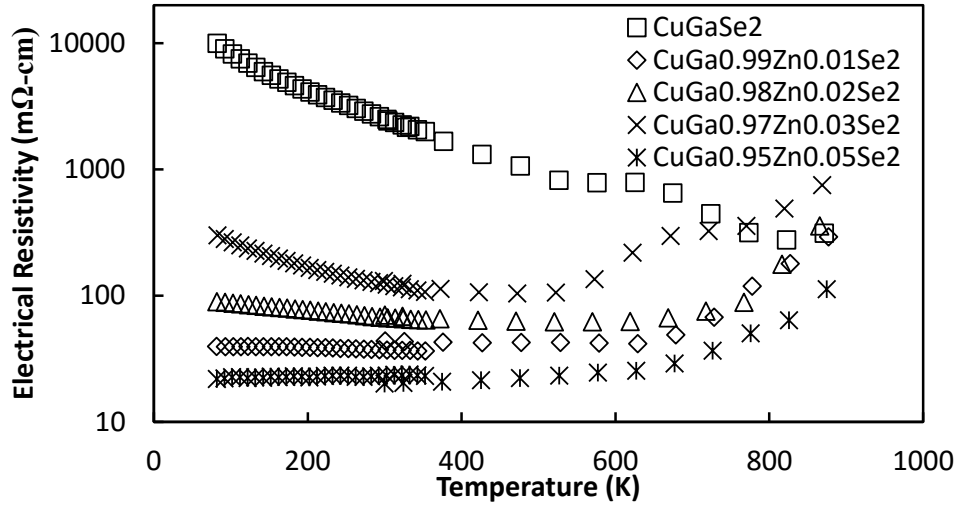


Figure 5.6: Electrical resistivity of the series  $\text{CuGa}_{1-x}\text{Zn}_x\text{Se}_2$  as a function of temperature.

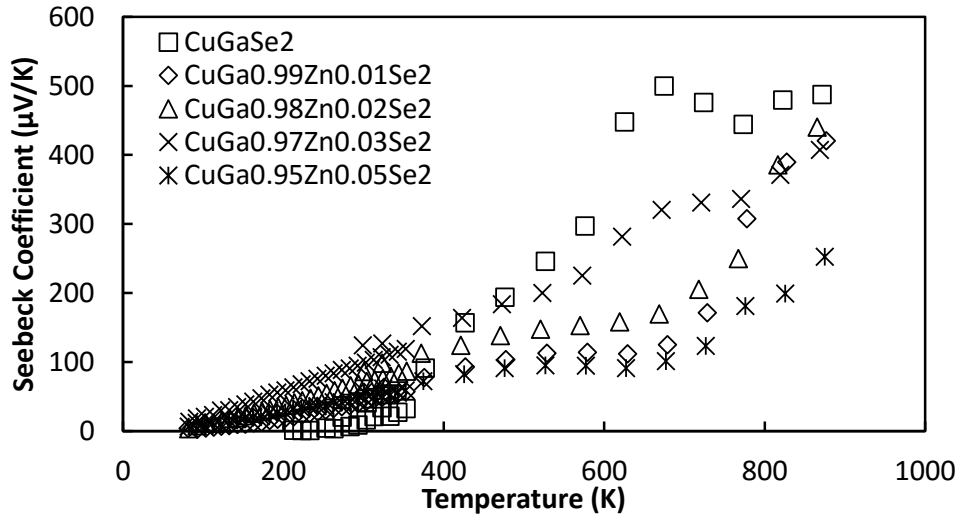


Figure 5.7: Seebeck coefficient of the series  $\text{CuGa}_{1-x}\text{Zn}_x\text{Se}_2$  as a function of temperature.

As seen in Figure 5.8 the power factor below 600K increases with increasing zinc concentration, with  $\text{CuGa}_{0.95}\text{Zn}_{0.05}\text{Se}_2$  showing the highest value below 600K. However, above this point the power factor of the undoped sample began to rapidly rise just as the Seebeck coefficient did. For the zinc doped samples, the power factor was less consistent. The 3% zinc sample had the highest electrical resistivity at 860 K, even higher than the undoped

sample, and as such showed the lowest power factor. However, the 1% and 2% zinc doped samples showed similar values to the undoped sample at 800K, with 5% zinc exhibiting a slightly lower value, and the 3% sample the highest value of all.

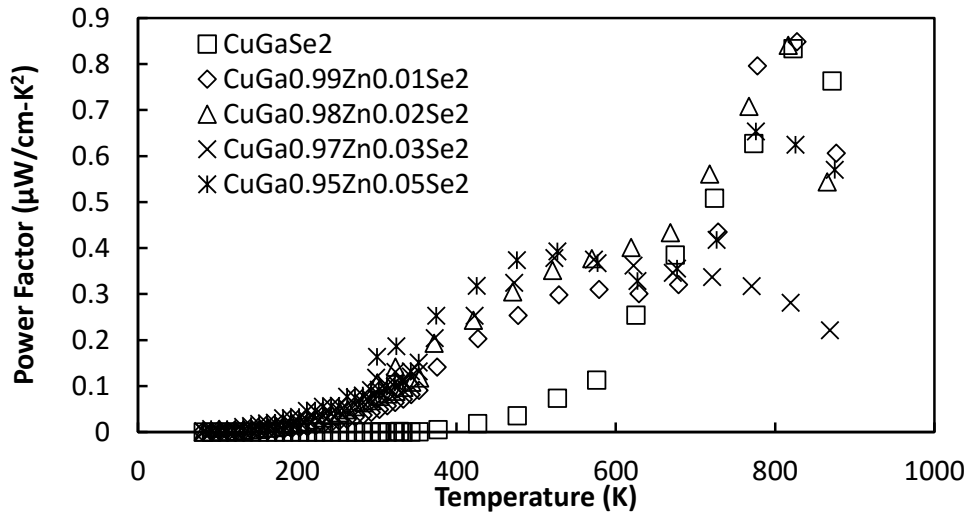


Figure 5.8: Power factor of the series  $\text{CuGa}_{1-x}\text{Zn}_x\text{Se}_2$  as a function of temperature.

The thermal conductivity for all samples was very similar, as expected. At 80K the values varied from  $5 - 8 \text{ W m}^{-1} \text{ K}^{-1}$ , likely due to small differences in defects, but at high temperatures the values were all within a small margin of each other, as shown in Figure 5.9

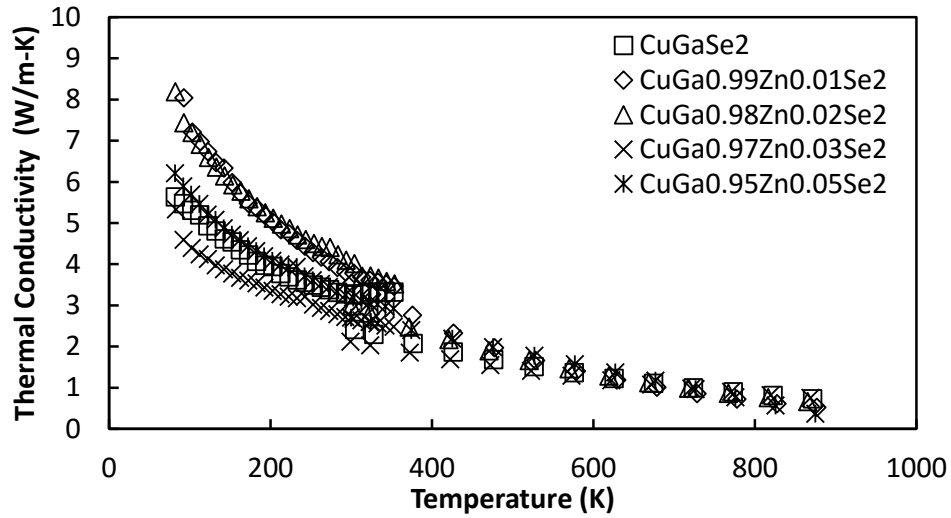


Figure 5.9: Thermal conductivity of the series  $\text{CuGa}_{1-x}\text{Zn}_x\text{Se}_2$  as a function of temperature.

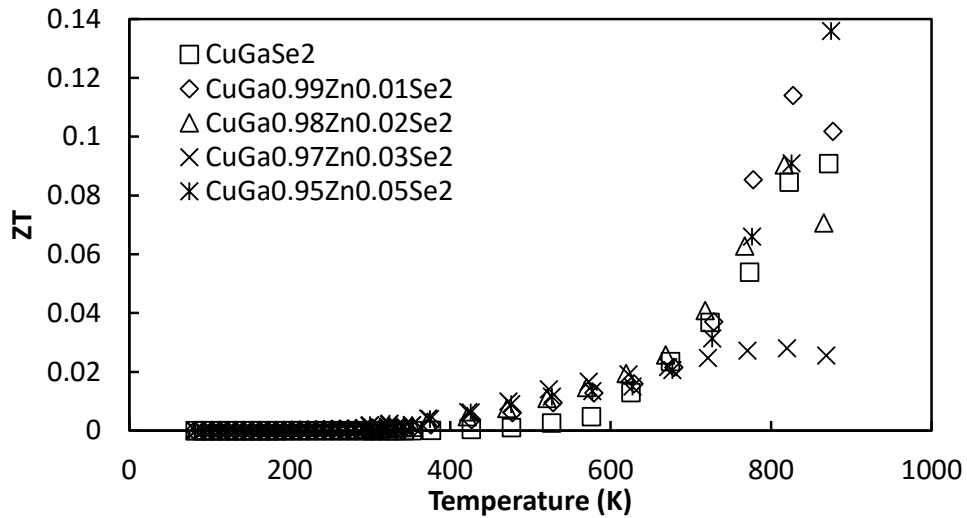


Figure 5.10:  $ZT$  of the series  $\text{CuGa}_{1-x}\text{Zn}_x\text{Se}_2$  as a function of temperature.

Ultimately the  $ZT$  values for pure, and zinc doped,  $\text{CuGaSe}_2$  were quite low. The heaviest doped sample showed the highest  $ZT$  value at 0.14, roughly an order of magnitude lower than that of the tellurium based sample, primarily due to the large values of electrical resistivity.

## 5.4 Solid Solutions

Full solid solutions of both  $\text{CuGaTe}_{2(1-x)}\text{Se}_{2x}$  and  $\text{CuInTe}_{2(1-x)}\text{Se}_{2x}$  were able to be formed, and their properties were measured. The gallium-based solid solution was densified using SPS, while the indium-based series was made twice; once using the hotpress to densify the samples, and then again using the SPS for comparison.

### 5.4.1 $\text{CuIn}_{0.99}\text{Zn}_{0.01}\text{Te}_{2(1-x)}\text{Se}_{2x}$ - Hotpressed

Initial samples of  $\text{CuInSe}_2$  were found to have high electrical resistance, so the solid solution was made with a 1% substitution of zinc on the indium site across the whole range, as was done in the solid solution of  $\text{CuIn}_{1-x}\text{Ga}_x\text{Te}_2$ .

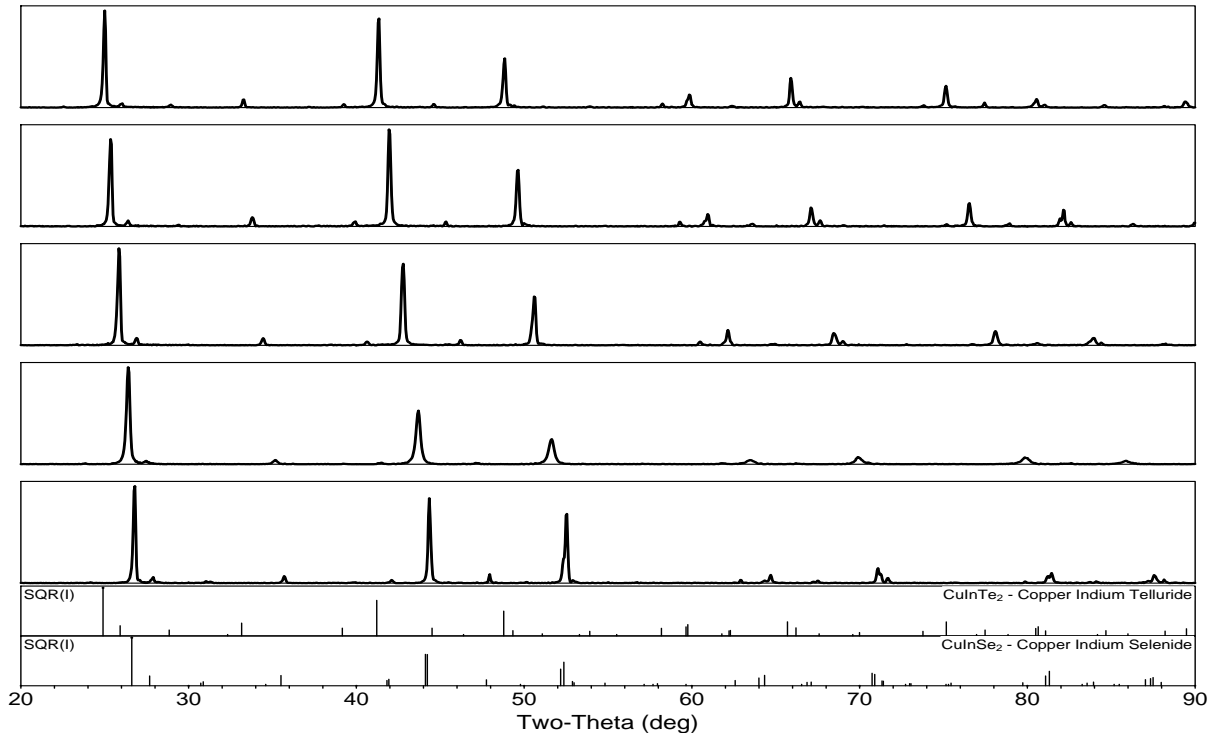


Figure 5.11: XRD patterns of the solid solution  $\text{CuIn}_{0.99}\text{Zn}_{0.01}\text{Te}_{2(1-x)}\text{Se}_{2x}$  with PDFs. The top pattern is for  $\text{CuIn}_{0.99}\text{Zn}_{0.01}\text{Te}_2$ , with each pattern showing substitutions in 25% increments. The y-scale is intensity, in arbitrary units. The patterns are PDF #01-082-0450 and #01-075-2916 for Te and Se respectively. [13, 11]

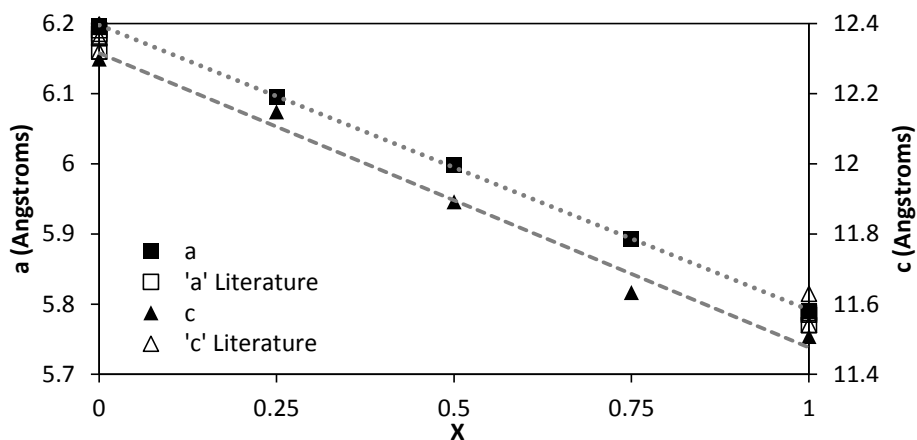


Figure 5.12: Lattice parameters of the solid solution  $\text{CuIn}_{0.99}\text{Zn}_{0.01}\text{Te}_{2(1-x)}\text{Se}_{2x}$  with literature values shown in open symbols. The dashed lines are to guide the eyes.[4, 14, 13, 6, 15, 8]

As shown in Figure 5.11 and Figure 5.12 there was a systematic shift of the peaks towards larger two-theta as selenium was substituted for tellurium, indicating a decrease in lattice parameters as expected from the smaller ionic radius of selenium. Viewing the lattice parameters as a function of selenium concentration in Figure 5.12 there was a clear linear trend in agreement with Vegard's law.[113]

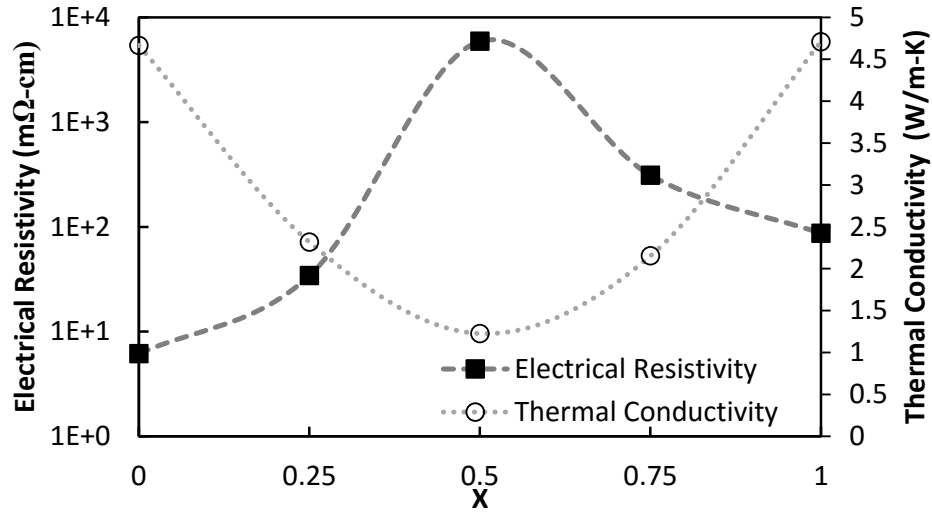


Figure 5.13: Thermal conductivity and electrical resistivity of  $\text{CuIn}_{0.99}\text{Zn}_{0.01}\text{Te}_{2(1-x)}\text{Se}_{2x}$  at 300K. Both show a strong dependence on selenium concentration.

As selenium was substituted for tellurium a parabolic trend was observed in the thermal conductivity with respect to composition as was expected.[57] This gave a minimum in the thermal conductivity at the composition  $\text{CuInTeSe}$  as shown in Figure 5.13. Similarly the electrical resistivity increases with selenium concentration until the halfway point, and then decreases again.

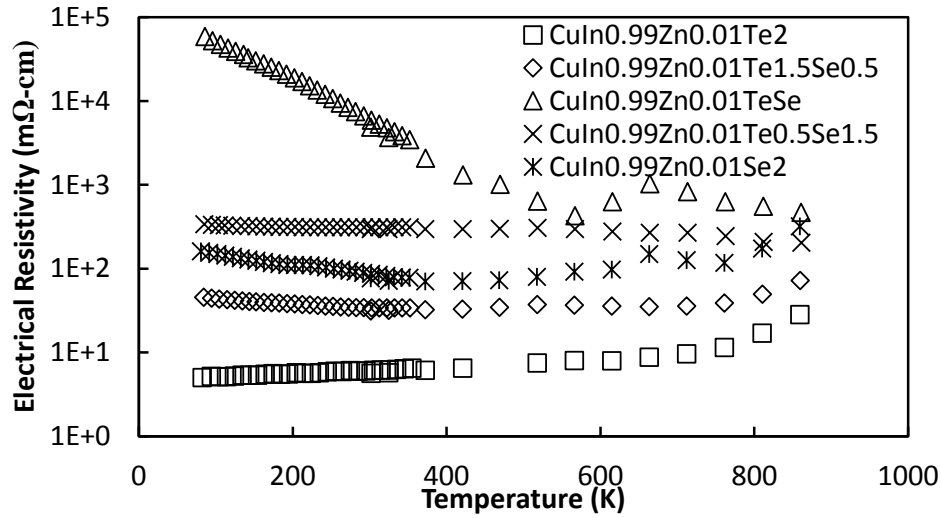


Figure 5.14: Electrical resistivity of the series  $\text{CuIn}_{0.99}\text{Zn}_{0.01}\text{Te}_{2(1-x)}\text{Se}_{2x}$  as a function of temperature, showing the strong dependence on selenium concentration.

However, unlike the thermal conductivity which decreased by a factor of roughly three at room temperature, the electrical resistivity increased by nearly three orders of magnitude. This indicates that the defects in the lattice disrupt the hole transport much more than the phonon transport. Both trends are present, but less dramatic, at high temperatures as shown in Figure 5.14 and Figure 5.15.

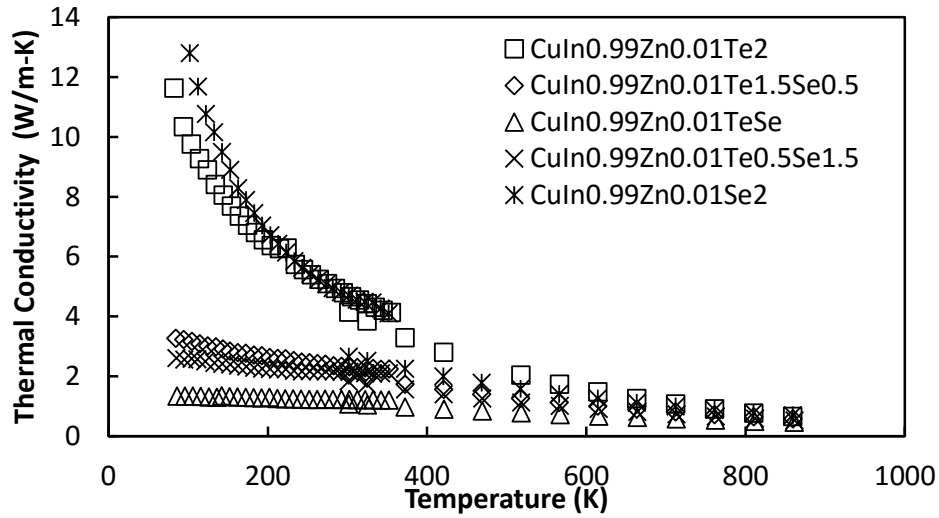


Figure 5.15: Thermal conductivity of the series  $\text{CuIn}_{0.99}\text{Zn}_{0.01}\text{Te}_{2(1-x)}\text{Se}_{2x}$  as a function of temperature, showing the strong dependence on selenium concentration

The trend in the Seebeck coefficient was less clear, as shown in Figure 5.16, with  $x = 0.25$  sample ( $\text{CuIn}_{0.99}\text{Te}_{1.5}\text{Se}_{0.5}$ ) displaying a much lower Seebeck coefficient than the other samples across the whole temperature range, and the  $x = 0.50$  ( $\text{CuIn}_{0.99}\text{Te}_1\text{Se}_1$ ) sample rising quite steeply to surpass all the other samples from 400K to 800K.

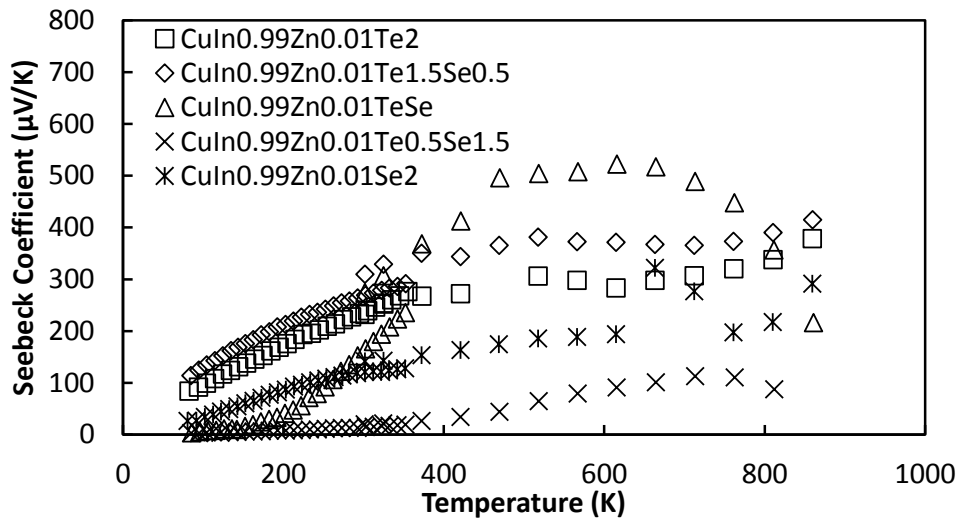


Figure 5.16: Seebeck coefficient of the series  $\text{CuIn}_{0.99}\text{Zn}_{0.01}\text{Te}_{2(1-x)}\text{Se}_{2x}$  as a function of temperature.

Overall, the power factor decreased dramatically with any amount of selenium substitution. The pure tellurium sample reached a value near  $12 \mu\text{W cm}^{-1} \text{K}^{-2}$ , but it dropped by a factor of 3 with 25% selenium substitution, and all of the other samples peaked at a value less than  $1 \mu\text{W cm}^{-1} \text{K}^{-2}$ , as seen in Figure 5.17. Ultimately a decrease in  $ZT$  was found for all samples with the substitution of selenium as compared to  $\text{CuIn}_{0.99}\text{Zn}_{0.01}\text{Te}_2$ .

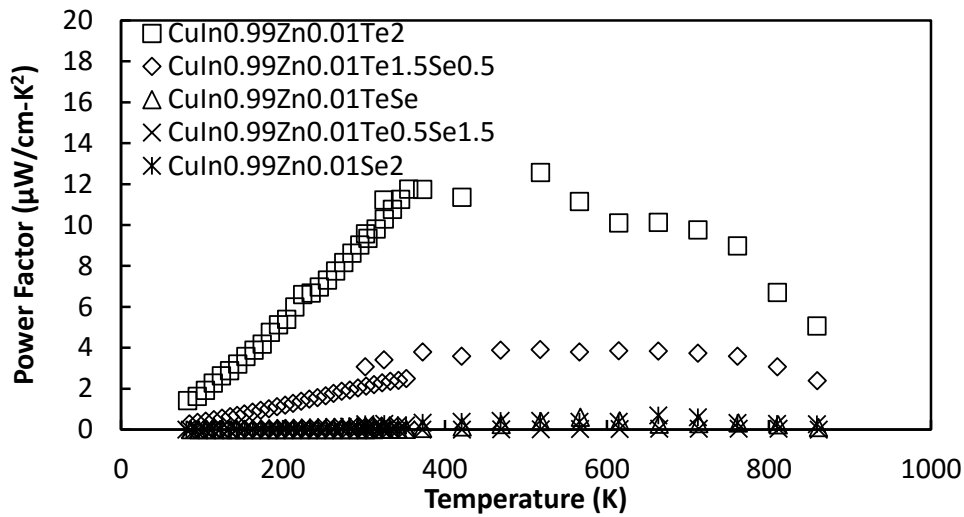


Figure 5.17: Power factor of the series  $\text{CuIn}_{0.99}\text{Zn}_{0.01}\text{Te}_{2(1-x)}\text{Se}_{2x}$  as a function of temperature.

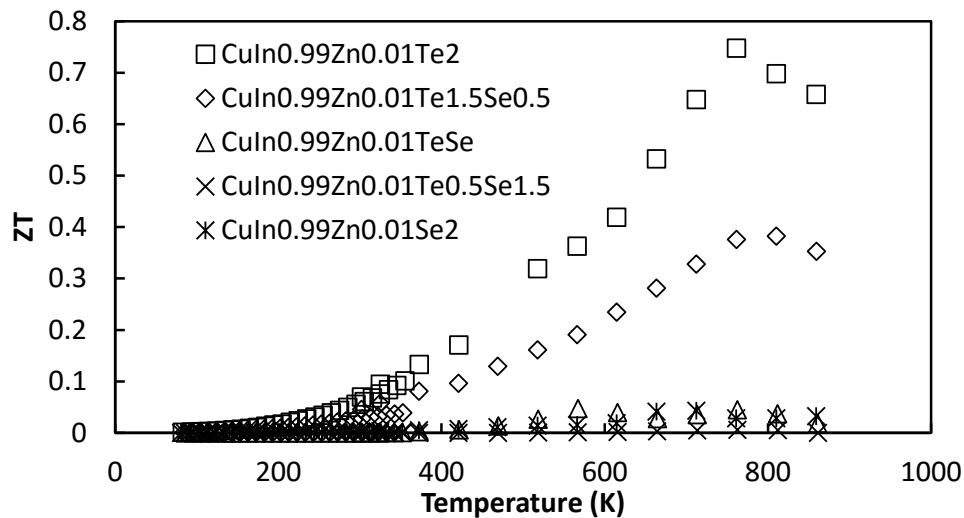


Figure 5.18:  $ZT$  of the series  $\text{CuIn}_{0.99}\text{Zn}_{0.01}\text{Te}_{2(1-x)}\text{Se}_{2x}$  as a function of temperature.

## 5.4.2 $\text{CuInTe}_{2(1-x)}\text{Se}_{2x}$ - Spark Plasma Sintered

Following the solid solution of  $\text{CuIn}_{0.99}\text{Zn}_{0.01}\text{Te}_{2(1-x)}\text{Se}_{2x}$ , the series was made again without the addition of zinc, and densified using the SPS. This was done to address concerns of variability in the density of the hotpressed samples. The samples made with the hotpress had densities of 93% - 99%, while the samples synthesized with the SPS were all greater than 98% theoretical density.

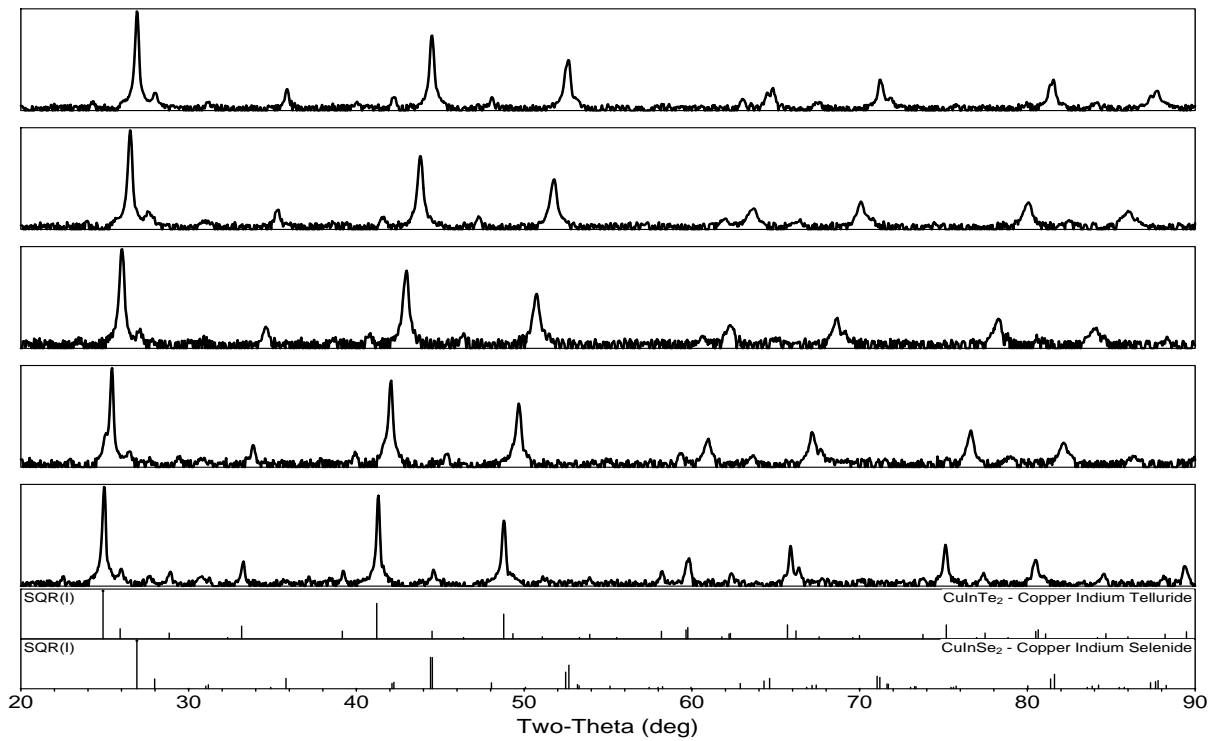


Figure 5.19: XRD patterns for the solid solution  $\text{CuInTe}_{2(1-x)}\text{Se}_{2x}$  densified via SPS with PDFs. The bottom pattern is for  $\text{CuInTe}_2$ , with each subsequent pattern showing substitutions in 25% increments. The y-scale is intensity, in arbitrary units. PDFs are #01-082-0450 and #01-075-2916 for Te and Se respectively. [13, 11]

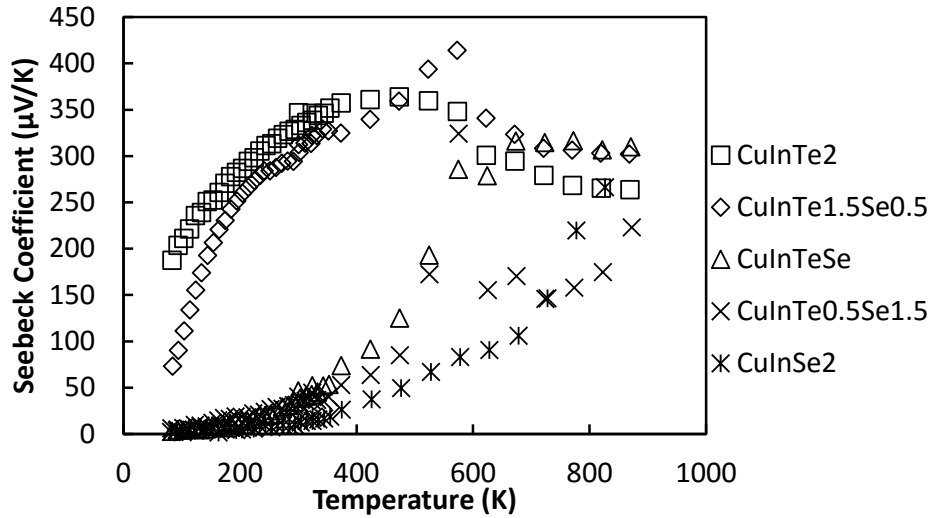


Figure 5.20: Seebeck coefficient of the series  $\text{CuInTe}_{2(1-x)}\text{Se}_{2x}$  as a function of temperature.

As shown in Figure 5.20, the  $x = 0$  ( $\text{CuInTe}_2$ ) and  $x = 0.25$  ( $\text{CuInTe}_{1.5}\text{Se}_{0.5}$ ) sample had Seebeck coefficients comparable to that of the zinc-doped and hotpressed samples in Figure 5.16. Both plots showed values starting around  $100 \mu\text{V K}^{-1}$  and then rising to level out around  $300\text{-}400 \mu\text{V K}^{-1}$ . The hot pressed  $x = 0$  and  $x = 0.25$  showed a slight up-tick above  $600\text{K}$  while the SPS densified samples did not. Also, shown in Figure 5.20, there was a very sharp peak for  $x = 0.25, 0.50,$  and  $0.75$  near  $600\text{K}$ . The drop in Seebeck coefficient for samples with  $x > 0.25$  was much more pronounced in the SPS samples than in the hotpressed samples.

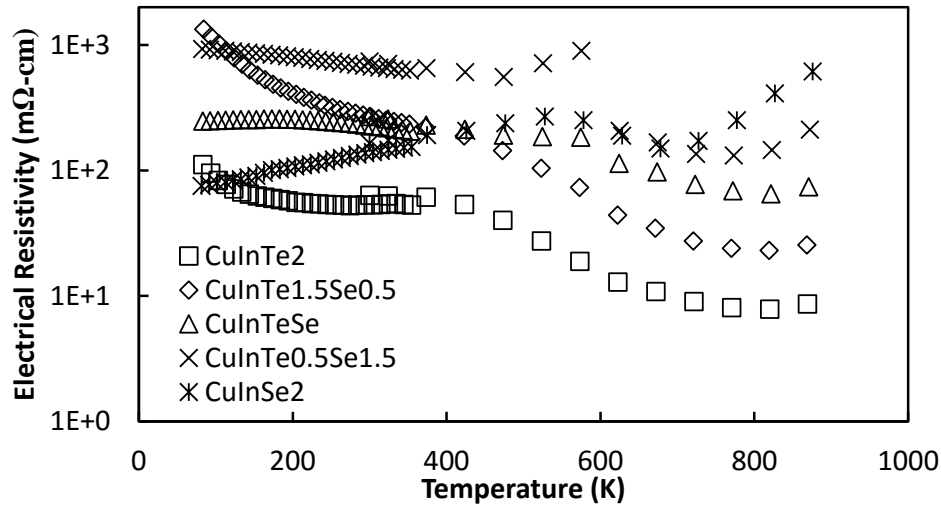


Figure 5.21: Electrical resistivity of the series  $\text{CuInTe}_{2(1-x)}\text{Se}_{2x}$  as a function of temperature.

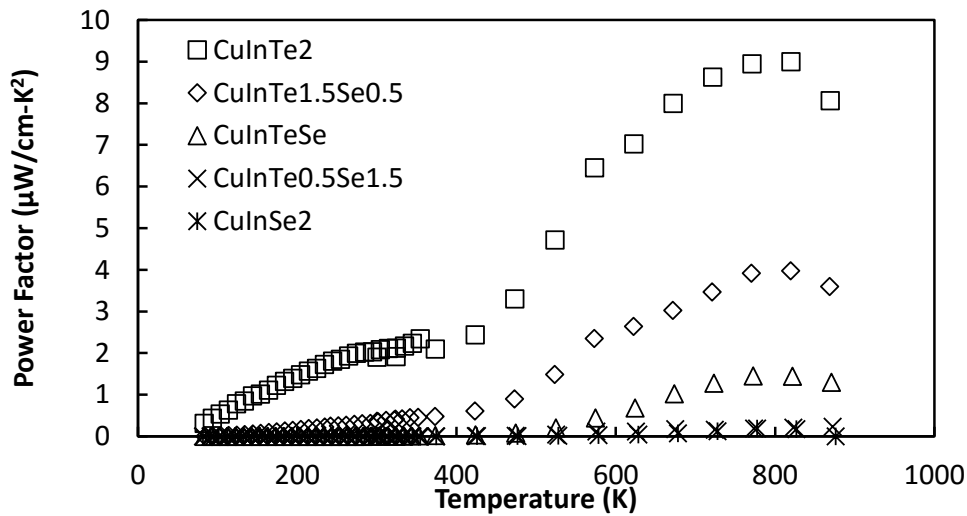


Figure 5.22: Power factor of the series  $\text{CuInTe}_{2(1-x)}\text{Se}_{2x}$  as a function of temperature.

The electrical resistivity varied over a much smaller range, as shown in Figure 5.21, when compared to the hotpressed version, but again at high temperatures showed a trend of higher electrical resistivity corresponding to higher selenium concentration. Likewise, the power factor decreased with each increase in selenium concentration, just as was found in the hotpressed version.

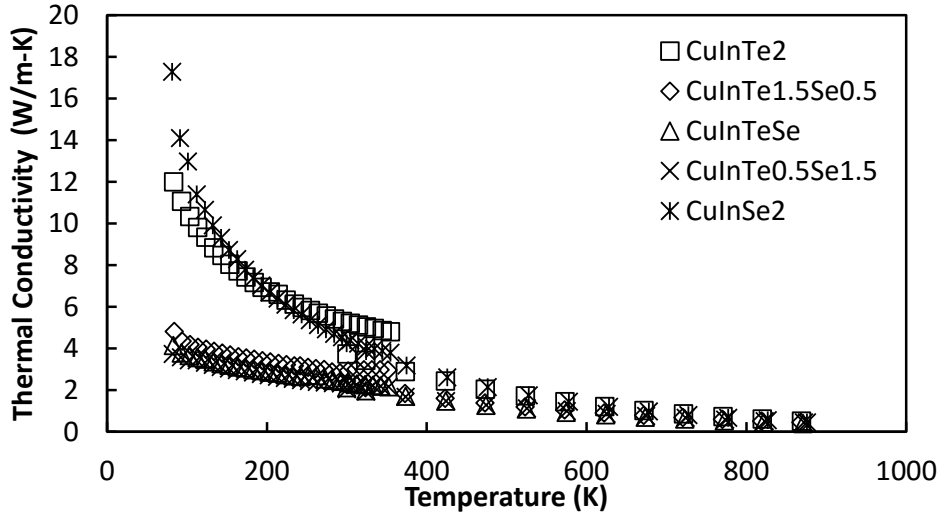


Figure 5.23: Thermal conductivity of the series  $\text{CuInTe}_{2(1-x)}\text{Se}_{2x}$  as a function of temperature.

As expected, the  $x = 0.25, 0.5,$  and  $0.75$  samples display a great reduction in thermal conductivity as compared to the end members of the series. However, when combined with the decrease in power factor, and with the reduction in thermal conductivity becoming less dramatic at high temperatures, the overall  $ZT$  of the series again decreases with increase selenium concentration, as shown in Figure 5.24.

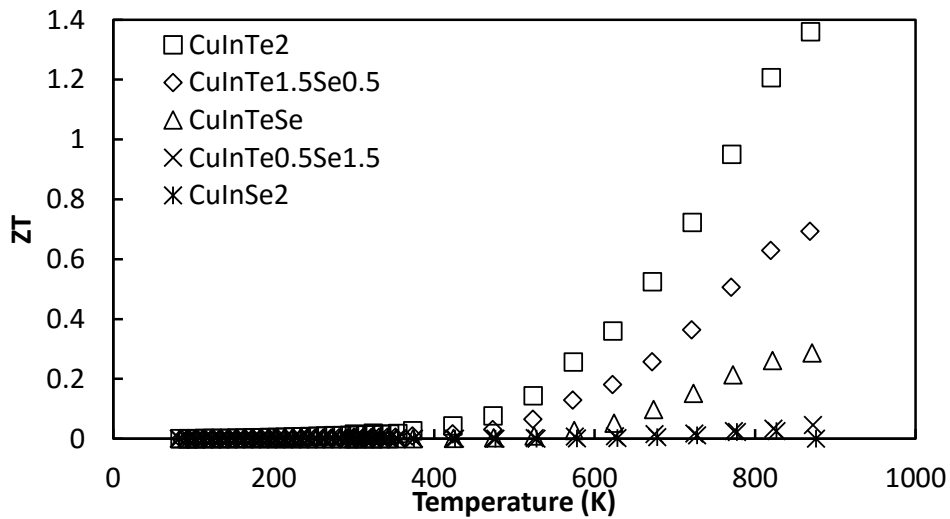


Figure 5.24:  $ZT$  of the series  $\text{CuInTe}_{2(1-x)}\text{Se}_{2x}$  as a function of temperature.

Some differences were observed for the SPS versus hotpressed samples. The samples made with the SPS showed higher thermal conductivity, with values at 300K for the  $\text{Te}_1\text{Se}_1$  sample of  $2\text{W m}^{-1}\text{K}^{-1}$  for the SPS sample versus  $1.2\text{W m}^{-1}\text{K}^{-1}$  for the hotpressed sample. There was also a large difference in electrical resistivity, with the SPS samples showing a value roughly one order of magnitude lower than the samples from the hotpress. The most likely cause for these differences is variance in the sample densities. Samples densified with the hot press were typically 95% theoretical density, while the samples made with the SPS were typically 98% or higher. This lower density meant more defects to scatter electrons and phonons, resulting in a lower thermal conductivity and a higher electrical resistivity for the hotpressed samples as compared to those made with SPS.  $\text{CuInTe}_2$  showed an increase in  $ZT$  from 0.75 to near 1.4 by densifying with SPS, a massive increase. The main factor was a slight decrease in electrical resistivity, and a 50% reduction in thermal conductivity at 860K, from  $0.73\text{ W m}^{-1}\text{K}^{-1}$  for the hot pressed sample to  $0.52\text{ W m}^{-1}\text{K}^{-1}$  for the sample densified by SPS.

### 5.4.3 $\text{CuIn}_{1-y}\text{Zn}_y\text{Te}_1\text{Se}_1$

Following the work on the solid solution of  $\text{CuInTe}_2$  with  $\text{CuInSe}_2$ , a series of samples were made with the composition  $\text{CuIn}_{1-y}\text{Zn}_y\text{Te}_1\text{Se}_1$  with  $y = 0, 0.01, 0.03, 0.05$  in hopes of maintaining the low thermal conductivity from the solid solution, while mitigating some of the rise in electrical resistivity. The samples were densified at  $450^\circ\text{C}$  for 15 minutes using the SPS.

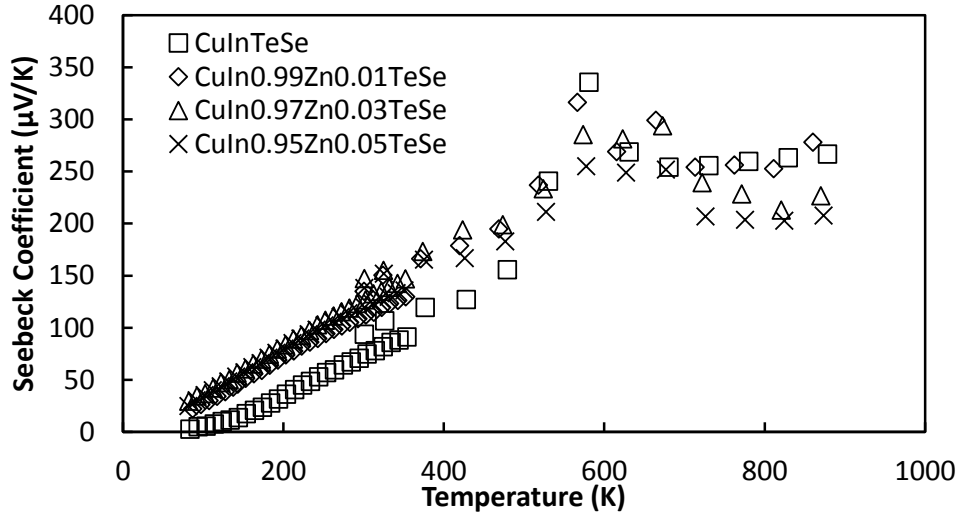


Figure 5.25: Seebeck coefficient of the series  $\text{CuIn}_{1-y}\text{Zn}_y\text{Te}_1\text{Se}_1$  as a function of temperature.

Regardless of doping level, the Seebeck coefficient of the samples showed a linear trend until approximately 500K, at which point they all displayed a sharp upward trend with a peak at 600K followed by a downward dip, as seen in Figure 5.25. This peak is also seen in the electrical resistivity as shown in Figure 5.26. It is suspected that this is indicative of an order-disorder phase transition. At high temperatures chalcopyrite compounds have been shown to transform into the simpler zinc-blende structure, in this case indicating that the copper and indium are no longer ordered with two each bonded to the group VI atom, but are rather randomly distributed on the cation site.[114, 109] Typically, this transition is seen at higher temperatures, e.g. in excess of 900K. [115, 116, 117] It is likely that transition temperature was decreased due to the strain present in the system from the disorder caused by the solid solution.

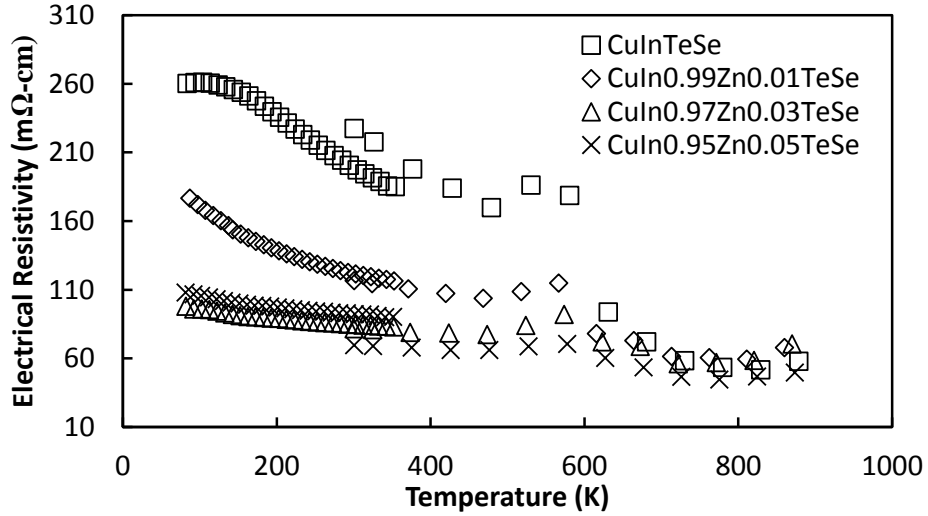


Figure 5.26: Electrical resistivity of the series  $\text{CuIn}_{1-y}\text{Zn}_y\text{Te}_1\text{Se}_1$  as a function of temperature.

The electrical resistivity data in Figure 5.26 shows zinc was effective as a p-type dopant, with each increase in zinc concentration further lowering the resistivity. Again, as seen in the Seebeck coefficient, a clear change in behavior is observed at roughly 600K. Pure  $\text{CuInTeSe}$  shows a drop in resistivity of 85  $\text{m}\Omega\text{cm}$ , decreasing by almost half, while  $\text{CuIn}_{0.95}\text{Zn}_{0.05}\text{TeSe}$  shows a drop of only 10  $\text{m}\Omega\text{cm}$ , a decrease of approximately 14%. Even with the drop in electrical resistivity and the sharp peak in Seebeck coefficient, the power factor for the samples still remained roughly a factor of 10 lower than that of  $\text{CuInTe}_2$ . The doped samples showed an increased power factor as compared to the undoped sample before the phase transition and also showed a pronounced peak at 600K, while the undoped sample showed a smooth increase up to 800K, reaching a higher final value.

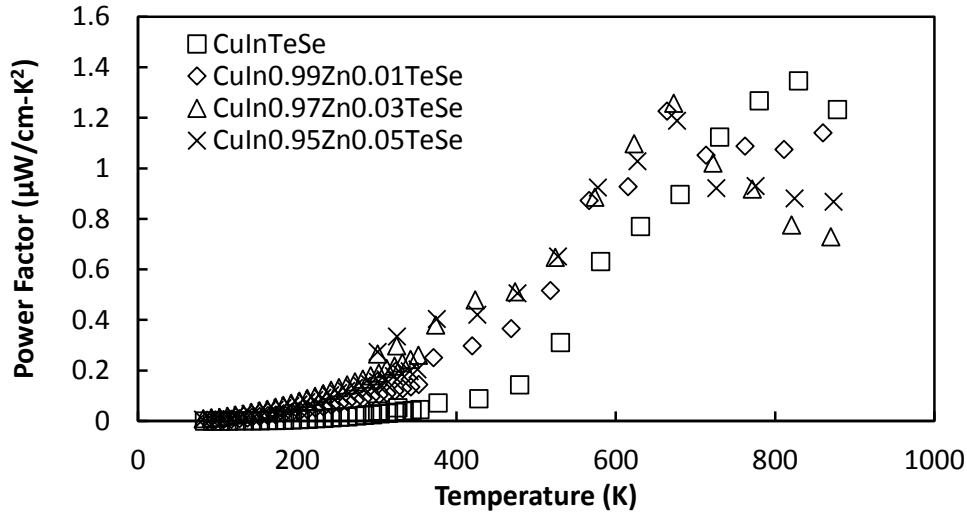


Figure 5.27: Power factor of the series  $\text{CuIn}_{1-y}\text{Zn}_y\text{Te}_1\text{Se}_1$  as a function of temperature.

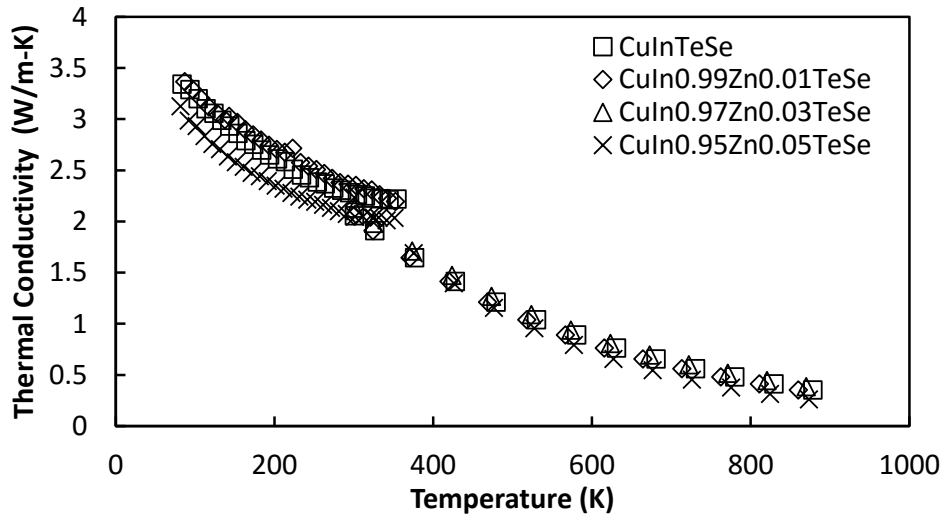


Figure 5.28: Thermal conductivity of the series  $\text{CuIn}_{1-y}\text{Zn}_y\text{Te}_1\text{Se}_1$  as a function of temperature.

The thermal conductivity values, as see in Figure 5.28, were lower than that of the end compounds of the solution, with room temperature values of  $2 \text{ W m}^{-1} \text{ K}^{-1}$ , and values at 860K of less than  $0.5 \text{ W m}^{-1} \text{ K}^{-1}$ . The low temperature data for  $y = 0.03$  is not shown here because there was a poor vacuum during measurement, which gave erroneous data for

thermal conductivity. With the exception of  $\text{CuIn}_{0.97}\text{Zn}_{0.03}\text{TeSe}$ , all the samples reached a  $ZT$  of approximately 0.3 at 860K, including the sample with no zinc addition.

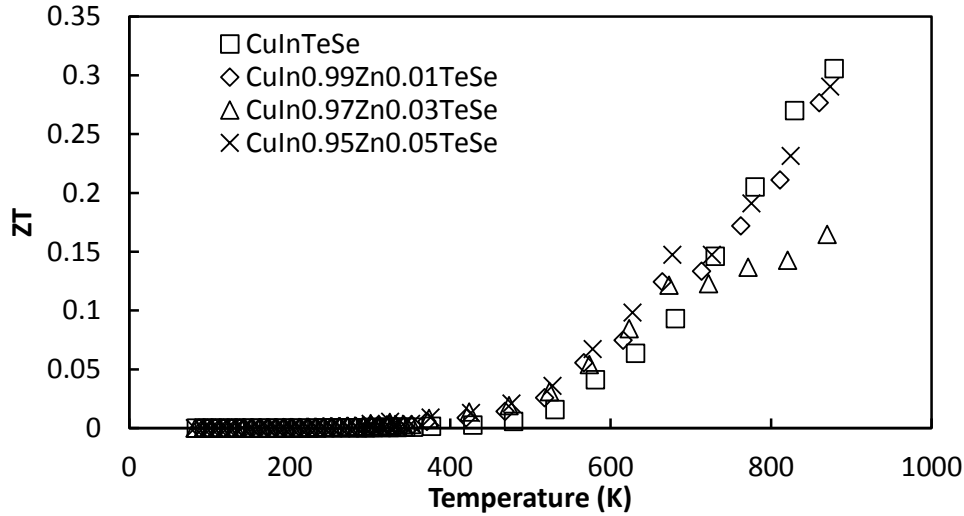


Figure 5.29:  $ZT$  of the series  $\text{CuIn}_{1-y}\text{Zn}_y\text{Te}_1\text{Se}_1$  as a function of temperature.

Overall the  $ZT$  for the series  $\text{CuIn}_{1-y}\text{Zn}_y\text{Te}_1\text{Se}_1$  showed little to no dependence on zinc concentration. The sample with 3% zinc showed a smaller values, but the 1% and 5% doped samples were well within measurement error of the undoped  $\text{CuInTeSe}$ . While the zinc did increase the power factor of the samples at low temperature, at high temperature the samples all displayed intrinsic carrier concentrations, and the zinc was ineffective at increase the peak  $ZT$ .

#### 5.4.4 $\text{CuGaTe}_{2(1-x)}\text{Se}_{2x}$

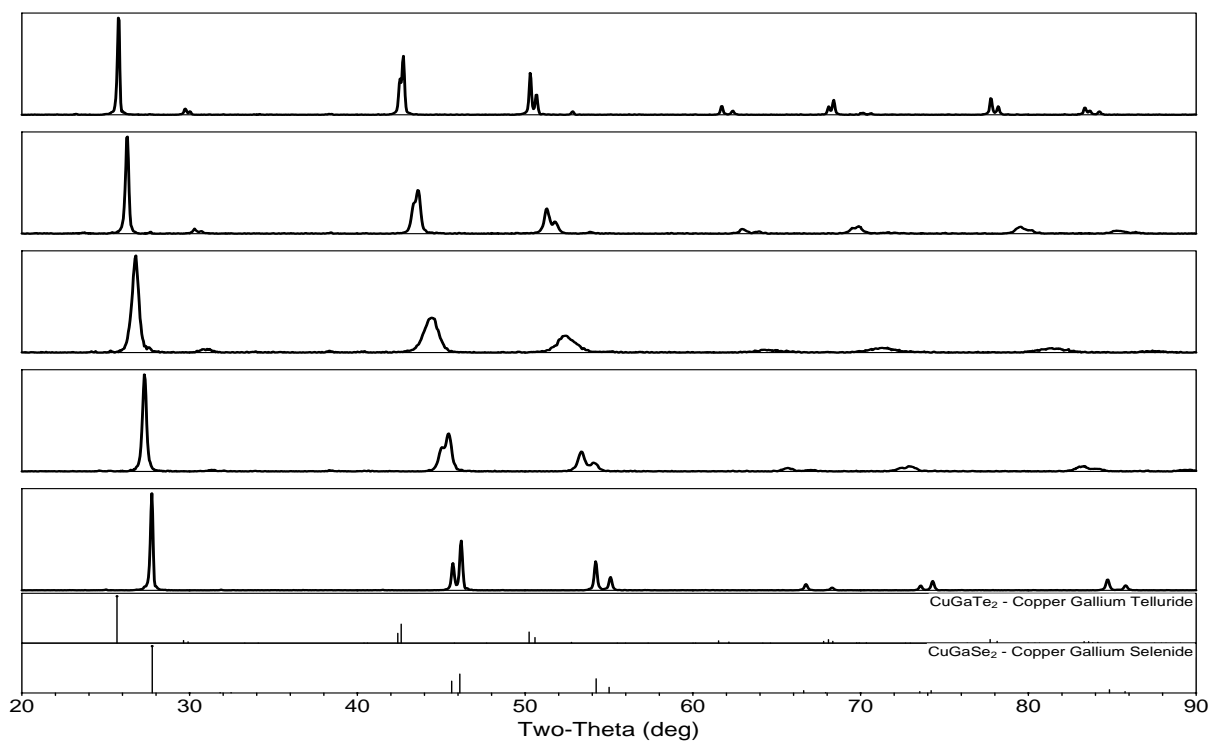


Figure 5.30: XRD patterns of the series  $\text{CuGaTe}_{2(1-x)}\text{Se}_{2x}$  with PDFs. The top pattern is for  $\text{CuGaTe}_2$ , with each pattern showing selenium substitutions in 25% increments, with  $\text{CuGaSe}_2$  shown at the bottom. The y-scale is intensity in arbitrary units. The PDFs are # 01-079-2331 and #01-075-2916 for Te and Se respectively. [7, 12]

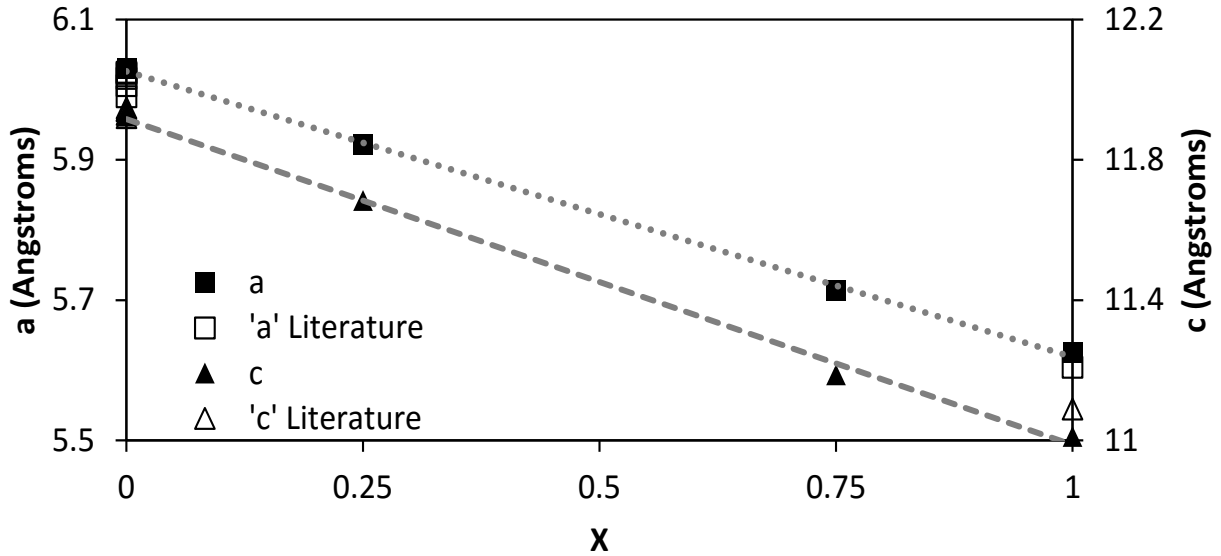


Figure 5.31: Lattice parameters of the series  $\text{CuGaTe}_2(1-x)\text{Se}_{2x}$ . Open symbols represent literature data, while the filled symbols are data from the study here. [4, 14, 13, 15, 8, 16]

Figure 5.30 displays the XRD patterns for this series of samples, together with the reference peaks from the PDF database. The lattice parameters extracted from these patterns are shown in Figure 5.31. Again, as with the indium based solid solution, the lattice parameters decreased linearly with increasing selenium concentration, however, lattice parameters were unable to be calculated from the pattern of  $\text{CuGaTeSe}$ . As the sample composition moved from the pure end compounds towards  $\text{CuGaTeSe}$  increased peak broadening was observed likely due to lattice strain from the size differences of selenium and tellurium. This broadening caused several of the doublet peaks to overlap in  $\text{CuGaTeSe}$  as shown in Figure 5.30, preventing a clear definition of peak positions.

Electronically, while both  $\text{CuInTe}_2$  and  $\text{CuInSe}_2$  had band gaps of around 1 eV,  $\text{CuGaTe}_2$  and  $\text{CuGaSe}_2$  have reported band gaps of 1.2 eV and 1.7 eV respectively.[8, 111] This large

difference was evident in the room temperature electrical resistivity, which showed an exponential dependence on selenium concentration as shown in Figure 5.32. This trend continued over the whole temperature range, as shown in Figure 5.33, with CuGaSe<sub>2</sub> displaying a resistivity roughly 100x greater than that of CuGaTe<sub>2</sub>.

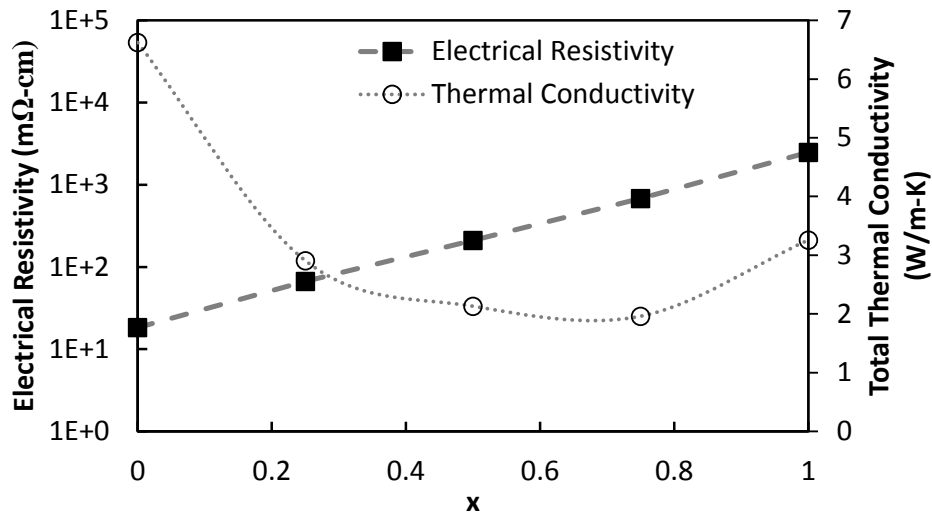


Figure 5.32: Thermal conductivity and electrical resistivity of the series  $\text{CuGaTe}_{2(1-x)}\text{Se}_{2x}$  at room temperature. Thermal conductivity shows the typical parabolic relationship, while the electrical resistivity shows an exponential dependence on selenium concentration.

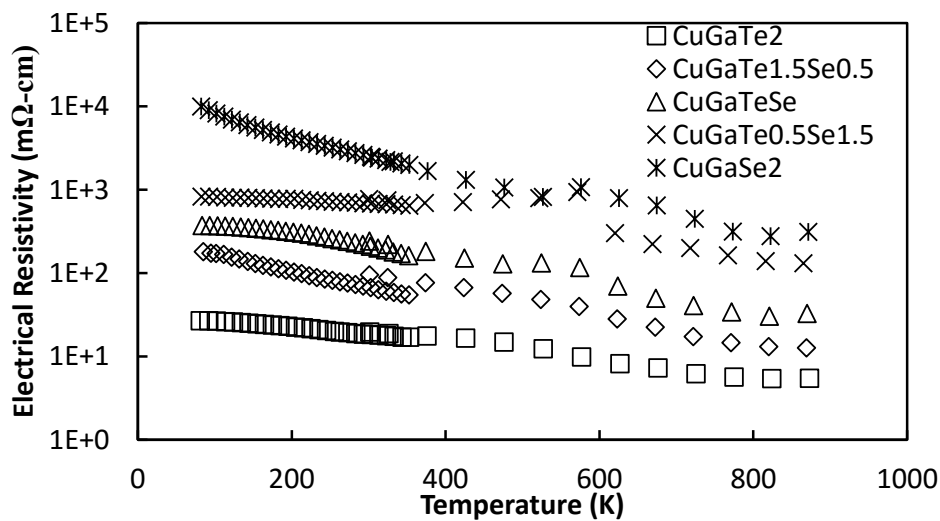


Figure 5.33: Electrical resistivity of the series  $\text{CuGaTe}_{2(1-x)}\text{Se}_{2x}$  as a function of temperature.

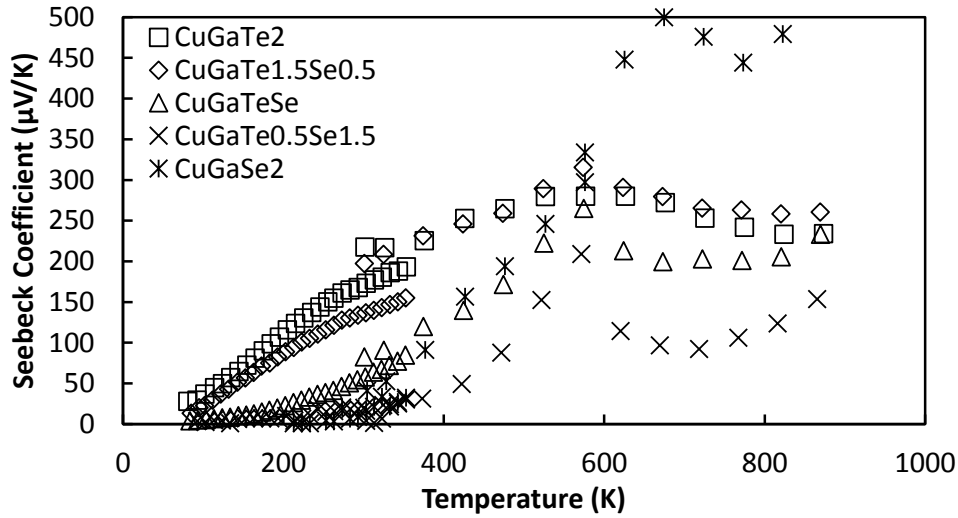


Figure 5.34: Seebeck coefficient of the series  $\text{CuGaTe}_{2(1-x)}\text{Se}_{2x}$  as a function of temperature.

The Seebeck coefficient of  $\text{CuGaTe}_2$  and  $\text{CuGaTe}_{1.5}\text{Se}_{0.5}$  were nearly identical, while that of  $\text{CuGaTeSe}$  and  $\text{CuGaTe}_{0.5}\text{Se}_{1.5}$  showed a sharp peak at 600K, just as was seen in the indium solid solution, again likely due to a order-disorder phase transition. The Seebeck coefficient of the pure selenide sample displayed a broad peak at 650K reaching a value of  $500\mu\text{V K}^{-1}$ , almost double that of  $\text{CuGaTe}_2$ .

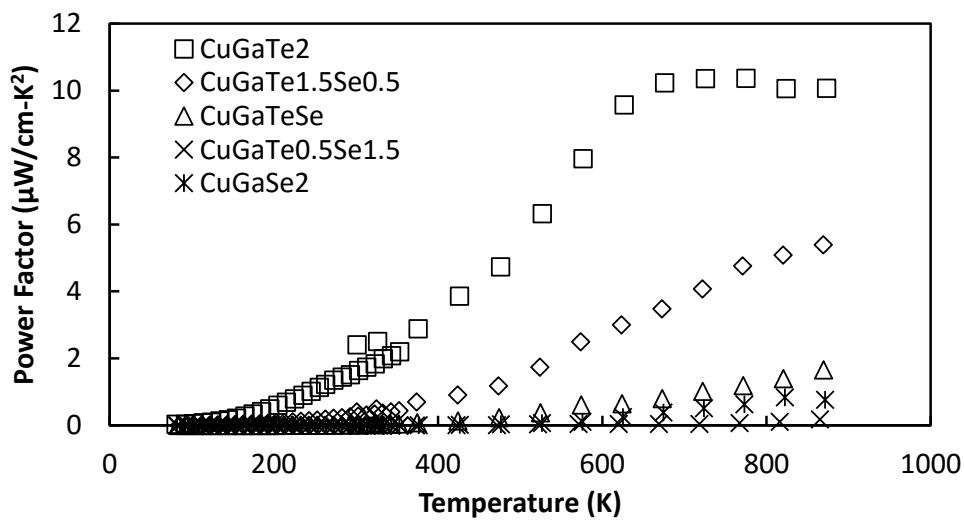


Figure 5.35: Power factor of the series  $\text{CuGaTe}_{2(1-x)}\text{Se}_{2x}$  as a function of temperature.

The power factor was found to decrease with increasing selenium concentration, primarily due to the large increase in electrical resistivity. By CuGaTeSe the power factor had dropped by almost a factor of 10, overwhelming the reduction in thermal conductivity. As Figure 5.32 shows, the thermal conductivity followed the expected parabolic trend in selenium concentration, while the electrical resistivity increased exponentially, leading to an overall decrease in  $ZT$ , as shown in Figure 5.37.

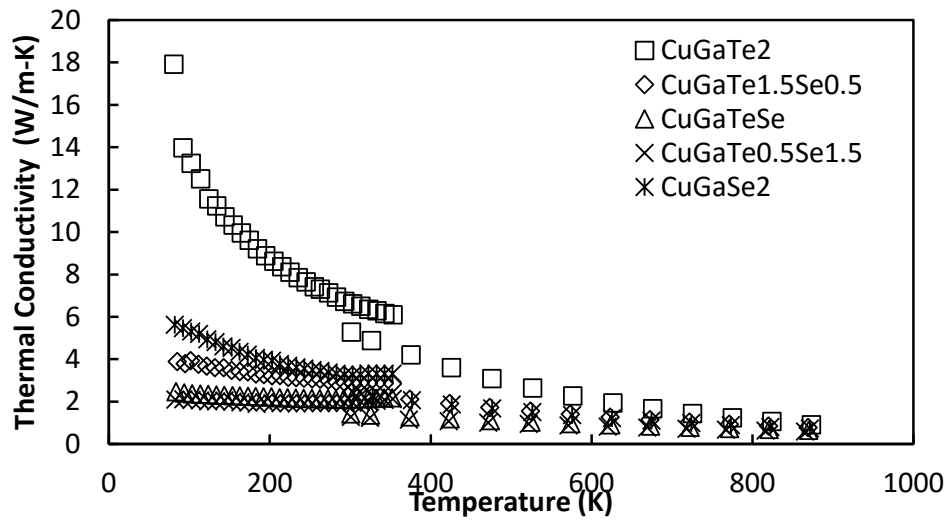


Figure 5.36: Thermal conductivity of the series  $\text{CuGaTe}_{2(1-x)}\text{Se}_{2x}$  as a function of temperature.

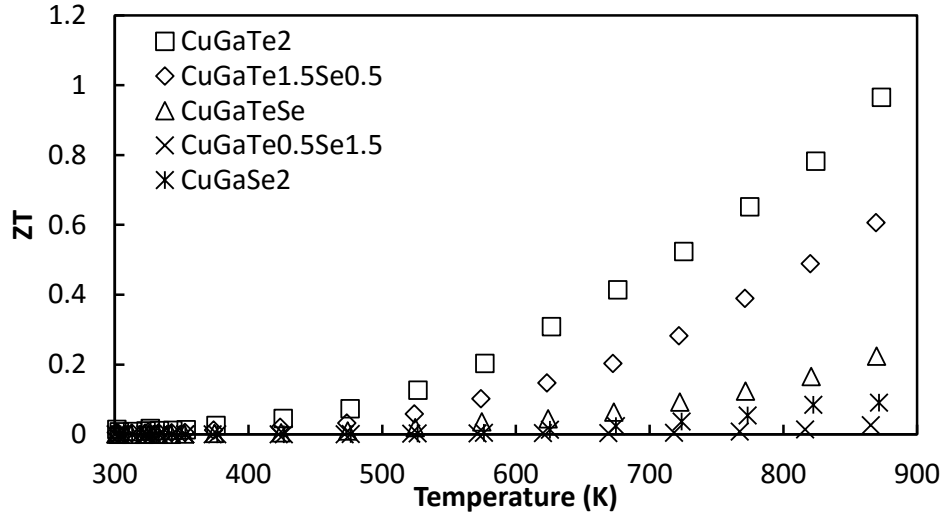


Figure 5.37:  $ZT$  of the series  $\text{CuGaTe}_{2(1-x)}\text{Se}_{2x}$  as a function of temperature.

#### 5.4.5 $\text{CuGa}_{1-y}\text{Zn}_y\text{TeSe}$

After the formation of the solid solution  $\text{CuGaTe}_{2(1-x)}\text{Se}_{2x}$  samples of the midpoint compound,  $\text{CuGaTeSe}$ , were synthesized with various levels of doping. Again, zinc was used to substitute for gallium as a p-type dopant. Compositions of  $\text{CuGa}_{1-y}\text{Zn}_y\text{TeSe}$  were made with  $y = 0.01, 0.02, 0.03,$  and  $0.05$ . The electrical resistivity of the samples decreased with increasing zinc substitution, but the reduction was minimal as shown in Figure 5.38.

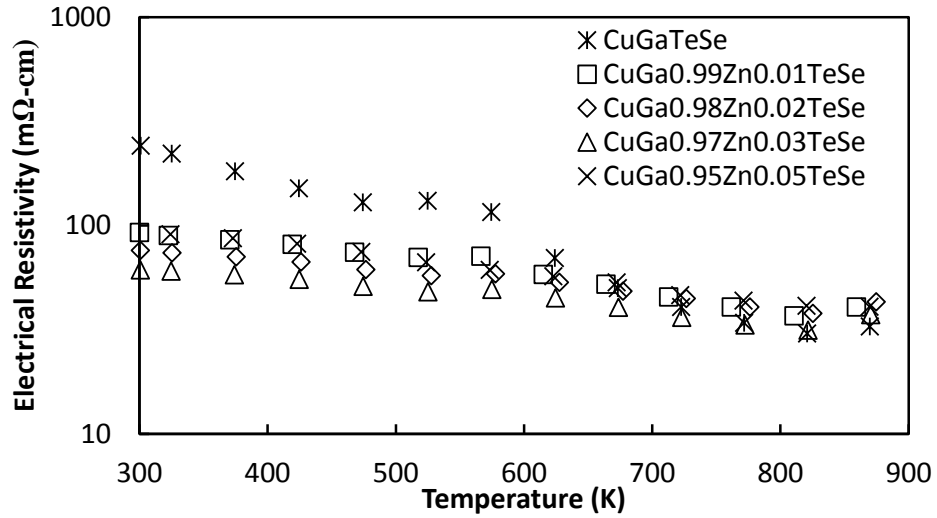


Figure 5.38: Electrical resistivity of the series  $\text{CuGa}_{1-y}\text{Zn}_y\text{TeSe}$  as a function of temperature.

The Seebeck coefficient again showed a peak at 600K, after which it dips down with all samples ending in the  $200\text{-}250\mu\text{V K}^{-1}$  range, as shown in Figure 5.39. The calculated power factor showed that the sample with 1% zinc had the best electronic properties, but did not improve on that of the undoped  $\text{CuGaTeSe}$  at 860K. A jump in the resistivity, and a peak in the Seebeck coefficient was once again observed near 600K for all of the samples. As with the case described in section 5.4.3, it was hypothesized that this is due to an order-disorder transition.

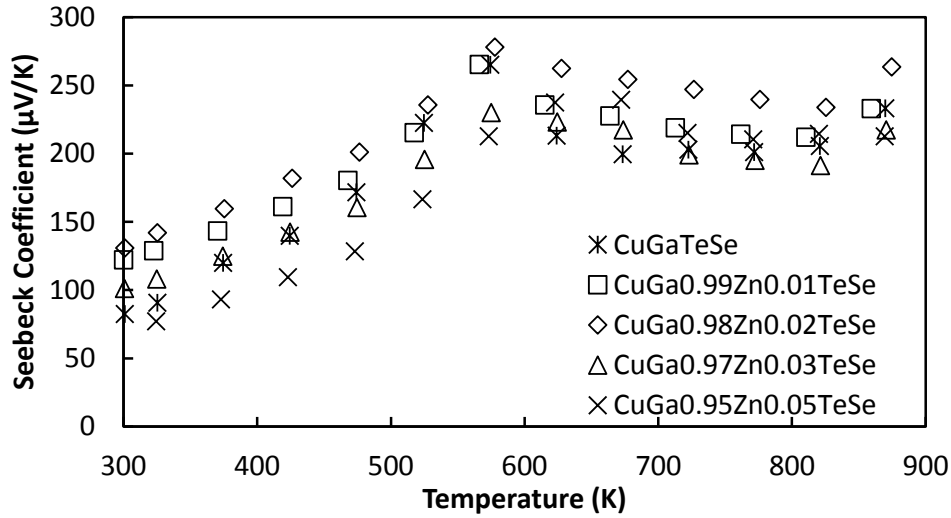


Figure 5.39: Seebeck coefficient of the series  $\text{CuGa}_{1-y}\text{Zn}_y\text{TeSe}$  as a function of temperature.

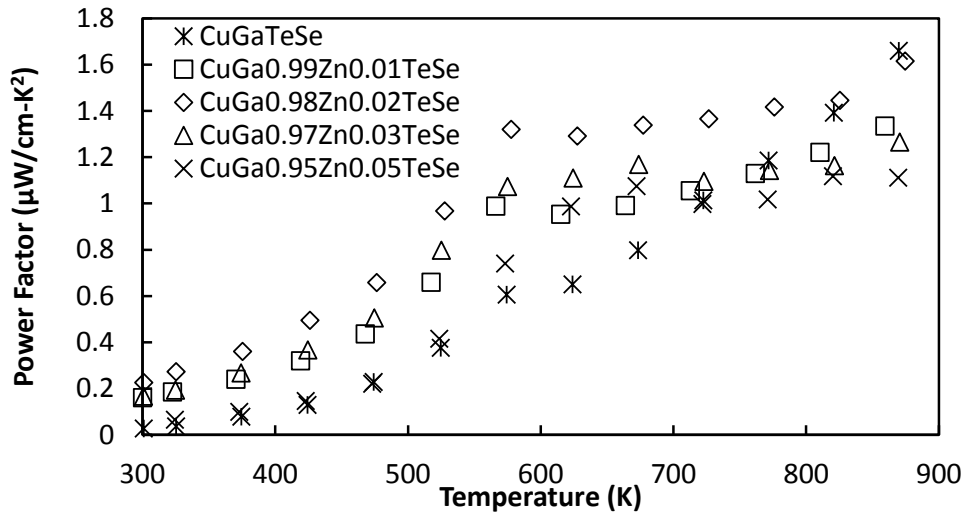


Figure 5.40: Power factor of the series  $\text{CuGa}_{1-y}\text{Zn}_y\text{TeSe}$  as a function of temperature.

The thermal conductivity for all of the samples showed similar values, reaching a minimum value of less than  $1.0 \text{ W m}^{-1} \text{ K}^{-1}$ , indicating that the dopant atoms had little effect on the thermal conductivity as expected. The final  $ZT$  calculations showed that the pure and the 2% doped sample had similar values, with the 2% showing a higher average  $ZT$  from 300K to 900K than the pure compound. The peak value of 0.20 is still much lower than that

of pure  $\text{CuGaTe}_2$ , which reached a value in excess of unity.

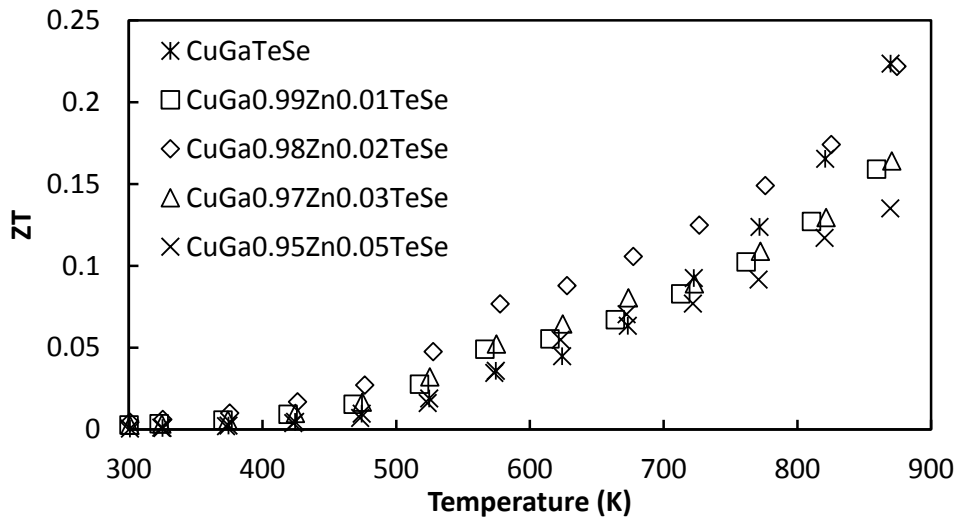


Figure 5.41:  $ZT$  versus temperature for the series  $\text{CuGa}_{1-y}\text{Zn}_y\text{TeSe}$ .

## 5.5 Conclusions

In this chapter full solid solutions of both  $\text{CuInTe}_{2(1-x)}\text{Se}_{2x}$  and  $\text{CuGaTe}_{2(1-x)}\text{Se}_{2x}$  were synthesized and measured. The indium solution was made using both the spark-plasma-sintering technique, as well as with the hotpress. For pure  $\text{CuInTe}_2$  it was found that the SPS lead to denser samples, and that in turn lead to better thermoelectric properties and a  $ZT$ . As shown in Figure 5.42 all three series displayed a parabolic relation between selenium concentration and thermal conductivity, with a minimum thermal conductivity observed at a ratio of Te:Se of 1:1. The indium based samples showed a lower thermal conductivity when densified with the SPS than with the hotpress.

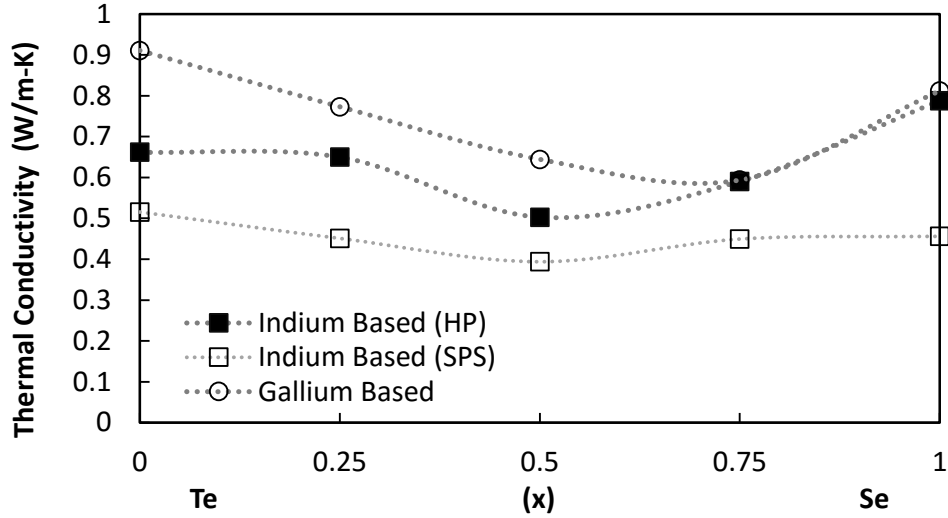


Figure 5.42: High temperature thermal conductivity of tellurium - selenium solid solutions as a function of selenium concentration. Compositions are  $\text{CuGaTe}_{2(1-x)}\text{Se}_{2x}$ ,  $\text{CuInTe}_{2(1-x)}\text{Se}_{2x}$  (SPS) and  $\text{CuIn}_{0.99}\text{Zn}_{0.01}\text{Te}_{2(1-x)}\text{Se}_{2x}$  (HP). Measurements were performed at 860K.

The electrical resistivities in Figure 5.43 exhibited two different trends.  $\text{CuGaTe}_{2(1-x)}\text{Se}_{2x}$  displayed an exponential dependence on selenium concentration, suggesting that the increasing band gap (1.2eV to 1.7eV) is the primary cause of the increase. However, this was also seen in the SPS densified series of composition  $\text{CuInTe}_{2(1-x)}\text{Se}_{2x}$ , where the band gap difference is negligible (both end compounds have theoretical values near 1eV). [107, 108, 109, 97, 98, 99] The indium based series densified via hotpress showed a less clear trend, showing the effect lower density had on transport properties.

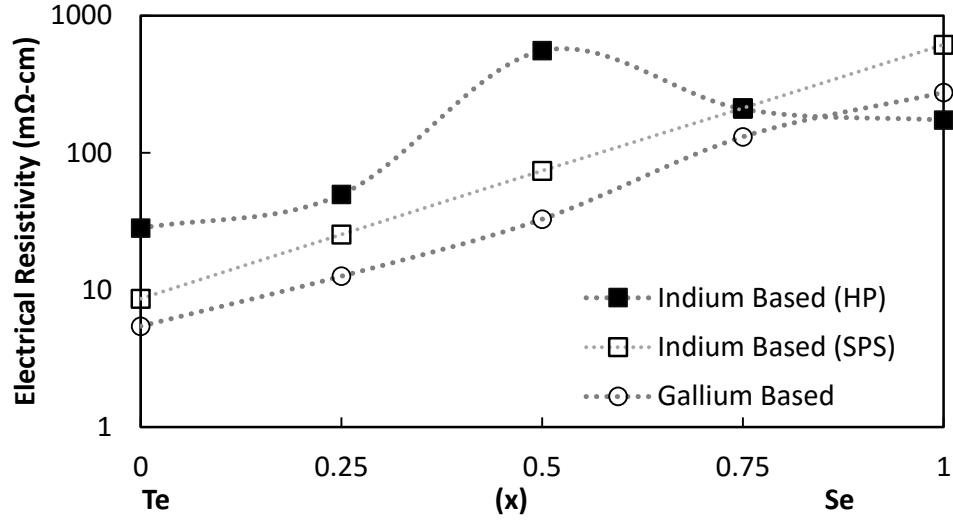


Figure 5.43: High temperature electrical resistivity of tellurium - selenium solid solutions as a function of selenium concentration. Compositions are  $\text{CuGaTe}_{2(1-x)}\text{Se}_{2x}$ ,  $\text{CuInTe}_{2(1-x)}\text{Se}_{2x}$  (SPS) and  $\text{CuIn}_{0.99}\text{Zn}_{0.01}\text{Te}_{2(1-x)}\text{Se}_{2x}$  (HP). Measurements were performed at 860K.

Ultimately neither solid solution offered an increase in the thermoelectric figure of merit. The rise in electrical resistivity with selenium substitution was more than offset by the reduction in the thermal conductivity that was obtained from the substitution. However, both series of compounds offered great tunability in electrical resistivity. Room temperature values increased exponentially with selenium concentration from a room temperature value of  $15\text{m}\Omega\text{ cm}$  for  $\text{CuGaTe}_2$  to up to  $2500\text{m}\Omega\text{ cm}$  for  $\text{CuGaSe}_2$ .  $\text{CuInTe}_{2(1-x)}\text{Se}_{2x}$  also showed a large range in resistivity, with values slightly higher than than of the gallium based sample.

# Chapter 6

## Sulfides

### 6.1 Family Overview

In the family of sulfides there are three compounds of interest:  $\text{CuInS}_2$ ,  $\text{CuGaS}_2$ , and  $\text{CuFeS}_2$ .  $\text{CuFeS}_2$  is distinct for being the only n-type material found in this study as well as for being the naturally occurring mineral for which chalcopyrite compounds are named. Again, the aluminum containing compound  $\text{CuAlS}_2$  was not studied due to the difficult synthesis required. In particular, the reaction between aluminum and sulfur to form  $\text{Al}_2\text{S}_3$  is extremely exothermic. Attempts to synthesize the compound from powdered Cu and  $\text{Al}_2\text{S}_3$  commercially available were unsuccessful, due to the rapid decomposition of  $\text{Al}_2\text{S}_3$  into  $\text{Al}_2\text{O}_3$  and  $\text{H}_2\text{S}$  on contact with air.

Quenching and annealing of samples, as was done with selenium and tellurium based compounds, lead to frequent cracking of ampoules during synthesis. Samples were successfully synthesized by slow heating to  $900^\circ\text{C}$ , holding for 24 hours, slow cooling to  $300^\circ\text{C}$ , holding for an additional 24 hours, and finally quenching into water.

## 6.2 CuFeS<sub>2</sub>

CuFeS<sub>2</sub> is the earth-abundant mineral known as chalcopyrite, after which the structure is named. The structure was originally reported in 1917 by Burdick and Ellis as being tetragonal with an  $a:c$  ratio of 1:0.985, but was later updated by Pauling and Brockway, and refined further by Hall and Stewart, where they obtained lattice parameter values of  $a = 5.289\text{\AA}$  and  $c = 10.423\text{\AA}$ , giving an  $a:c$  ratio of 1:1.97. [118, 119, 26] Current literature values for lattice parameters agree with those obtained by Hall, and samples synthesized in this work had  $a$  and  $c$  values of  $5.286\text{\AA}$  and  $10.431\text{\AA}$  respectively.

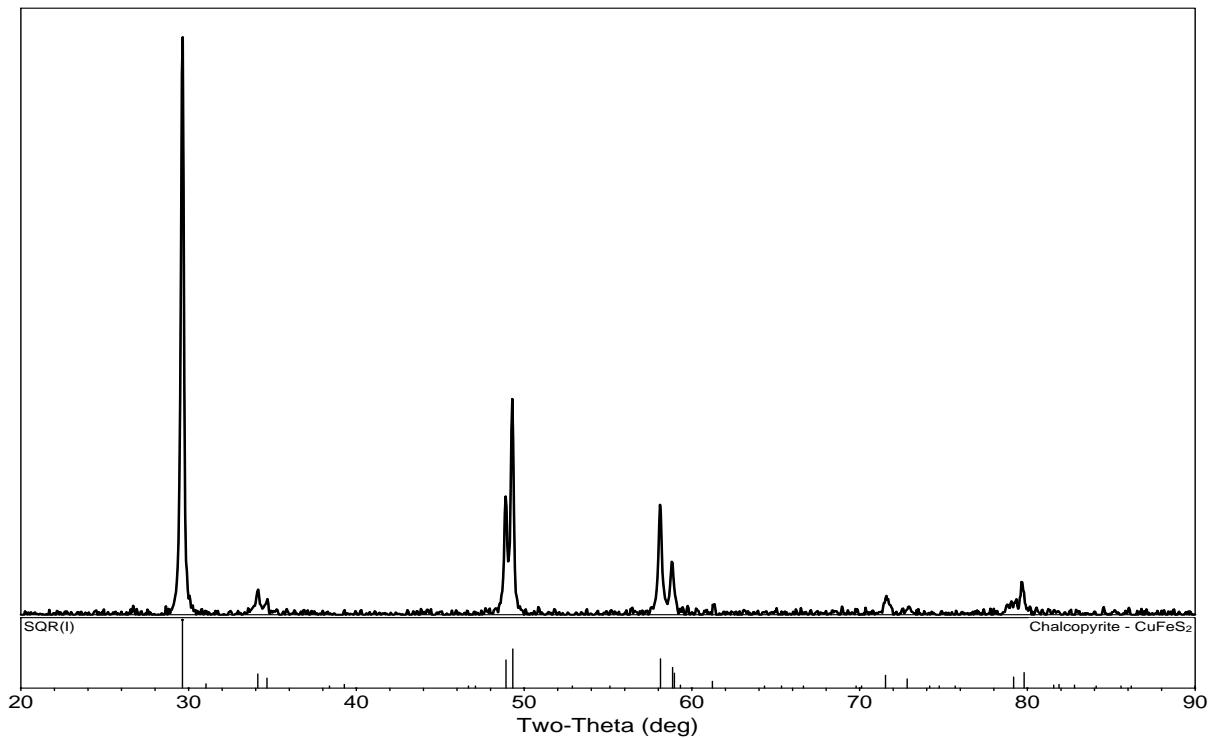


Figure 6.1: XRD pattern of CuFeS<sub>2</sub>. The pattern shown below is PDF# 01-083-0983.[17]

The reported band gap of CuFeS<sub>2</sub> ranges from 0.3 to 0.6 eV, with recent studies typically citing values near 0.5 eV. [120, 121, 23] That value is much smaller than the 1.5 eV or 2.5 eV found in the indium and gallium containing compounds, however band structure calculations

show the conduction band is almost entirely due to d-levels of iron which lie in a narrow band right above the Fermi level, breaking up what would otherwise be a larger band gap between the copper and sulfur levels.[121]  $\text{CuFeS}_2$  was found to be less stable than the previously studied compounds, showing a mass loss around 700K for samples densified via SPS, attributed to sulfur sublimation.[18, 19] Due to this stability issue, properties of  $\text{CuFeS}_2$  were measured only up to 450C, or 723K.

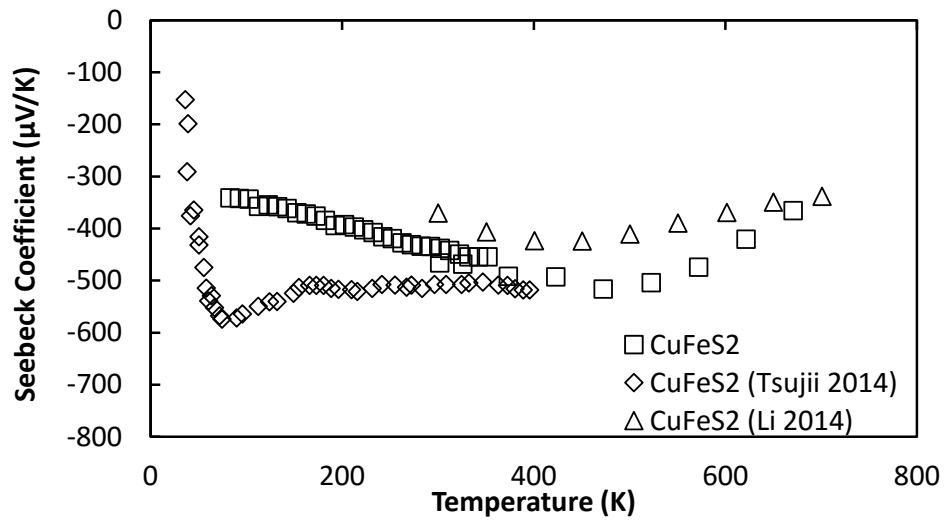


Figure 6.2: Seebeck coefficient of  $\text{CuFeS}_2$  as a function of temperature as compared to literature reports. Data is from Tsujii *et al.* and Li *et al.*. [18, 19, 20]

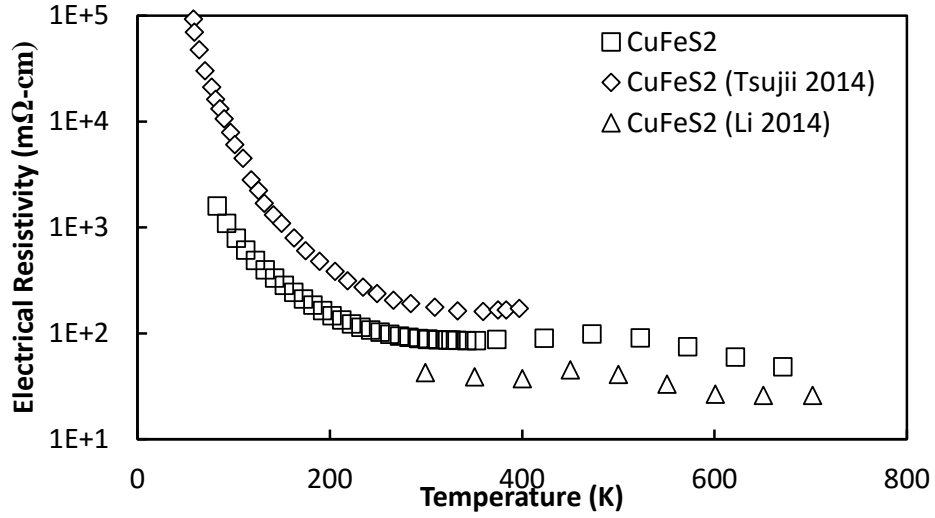


Figure 6.3: Electrical resistivity of  $\text{CuFeS}_2$  as a function of temperature as compared to literature reports. Data is from Tsujii *et al.* and Li *et al.*. [18, 19, 20]

As shown in Figure 6.2,  $\text{CuFeS}_2$  exhibited a negative Seebeck coefficient, indicating n-type carriers. The samples synthesized here agreed well with other reported measurements, with the electrical resistivity lying directly between two reported values. [19, 20] Both the Seebeck coefficient from the samples in this study, and the sample measured by Tsujii *et al.* displayed a broad flat temperature dependence, with magnitudes of  $300 - 500 \mu\text{V K}^{-1}$  across the whole temperature range.[18, 19] This leads to a maximum power factor of  $3 \mu\text{W cm}^{-1} \text{K}^{-2}$  from 400K to 650K for the sample synthesized in this study.

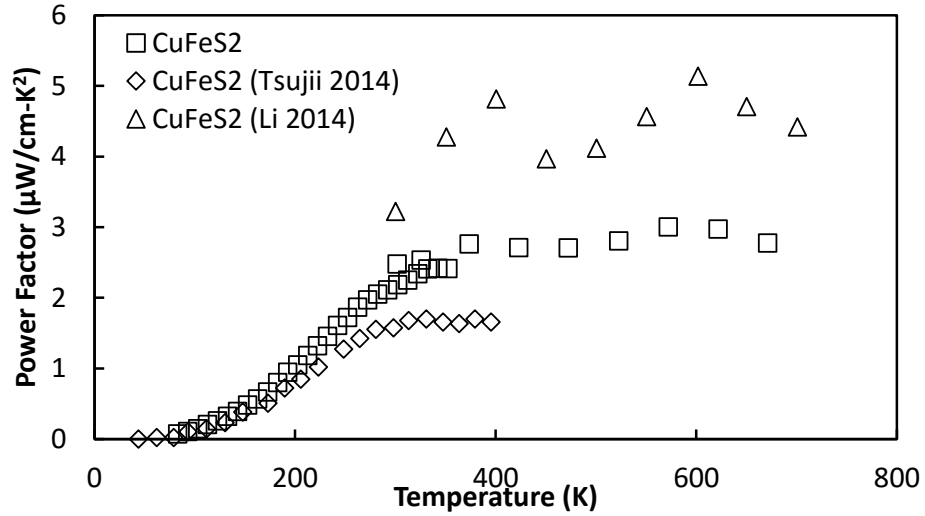


Figure 6.4: Power factor of  $\text{CuFeS}_2$  as a function of temperature as compared to literature reports. Data is from Tsujii *et al.* and Li *et al.*. [18, 19, 20]

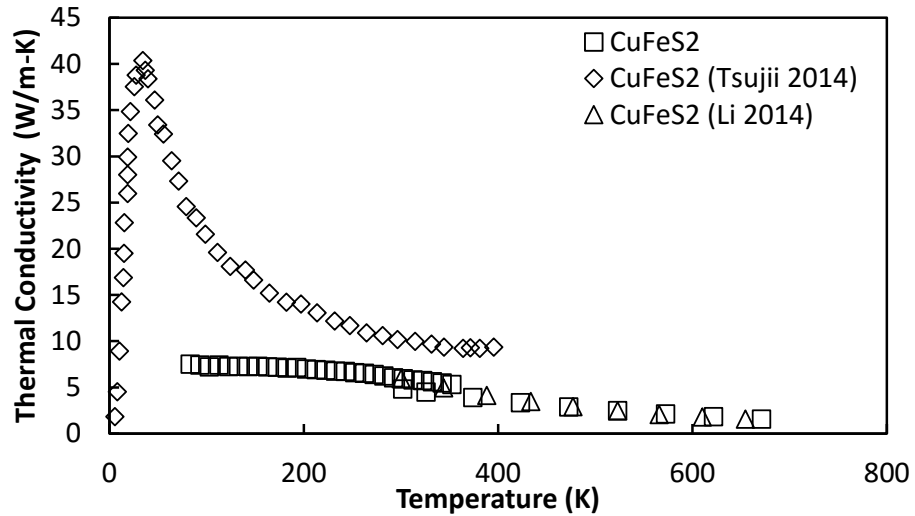


Figure 6.5: Thermal conductivity of  $\text{CuFeS}_2$  as a function of temperature as compared to literature reports. Data is from Tsujii *et al.* and Li *et al.*. [18, 19, 20]

The thermal conductivity shows typical behavior, with the expected  $1/T$  temperature dependence. At 723K a minimum value of  $1.5 \text{ W m}^{-1} \text{ K}^{-1}$  was measured, in close agreement with that of previous results as shown in Figure 6.5. The thermal conductivity of the sample made by Tsujii *et al.* showed a strong peak in thermal conductivity at low temperature,

along with with higher electrical resistivity as seen in reference Figure 6.3, indicating the sample likely had a lower amount of defects in comparison to the sample synthesized here. The peak  $ZT$  value obtained in this study for pure  $\text{CuFeS}_2$  was 0.12, while that in the literature reaches a peak of 0.21, primarily due to a higher electrical resistivity found in samples studied here.[20]

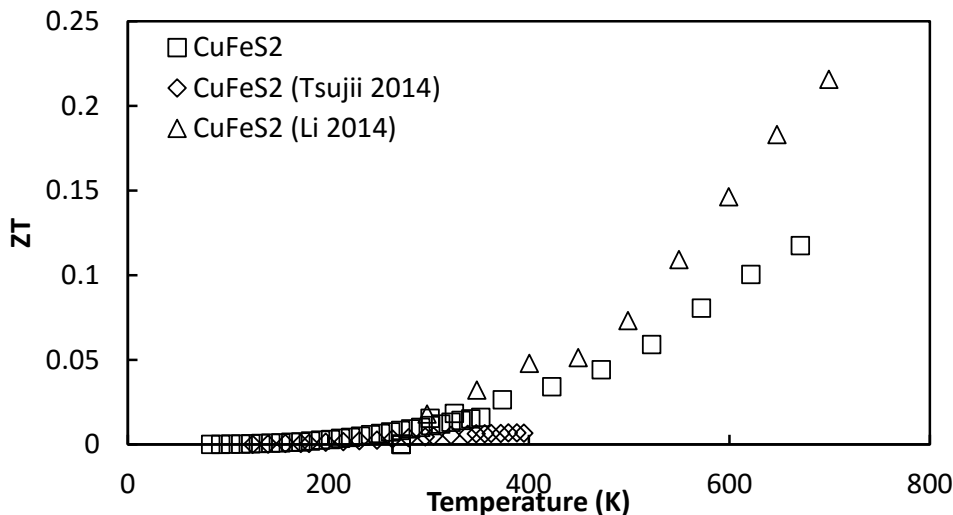


Figure 6.6:  $ZT$  of  $\text{CuFeS}_2$  as a function of temperature as compared to literature reports. Data is from Tsujii *et al.* and Li *et al.*. [18, 19, 20]

### 6.2.1 Electronic Doping

As with other samples, zinc was used as a dopant element for  $\text{CuFeS}_2$ . However, since  $\text{CuFeS}_2$  was found to be n-type, zinc was substituted on the copper site, rather than for the group three element. This replaced a monovalent atom with a divalent one, the latter acting as an n-type donor. Samples were synthesized with 1% and 2% zinc substituting for copper. Hall measurements showed an increase in carrier concentration from  $6 \times 10^{18} \text{ cm}^{-3}$  at 300K for the undoped sample, up to a value of  $1 \times 10^{20} \text{ cm}^{-3}$  for both the 1% and 2% zinc doped samples.

The effective mass (calculated by fitting carrier concentration and Seebeck data to equations (2.21) and (2.43)) for the samples increased from  $3.1 m_e$  for the pure sample up to  $3.3 m_e$  and  $4.1 m_e$  for the 1% and 2% zinc containing samples. The values were larger than typical for an n-type semiconductor, but agreed with previous studies by Tsujii *et al.*[19] Band structure calculations show  $\text{CuFeS}_2$  has a broad flat conduction band, in agreement with the high values of effective mass obtained by Hall measurements here. [121]

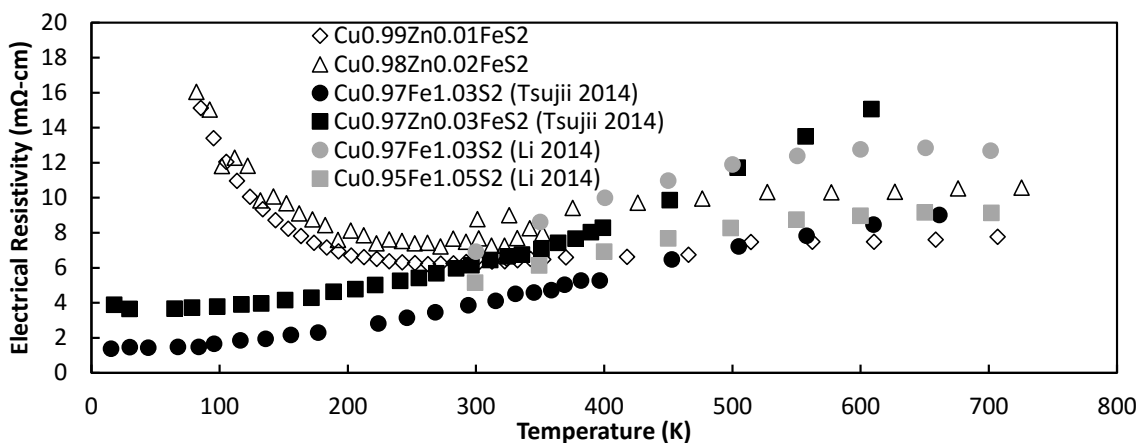


Figure 6.7: Electrical resistivity of the series  $\text{Cu}_{1-y}\text{Zn}_y\text{FeS}_2$  as a function of temperature as compared to literature reports. Open symbols represent data obtained here, while the filled symbols represent data from Tsujii *et al.* and Li *et al.* [18, 19, 20]

As is seen when comparing Figure 6.3 and Figure 6.7, zinc was an effective dopant atom, lowering the electrical resistivity greatly when compared to the nominally undoped samples in agreement with the Hall measurements. At low temperatures the difference in electrical resistivity between the doped and undoped sample was roughly two orders of magnitude, while at room temperature the difference was one order of magnitude. Between the 1% and 2% zinc doped samples there was little difference in electrical resistivity values, with both samples exhibiting values on the order of  $10 \text{ m}\Omega \text{ cm}$  in good agreement with results in the literature, as shown in Figure 6.7.

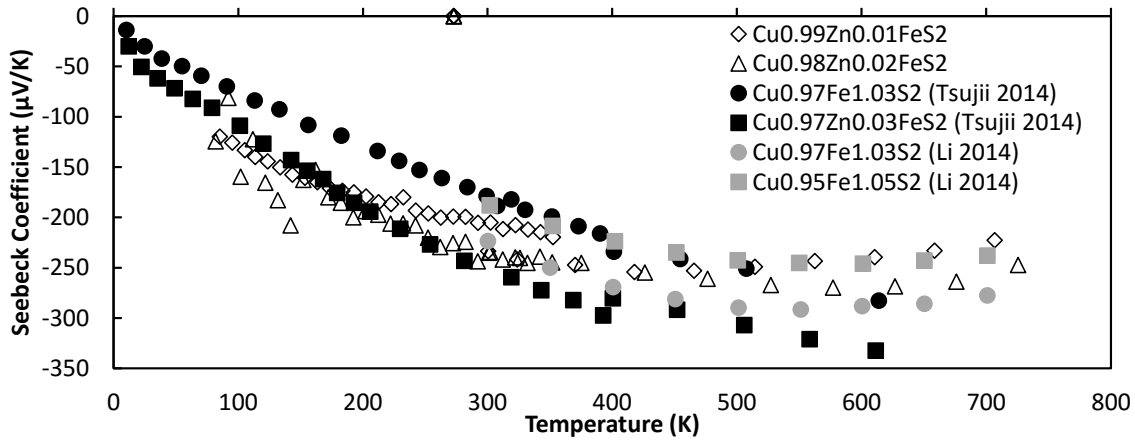


Figure 6.8: Seebeck coefficient of the series  $\text{Cu}_{1-y}\text{Zn}_y\text{FeS}_2$  as a function of temperature as compared to literature reports. Open symbols represent data obtained here, while the filled symbols represent data is from Tsujii *et al.* and Li *et al.*. [18, 19, 20]

The Seebeck coefficient showed typical degenerate semiconductor character, increasing in magnitude linearly with temperature up to 400K, at which point the Seebeck coefficient for all the samples start to level out, likely due to an excitation of minority carriers. Again, the literature data matched closely to that obtained in this study.

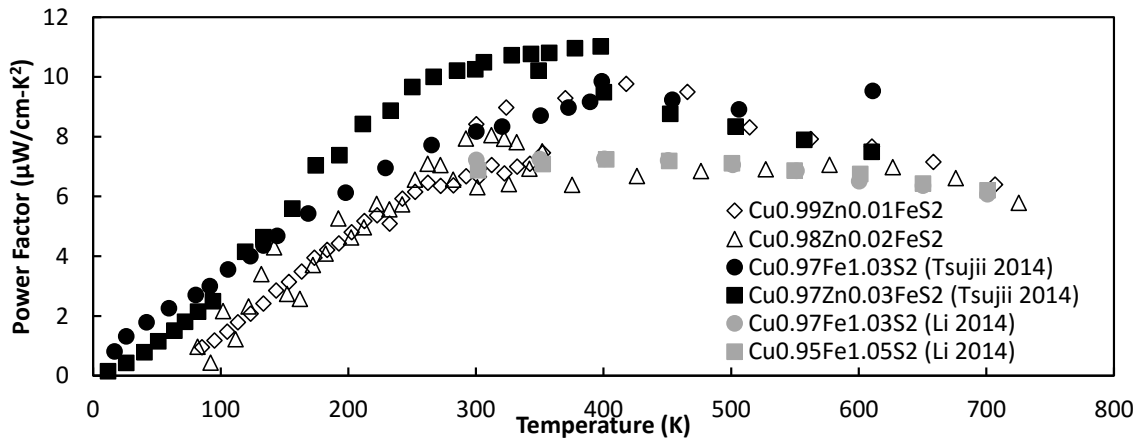


Figure 6.9: Power factor of the series  $\text{Cu}_{1-y}\text{Zn}_y\text{FeS}_2$  as a function of temperature as compared to literature reports. Data is from Tsujii *et al.* and Li *et al.*. [18, 19, 20]

The resulting power factor data showed that the 1% and 2% zinc samples are nearly indis-

tinguishable at low temperatures, but from 300K to 600K the power factor of  $\text{Cu}_{0.99}\text{Zn}_{0.01}\text{FeS}_2$  was higher. As shown in Figure 6.9  $\text{Cu}_{0.98}\text{Zn}_{0.02}\text{FeS}_2$  matched the 3% and 5% doped samples shown in the work by Li *et al.*, while the higher value of  $\text{Cu}_{0.99}\text{Zn}_{0.01}\text{FeS}_2$  agreed with the data from the work of Tsujii *et al.* [19, 20].

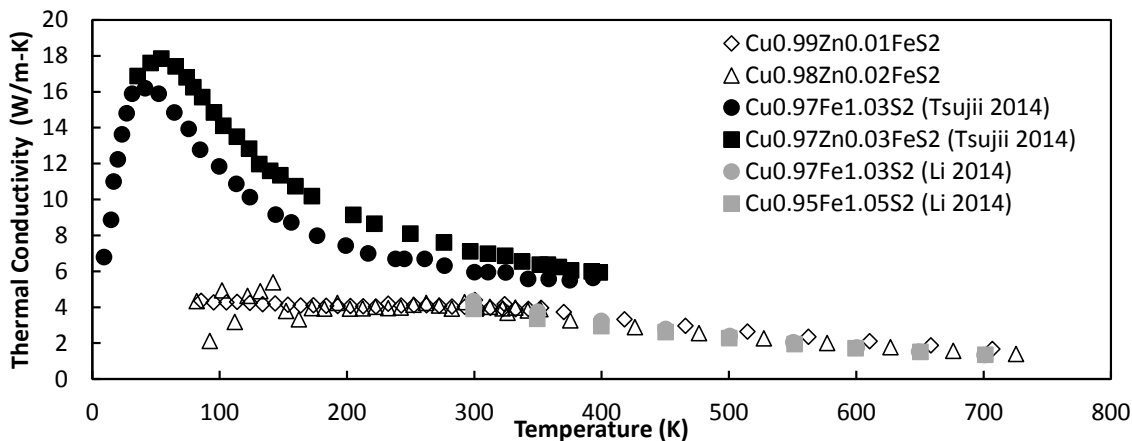


Figure 6.10: Thermal conductivity of the series  $\text{Cu}_{1-y}\text{Zn}_y\text{FeS}_2$  as a function of temperature as compared to literature reports. Data is from Tsujii *et al.* and Li *et al.* [18, 19, 20]

Previous studies on  $\text{Cu}_{(1-x)}\text{Fe}_{(1+x)}\text{S}_2$  showed a large reduction in thermal conductivity, which was attributed to strain from changes in the iron-sulfur and copper-sulfur bond lengths. Here similar effects were observed with the substitution of zinc for copper, though to a smaller extent. The reduction at 80K is significant, from near  $7 \text{ W m}^{-1} \text{ K}^{-1}$  for pure  $\text{CuFeS}_2$  down to around  $4.5 \text{ W m}^{-1} \text{ K}^{-1}$  for the zinc doped samples, however at 725K all the samples showed values near  $1.5 \text{ W m}^{-1} \text{ K}^{-1}$ . Again, good agreement was found between the values obtained in this study and those available in literature. [20, 19]

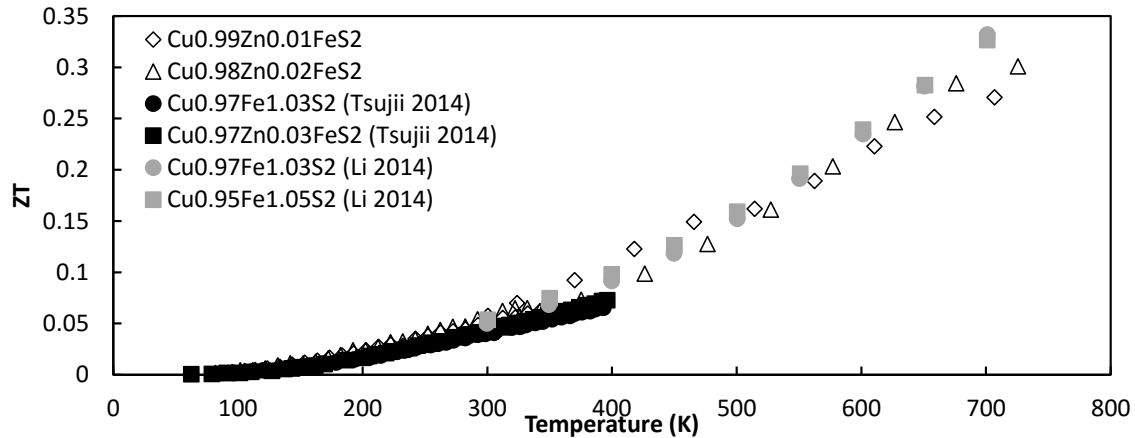


Figure 6.11:  $ZT$  of the series  $\text{Cu}_{1-y}\text{Zn}_y\text{FeS}_2$  as a function of temperature as compared to literature reports. Data is from Tsujii *et al.* and Li *et al.* [18, 19, 20]

The peak  $ZT$  for the samples in this study matched very closely to that of Li *et al.* as shown in Figure 6.11, reaching a modest value of 0.3 at around 700K for both the 1% and 2% zinc doped samples.[20] While this value was lower than that obtained from  $\text{CuInTe}_2$  or  $\text{CuGaTe}_2$ , it did offer a low cost, earth-abundant option.

## 6.2.2 $\text{CuFeS}_2$ Rapid SPS Synthesis

The synthesis of  $\text{CuFeS}_2$  required a long slow heating process to avoid the rapid vaporization of sulfur and subsequent ampoule explosion. Li *et al.* showed in 2013 that  $\text{CuFeS}_2$  could be synthesized by mechanical alloying and spark-plasma-sintering. [23] That study found that planetary milling raw copper, iron, and sulfur powders for 13 hours at 450rpm, followed by sintering at 650°C via SPS, single phase material could be obtained.

As an alternative approach a study was done on the direct reaction of binary powders by spark-plasma-sintering. Raw binary powders ( $\text{CuS}$  99.8% 200 mesh and  $\text{FeS}$  99.9% 100 mesh) were weighed out in a 1:1 stoichiometric ratio and placed into a zirconia vibratory

mill jar. The powder was milled for five minutes to ensure homogeneous mixing, after which the powder was densified via spark plasma sintering at either 450°C, 500°C, or 550°C with a holding time of either 5, 10, or 20 minutes. The results showed that samples densified at 450°C were multiphase, even with a hold time of twenty minutes, while those samples synthesized at 500°C or above were single phase in as little as five minutes.

As shown below, the ball milling mixed the binary powders but did not result in any initial mechanical alloying. However, after SPS, samples made at 500°C were found to be single phase.

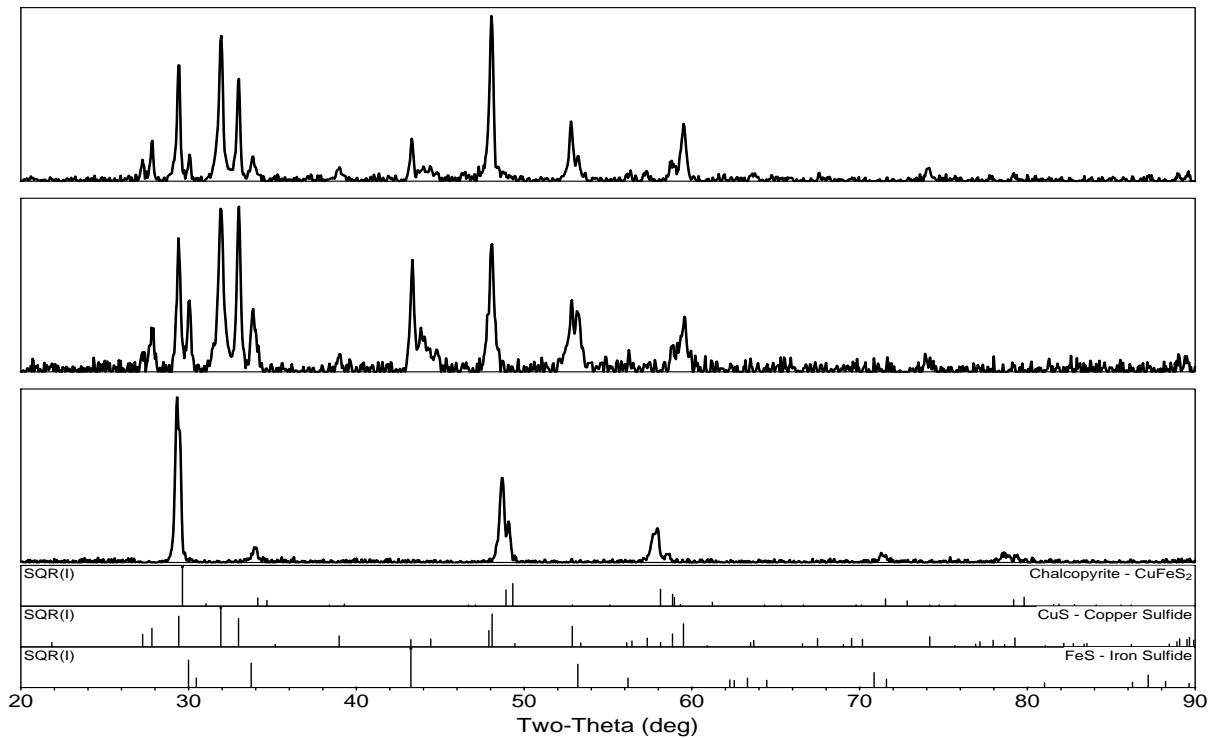


Figure 6.12: The top pattern is for two powders mixed by hand, the middle pattern is the powder after 5 minutes of vibratory milling, and the bottom pattern is taken after the powder has been densified by the SPS. The patterns shown below are PDF# 01-083-0983, PDF# 01-079-2321, and PDF# 03-065-6841 for CuFeS<sub>2</sub>, CuS, and FeS respectively.[17, 21, 22]

Table 6.1: Density of samples of  $\text{CuFeS}_2$  synthesized by direct SPS reaction. The theoretical density of  $\text{CuFeS}_2$  is  $4.1823 \text{ g cm}^{-3}$  using the lattice parameters obtained from XRD.

—	450°C	500°C	550°C
5 min	Failed	$4.1594 \text{ g cm}^{-3}$	$4.1566 \text{ g cm}^{-3}$
10 min	Failed	$4.2150 \text{ g cm}^{-3}$	$4.2002 \text{ g cm}^{-3}$
20 min	Failed	$4.1950 \text{ g cm}^{-3}$	$4.2190 \text{ g cm}^{-3}$

As shown in Table 6.1 above, the samples held for five minutes showed a marked decrease in density as compared to those held for ten or twenty minutes. For comparison, the density of  $\text{CuFeS}_2$  made with the conventional furnace heating and hot pressing had a measured density of  $4.005 \text{ g cm}^{-3}$ . The samples held at  $550^\circ\text{C}$  displayed a much more brittle character, often chipping and cracking while cutting. There is no high temperature thermal conductivity for the samples synthesized at  $550^\circ\text{C}$  due to the laser-flash discs cracking during the cutting and sanding process.

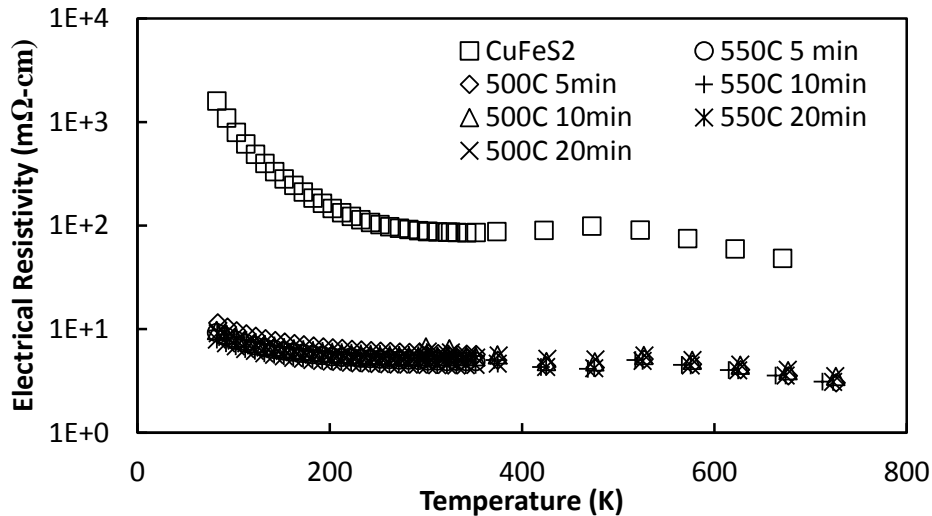


Figure 6.13: Electrical resistivity of several samples of  $\text{CuFeS}_2$  as a function of temperature. Samples were synthesized by direct reaction during SPS. The squares represents  $\text{CuFeS}_2$  made by traditional melting and hotpressing.

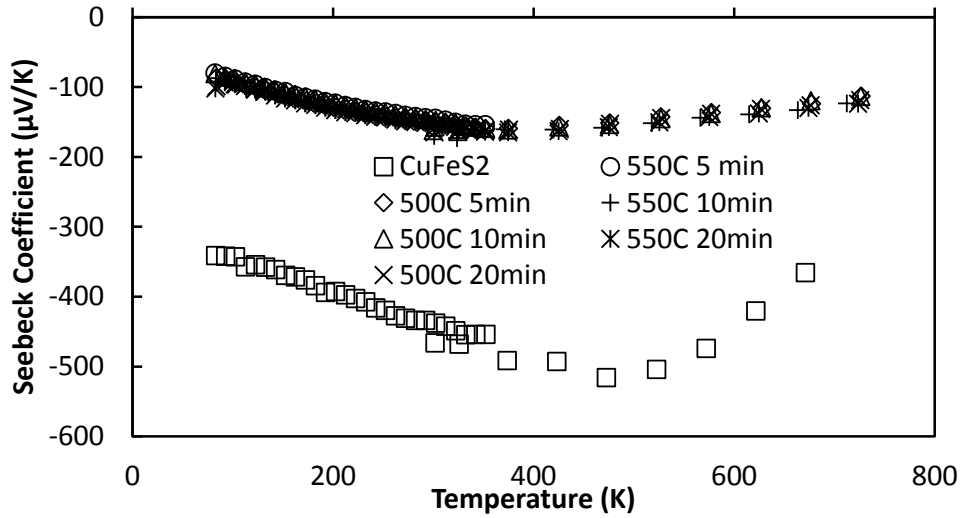


Figure 6.14: Seebeck coefficient of several samples of  $\text{CuFeS}_2$  as a function of temperature. Samples were synthesized by direct reaction during SPS. The squares represents  $\text{CuFeS}_2$  made by traditional melting and hotpressing.

Figure 6.13 shows that the SPS synthesized samples were much more electrically conductive, with the data for the SPS samples consistently an order of magnitude or more below the hotpressed sample. In line with this, Figure 6.14 showed a large decrease in the magnitude of the Seebeck coefficient as compared the hotpressed sample.

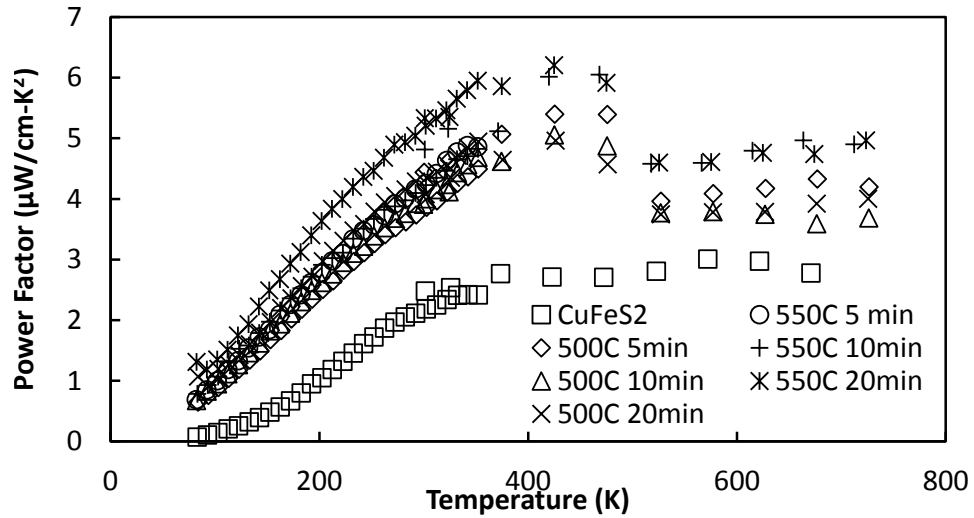


Figure 6.15: Power factor of several samples of  $\text{CuFeS}_2$  as a function of temperature. Samples were synthesized by direct reaction during SPS. The squares represents  $\text{CuFeS}_2$  made by traditional melting and hotpressing.

As Figure 6.15 shows, the compounds directly reacted in the SPS displayed a much improved power factor, though still less than the zinc doped samples of  $\text{CuFeS}_2$  displayed previously in Figure 6.9. The samples synthesized at  $550^\circ\text{C}$  show larger values than the samples sintered at  $500^\circ\text{C}$ , however as mentioned above, they were mechanically less robust, and prone to chipping.

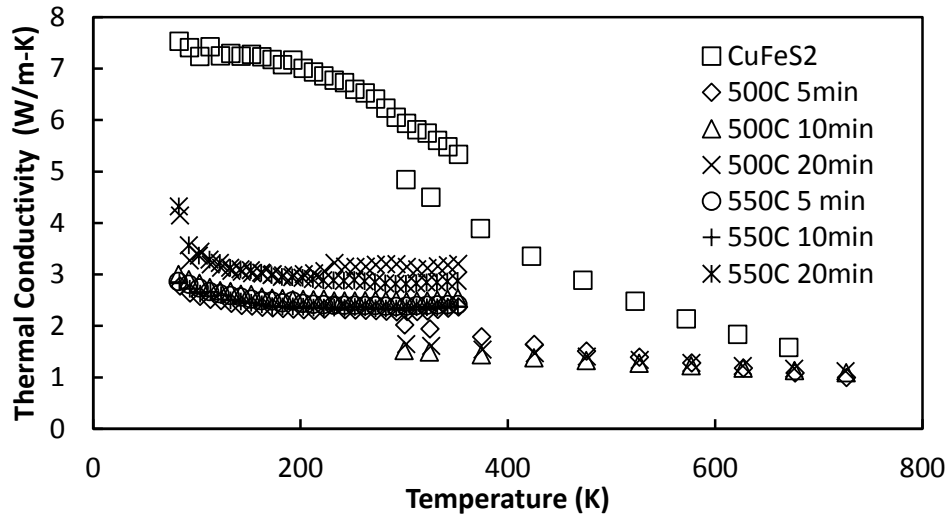


Figure 6.16: Thermal conductivity of several samples of CuFeS<sub>2</sub> as a function of temperature. Samples were synthesized by direct reaction during SPS. The squares represents CuFeS<sub>2</sub> made by traditional melting and hotpressing.

The thermal conductivity also shows a large reduction with SPS synthesis. This effect could be due to the small particle size (100 and 200 mesh, or 150 and 75 micron) starting powders leading to a smaller grain size after sintering, which in turn lead to increased phonon scattering.

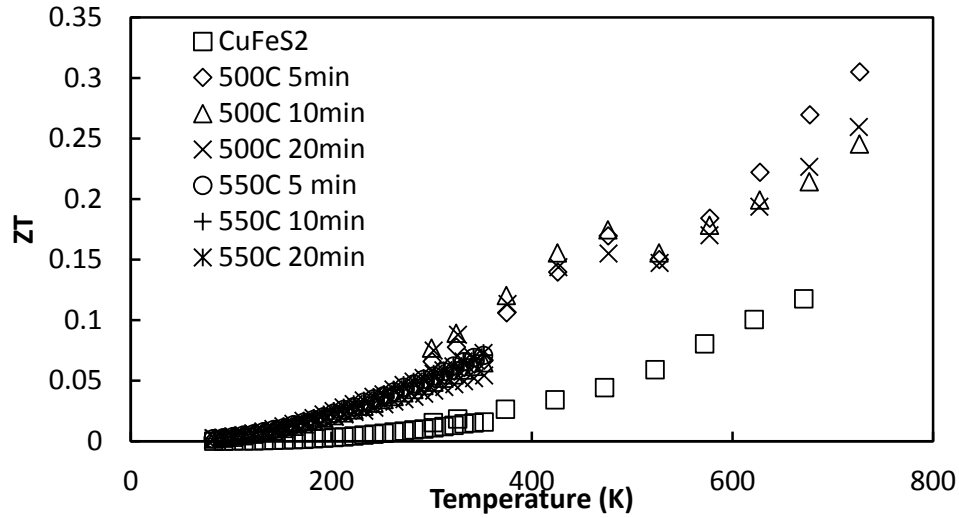


Figure 6.17:  $ZT$  of several samples of  $\text{CuFeS}_2$  as a function of temperature. Samples were synthesized by direct reaction during SPS. The squares represents  $\text{CuFeS}_2$  made by traditional melting and hotpressing.

In attempting to understand the differences in the SPS direct reaction samples as compared to the conventionally made samples one concern was sulfur sublimation during synthesis. This seems to be a likely occurrence, and comparison to work by Li *et al.* appeared to confirm the hypothesis. Their work studied synthesis of  $\text{CuFeS}_2$  by mechanical alloying via planetary milling, and also studied intentionally sulfur deficient chalcopyrite,  $\text{CuFeS}_{2-x}$ . [23] They showed that the sintering temperature was crucial for controlling sulfur loss, and reported properties on intentionally sulfur deficient samples.

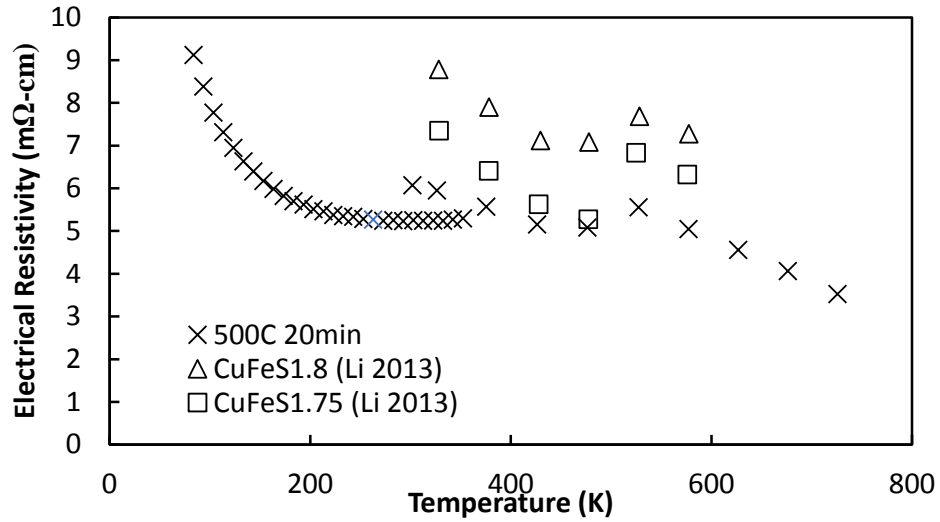


Figure 6.18: Electrical resistivity of several samples of  $\text{CuFeS}_2$  synthesized by direct reaction during SPS compared to literature values for  $\text{CuFeS}_{2-\delta}$ . The X symbol represents the data from samples made in this study, the other symbols are from Li *et al.*[23]

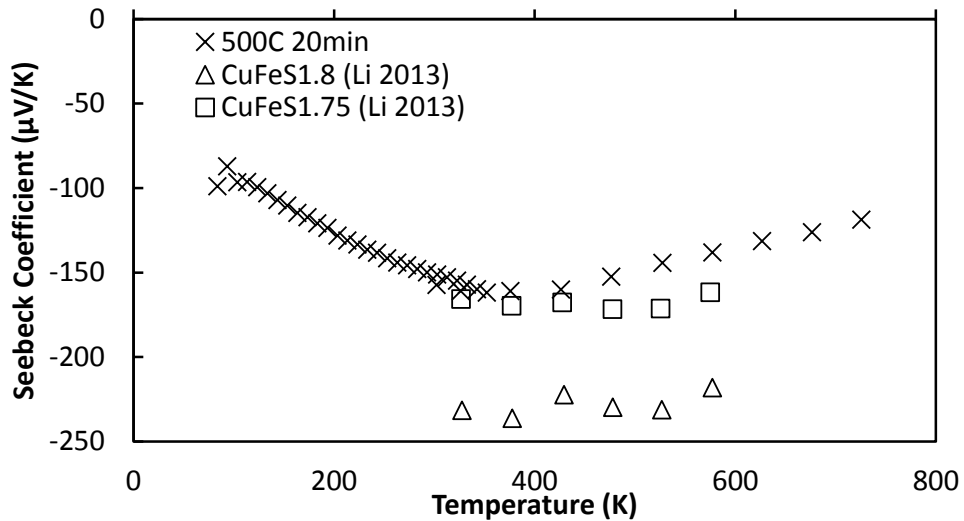


Figure 6.19: Seebeck coefficient of several samples of  $\text{CuFeS}_2$  synthesized by direct reaction during SPS compared to literature values for  $\text{CuFeS}_{2-\delta}$ . The X symbol represents the data from samples made in this study, the other symbols are from Li *et al.*[23]

Comparing the electrical properties, the samples synthesized here appear to be roughly  $\text{CuFeS}_{1.75}$ , as is seen by comparing Figure 6.18 and Figure 6.19. This sulfur loss is somewhat unsurprising, as one of the binary powders,  $\text{CuS}$ , is reported to decompose at  $507^\circ\text{C}$ . [122]

This indicates that the majority of the CuS is reacting with FeS, but in the process some of the sulfur is sublimating too quickly to react.

### 6.3 $\text{CuInS}_2$

$\text{CuInS}_2$  has a reported band gap of 1.47 eV to 1.55 eV and can reportedly be doped either n- or p-type, however the samples synthesized in this study were repeatedly found to be p-type and highly resistive.[123, 124] The sample shown below was synthesized in the same manner as  $\text{CuFeS}_2$ , with densification performed by hotpressing. Figure 6.20 shows a clean single phase XRD pattern, indicating the sample purity was high. Shown below is the electrical resistivity and thermal conductivity. No high temperature properties were measured, as the sample was too resistive to be measured in the ZEM3.

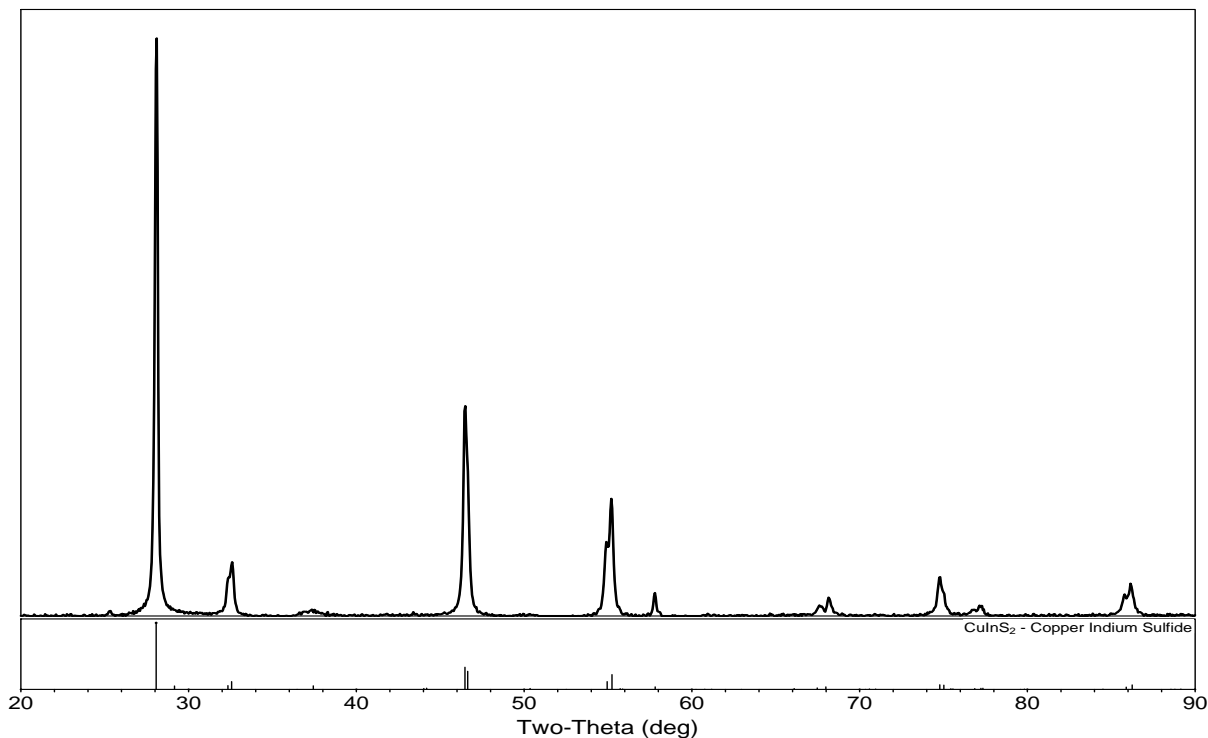


Figure 6.20: XRD pattern of  $\text{CuInS}_2$ . The pattern shown below is PDF# 01-075-6866.[24]

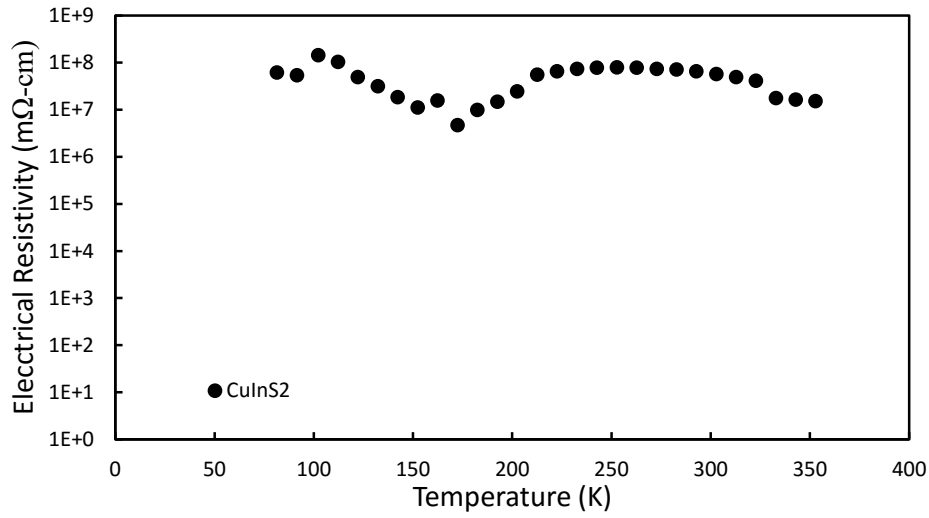


Figure 6.21: Electrical resistivity of CuInS<sub>2</sub> as a function of temperature

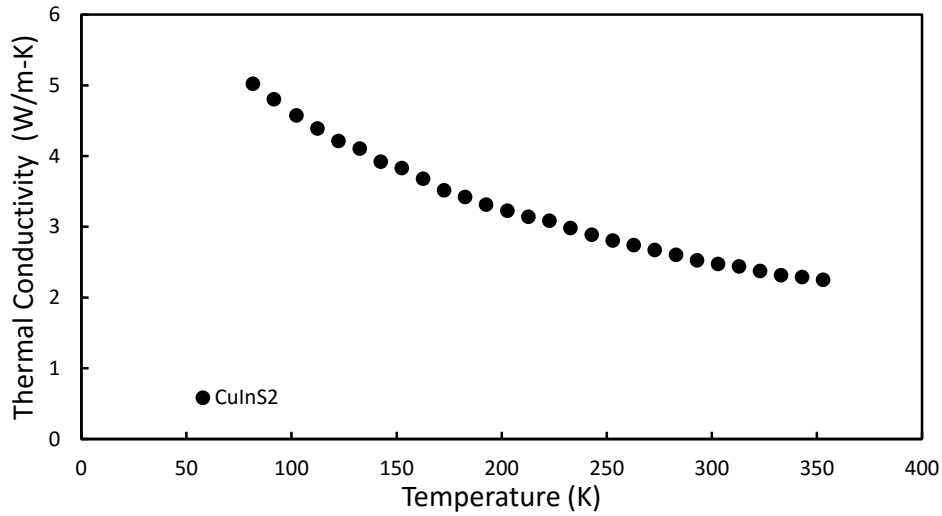


Figure 6.22: Thermal conductivity of CuInS<sub>2</sub> as a function of temperature

## 6.4 CuGaS<sub>2</sub>

CuGaS<sub>2</sub> is a wide gap semiconductor, with a reported band gap of 2.4 to 2.5 eV.[125, 110, 25]

Studies by Tell *et al.* found that samples that were annealed under high sulfur pressure displayed a room temperature electrical resistivity of  $1 \times 10^3$  mΩ cm, while samples annealed

under a low pressure of sulfur had a room temperature electrical resistivity greater than  $1 \times 10^8 \text{ m}\Omega \text{ cm}$ . [125, 110] As seen in Figure 6.23, data from work by Julian *et al.* shows similar results, with electrical resistivities in excess of  $1 \times 10^7 \text{ m}\Omega \text{ cm}$ . [25] Due to the high electrical resistivity and large band gap, no samples of  $\text{CuGaS}_2$  were synthesized in this study.

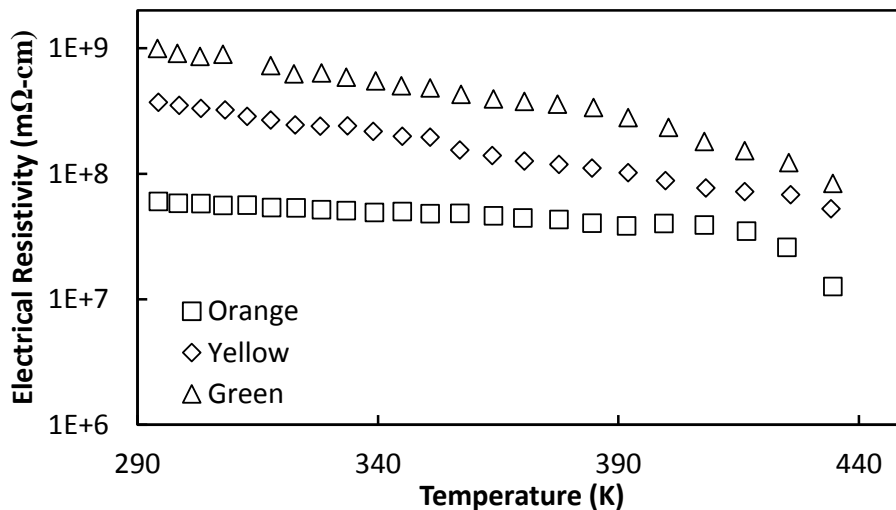


Figure 6.23: Electrical resistivity of several samples of  $\text{CuGaS}_2$  from work by Julien *et al.* The samples were simply described by their apparent colors. [25]

## 6.5 Solid Solutions

### 6.5.1 $\text{CuFeS}_{2(1-x)}\text{Se}_{2x}$

Although  $\text{CuFeSe}_2$  does not form in the chalcopyrite structure, and as such a full solid solution was unable to be formed, the solubility limit of selenium for sulfur was nonetheless studied. [105, 106, 126] Samples were made with 5% increments of selenium substitution up to 30%, above which point secondary phases were discovered by XRD and DSC.

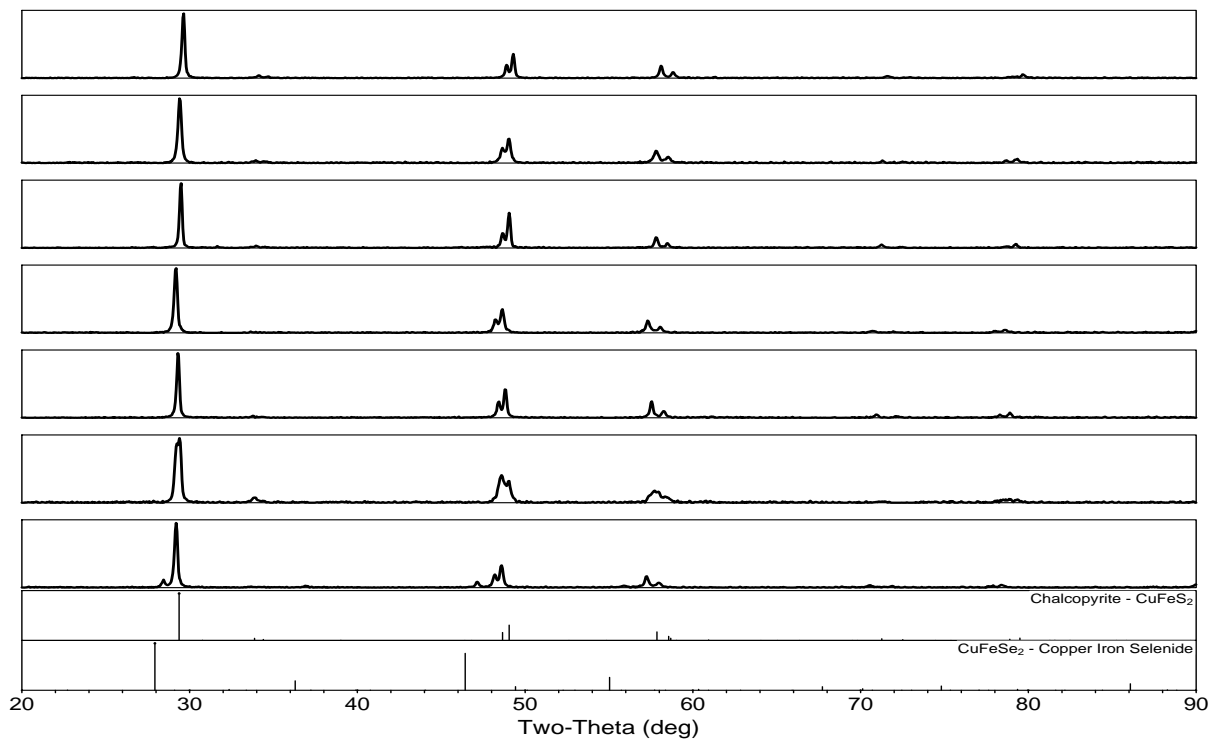


Figure 6.24: XRD patterns of the series  $\text{CuFeS}_2(1-x)\text{Se}_2x$ . The top pattern is pure  $\text{CuFeS}_2$ , with each pattern beneath it increasing  $x$  by 0.05, the at the bottom being final pattern  $\text{CuFeS}_{1.4}\text{Se}_{0.6}$ . Note the additional peaks in the bottom pattern, indicating the presence of a secondary phase. PDFs for patterns are #01-075-6866 and #01-081-1959 for  $\text{CuFeS}_2$  and  $\text{CuFeSe}_2$  respectively. [26, 27]

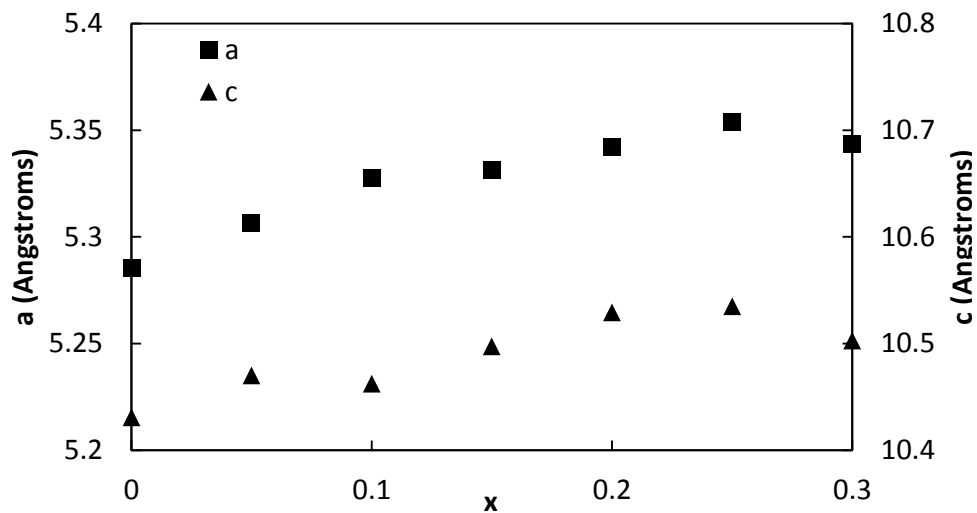


Figure 6.25: Lattice parameters of the series  $\text{CuFeS}_{2(1-x)}\text{Se}_{2x}$  as a function of  $x$ . Increasing selenium leads to a larger lattice, however at  $x = 0.3$  the growth stops, as a solubility limit is reached.

As shown in Figure 6.25, selenium substitution caused a shift in the XRD peaks towards lower  $2\theta$ , indicating an increase in the unit cell size as expected from the larger ionic radius of selenium. As shown in Figure 6.25 both the  $a$  and  $c$  lattice parameters increase linearly in selenium concentration up to  $x = 0.25$  ( $\text{CuFeS}_{1.5}\text{Se}_{0.5}$ ), but above this the  $x = 0.3$  sample shows nearly identical parameters as that of  $x = 0.25$ , indicating the selenium is no longer going in to the structure substitutionally for sulfur.

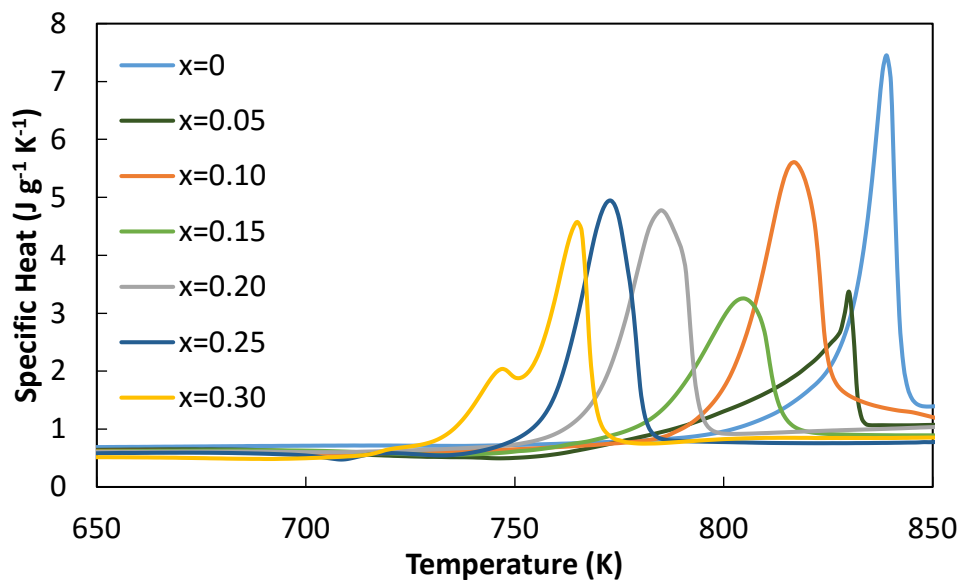


Figure 6.26: Specific heat of the series  $\text{CuFeS}_2(1-x)\text{Se}_{2x}$  as a function of temperature. The peaks indicate decomposition into a mixture of binary phases, followed by the sublimation of sulfur.

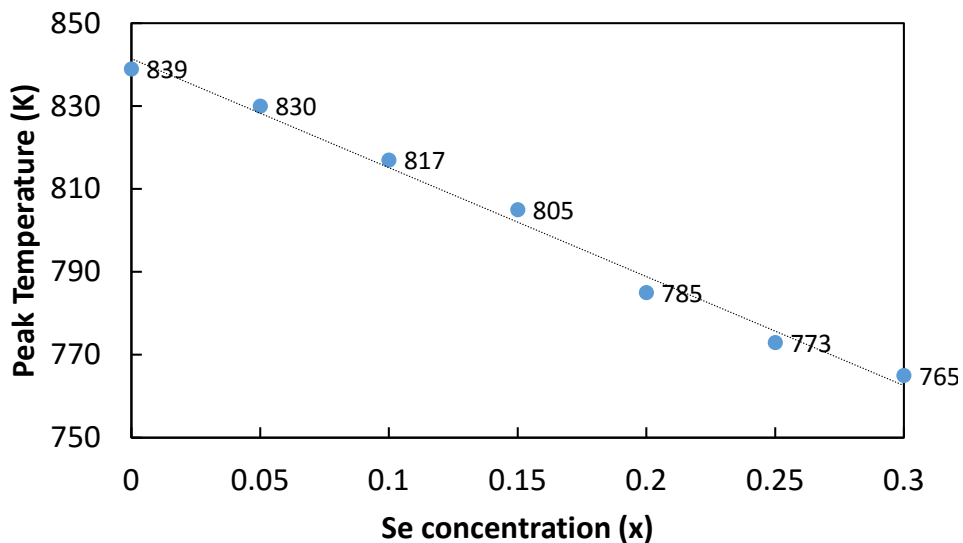


Figure 6.27: Temperature of the peak in the DSC curve for the series  $\text{CuFeS}_2(1-x)\text{Se}_{2x}$ . The peaks indicate decomposition into a mixture of binary phases, followed by the sublimation of sulfur.

As the specific heat data shows in Figure 6.26, a large peak is observed for all the

samples at high temperature. Work by Tsujii *et al.* using thermogravimetric and differential thermal analysis (TG-DTA) found that at 820K  $\text{CuFeS}_2$  decomposed in to a mixture of  $\text{FeS}_2$ ,  $\text{CuS}$ , and  $\text{FeS}$ , and shortly above that temperature sulfur sublimated.[19] This aligns very well with the observed data from our DSC measurements, where a peak in specific heat is observed at 840K. As we see, with increasing selenium concentration, the peak shifts to lower temperatures. It is surmised that lattice strain from the larger atomic radius of selenium pushes the transition to lower temperatures. A linear trend was found between the selenium concentration and the temperature at which the specific heat curve peaked, as shown in Figure 6.27. For the  $x = 0.30$  sample, ( $\text{CuFeS}_{1.4}\text{Se}_{0.6}$ ) a second peak was observed in the DSC. This, along with the extra peaks in XRD confirmed the material was two phase and that a solubility limit had been reached between 25% and 30%.

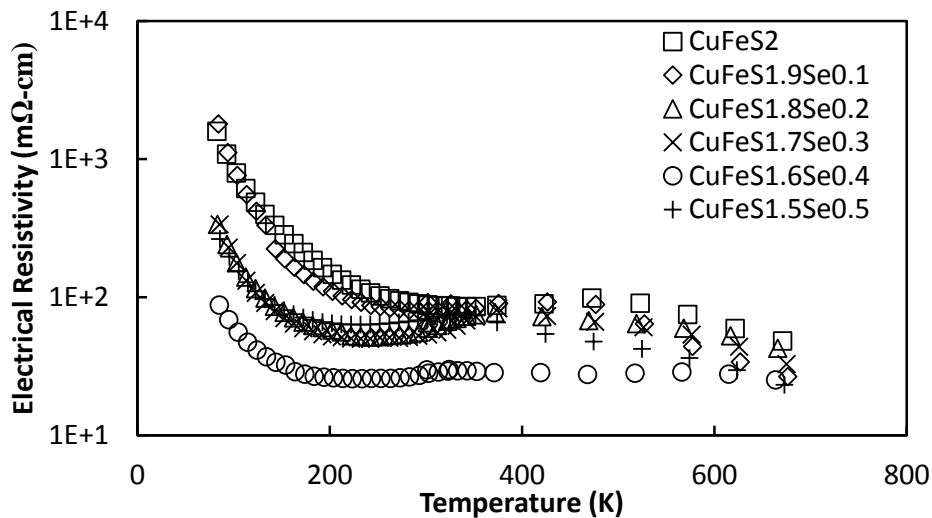


Figure 6.28: Electrical resistivity of the series  $\text{CuFeS}_{2(1-x)}\text{Se}_{2x}$  as a function of temperature.

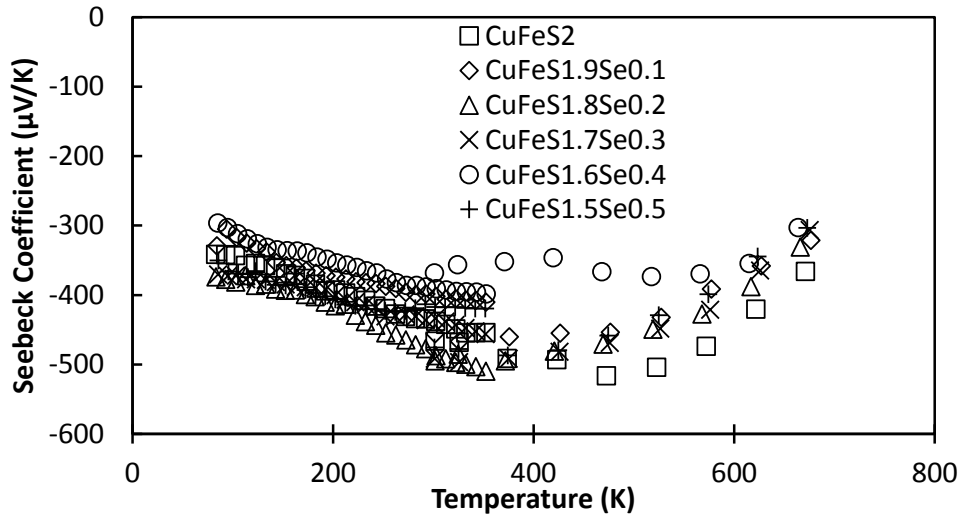


Figure 6.29: Seebeck coefficient of the series  $\text{CuFeS}_{2(1-x)}\text{Se}_{2x}$  as a function of temperature.

Figure 6.28 shows that increasing selenium substitution lead to a decrease in electrical resistivity. As the substitution is isoelectronic, it is suspected that a decrease in the band gap is causing this effect, rather than doping. The Seebeck coefficient showed a slight decrease in magnitude with increasing selenium concentration as shown in Figure 6.30, in line with the decreased electrical resistivity, but all samples still displayed negative values indicating n-type carriers.

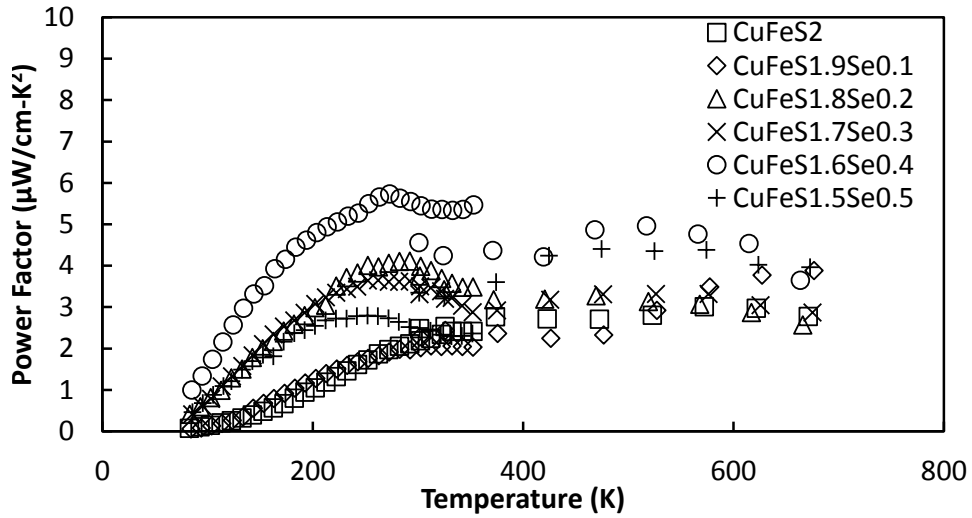


Figure 6.30: Power factor of the series  $\text{CuFeS}_{2(1-x)}\text{Se}_{2x}$  as a function of temperature.

The increase in the electrical conductivity combined with the minimal drop in Seebeck coefficient magnitude lead to a rise in power factor, with  $\text{CuFeS}_{1.6}\text{Se}_{0.4}$  showing the highest value. The broad flat peak in Seebeck coefficient is mirrored in the power factor, with values above 350K nearly temperature independent. The values are comparable to that obtained from the samples synthesized by direct SPS reaction of powders.

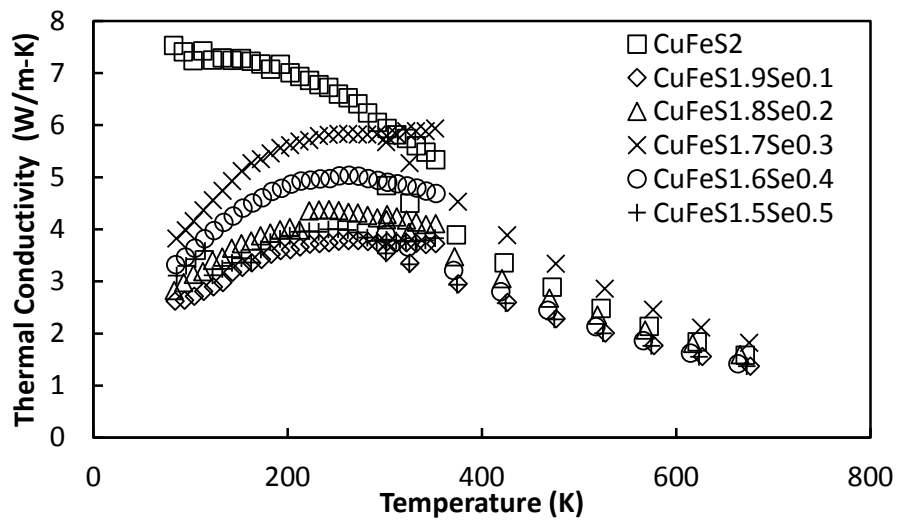


Figure 6.31: Thermal conductivity of the series  $\text{CuFeS}_{2(1-x)}\text{Se}_{2x}$  as a function of temperature.

The isoelectronic substitution of selenium for sulfur caused a large drop in thermal conductivity at low temperatures, as shown in Figure 6.31, and with the exception of  $\text{CuFeS}_{1.7}\text{Se}_{0.3}$  all the selenium containing samples exhibit lower thermal conductivity than the pure  $\text{CuFeS}_2$  sample. Ultimately, values near  $1.3 - 1.5 \text{ W m}^{-1} \text{ K}^{-1}$  are obtained for all the samples at 700K.

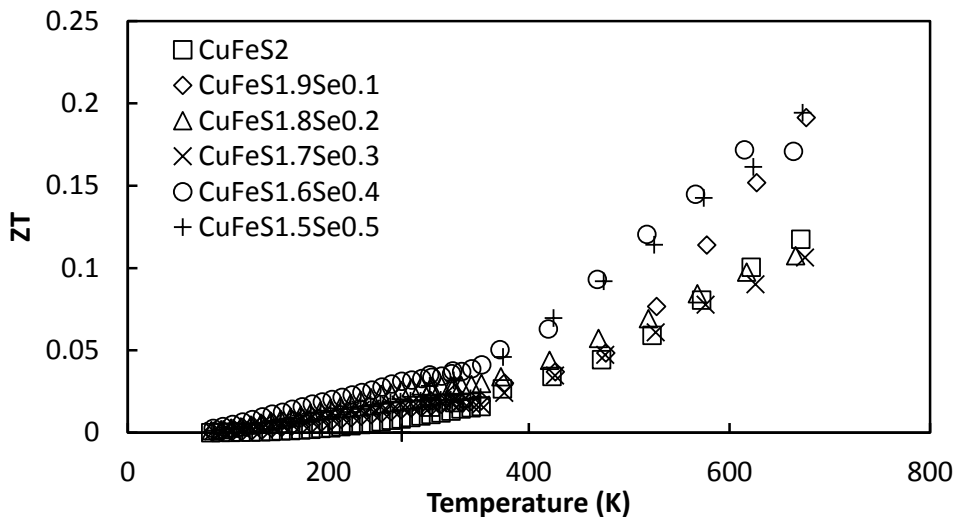


Figure 6.32:  $ZT$  of the series  $\text{CuFeS}_{2(1-x)}\text{Se}_{2x}$  as a function of temperature.

Overall the  $ZT$  is increased for three samples:  $\text{CuFeS}_{1.9}\text{Se}_{0.1}$ ,  $\text{CuFeS}_{1.6}\text{Se}_{0.4}$ , and  $\text{CuFeS}_{1.5}\text{Se}_{0.5}$ , while for the other samples the resulting  $ZT$  is the same as that of the unmodified  $\text{CuFeS}_2$ . A trade off is also found with selenium concentration, as increasing the selenium content lowers the maximum operating temperatures, as shown by DSC measurements.

### 6.5.2 $\text{CuFeS}_{2(1-x)}\text{Te}_{2x}$

As stated in the introduction,  $\text{CuFeTe}_2$  does not form in the chalcopyrite structure, but rather forms a layered structure with space group  $P4/nmm$ . [127, 128] It is reported as zero gap semiconductor, with a reported room temperature carrier concentration on the order of

$1 \times 10^{20} \text{ cm}^{-3}$  to  $1 \times 10^{21} \text{ cm}^{-3}$ . [129, 130] Samples of  $\text{CuFeTe}_2$  were not synthesized in this study, due to their different structure, and the zero gap nature making  $\text{CuFeTe}_2$  ill suited for thermoelectrics. However, samples with low amounts of tellurium were synthesized to establish the solubility limit of tellurium in  $\text{CuFeS}_2$ . As Figure 6.33 shows, even with only 5% of sulfur replaced with tellurium extra peaks were observed.

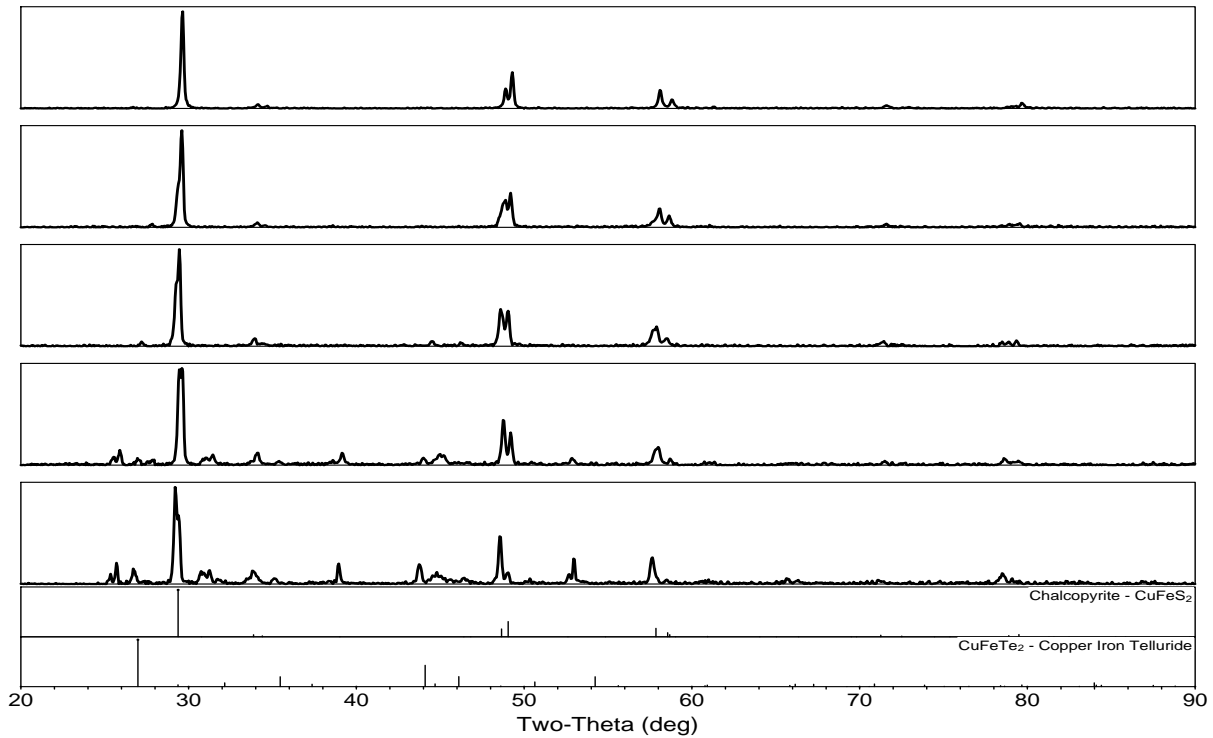


Figure 6.33: XRD Patterns of  $\text{CuFeS}_2(1-x)\text{Te}_2x$ . The top pattern is for pure  $\text{CuFeS}_2$ , followed by  $x = 0.05, 0.10, 0.2,$  and  $0.3$ . The patterns below are from PDF #01-075-6866 and #01-070-3094 for  $\text{CuFeS}_2$  and  $\text{CuFeTe}_2$  respectively. [26, 28]

### 6.5.3 $\text{CuFe}_{1-x}\text{Ga}_x\text{S}_2$

An attempt was made to form a solid solution of  $\text{CuFeS}_2$  with  $\text{CuGaS}_2$ . While the two compounds are electronically very different (reported band gap of  $0.5\text{eV}$  versus  $2.4\text{eV}$ ) [125, 110, 25, 120, 121, 23] the lattice parameters are very similar. However, all attempts to make a solid solution yielded a multi-phase material, typically consisting of a mixture of

CuFeS<sub>2</sub>, CuGaS<sub>2</sub>, and GaS. The samples were also very prone to cracking the ampoules upon quenching.

## 6.6 Conclusions

The sulfide compounds were found to be overall less promising than the telluride compounds for thermoelectric applications. CuInS<sub>2</sub> and CuGaS<sub>2</sub> displayed large electrical resistivities, as was expected from their larger band gaps (roughly 1.5 eV and 2.5 eV respectively). However, the earth-abundant mineral for CuFeS<sub>2</sub> showed intriguing properties. It displayed n-type conduction, standing out from all of the other materials studied in this family, as well as a smaller band gap (0.3 eV - 0.5 eV) when compared to other compounds studied in this work. However, the performance is limited somewhat by sulfur sublimation, limiting the operating temperature to less than 450 °C.

CuFeS<sub>2</sub> also showed poor solubility limits with isoelectronic elements. Attempts to substitute gallium for iron or tellurium for sulfur was unsuccessful on all levels, and only yielded multi phase material. The solubility limit for selenium on the sulfur site was found to be between 25% and 30%, however, substituting selenium pushed the sublimation point to lower temperatures, lowering the possible operating temperature further. Zinc was found to be an effective dopant for CuFeS<sub>2</sub>, giving an increase in  $ZT$  to a peak value of 0.3 at 725K. It was also found that sulfur deficient CuFeS<sub>2</sub> could be rapidly synthesized by directly spark-plasma-sintering mixtures of CuS and FeS, with peak  $ZT$  values again near 0.3.

Overall CuFeS<sub>2</sub> does offer promise as a reasonably good thermoelectric with n-type properties that could be paired with one of the many other p-type chalcopyrite compounds.

# Chapter 7

## Related Materials

As part of our study of chalcopyrite compounds some similar and related phases have been investigated as well. These include a naturally occurring mineral called bornite ( $\text{Cu}_5\text{FeS}_4$ ), as well as several defect-chalcopyrite phases.

### 7.1 Bornite: $\text{Cu}_5\text{FeS}_4$

Bornite is a naturally occurring sulfide mineral, as is  $\text{CuFeS}_2$ , however the structure of bornite is much more complex. It has reported structural phase transitions at both  $200^\circ\text{C}$  and at  $265^\circ\text{C}$ . [131, 132, 133] The high temperature phase is a cubic structure (space group  $\text{Fm}\bar{3}\text{m}$ ) with a reported lattice constant  $a$  of  $5.49 \text{ \AA}$ , consisting of an FCC sulfur lattice, with copper, iron, and vacancies on the eight tetrahedral interstitial sites. At intermediate temperatures the compound forms a superstructure (still  $\text{Fm}\bar{3}\text{m}$ ) with a lattice parameter  $a$  of  $10.95 \text{ \AA}$ , which one can picture as a double of the cell in all three crystallographic directions, with long range order. Below  $200^\circ\text{C}$  the compound forms a more complex superstructure which is orthorhombic (spacegroup  $\text{Pbca}$ ) with  $a = b = 10.95 \text{ \AA}$  and  $c = 21.862 \text{ \AA}$ . [30]

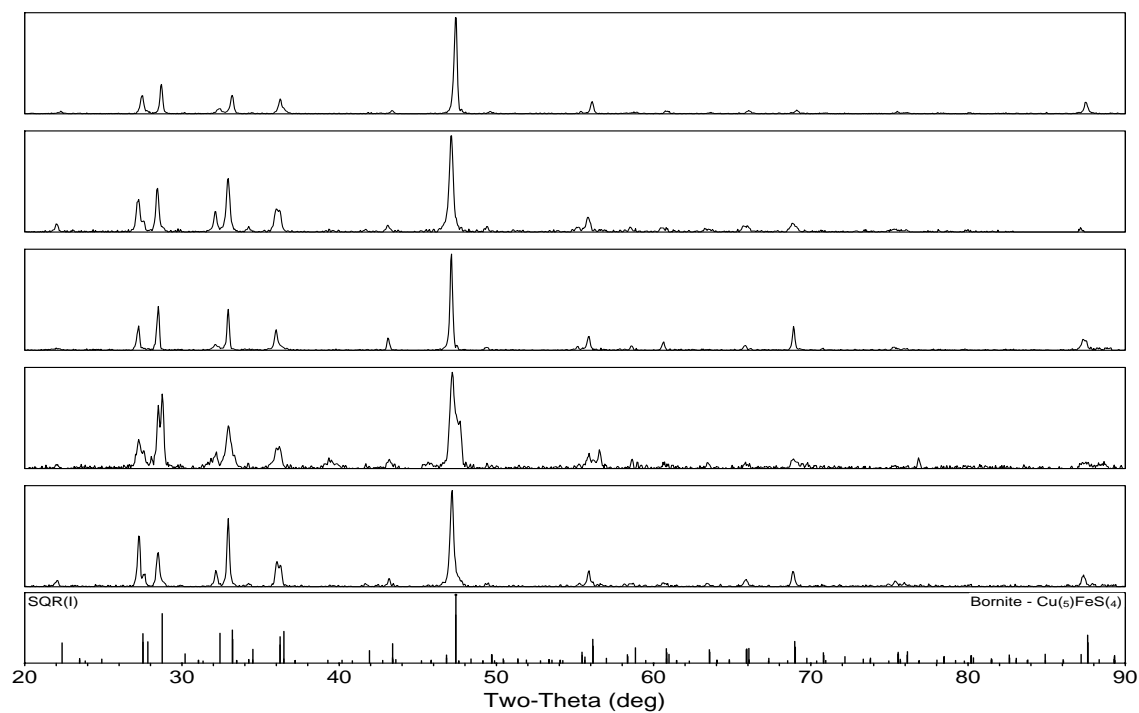


Figure 7.1: XRD pattern of nominally pure bornite ( $\text{Cu}_5\text{FeS}_4$ ) and four doped compositions. The top pattern is pure  $\text{Cu}_5\text{FeS}_4$ , followed by the 1% and 5% p-type doped samples, and finally the 1% and 5% n-type doped samples. The extra peaks observed in the 1% n-type sample are due to a secondary phase of FeS. The y-scale is intensity, in arbitrary units. Source: PDF #98-000-0123.[29]

In this work, samples of pure bornite, along with four zinc doped samples were synthesized. Bornite has been shown to exhibit both n- and p-type conduction, and so doping was attempted with zinc on both the copper (nominally monovalent) and the iron (nominally trivalent) sites in an attempt to dope it both p- and n-type. As shown Figure 7.1 the 1% n-type doped sample ( $\text{Cu}_{4.95}\text{Zn}_{0.05}\text{FeS}_4$ ) showed extra peaks, which were identified as FeS, however the other samples all appeared to be single phase, matching well to the database pattern.[29]

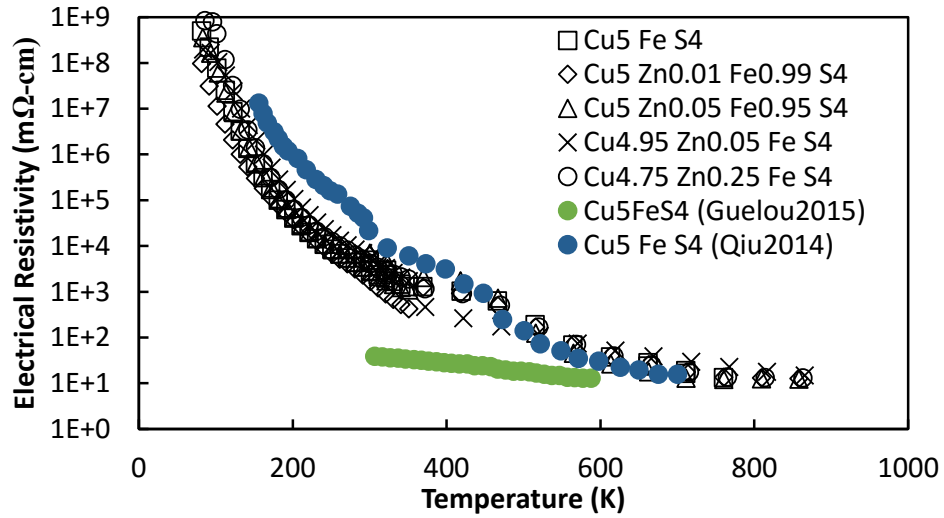


Figure 7.2: Electrical resistivity of samples of nominally pure bornite ( $\text{Cu}_5\text{FeS}_4$ ) and four doped compositions as a function of temperature. Literature data is shown with colored symbols for comparison.[30, 31]

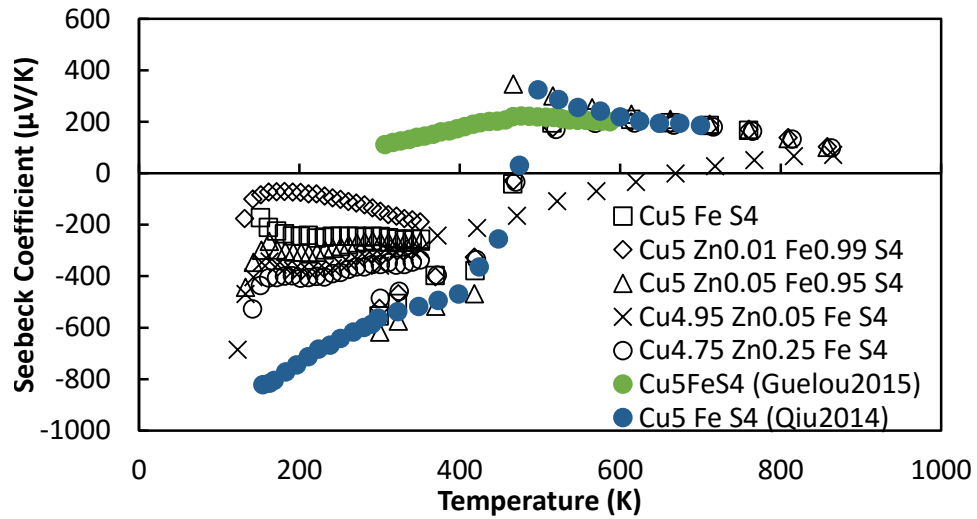


Figure 7.3: Seebeck coefficient of samples of nominally pure bornite ( $\text{Cu}_5\text{FeS}_4$ ) and four doped compositions as a function of temperature. Literature data is shown with colored symbols for comparison.[30, 31]

As seen in Figure 7.2 bornite displayed a very large electrical resistivity at 80K, with the pure sample, as well as the doped samples, showing an electrical resistivity near  $1 \times 10^9$   $\text{m}\Omega\text{cm}$ . The value dropped dramatically with temperature, possibly indicating a narrow

band gap, with all samples measured here, as well as literature values, dropping to 10-15 m $\Omega$  cm at 800K.[30, 31]

The Seebeck coefficient at low temperatures displayed n-type conduction for all samples. The data from the ZEM showed a larger magnitude than the cryostat data at 300K, giving an offset in the data, for all samples except  $\text{Cu}_{4.95}\text{Zn}_{0.05}\text{FeS}_4$ . Again, with the exception of  $\text{Cu}_{4.95}\text{Zn}_{0.05}\text{FeS}_4$  which showed impurities in XRD, the Seebeck coefficient for the samples show a change in trend near 420K ( 150°C) with a large upward swing. Over the range from 420K to 520K°C the Seebeck coefficient of  $\text{Cu}_5\text{FeS}_4$  increases from  $-378 \mu\text{V K}^{-1}$  to  $+195 \mu\text{V K}^{-1}$ , a change of nearly  $600 \mu\text{V K}^{-1}$ . This swing corresponds to the initial phase transition, which was reported to occur at 470K. Above 520K, the Seebeck coefficient displays a small downward trend, with the samples remaining positive for the remainder of the measurement.

While the electrical resistivity is very similar for all five samples, regardless of the zinc doping level, the Seebeck coefficient did show a difference at low temperature. There was no clear trend with zinc concentration, indicating zinc was ineffective as a dopant. With the high amount of vacancies in the compound, it is difficult to know where the zinc will sit in the lattice.

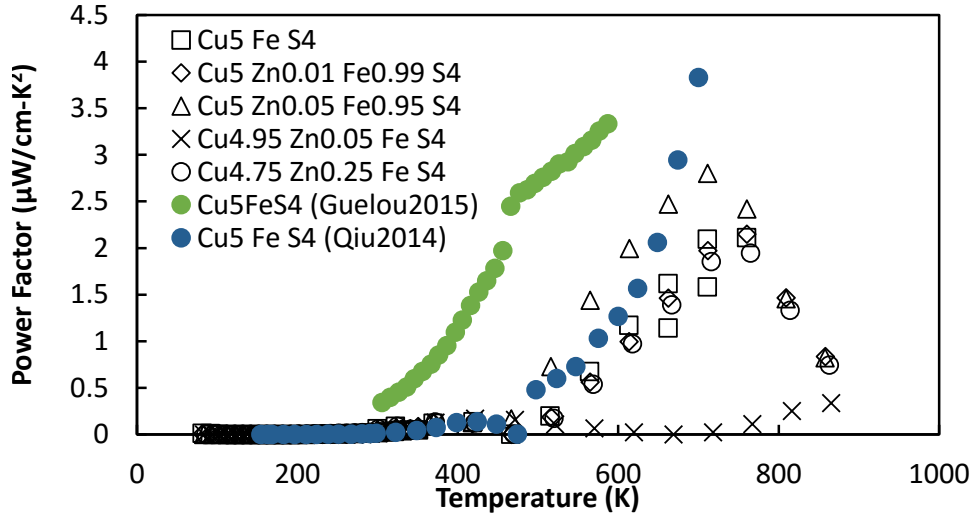


Figure 7.4: Power factor of samples of nominally pure bornite ( $\text{Cu}_5\text{FeS}_4$ ) and four doped compositions as a function of temperature. Literature data is shown with colored symbols for comparison.[30, 31]

The strong decrease in electrical resistivity along with the relatively flat Seebeck coefficient above 500K leads to a sharp increase in the power factor. All of the samples peak near 700K, with peak values ranging of  $2\text{-}3 \mu\text{W cm}^{-1} \text{K}^{-2}$ . The samples synthesized here match well with the data published by Qiu *et al.*, while that from Guelou *et al.* differs. The samples in the study by Guelou were synthesized by mechanical alloying; the raw elemental powders were ball milled for 20 hours before hot pressing.[31] Those synthesized in the report by Qiu were synthesized in the same furnace technique as those samples measured in this study.[30] The higher power factor seen in the study by Guelou as compared to that obtained in work here and the data reported by Qiu, could be due to the high sensitivity to defects or stoichiometry. The different synthesis techniques (mechanical alloying by Guelou versus traditional melt and quench technique used in this work and by Qiu) could also play an important role in controlling the electronic properties of the material.

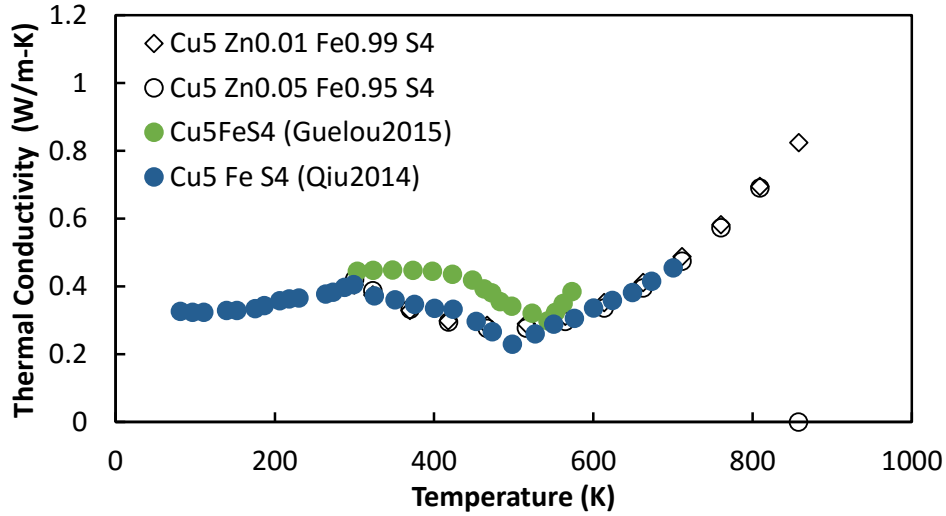


Figure 7.5: Thermal conductivity of samples of nominally pure bornite ( $\text{Cu}_5\text{FeS}_4$ ) and four doped compositions as a function of temperature. Literature data is shown with colored symbols for comparison.[30, 31]

The thermal conductivity for all samples showed very low values, less than  $1.0 \text{ W m}^{-1} \text{ K}^{-1}$ . As shown in Figure 7.5 the thermal conductivity initially showed a rise with temperature, with a peak near 300K, after which the values drop to a minimum at 500K, the same temperature at which the Seebeck coefficient changed sign, corresponding to the phase transition. The thermal conductivity shows a rise above this temperature, however the value for the samples remained below  $1 \text{ W m}^{-1} \text{ K}^{-1}$ . Thermal conductivity is not shown for the pure bornite, or for  $\text{Cu}_{4.95}\text{Zn}_{0.05}\text{FeS}_4$  or  $\text{Cu}_{4.75}\text{Zn}_{0.25}\text{FeS}_4$  because the laser flash discs broke. Bornite was found to be brittle, and the discs were prone to cracking.

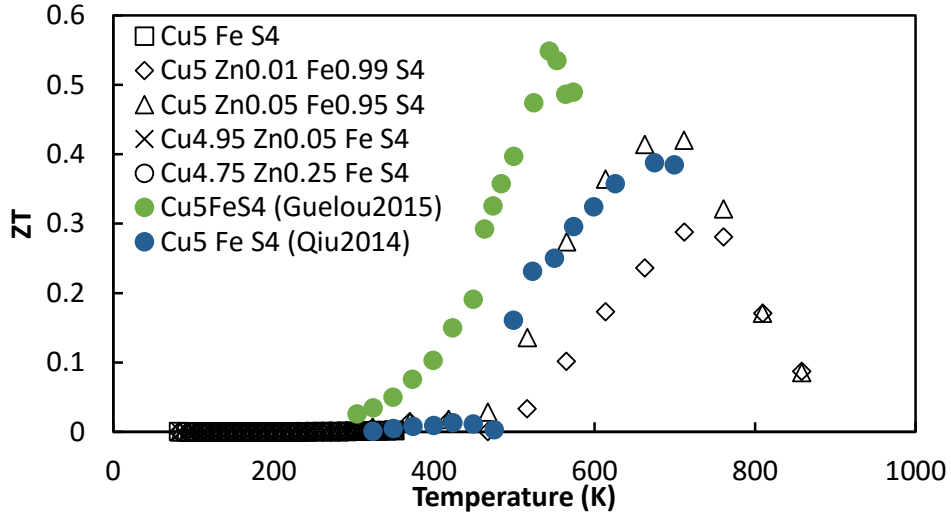


Figure 7.6:  $ZT$  of samples of nominally pure bornite ( $\text{Cu}_5\text{FeS}_4$ ) and four doped compositions as a function of temperature. Literature data is shown with colored symbols for comparison.[30, 31]

The resulting  $ZT$  is shown in Figure 7.6. Work by Guelou *et al.* showed a peak  $ZT$  of near 0.55 at 540K, while the data from Qiu *et al.*, as well as data for samples in this study showed a peak in the  $ZT$  at 700K, with a peak value of just over 0.40 for  $\text{Cu}_{4.95}\text{Zn}_{0.05}\text{Fe}_{0.95}\text{S}_4$ .  $ZT$  is not shown for the other samples at high temperature because the laser flash discs broke, and no thermal conductivity data was available. Bornite has also been reported to be a copper ionic conductor, which would be detrimental to its use as a thermoelectric. However, further studies in to doping could alleviate this issue, as has been shown with tetrahedrite. [134, 135]

## 7.2 Defect Chalcopyrite: $\text{Zn}_{0.5}\text{GaTe}_2$ and $\text{Zn}_{0.5}\text{InTe}_2$

The defect chalcopyrite structure can be thought of as replacing half of the monovalent atoms with a divalent atom while leaving the other half empty as vacancies, maintaining the average valence count of 4 per atom. In this work divalent zinc was substituted for half of

the monovalent copper. The compounds  $\text{Zn}_{0.50}\text{GaTe}_2$ ,  $\text{Zn}_{0.475}\text{GaTe}_2$ , and  $\text{Zn}_{0.50}\text{InTe}_2$  were synthesized and the low temperature properties were measured.

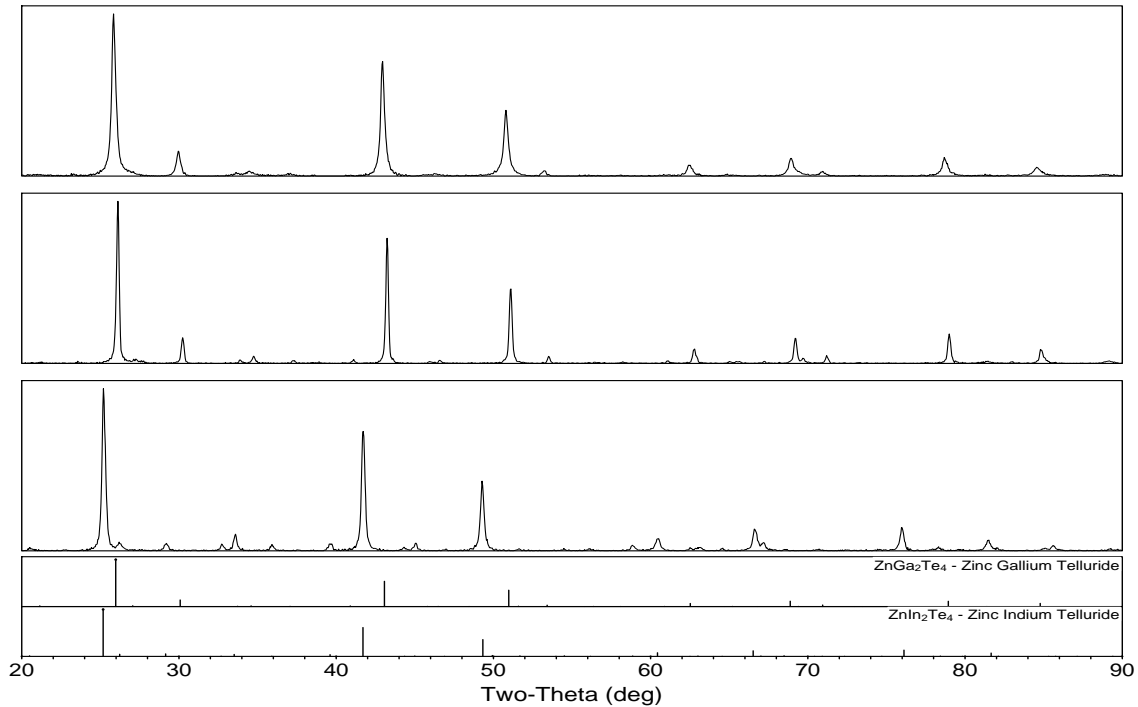


Figure 7.7: XRD patterns of the defect chalcopyrite compounds:  $\text{Zn}_{0.5}\text{GaTe}_2$ ,  $\text{Zn}_{0.475}\text{GaTe}_2$ , and  $\text{Zn}_{0.5}\text{InTe}_2$  from top to bottom respectively. The y-scale is intensity, in arbitrary units. Source: PDF #01-089-4209 and #01-074-0218 for  $\text{Zn}_{0.5}\text{GaTe}_2$  and  $\text{Zn}_{0.5}\text{InTe}_2$  respectively. [4]

First principle calculations performed on  $\text{Zn}_{0.5}\text{GaS}_2$ ,  $\text{Zn}_{0.5}\text{GaSe}_2$ , and  $\text{Zn}_{0.5}\text{GaTe}_2$  predicted the band gap of  $\text{Zn}_{0.5}\text{GaTe}_2$  to be 0.53 eV, very close to that of  $\text{CuFeS}_2$ . [136] The reported lattice parameters for  $\text{Zn}_{0.5}\text{GaTe}_2$  are  $a = 5.26 \text{ \AA}$  and  $c = 10.39 \text{ \AA}$ , giving a c:a ratio of 1.98:1. The XRD patterns shown in Figure 7.7 match to the published patterns by Hahn *et al.* for both  $\text{Zn}_{0.5}\text{GaTe}_2$  and  $\text{Zn}_{0.5}\text{InTe}_2$ .

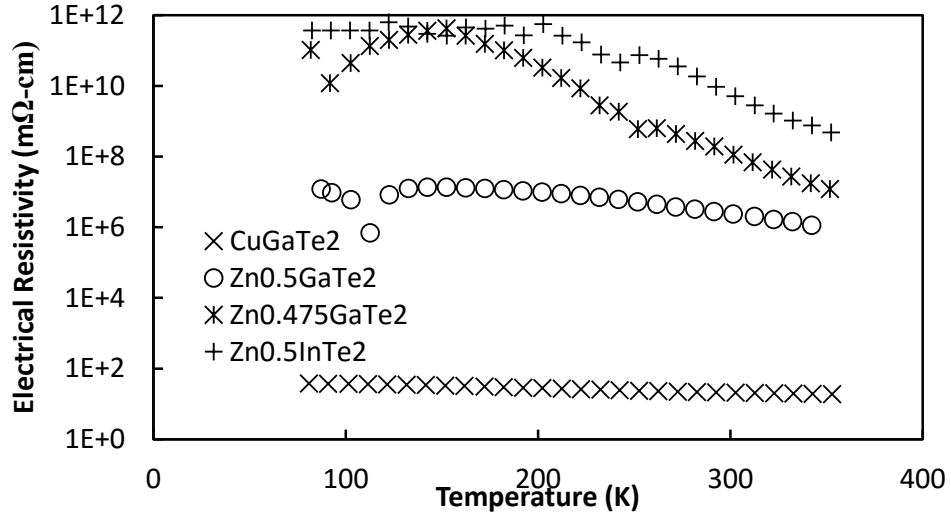


Figure 7.8: Electrical resistivity of defect chalcopyrite compounds, with  $\text{CuGaTe}_2$  as a reference, as a function of temperature.

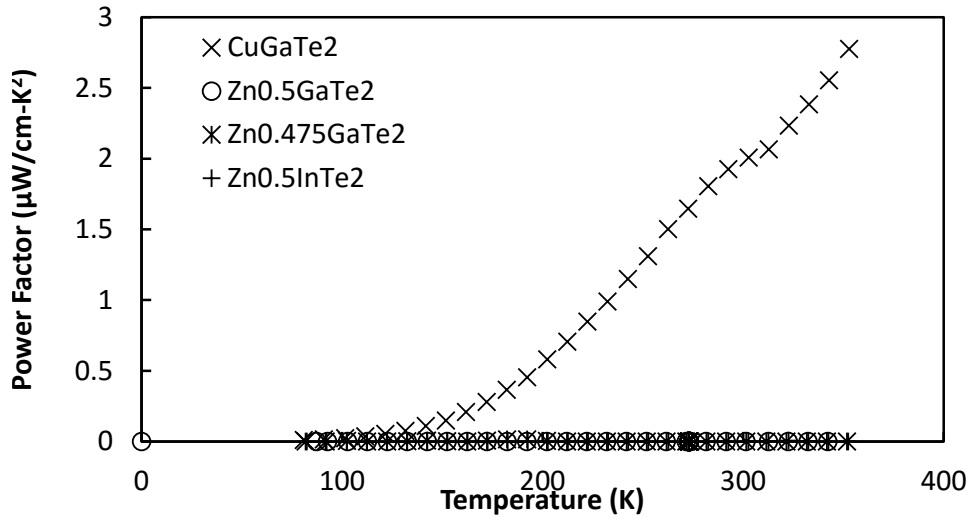


Figure 7.9: Power factor of defect chalcopyrite compounds, with  $\text{CuGaTe}_2$  as a reference, as a function of temperature.

As shown in Figure 7.8, the electrical resistivity of the defect samples was much higher than that of the nominally undoped  $\text{CuGaTe}_2$ .  $\text{Zn}_{0.50}\text{GaTe}_2$  displayed an electrical resistivity near  $1 \times 10^7 \text{ m}\Omega \text{ cm}$  from 80-350K, while the indium containing sample, and the vacancy heavy sample ( $\text{Zn}_{0.475}\text{GaTe}_2$ ) both displayed an electrical resistivity several orders of mag-

nitude higher. The Seebeck coefficient data is not shown here, as the high resistivity made the value difficult to measure. Nonetheless the power factor is shown in Figure 7.9, and it can be seen that the defect structure has an effective power factor of zero when compared to  $\text{CuGaTe}_2$ .

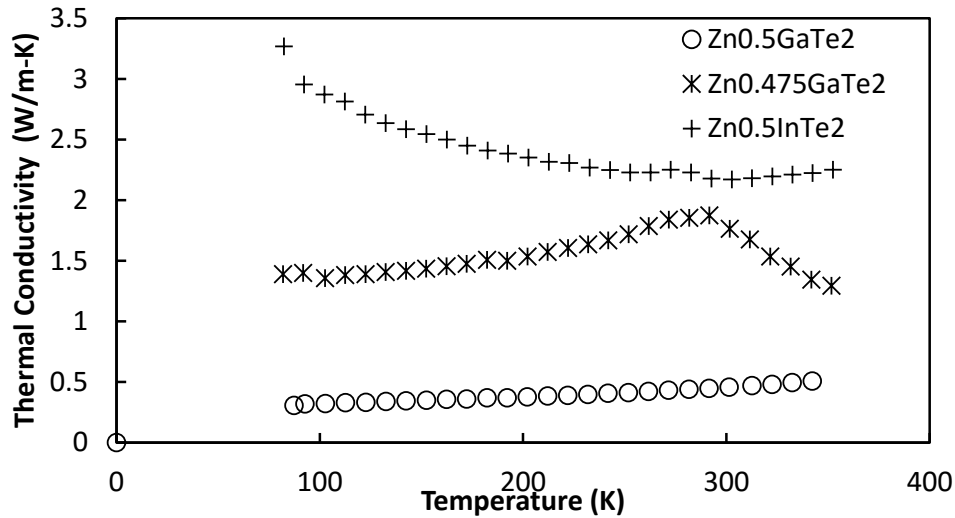


Figure 7.10: Thermal conductivity of defect chalcopyrite compounds as a function of temperature.

The thermal conductivity showed remarkably low values, as shown in Figure 7.10. All of the defect samples show values much lower than the normal chalcopyrite structure compound. The room temperature thermal conductivity of  $\text{CuInTe}_2$  is near  $4.5 \text{ W m}^{-1} \text{ K}^{-1}$ , while  $\text{Zn}_{0.50}\text{InTe}_2$  is nearly half of that, with a room temperature value of  $2.5 \text{ W m}^{-1} \text{ K}^{-1}$ .

The gallium containing compound showed an even larger deduction; the room temperature thermal conductivity of  $\text{CuGaTe}_2$  was  $7.0 \text{ W m}^{-1} \text{ K}^{-1}$ , while that of  $\text{Zn}_{0.50}\text{GaTe}_2$  is only  $0.45 \text{ W m}^{-1} \text{ K}^{-1}$ , and that of  $\text{Zn}_{0.475}\text{GaTe}_2$  is  $1.75 \text{ W m}^{-1} \text{ K}^{-1}$ . This drastic reduction in thermal conductivity, especially when comparing the indium containing sample to the gallium containing sample, is not fully understood at the time.

Previous works comparing the defect zinc-blende compounds  $\text{In}_2\text{Te}_3$  and  $\text{Ga}_2\text{Te}_3$  found

the thermal conductivity of  $\text{In}_2\text{Te}_3$  to be roughly three times as large as that of  $\text{Ga}_2\text{Te}_3$  at room temperature. Work by Kurosaki found that  $\text{Ga}_2\text{Te}_3$  naturally formed superlattice structures with ordered layers of vacancies throughout the structure, and attributed the difference in thermal conductivity values to that.[137] Whether a similar mechanism is responsible in  $\text{Zn}_{0.50}\text{GaTe}_2$  is unknown at this time, future work on this material would be enlightening.

While the thermal conductivity drop was dramatic, the power factor negated all the benefit, and the resulting  $ZT$  was effectively zero for the full defect compounds, as shown in Figure 7.11.

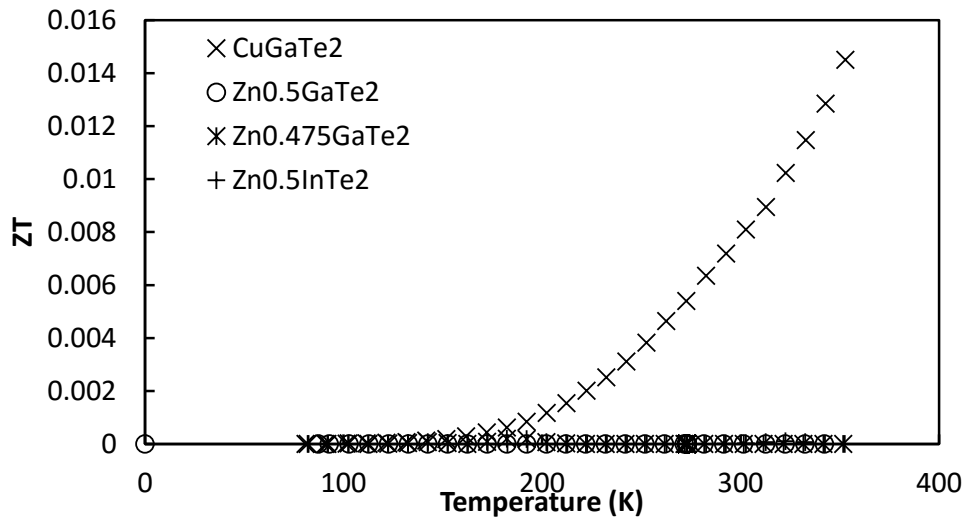


Figure 7.11:  $ZT$  of defect chalcopyrite compounds as a function of temperature.

### 7.2.1 Solid Solution: $\text{CuGaTe}_2$ - $\text{Zn}_{0.5}\text{GaTe}_2$

In attempt to gain some of the thermal conductivity benefits of  $\text{Zn}_{0.5}\text{GaTe}_2$  while maintaining the electrical properties of  $\text{CuGaTe}_2$  a solid solution was formed starting from  $\text{CuGaTe}_2$  and substituting small amounts of  $\text{Zn}_{0.5}\text{GaTe}_2$ . As shown in Figure 7.12 there was no visible change in XRD pattern up to  $\text{Cu}_{0.8}\text{Zn}_{0.1}\text{GaTe}_2$ .

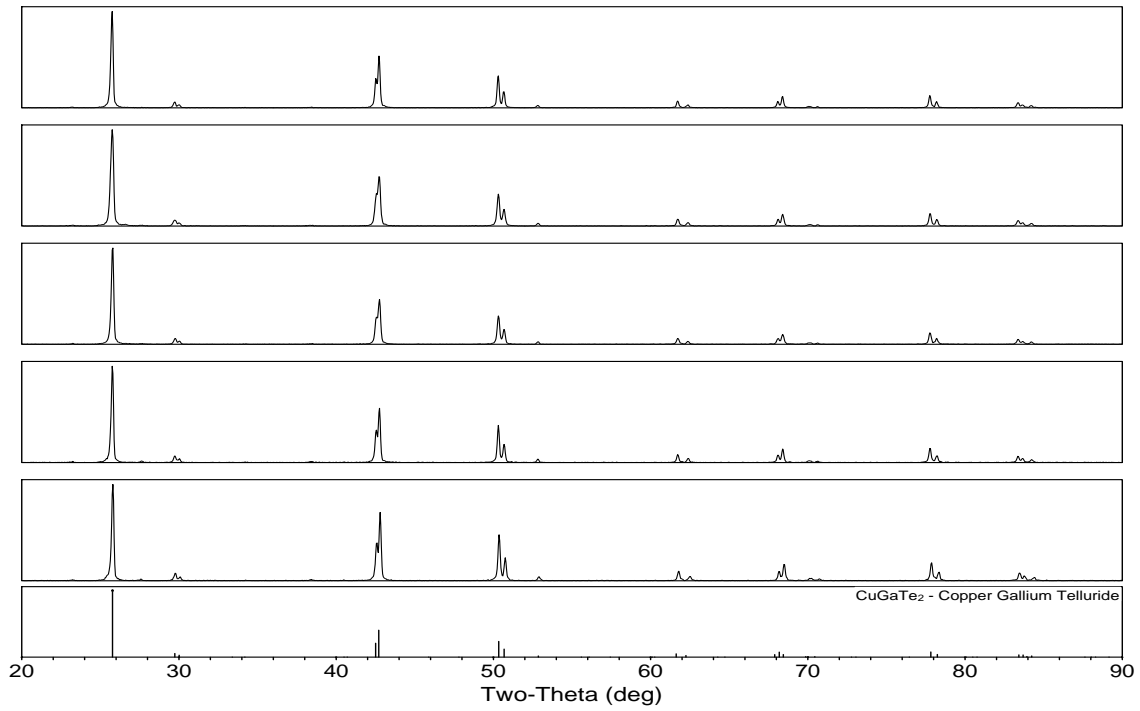


Figure 7.12: XRD patterns of the partial solid solution of  $\text{CuGaTe}_2$  and  $\text{Zn}_{0.5}\text{GaTe}_2$ . The top pattern is  $\text{CuGaTe}_2$ , followed by  $\text{Cu}_{0.995}\text{Zn}_{0.0025}\text{GaTe}_2$ ,  $\text{Cu}_{0.990}\text{Zn}_{0.0050}\text{GaTe}_2$ ,  $\text{Cu}_{0.900}\text{Zn}_{0.0500}\text{GaTe}_2$ , and at the bottom  $\text{Cu}_{0.800}\text{Zn}_{0.1000}\text{GaTe}_2$ . The PDF overlay is for  $\text{CuGaTe}_2$ . The y-scale is intensity, in arbitrary units. Source: PDF #01-079-2331. [7]

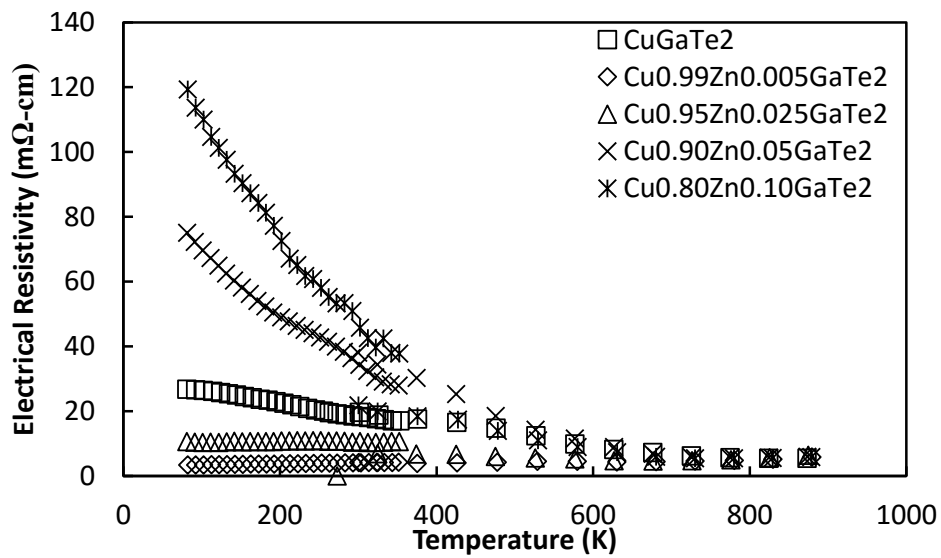


Figure 7.13: Electrical resistivity of the partial solid solution  $\text{CuGaTe}_2 - \text{Zn}_{0.5}\text{GaTe}_2$  as a function of temperature.

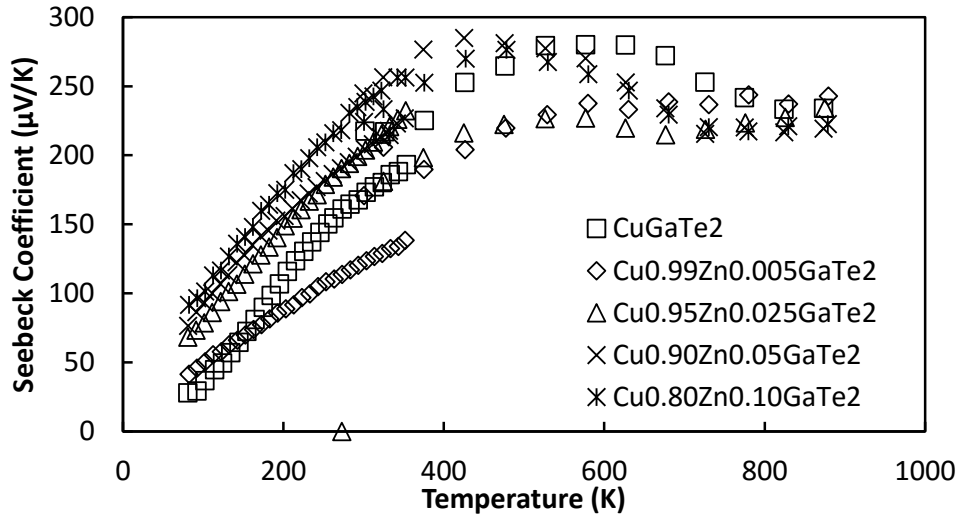


Figure 7.14: Seebeck coefficient of the partial solid solution  $\text{CuGaTe}_2 - \text{Zn}_{0.5}\text{GaTe}_2$  as a function of temperature.

The electrical resistivity showed a slight decrease with small amounts of vacancies, but for larger amounts the resistivity increased to values greater than the pure compound. This was most evident at low temperatures, at high temperatures all samples showed similar values for electrical resistivity, as shown in Figure 7.13. The Seebeck coefficient showed similar results, with more electrically conductive samples displaying lower thermopower values as is typical. As shown in Figure 7.14 the Seebeck coefficient of all samples ranged from 200 - 250  $\mu\text{V K}^{-1}$ .

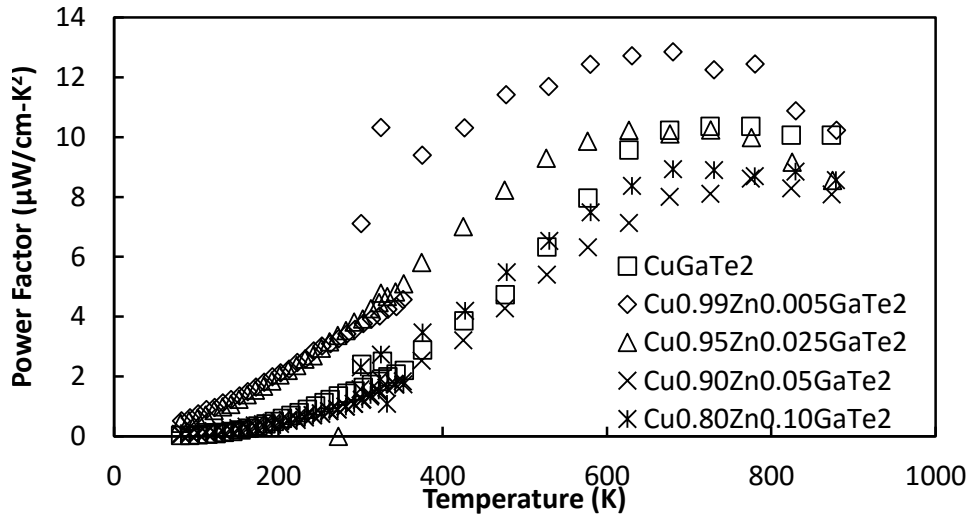


Figure 7.15: Power factor of the partial solid solution  $\text{CuGaTe}_2 - \text{Zn}_{0.5}\text{GaTe}_2$  as a function of temperature.

Combining the electrical resistivity and Seebeck coefficient, the power factor showed an increase with 0.005 and 0.025 zinc concentrations, and a decrease for higher amounts. The value at 870K was similar, but the samples with small amounts of zinc showed a higher peak and average value, as shown in Figure 7.15.

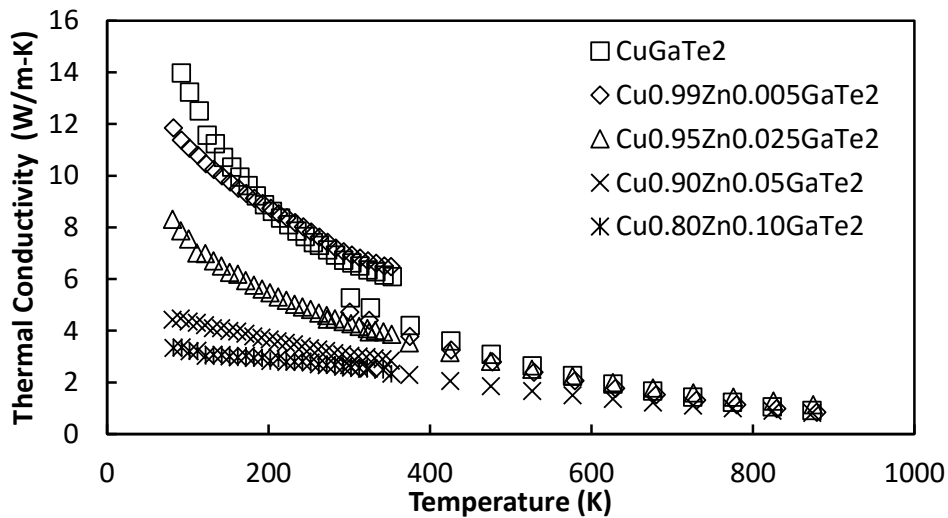


Figure 7.16: Thermal conductivity of the partial solid solution  $\text{CuGaTe}_2 - \text{Zn}_{0.5}\text{GaTe}_2$  as a function of temperature.

The goal in mind with the solid solution was to lower the thermal conductivity, and as shown in Figure 7.16 the effort was somewhat successful. The substitution of zinc and vacancies on the copper site decreased the thermal conductivity with each increase, however as with other solid solutions studied here, at high temperatures the decrease was small.

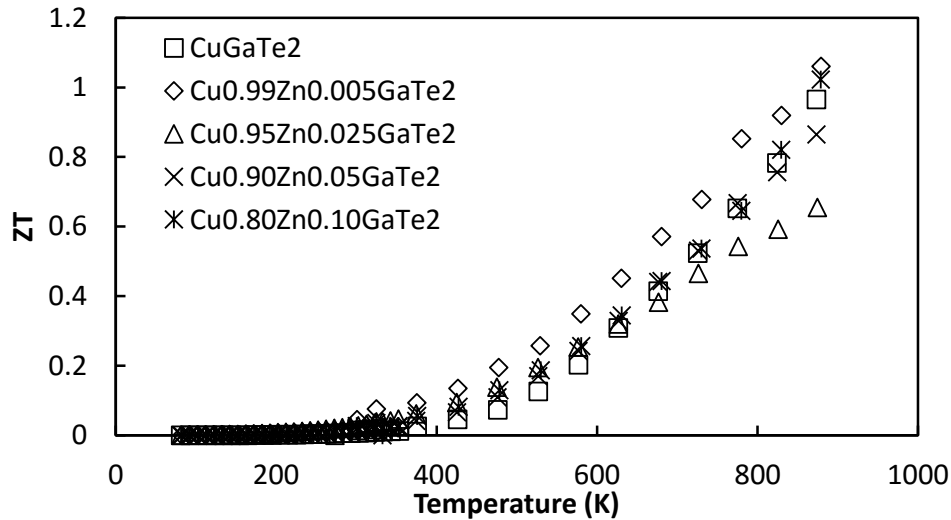


Figure 7.17:  $ZT$  of the partial solid solution  $\text{CuGaTe}_2 - \text{Zn}_{0.5}\text{GaTe}_2$  as a function of temperature

The peak  $ZT$  was slightly enhanced for  $\text{Cu}_{0.99}\text{Zn}_{0.005}\text{GaTe}_2$  and  $\text{Cu}_{0.95}\text{Zn}_{0.025}\text{GaTe}_2$ , and the average  $ZT$  was increased for  $\text{Cu}_{0.99}\text{Zn}_{0.005}\text{GaTe}_2$ .

### 7.3 Copper Deficient $\text{CuGaTe}_2$

Studying  $\text{Cu}_{0.90}\text{Zn}_x\text{GaTe}_2$  to find the optimum zinc concentration, it was found that samples with no zinc at all, and a simple 10% copper deficiency had the best properties. That result led to a series of samples with composition  $\text{Cu}_{1-x}\text{GaTe}_2$  and  $x = 0, 0.05, 0.10,$  and  $0.15$ . Figure 7.18 showed no discernible change in the XRD patterns up to 15% copper deficiency.

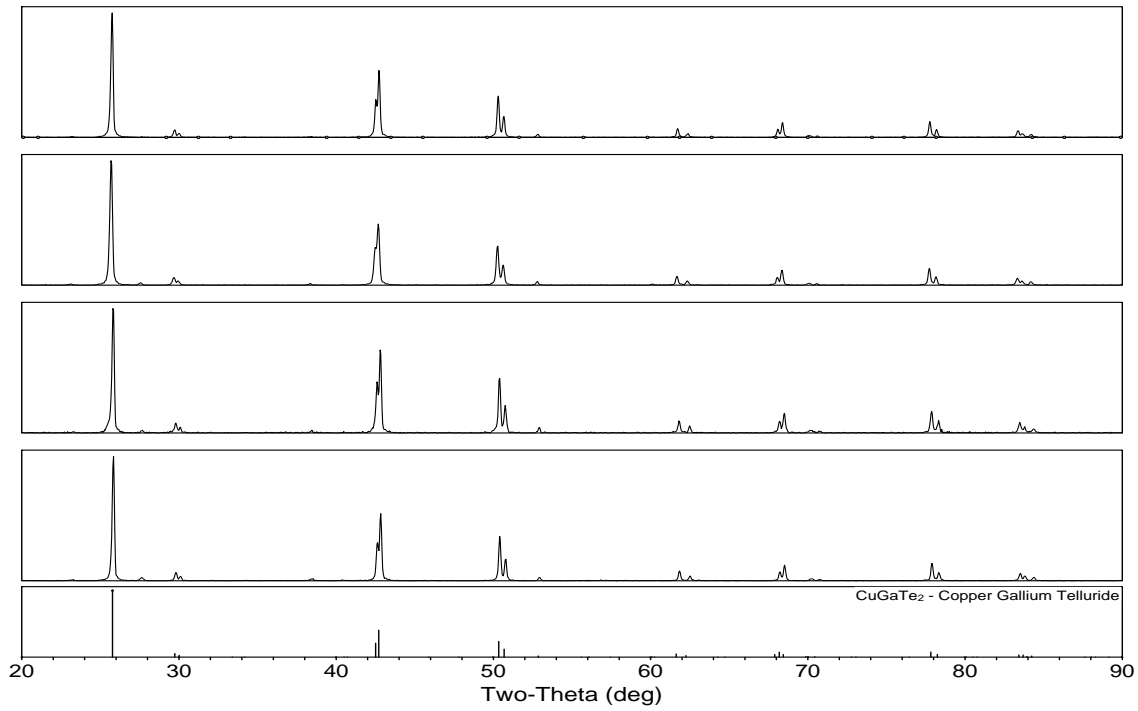


Figure 7.18: XRD pattern of copper deficient CuGaTe<sub>2</sub>. The top pattern is CuGaTe<sub>2</sub>, followed by the 5%, 10%, and 15% copper deficiency samples respectively. The y-scale is intensity, in arbitrary units. Source: PDF #01-079-2331. [7]

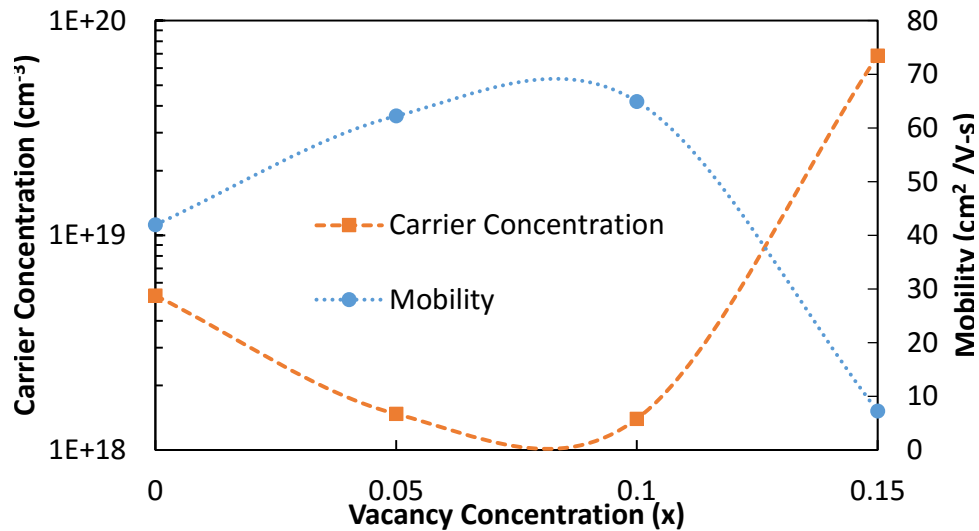


Figure 7.19: Carrier concentration and mobility at 300K for the series Cu<sub>1-x</sub>GaTe<sub>2</sub> as a function of vacancy concentration (x).

As shown in Figure 7.19, Hall measurements revealed that the removal of small amounts

of copper caused a drop in carrier concentration, and an increase in the mobility. Above 10% copper deficiency a large increase in the carrier concentration and a decrease in the mobility was observed. It is suspected that the large vacancy concentration causes increased scattering, lowering the mobility, and the removal of copper acted as a p-type dopant. However, the initial drop in carrier concentration for low amounts of vacancies is not fully understood. The electrical resistivity, shown in Figure 7.20, also showed interesting trends.  $\text{Cu}_{0.90}\text{GaTe}_2$  in particular displayed an initial increase in electrical resistivity, followed by a peak and then followed a trend similar to the other samples. High temperature Hall measurements would add much needed information and possibly explain the mechanism causing this behavior.

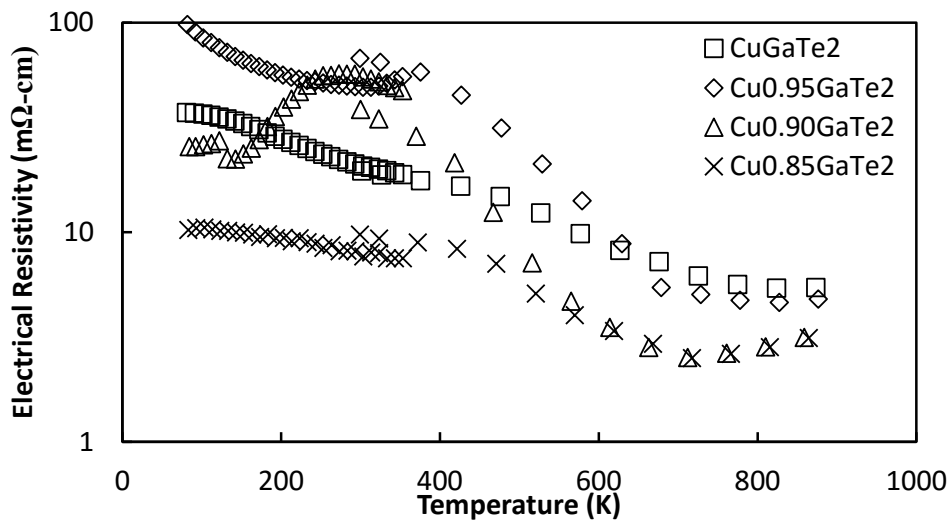


Figure 7.20: Electrical resistivity of the series  $\text{Cu}_{1-x}\text{GaTe}_2$  as a function of temperature.

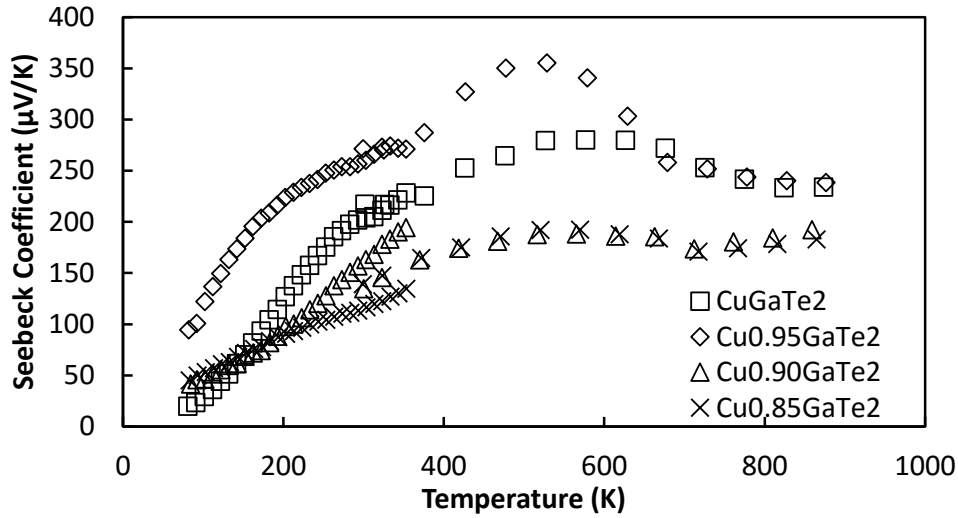


Figure 7.21: Seebeck coefficient of the series  $\text{Cu}_{1-x}\text{GaTe}_2$  as a function of temperature.

The 5% copper deficient sample displayed an increase in Seebeck coefficient as compared to the pure compound until 650K, at which point the two samples were nearly indistinguishable. However, the 10% and 15% showed a drop of about  $50\mu\text{V K}^{-1}$  across most of the temperature range, as shown in Figure 7.21

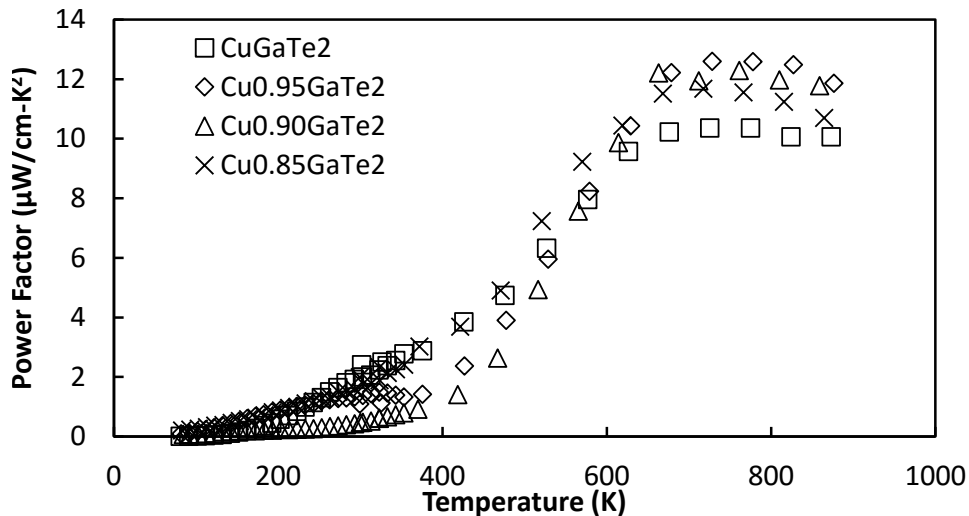


Figure 7.22: Power factor of the series  $\text{Cu}_{1-x}\text{GaTe}_2$  as a function of temperature.

The power factor for all four samples is similar in trend, with a steep increase near 400K,

and flattening out at 650K. All three copper deficient samples showed values higher than the pure  $\text{CuGaTe}_2$ , with the 5% sample being the highest by a small margin.

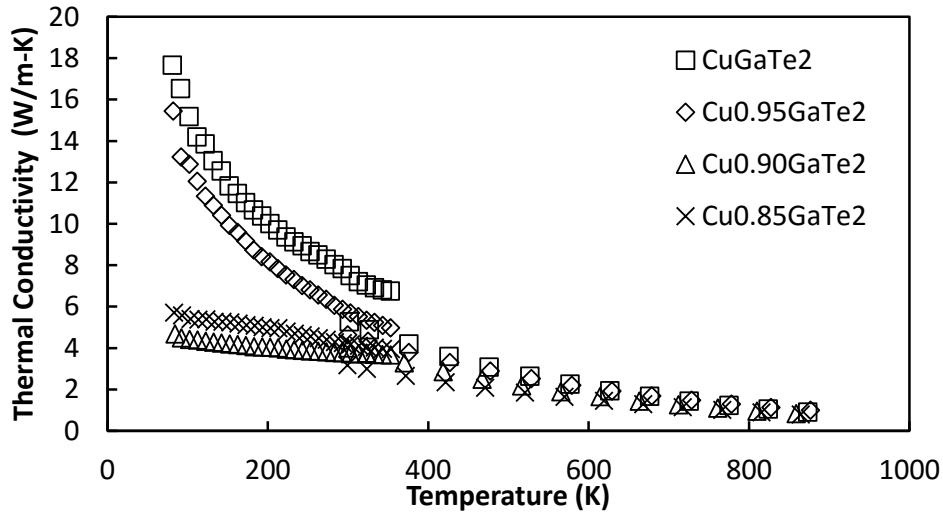


Figure 7.23: Thermal conductivity of the series  $\text{Cu}_{1-x}\text{GaTe}_2$  as a function of temperature.

Figure 7.23 shows that the copper deficiency caused a decrease in thermal conductivity, as was expected from the addition of vacancies. The 5% copper deficient sample showed only a minimal decrease, but the 10% and 15% sample had room temperature values roughly half that of the pure  $\text{CuGaTe}_2$ , which combined with the increased peak power factor, lead to an increase in  $ZT$ . The  $ZT$  was higher for all of the copper deficient samples, with  $\text{Cu}_{0.90}\text{GaTe}_2$  and  $\text{Cu}_{0.85}\text{GaTe}_2$  matching closely over the whole range. A peak value of 1.22 was reached for  $\text{Cu}_{0.90}\text{GaTe}_2$ , as compared to  $\text{CuGaTe}_2$  which had a peak value of 0.97 at 870K.

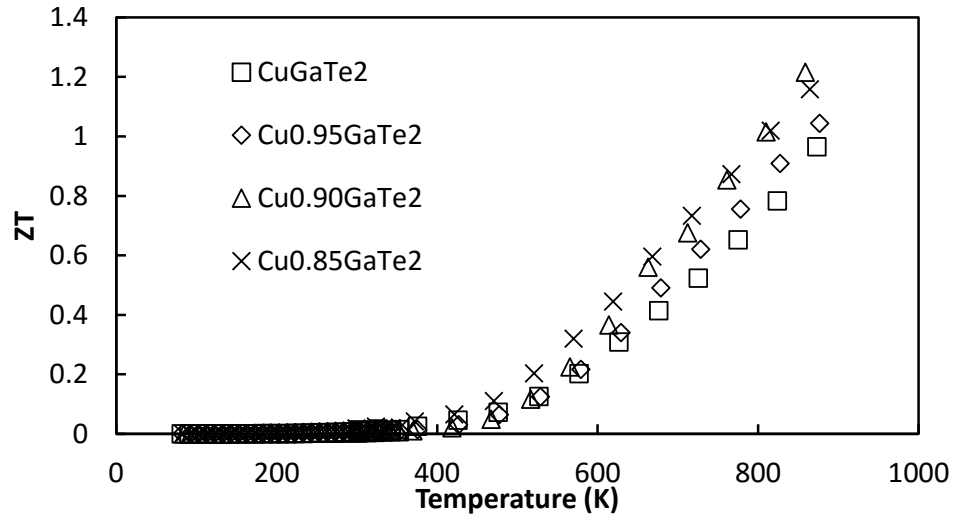


Figure 7.24:  $ZT$  of the series  $\text{Cu}_{1-x}\text{GaTe}_2$  as a function of temperature.

# Chapter 8

## Conclusions and Future Work

The goal of this work was to understand the underlying physics of the chalcopyrite family of semiconductors and to study how to tune the electronic and thermal transport properties. The chalcopyrite family contains a large number of compounds with a wide range of electronic and thermal properties. The band gap of copper based chalcopyrite compounds ranges from 0.53 eV for  $\text{CuFeS}_2$  up to 3.49 eV for  $\text{CuAlS}_2$  which offers a wide range for thermoelectric or photo-voltaic applications, as well as offering an ability to understand the connection between the band structure and the physics of the transport properties.

This wide range of band gap values is reflected in the great range of electrical resistivities reported in this work, shown in Figure 8.1.[92, 23] Further more as shown in Figure 8.2, the complex crystal structure of the chalcopyrite compounds lead to thermal conductivity values at or below  $1 \text{ W m}^{-1} \text{ K}^{-1}$  at high temperatures for all of the compounds studied here, and the defect chalcopyrite compounds showed that vacancy substitution could reduce those value even further. The electronic properties covered a wide range, and while the compounds were not intrinsically very conductive, p-type doping was effective in increasing the carrier concentration and reducing the electrical resistivity with most of the compounds in this study.

It should also be noted that for a “pure” intrinsic semiconductor the equations discussed

in Chapter 2 give a room temperature carrier concentration on the order of  $10^{10} - 10^{13} \text{ cm}^{-3}$ . However, the nominally undoped samples synthesized in this study all showed much higher room temperature carrier concentrations, typically on the order of  $10^{17} - 10^{18} \text{ cm}^{-3}$ . This indicates a high level of intrinsic defects in the samples that result from the synthesis techniques. The mostly likely source of defects is chalcogen deficiency; sulfur, selenium, and tellurium all boil at  $900^\circ\text{C}$  in the ampoule, which makes some loss of chalcogen atoms unavoidable. Due to this, it is likely that the samples synthesized in this study could be expressed as  $\text{I-III-VI}_{2-\delta}$  where  $\delta$  is a small number.

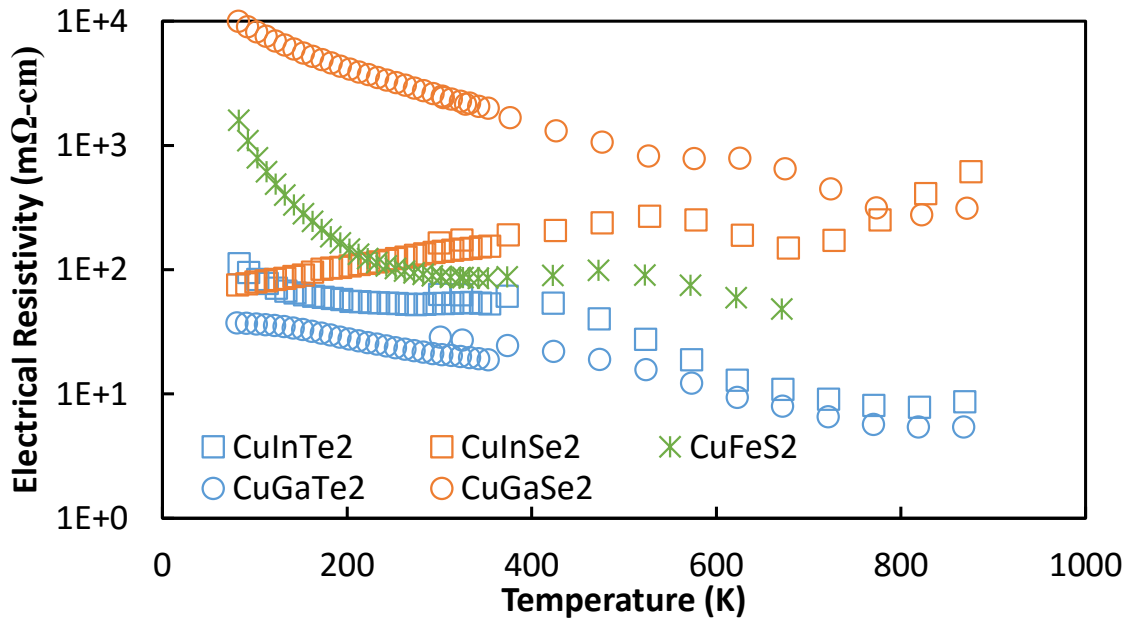


Figure 8.1: Comparison of the electrical resistivity of the base compounds  $\text{CuInTe}_2$ ,  $\text{CuGaTe}_2$ ,  $\text{CuInSe}_2$ ,  $\text{CuGaSe}_2$ , and  $\text{CuFeS}_2$ .  $\text{CuInS}_2$  is not shown here, but the values are on the order of  $10^8 \text{ m}\Omega \text{ cm}$ .

Based on our understanding of the underlying fundamental transport properties three compounds stood out in this work as promising for thermoelectric applications:  $\text{CuGaTe}_2$ ,  $\text{CuInTe}_2$ , and  $\text{CuFeS}_2$ .  $\text{CuGaTe}_2$  and  $\text{CuInTe}_2$  both possess a  $ZT$  in excess of unity, and the formation of full solid-solution allowed further optimization of the electronic and thermal

properties. Further, densifying the samples with SPS rather than traditional hotpressing yielded samples with higher density, and in the case of  $\text{CuInTe}_2$  an increase in  $ZT$  to near 1.4, near that of bulk optimized  $\text{PbTe-PbSe}$  alloys, and greater than average values reported for skutterudite or TAGS ( $\text{Te-Ag-Ge-Sb}$  alloys), placing this compound among the best performing p-type materials in the 400-800K temperature range.[138, 139, 140]

The selenide samples showed poor electronic properties as compared to the tellurium based compounds.  $\text{CuGaSe}_2$  had the largest band gap of any material studied here at 1.68 eV, which is much larger than typically selected as ideal for thermoelectric materials.[92, 141] Polycrystalline samples of  $\text{CuGaSe}_2$  also suffer from low hole mobility (calculated from Hall measurements), in the range of  $10 - 20 \text{ cm}^2 \text{ V}^{-1} \text{ s}^{-1}$  which is much lower than that of  $\text{CuGaTe}_2$  which was found in this study to have a room temperature mobility near  $100 \text{ cm}^2 \text{ V}^{-1} \text{ s}^{-1}$ . [112] This partly explains the more than two order of magnitude difference in electrical conductivity between the two gallium containing samples, as shown in Figure 8.1 below.

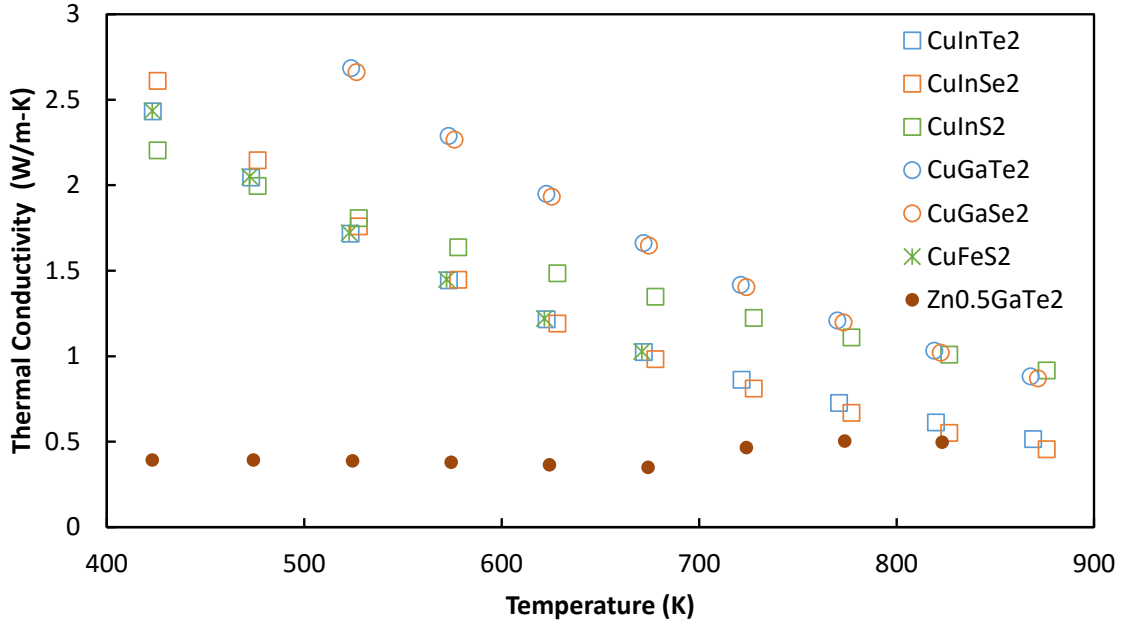


Figure 8.2: Comparison of the thermal conductivity of the base chalcopyrite compounds.

CuInSe<sub>2</sub> has a reported band gap of 1.04 eV, very close to that of CuInTe<sub>2</sub>. [142] However, despite that similarity the two materials showed very distinct electronic properties. CuInTe<sub>2</sub> was found to have a very high hole mobility in this study, with a measured value of 250 cm<sup>2</sup> V<sup>-1</sup> s<sup>-1</sup> at 300K and numerous studies showing values near or above 100 cm<sup>2</sup> V<sup>-1</sup> s<sup>-1</sup>, while studies on CuInSe<sub>2</sub> report values in the range of 20-25 cm<sup>2</sup> V<sup>-1</sup> s<sup>-1</sup>. [6, 143, 144, 145] This large decrease in hole mobility again leads to a large increase in electrical resistivity.

This difference in mobility between the selenide and telluride compounds is unexplained at this time. Some have suggested that it could be due to the amount of tetragonal distortion in the compound, i.e. how far the *c*:*a* ratio varies from 2.0. However, no correlation was found in this study or in a review of literature values, between lattice constants and mobility values. Another possibility is the low mobility is due to the electro-negativity differences. For CuInTe<sub>2</sub> and CuGaTe<sub>2</sub> the average electro-negativity difference is 0.26 and 0.25 respectively. On the other hand for CuInSe<sub>2</sub> and CuGaSe<sub>2</sub> the differences are 0.71

and 0.70 respectively. Data compiled by Slack, as well as work by Pauling, showed that the weighted mobility (defined as  $\mu(m^*/m_0)^{3/2}$ ) decreased rapidly with increasing average electro-negativity differences.[146, 147] High temperature Hall measurements could yield useful information on the nature of the low mobility and clarify the underlying physics.

CuFeS<sub>2</sub> showed promise as a low-cost material made from earth abundant materials. In the work presented here, CuFeS<sub>2</sub> was the only n-type material discovered. It is also the naturally occurring mineral for which the family is named; in fact chalcopyrite minerals are the most abundant source of copper on the Earth. While the undoped compound only displayed a  $ZT$  of 0.1, doping with zinc increased that value to 0.3; other reports showed varying the ratio of Cu:Fe was also effective in doping the compound, and produced very similar values. However, the compound is limited in comparison to the tellurium based materials in that it is only stable in air to around 450C before sulfur sublimation occurs. CuFeS<sub>2</sub> also appeared to be limited electronically by a low carrier mobility. However, given the very low cost of the elements in the compound, future studies to improve the performance would be very valuable.

Further work on transition metal doping could also show interesting physics. The band gap of CuFeS<sub>2</sub> is much smaller than that of CuGaS<sub>2</sub>, even though their lattice parameters are nearly identical and iron and gallium have the same valence and very similar electro-negativity values. Band structure calculations showed that the valence band in CuFeS<sub>2</sub> arose primarily from the iron d levels, so other transition metals may show interesting properties as well.[121] The possibility of creating an n-type material other than CuFeS<sub>2</sub> is also very intriguing. While attempts in this work were all unsuccessful, many possible elements for doping still remain. Future band structure calculations would assist greatly in understanding the physics of differing dopant atoms and possibly predict elements which would be more

effective as n-type dopants.

Future studies on the defect chalcopyrite compounds could be very enlightening. The extremely low thermal conductivity, especially that found in  $\text{Zn}_{0.5}\text{GaTe}_2$ , shows the strong impact vacancies can have on the physics of phonon scattering. The electronic properties of defect chalcopyrite compounds are rather unexplored, and future work on understanding the physics of the electronic transport would be insightful. The reported band gaps of the defect compounds are larger than those found in chalcopyrite compounds, and the two materials studied here were found to be highly resistive.[148] If the electronic properties could be controlled while maintaining the low thermal conductivity from the defect structure, the defect compounds would be very promising thermoelectric materials.

Overall, the chalcopyrite family of compounds offers a wide range of interesting physics in terms of electronic and thermal transport. A better understanding of the transport mechanisms and their interactions with the defects and changes in the structure and stoichiometry could lead to wide use of chalcopyrite materials in thermoelectrics. Already they are being used successfully in solar applications, and their future in thermoelectrics looks to be promising with the high  $ZT$  values obtained in this work, and in other studies.

# REFERENCES

# REFERENCES

- [1] Alphabet Energy Inc. Alphabet Energy E1. <https://www.alphabetenergy.com/product/e1/>, 2016.
- [2] Daifeng Zou, Shuhong Xie, Yunya Liu, Jianguo Lin, and Jiangyu Li. First-principles study of thermoelectric and lattice vibrational properties of chalcopyrite CuGaTe<sub>2</sub>. *J. Alloys Compd.*, 570:150–155, sep 2013.
- [3] Irene Aguilera, Julien Vidal, Perla Wahnón, Lucia Reining, and Silvana Botti. First-principles study of the band structure and optical absorption of CuGaS<sub>2</sub>. *Phys. Rev. B*, 84(8):085145, aug 2011.
- [4] Harry Hahn, Gnter Frank, Wilhelm Klingler, Anne Dorothee Strger, and Georg Strger. Untersuchungen ber ternre Chalkogenide. VI. ber Ternre Chalkogenide des Aluminiums, Galliums und Indiums mit Zink, Cadmium und Quecksilber. *Zeitschrift fr Anorg. und Allg. Chemie*, 279(5-6):241–270, jul 1955.
- [5] M Leon, J. M. Merino, J. L. Martin De Vidales, and M. Leon. Comparative study of the crystal structure of synthesized CuGa<sub>1-y</sub>In<sub>y</sub>Te<sub>2</sub> compounds. *J. Vac. Sci. Technol. A Vacuum, Surfaces, Film.*, 11(5):2430, sep 1993.
- [6] Ruiheng Liu, Lili Xi, Huili Liu, Xun Shi, Wenqing Zhang, and Lidong Chen. Ternary compound CuInTe<sub>2</sub>: a promising thermoelectric material with diamond-like structure. *Chem. Commun.*, 48(32):3818, apr 2012.
- [7] M. Leon, J. M. Merino, and J. L. Martin De Vidales. Crystal structure of synthesized CuGaTe<sub>2</sub> determined by X-ray powder diffraction using the Rietveld method. *J. Mater. Sci.*, 27(16):4495–4500, jan 1992.
- [8] Theerayuth Plirdpring, Ken Kurosaki, Atsuko Kosuga, Tristan Day, Samad Firdosy, Vilupanur Ravi, G Jeffrey Snyder, Adul Harnwungmoung, Tohru Sugahara, Yuji Ohishi, Hiroaki Muta, and Shinsuke Yamanaka. Chalcopyrite CuGaTe<sub>2</sub>: A High-Efficiency Bulk Thermoelectric Material. *Adv. Mater.*, 24(27):3622–3626, jul 2012.
- [9] Yapeng Li, Qingsen Meng, Yuan Deng, Hong Zhou, Yulan Gao, Yiyun Li, Jiangfeng Yang, and Jiaolin Cui. High thermoelectric performance of solid solutions CuGa<sub>1-x</sub>In<sub>x</sub>Te<sub>2</sub> (x=0.1). *Appl. Phys. Lett.*, 100(23):231903, 2012.

- [10] Harry Hahn, Gnter Frank, Wilhelm Klingler, Anne-Dorothee Meyer, and Georg Strger. Untersuchungen ber ternre Chalkogenide. V. ber einige ternre Chalkogenide mit Chalkopyritstruktur. *Zeitschrift fr Anorg. und Allg. Chemie*, 271(3-4):153–170, feb 1953.
- [11] J.M. Merino, M. Di Michiel, and M. León. Structural analysis of CuInSe<sub>2</sub> and CuIn<sub>3</sub>Se<sub>5</sub> at different temperatures with synchrotron radiation. *J. Phys. Chem. Solids*, 64(9-10):1649–1652, sep 2003.
- [12] B. Grzeta-Plenkovic, S. Popović, B. Čelustka, and B. Šantić. Crystal data for AgGa<sub>x</sub>In<sub>1-x</sub>Se<sub>2</sub> and CuGa<sub>x</sub>In<sub>1-x</sub>Se<sub>2</sub>. *J. Appl. Crystallogr.*, 13(3):311–315, jun 1980.
- [13] M Leon, J. M. Merino, and J. L. Martin De Vidales. Crystal structure of synthesized CuGa<sub>0.5</sub>In<sub>0.5</sub>Te<sub>2</sub> determined by x-ray powder diffraction using the Rietveld method. *J. Mater. Sci.*, 28:2466–2470, sep 1993.
- [14] N. A. Goryunova. *The Chemistry of Diamond-like Semiconductors*. MIT Press, Cambridge MA, 1965.
- [15] J C Woolley. Some Cross-Substitutional Alloys of CdTe. *J. Electrochem. Soc.*, 113(9):2–4, 1966.
- [16] Carlos Rincon and F. J. Ramirez. Lattice vibrations of CuInSe<sub>2</sub> and CuGaSe<sub>2</sub> by Raman microspectrometry. *J. Appl. Phys.*, 72(9):4321, 1992.
- [17] T Kratz and H Fuess. Simultane Strukturbestimmung von Kupferkies und Bornit an einem Kristall. *Zeitschrift für Krist.*, 186:167–169, 1989.
- [18] Naohito Tsujii and Takao Mori. High Thermoelectric Power Factor in a Carrier-Doped Magnetic Semiconductor CuFeS<sub>2</sub>. *Appl. Phys. Express*, 6(4):043001, apr 2013.
- [19] Naohito Tsujii, Takao Mori, and Yukihiro Isoda. Phase Stability and Thermoelectric Properties of CuFeS<sub>2</sub>-Based Magnetic Semiconductor. *J. Electron. Mater.*, 43(6):2371–2375, jun 2014.
- [20] Yulong Li, Tiansong Zhang, Yuting Qin, Tristan Day, G. Jeffrey Snyder, Xun Shi, and Lidong Chen. Thermoelectric transport properties of diamond-like Cu<sub>1-x</sub>Fe<sub>1+x</sub>S<sub>2</sub> tetrahedral compounds. *J. Appl. Phys.*, 116(20), 2014.
- [21] H J Gotsis, a C Barnes, and P Strange. Experimental and theoretical investigation of the crystal structure of CuS. *J. Phys. Condens. Matter*, 4(50):10461–10468, 1992.

- [22] E. J. Fasiska. Some defect structures of iron sulfide. *Phys. Status Solidi*, 10(1):169–173, 1972.
- [23] Jianhui Li, Qing Tan, and Jing-Feng Li. Synthesis and property evaluation of CuFeS<sub>2</sub>x as earth-abundant and environmentally-friendly thermoelectric materials. *J. Alloys Compd.*, 551:143–149, feb 2013.
- [24] G. Brandt, A. Räuber, and J. Schneider. ESR and x-ray analysis of the ternary semiconductors CuAlS<sub>2</sub>, CuInS<sub>2</sub> and AgGaS<sub>2</sub>. *Solid State Commun.*, 12(6):481–483, mar 1973.
- [25] C Julien and S Barnier. Properties of several varieties of CuGaS<sub>2</sub> microcrystals. *Mater. Sci. Eng. B*, 86:152–156, 2001.
- [26] S. R. Hall and J. M. Stewart. The crystal structure refinement of chalcopyrite, CuFeS<sub>2</sub>. *Acta Crystallogr. Sect. B Struct. Crystallogr. Cryst. Chem.*, 29(3):579–585, mar 1973.
- [27] J.M. Delgado, G. Diaz de Delgado, M. Quintero, and J.C. Woolley. The crystal structure of copper iron selenide, CuFeSe<sub>2</sub>. *Mater. Res. Bull.*, 27(3):367–373, mar 1992.
- [28] A A Vaipolin, V D Prochukhan, Yu V Rud, and E V Skoriukin. No Title. *Izv. Akad. Nauk SSSR Neorg. Mater.*, 20:578, 1984.
- [29] K. Koto and Nobuo Morimoto. Superstructure investigation of bornite, Cu<sub>5</sub>FeS<sub>4</sub>, by the modified partial Patterson function. *Acta Crystallogr. Sect. B Struct. Crystallogr. Cryst. Chem.*, 31(9):2268–2273, sep 1975.
- [30] Pengfei Qiu, Tiansong Zhang, Yuting Qiu, Xun Shi, and Lidong Chen. Sulfide bornite thermoelectric material: a natural mineral with ultralow thermal conductivity. *Energy Environ. Sci.*, 00:1–7, oct 2014.
- [31] Gabin Guelou, Anthony V Powell, and Paz Vaqueiro. Ball milling as an effective route for the preparation of doped bornite: synthesis, stability and thermoelectric properties. *J. Mater. Chem. C*, 2015.
- [32] T.J Seebeck. Ueber die magnetische Polarisation der Metalle und Erze durch Temperatur-Differenz. *Ann. Phys.*, 82(2):133–160, 1826.
- [33] J. C. Peltier. Nouvelles expériences sur la calorité des courants électriques. *Ann. Chim. Phys.*, 56(371):371, 1834.

- [34] W. Thomson. Account of Researches in Thermo-Electricity. *Proc. R. Soc. London*, 7(0):49–58, jan 1854.
- [35] E. Altenkirch. No Title. *Phys. Zeitschrift*, 12:920, 1911.
- [36] E. Altenkirch. Uber den Nutzeffekt der Thermosaule. *Phys. Zeitschrift*, 10:560–580, 1909.
- [37] Lars Onsager. Reciprocal relations in irreversible processes. I. *Phys. Rev.*, 37:405–426, 1931.
- [38] Lars Onsager. Reciprocal relations in irreversible processes. II. *Phys. Rev.*, 38(4):2265–2279, 1931.
- [39] The Nobel Prize in Chemistry 1968, 2014.
- [40] H J Goldsmid and R W Douglas. the Use of Semiconductors in Thermoelectric Refrigeration. *Br. J. Appl. Phys.*, 5(NOV):386–390, 1954.
- [41] H J Goldsmid. The Electrical Conductivity and Thermoelectric Power of Bismuth Telluride. *Proc. Phys. Soc. London*, 71(460):633–646, 1958.
- [42] Maria Telkes. The efficiency of thermoelectric generators. I. *J. Appl. Phys.*, 18(12):1116–1127, 1947.
- [43] Maria Telkes. Power Output of Thermoelectric Generators. *J. Appl. Phys.*, 25(8):1058, 1954.
- [44] Maria Telkes. Solar thermoelectric generators. *J. Appl. Phys.*, 25(6):765–777, 1954.
- [45] A. F. Joffé. HEAT TRANSFER IN SEMICONDUCTORS. *Can. J. Phys.*, 34(12A):1342–1355, dec 1956.
- [46] M. C. Steele and F. D. Rosi. Thermal conductivity and thermoelectric power of germanium-silicon alloys. *J. Appl. Phys.*, 29(11):1517–1520, 1958.
- [47] R. Bowers, J. E. Bauerle, and A. J. Cornish. InAs<sub>1-x</sub>P<sub>x</sub> as a thermoelectric material. *J. Appl. Phys.*, 30(7):1050–1054, 1959.
- [48] Donald D. Glower and Duane C. Wallace. Thermal Studies of Ca<sub>x</sub>Ba<sub>1-x</sub>TiO<sub>3</sub>. *J. Phys. Soc. Japan*, 18(5):679–684, may 1963.

- [49] L.E. DeLong and G.P. Meisner. The pressure dependence of the superconducting transition temperature of LaT<sub>4</sub>P<sub>12</sub>(T = Fe, Ru, Os). *Solid State Commun.*, 53(2):119–123, jan 1985.
- [50] D. Jung, M. Whangbo, and S. Alvarez. Importance of the X<sub>4</sub> Ring Orbitals for the Semiconducting, Metallic, or Superconducting Properties of Skutterudites MX<sub>3</sub> and RM<sub>4</sub>X<sub>12</sub>. *Inorg. Chem.*, 29:2252–2255, 1990.
- [51] Bo Brummerstedt Iversen, Anders E.C. Palmqvist, David E Cox, George S Nolas, Galen D Stucky, Nick P Blake, and Horia Metiu. Why are Clathrates Good Candidates for Thermoelectric Materials? *J. Solid State Chem.*, 149(2):455–458, feb 2000.
- [52] Donald T. Morelli and Gregory P. Meisner. Low temperature properties of the filled skutterudite CeFe<sub>4</sub>Sb<sub>12</sub>. *J. Appl. Phys.*, 77(8):3777, 1995.
- [53] Jean-Pierre Fleurial, Alex Borshchevsky, and Thierry Caillat. High Figure of Merit in Ce-Filled Skutterudites. *15th Int. Conf. Thermoelectr.*, 3:91–95, 1996.
- [54] H. Nakagawa, H. Tanaka, A. Kasama, K. Miyamura, H. Masumoto, and K. Matsubara. Thermoelectric properties of CoSb<sub>3</sub> prepared by copper mold quenching technique. *Fifteenth Int. Conf. Thermoelectr. Proc. ICT '96*, pages 117–121, 1996.
- [55] A Borshchevsky, T Caillat, and J.-P. Fleurial. Solid solution formation: improving the thermoelectric properties of skutterudites. In *Fifteenth Int. Conf. Thermoelectr. Proc. ICT '96*, pages 112–116. IEEE, 1996.
- [56] K. Matsubara, T Sakakibara, Y Notohara, H Anno, H Shimizu, and T Koyanagi. Electronic transport properties of the Skutterudite CoSb<sub>3</sub> and mixed alloys. In *Fifteenth Int. Conf. Thermoelectr. Proc. ICT '96*, number 1, pages 96–99. IEEE, 1996.
- [57] B. Abeles. Lattice thermal conductivity of disordered semiconductor alloys at high temperatures. *Phys. Rev.*, 131(5):1906–1911, sep 1963.
- [58] T. Koyanagi, T Tsubouchi, M Ohtani, K Kishimoto, H Anno, and K. Matsubara. Thermoelectric properties of Co(M<sub>x</sub>Sb<sub>1-x</sub>)<sub>3</sub> (M=Ge, Sn, Pb) compounds. In *Fifteenth Int. Conf. Thermoelectr. Proc. ICT '96*, pages 107–111. IEEE, 1996.
- [59] L. D. Hicks and M. S. Dresselhaus. Effect of quantum-well structures on the thermomagnetic figure of merit. *Phys. Rev. B*, 47(19):727–731, 1993.

- [60] L. D. Hicks and M. S. Dresselhaus. Thermoelectric figure of merit of a one-dimensional conductor. *Phys. Rev. B*, 47(24):16631–16634, 1993.
- [61] L. D. Hicks, T. C. Harman, X. Sun, and M. S. Dresselhaus. Experimental study of the effect of quantum-well structures on the thermoelectric figure of merit. *Phys. Rev. B*, 53(16):R10493–R10496, 1996.
- [62] M. S. Dresselhaus, G. Dresselhaus, X. Sun, Z. Zhang, S. B. Cronin, and T. Koga. Low-dimensional thermoelectric materials. *Phys. Solid State*, 41(5):679–682, may 1999.
- [63] R Venkatasubramanian, E Siivola, T Colpitts, and B O’Quinn. Thin-film thermoelectric devices with high room-temperature figures of merit. *Nature*, 413(6856):597–602, 2001.
- [64] E. Godoy, N.J. Scenna, and S.J. Benz. Families of optimal thermodynamic solutions for combined cycle gas turbine (CCGT) power plants. *Appl. Therm. Eng.*, 30(6-7):569–576, may 2010.
- [65] Manuel Valdés and José L. Rapún. Optimization of heat recovery steam generators for combined cycle gas turbine power plants. *Appl. Therm. Eng.*, 21(11):1149–1159, aug 2001.
- [66] Lloyd I. Shure and Harvey J. Schwartz. Nasa Tm X-52158 N66-14775. Technical report, Lewis Research Center, Cleveland, OH, 1965.
- [67] NASA. Space Radioisotope Power Systems: Multi-Mission Radioisotope Thermoelectric Generator, 2008.
- [68] RGS B.V. Development. Application Areas. <http://www.rgsdevelopment.nl/page24.html>, 2016.
- [69] A. F. Ioffe. *Semiconductor Thermoelements and Thermoelectric Cooling*. Infosearch Limited, London, 1957.
- [70] Neil W. Ashcroft and N. David Mermin. *Solid State Physics*. Thomson Press, 1976.
- [71] V. Fistul. *Heavily Doped Semiconductors*. Plenum Press, New York, 1969.
- [72] S. M. Sze. *Physics of Semiconductor Devices*. Wiley-Interscience, second edition, 1981.

- [73] J. Bardeen and W. Shockley. Deformation potentials and mobilities in non-polar crystals. *Phys. Rev.*, 80(1):72–80, 1950.
- [74] E. Conwell and V. F. Weisskopf. Theory of Impurity Scattering in Semiconductors. *Phys. Rev.*, 77(3):388–390, feb 1950.
- [75] Eric S. Toberer, Andrew F. May, and G. Jeffrey Snyder. Zintl Chemistry for Designing High Efficiency Thermoelectric Materials . *Chem. Mater.*, 22(3):624–634, feb 2010.
- [76] Joseph P. Heremans, Vladimir Jovovic, Eric S. Toberer, Ali Saramat, Ken Kurosaki, Anek Charoenphakdee, Shinsuke Yamanaka, and G Jeffrey Snyder. Enhancement of Thermoelectric Efficiency in PbTe by Distortion of the Electronic Density of States. *Science (80-. )*, 321(5888):554–557, jul 2008.
- [77] Kanishka Biswas, Jiaqing He, Qichun Zhang, Guoyu Wang, Ctirad Uher, Vinayak P Dravid, and Mercouri G Kanatzidis. Strained endotaxial nanostructures with high thermoelectric figure of merit. *Nat. Chem.*, 3(2):160–6, feb 2011.
- [78] R. Franz and G. Wiedemann. Ueber die Wärme-Leitungsfähigkeit der Metalle. *Ann. der Phys. und Chemie*, 165(8):497–531, 1853.
- [79] R. Berman. *Thermal Conduction in Solids*. Oxford University Press, Oxford, 1 edition, 1976.
- [80] H.B.G. Casimir. Note on the conduction of heat in crystals. *Physica*, 5(6):495–500, 1938.
- [81] I. Pomeranchuk. No Title. *J. Phys. U.S.S.R.*, 6:237, 1942.
- [82] Glen A. Slack. Effect of Isotopes on Low-Temperature Thermal Conductivity. *Phys. Rev.*, 105(3):829–831, feb 1957.
- [83] Donald T. Morelli, Thomas A. Perry, and John W. Farmer. Phonon scattering in lightly neutron-irradiated diamond. *Phys. Rev. B*, 47(1):131–139, 1993.
- [84] John William Strutt and Baron Rayleigh. *The Theory of Sound*. Macmillan And Co, New York, 2 edition, 1896.
- [85] P G Klemens. The Scattering of Low-Frequency Lattice Waves by Static Imperfections. *Proc. Phys. Soc. Sect. A*, 68(12):1113–1128, 1955.

- [86] Glen A. Slack. Thermal Conductivity of Potassium Chloride Crystals Containing Calcium. *Phys. Rev.*, 105(3):832–842, feb 1957.
- [87] E. V. Mielczarek and H. P. R. Frederikse. Thermal Conductivity of Indium Antimonide at Low Temperatures. *Phys. Rev.*, 14(4):888, 1959.
- [88] C. J. Glassbrenner and Glen A. Slack. Thermal Conductivity of Silicon and Germanium from 3K to the Melting Point. *Phys. Rev.*, 134(4A):A1058–A1069, may 1964.
- [89] G.A. Slack. Nonmetallic crystals with high thermal conductivity. *J. Phys. Chem. Solids*, 34(2):321–335, jan 1973.
- [90] Sl Shindé and J Goela. *High thermal conductivity materials*. Springer US, 2006.
- [91] Glen A. Slack. The Thermal Conductivity of Nonmetallic Crystals. In *Solid State Phys. - Adv. Res. Appl.*, volume 34, pages 1–71. Academic Press, 1979.
- [92] J. Jaffe and Alex Zunger. Theory of the band-gap anomaly in ABC<sub>2</sub> chalcopyrite semiconductors. *Phys. Rev. B*, 29(4):1882–1906, feb 1984.
- [93] T. Bekkay, M. Boustani, K. El Assali, A. Khiara, J.C. Bernéde, and J. Pouzet. Structural and optical properties of CuAlTe<sub>2</sub> thin films prepared by RF. sputtering. *Int. J. Electron.*, 92(8):445–449, aug 2005.
- [94] N A Mohsen, S N Elsayed, and A H A El-Ela. Electrical conductivity, thermoelectric power and thermal conductivity of CuTlTe<sub>2</sub> in the solid and liquid states. *Acta Phys. Hungarica*, 67(1-2):223–228, 1990.
- [95] L V Kradinova, A M Polubotko, V V Popov, V D Prochukhan, Yu V Rud, and V E Skoriukin. Novel zero-gap compounds, magnetics: CuFeS<sub>2</sub> and CuFeTe<sub>2</sub>. *Semicond. Sci. Technol.*, 8(8):1616–1619, aug 1993.
- [96] V. V. Popov, P. P. Konstantinov, and Yu. V. Rud'. Kinetic phenomena in zero-gap semiconductors CuFeS<sub>2</sub> and CuFeTe<sub>2</sub>: Effect of pressure and heat treatment. *J. Exp. Theor. Phys.*, 113(4):683–691, nov 2011.
- [97] I G Austin, C H L Goodman, and A E Pengelly. New Semiconductors with the Chalcopyrite Structure. *J. Electrochem. Soc.*, 103(11):609, 1956.

- [98] G Marin, Carlos Rincon, S. M. Wasim, Ch. Power, and G. Sanchez Perez. Temperature dependence of the fundamental absorption edge in CuInTe<sub>2</sub>. *J. Appl. Crystallogr.*, 81(11):7580–7583, 1997.
- [99] I.V. Bodnar, A. Eifler, Th. Doering, W. Schmitz, K. Bente, V.F. Gremenok, I.A. Victorov, and V. Riede. Growth and Characterisation of (CuInTe<sub>2</sub>)<sub>1-x</sub>(2 ZnTe)<sub>x</sub> Solid Solution Single Crystals. *Cryst. Res. Technol.*, 35(10):1135–1140, oct 2000.
- [100] M Leon, J. M. Merino, and J. L. Martin De Vidales. Crystal structure of synthesized CuGaTe<sub>2</sub> determined by X-ray powder diffraction using the Rietveld method. *J. Mater. Sci.*, 27:4495–4500, 1992.
- [101] V. P. Zhuze, W. M. Sergeeva, and E. L. Shtrum. No Title. *J. Tech. Phys.*, 28:2093, 1958.
- [102] Vijay Kumar Gudelli, V. Kanchana, G. Vaitheeswaran, A. Svane, and N. E. Christensen. Thermoelectric properties of chalcopyrite type CuGaTe<sub>2</sub> and chalcostibite CuSbS<sub>2</sub>. *J. Appl. Phys.*, 114(22):223707, 2013.
- [103] Jueming Yang, Yuli Yan, Yuan Xu Wang, and Gui Yang. Improved thermoelectric performance of CuGaTe<sub>2</sub> with convergence of band valleys: a first-principles study. *RSC Adv.*, 4(54):28714, 2014.
- [104] J. Jaffe and Alex Zunger. Electronic structure of the ternary chalcopyrite semiconductors CuAlS<sub>2</sub>, CuGaS<sub>2</sub>, CuInS<sub>2</sub>, CuAlSe<sub>2</sub>, CuGaSe<sub>2</sub>, and CuInSe<sub>2</sub>. *Phys. Rev. B*, 28(10):5822–5847, 1983.
- [105] J. Lamazares, F. Gonzalez-Jimenez, E Jaimes, L. D’Onofrio, R Iraldi, G. Sanchez-Porrás, M. Quintero, J. Gonzalez, J.C. Woolley, and G. Lamarche. Magnetic, transport, X-ray diffraction and Mössbauer measurements on CuFeSe<sub>2</sub>. *J. Magn. Magn. Mater.*, 104-107:997–998, feb 1992.
- [106] D. Berthebaud, O.I. Lebedev, and A. Maignan. Thermoelectric properties of n-type cobalt doped chalcopyrite Cu<sub>1-x</sub>CoxFeS<sub>2</sub> and p-type eskebornite CuFeSe<sub>2</sub>. *J. Mater.*, 1(1):68–74, mar 2015.
- [107] B. Tell, J. L. Shay, and H. M. Kasper. Room-temperature electrical properties of ten I-III-VI<sub>2</sub> semiconductors. *J. Appl. Phys.*, 43(1972):2469–2470, 1972.
- [108] J. Rodríguez, L Quiroga, A Camacho, and R Baquero. Electronic band structure of CuInSe<sub>2</sub>: Bulk and (112) surface. *Phys. Rev. B*, 59(3):1555–1558, jan 1999.

- [109] J. L. Shay, J. H. Wernick, and B. R. Pamplin. *Ternary Chalcopyrite Semiconductors: Growth, Electronic Properties, and Applications*. Pergamon Press Inc., 1975.
- [110] B. Tell and P. Bridenbaugh. Aspects of the band structure of  $\text{CuGaS}_2$  and  $\text{CuGaSe}_2$ . *Phys. Rev. B*, 12(8):3330–3335, oct 1975.
- [111] Yu-Jun Zhao and Alex Zunger. Electronic structure and ferromagnetism of Mn-substituted  $\text{CuAlS}_2$ ,  $\text{CuGaS}_2$ ,  $\text{CuInS}_2$ ,  $\text{CuGaSe}_2$ , and  $\text{CuGaTe}_2$ . *Phys. Rev. B*, 69(10):104422, mar 2004.
- [112] Susanne Siebentritt and Steffen Schuler. Defects and transport in the wide gap chalcopyrite  $\text{CuGaSe}_2$ . *J. Phys. Chem. Solids*, 64(9-10):1621–1626, 2003.
- [113] L. Vegard. Die Konstitution der Mischkristalle und die Raumfüllung der Atome. *Zeitschrift für Phys.*, 5(1):17–26, jan 1921.
- [114] S. R. Hall. Crystal Structures of the Chalcopyrite Series. *Can. Mineral.*, 13:168–172, 1975.
- [115] P. Grima Gallardo. Order-Disorder Phase Transitions in Alloy Systems. *Phys Stat Sol*, 134:119–125, 1992.
- [116] Su-Huai Huai Wei, L. G. Ferreira, and Alex Zunger. First-principles calculation of the order-disorder transition in chalcopyrite semiconductors. *Phys. Rev. B*, 45(5):2533–2536, feb 1992.
- [117] Alex Zunger. Order-disorder transformation in ternary tetrahedral semiconductors. *Appl. Phys. Lett.*, 50(3):164–166, jan 1987.
- [118] Charles L. Burdick and James H. Ellis. THE CRYSTAL STRUCTURE OF CHALCOPYRITE DETERMINED BY X-RAYS. *J. Am. Chem. Soc.*, 39(12):2518–2525, dec 1917.
- [119] Linus Pauling and L. O. Brockway. The Crystal Structure of Chalcopyrite  $\text{CuFeS}_2$ . *Zeitschrift für Krist. - Cryst. Mater.*, 82(1-6), jan 1932.
- [120] Teruo Teranishi, Katsuaki Sato, and Ken'ichi Kondo. Optical Properties of a Magnetic Semiconductor: Chalcopyrite  $\text{CuFeS}_2$  .: I. Absorption Spectra of  $\text{CuFeS}_2$  and Fe-Doped  $\text{CuAlS}_2$  and  $\text{CuGaS}_2$ . *J. Phys. Soc. Japan*, 36(6):1618–1624, jun 1974.

- [121] Toshiki Hamajima, Takeshi Kambara, and Ken Ichiro Gondaira. Self-consistent electronic structures of magnetic semiconductors by a discrete variational Xa calculation. Chalcopyrite CuFeS<sub>2</sub>. *Phys. Rev. B*, 24(6):3349–3353, 1981.
- [122] R. Blachnik and A. Müller. The formation of Cu<sub>2</sub>S from the elements: I. Copper used in form of powders. *Thermochim. Acta*, 361:31–52, 2000.
- [123] S. Mishra and B. Ganguli. Effect of Na substitution on electronic and optical properties of CuInS<sub>2</sub> chalcopyrite semiconductor. *J. Solid State Chem.*, 232:131–137, dec 2015.
- [124] B. Tell, J. L. Shay, and H. M. Kasper. Electrical Properties, Optical Properties, and Band Structure of CuGaS<sub>2</sub> and CuInS<sub>2</sub>. *Phys. Rev. B*, 4(8):2463–2471, 1971.
- [125] B. Tell, J. L. Shay, and H. M. Kasper. Room-temperature electrical properties of ten I-III-VI<sub>2</sub> semiconductors. *J. Appl. Phys.*, 43(5):2469–2470, 1972.
- [126] Winston D. Carr and Donald T. Morelli. The Thermoelectric Properties and Solubility Limit of CuFeS<sub>2</sub>(1-x)Se<sub>2x</sub>. *J. Electron. Mater.*, 2, sep 2015.
- [127] A.-M Lamarche, J.C Woolley, G Lamarche, I.P Swainson, and T.M Holden. Structure and magnetic properties of the ternary compound copper iron telluride. *J. Magn. Magn. Mater.*, 186(1-2):121–128, 1998.
- [128] T. Nomiya, H. Kuriyaki, and K. Hirakawa. Photo-rechargeable battery using new layer compound CuFeTe<sub>2</sub>. *Synth. Met.*, 71(1-3):2237–2238, 1995.
- [129] L V Kradinova, A M Polubotko, V V Popov, V D Prochukhan, Yu V Rud, and V E Skoriukin. Novel zero-gap compounds, magnetics: CuFeS<sub>2</sub> and CuFeTe<sub>2</sub>. *Semicond. Sci. Technol.*, 8(8):1616–1619, aug 1993.
- [130] A A Vaipolin, S A Kijaev, L V Kradinova, A M Polubotko, V V Popov, V D Prochukhan, Yu V Rud, and V E Skoriukin. Investigation of the gapless state in CuFeTe<sub>2</sub>. *J. Phys. Condens. Matter*, 4(40):8035–8038, oct 1992.
- [131] Alfred J. Frueh. An extension of the ‘Difference Patterson’ to facilitate the solution of orderdisorder problems. *Acta Crystallogr.*, 6(6):454–456, jun 1953.
- [132] Benjamin A. Grguric, Andrew Putnis, and Richard J. Harrison. An investigation of the phase transitions in bornite ( Cu<sub>5</sub>FeS<sub>4</sub> ) using neutron diffraction and differential scanning calorimetry. *Am. Mineral.*, 83(1978):1231–1239, 1998.

- [133] Richard A Robie, Robery R. Seal, and Bruce S. Hemingway. Heat capacity and entropy of bornite ( $\text{Cu}_5\text{FeS}_4$ ) between 6 and 760 K and the thermodynamic properties of phases in the system Cu-Fe-S. *Can. Mineral.*, 32:945–956, 1994.
- [134] J SHEMILT, B STEELE, and J WESTON. Thermodynamics and mobility of copper in bornite ( $\text{Cu}_5\text{FeS}_4$ ). *Solid State Ionics*, 2(2):73–85, apr 1981.
- [135] Emil Makovicky and Brian J. Skinner. STUDIES OF THE SULFOSALTS OF COPPER VII. CRYSTAL STRUCTURES OF THE EXSOLUTION PRODUCTS  $\text{Cu}_{12.3}\text{Sb}_4\text{S}_{13}$  AND  $\text{Cu}_{13.8}\text{Sb}_4\text{S}_{13}$  OF UNSUBSTITUTED SYNTHETIC TETRAHEDRI. *Can. Mineral.*, 17:619–634, 1979.
- [136] Jiang Xiao-Shu, Yan Ying-Ce, Yuan Shi-Min, Mi Shu, Niu Zhen-Guo, and Liang Jiu-Qing. Trends in the band-gap pressure coefficients and bulk moduli in different structures of  $\text{ZnGa}_2\text{S}_4$ ,  $\text{ZnGa}_2\text{Se}_4$  and  $\text{ZnGa}_2\text{Te}_4$ . *Chinese Phys. B*, 19(10):107104, 2010.
- [137] Ken Kurosaki, Hideaki Matsumoto, Anek Charoenphakdee, Shinsuke Yamanaka, Manabu Ishimaru, and Yoshihiko Hirotsu. Unexpectedly low thermal conductivity in natural nanostructured bulk  $\text{Ga}_2\text{Te}_3$ . *Appl. Phys. Lett.*, 93(1):3–5, 2008.
- [138] Yanzhong Pei, Xiaoya Shi, Aaron LaLonde, Heng Wang, Lidong Chen, and G Jeffrey Snyder. Convergence of electronic bands for high performance bulk thermoelectrics. *Nature*, 473(7345):66–9, may 2011.
- [139] G Jeffrey Snyder and Eric S Toberer. Complex thermoelectric materials. *Nat. Mater.*, 7(2):105–14, feb 2008.
- [140] Jin-cheng Zheng. Recent advances on thermoelectric materials. *Front. Phys. China*, 3(3):269–279, jul 2008.
- [141] J. Shay, B. Tell, H. Kasper, and L. Schiavone. p-d Hybridization of the Valence Bands of I-III-VI<sub>2</sub> Compounds. *Phys. Rev. B*, 5(12):5003–5005, jun 1972.
- [142] J. Shay, B. Tell, H. Kasper, and L. Schiavone. Electronic Structure of  $\text{AgInSe}_2$  and  $\text{CuInSe}_2$ . *Phys. Rev. B*, 7(10):4485–4490, 1973.
- [143] Yubo Luo, Junyou Yang, Qinghui Jiang, Weixin Li, Ye Xiao, Liangwei Fu, Dan Zhang, Zhiwei Zhou, and Yudong Cheng. Large enhancement of thermoelectric performance of  $\text{CuInTe}_2$  via a synergistic strategy of point defects and microstructure engineering. *Nano Energy*, 2015.

- [144] Barry P. Rand, Jan Genoe, Paul Heremans, and Jef Poortmans. Solar Cells Utilizing Small Molecular Weight Organic Semiconductors. *Prog. Photovolt Res. Appl.*, 15(February 2013):659–676, 2007.
- [145] Yi Tang, R. Braunstein, and Bolko Von Roedern. Determination of drift mobility and lifetime for dominant charge carriers in polycrystalline CuInSe<sub>2</sub> by photomixing. *Appl. Phys. Lett.*, 63(17):2393–2395, 1993.
- [146] Glen Slack. CRC-95-Chapter 34.pdf. In *CRC Handb. Thermoelectr.*, pages 407–440. CRC Press, 1995.
- [147] Linus Pauling. The Nature of the Chemical Bond. *J. Chem. Educ.*, 69(7):656, jul 1992.
- [148] Xiaoshu Jiang and Walter R. L. Lambrecht. Electronic band structure of ordered vacancy defect chalcopyrite compounds with formula I-III<sub>2</sub>-VI<sub>4</sub>. *Phys. Rev. B*, 69(3):035201, jan 2004.